

Pathways and variability  
of the circulation in the  
subpolar eastern North Atlantic  
studied with inverted echo sounders  
and model data

Hannah Nowitzki

University of Bremen, 2021



# Pathways and variability of the circulation in the subpolar eastern North Atlantic studied with inverted echo sounders and model data

Vom Fachbereich für Physik und Elektrotechnik  
der Universität Bremen genehmigte Dissertation  
zur Erlangung des akademischen Grades  
Doktor der Naturwissenschaften (Dr. rer. nat.)

von  
Hannah Nowitzki  
aus Bielefeld

1. Gutachterin: Prof. Dr. Monika Rhein
2. Gutachter: Dr. Gunnar Spreen

Eingereicht am: 18. Juni 2021

Tag des Promotionskolloquiums: 29. Juli 2021



## Abstract

The North Atlantic Current (NAC) as part of the Atlantic Meridional Overturning Circulation (AMOC) is the major pathway for warm and saline water from the subtropics into the subpolar North Atlantic. Due to buoyancy loss along its flow path and subsequent deep water formation, it connects the upper warm limb of the AMOC with the deeper cold limb. Associated volume fluxes and their variability are thus of great interest, especially in the context of climate change.

The main branch of the NAC and related transports are widely studied. The NAC crosses  $47^{\circ}/48^{\circ}\text{N}$  in the western North Atlantic and further north the Mid-Atlantic Ridge (MAR) before entering the eastern subpolar basin where it partly feeds the Subpolar Gyre or flows into the Nordic Seas. To quantify the meridional exchange of water between the subtropical and subpolar regime in the interior eastern North Atlantic where studies are scarce, in this work, long-term (1993 to 2017) transport time series were calculated by combining data from inverted echo sounders taken in 2016 and 2017 with satellite altimetry. The results obtained from observational data are complemented with transport time series calculated from high resolution model output of the ANHA12 configuration of the NEMO model and with the analysis of particle trajectories calculated from the Lagrangian model ARIANE.

The observational data reveal an additional more direct pathway from the south across  $47^{\circ}/48^{\circ}\text{N}$  into the subpolar eastern North Atlantic with a mean northward transport of  $+9.1\text{ Sv} \pm 0.8\text{ Sv}$  contributing about 22 % to the total inflow of  $+41.4\text{ Sv}$  into the eastern basin. The meridional transport of this pathway is significantly anticorrelated to the transport across the MAR ( $R = -0.7$ ), damping the interannual variability of the total inflow into the subpolar eastern North Atlantic. Moreover, for the meridional transport in the interior eastern basin, a positive trend of  $+2.0\text{ Sv} \pm 1.5\text{ Sv}$  per decade is found, partly balancing the negative decadal trend of  $-6.0\text{ Sv} \pm 5.7\text{ Sv}$  observed for the interior western basin. The mean transport imbalance at the  $47^{\circ}/48^{\circ}\text{N}$  transect between Newfoundland and  $15^{\circ}\text{W}$  was found to be  $-2.2\text{ Sv}$  which is likely to be compensated by the flow east of  $15^{\circ}\text{W}$ .

In the model, the overall circulation pattern in the subpolar North Atlantic as well as the main regions for water mass transformation are very similar to what is found from observations. However, also substantial differences between the model and observations were found such as a surplus northward flow across  $47^{\circ}/48^{\circ}\text{N}$  in the western basin, a weaker coupling between the western and eastern basin, and a smaller total inflow into the eastern subpolar North Atlantic of  $+24.2\text{ Sv}$ . Moreover, the analysis of particle trajectories reveals that about 60 % of the water at  $47^{\circ}/48^{\circ}\text{N}$  and the MAR originates in the subtropics and about 11 % flows into the Nordic Seas.



# Contents

<b>1</b>	<b>Introduction</b>	<b>1</b>
1.1	Main circulation in the subpolar North Atlantic . . . . .	3
1.1.1	The North Atlantic Current . . . . .	3
1.1.2	Deep water formation in the subpolar North Atlantic . . . . .	7
1.2	Thesis objectives . . . . .	9
<b>2</b>	<b>Data</b>	<b>13</b>
2.1	Observational data . . . . .	13
2.1.1	PIES . . . . .	13
2.1.2	Hydrographic data . . . . .	15
2.1.3	Satellite altimetry . . . . .	17
2.2	Model data . . . . .	18
2.2.1	ANHA12 model configuration of the NEMO model . . . . .	18
2.2.2	The Lagrangian model ARIANE . . . . .	24
2.3	Reanalysis data . . . . .	27
<b>3</b>	<b>Methodology</b>	<b>29</b>
3.1	Sea surface height fluctuations and volume transport obtained from PIES data	29
3.1.1	Pre-processing of PIES data obtained by telemetry . . . . .	29
3.1.2	Transfer of PIES measured travel times into specific volume anomaly . .	30
3.1.3	Barotropic and baroclinic sea surface height fluctuations . . . . .	34
3.1.4	Barotropic and baroclinic transport fluctuations . . . . .	36
3.1.5	Absolute PIES transport time series . . . . .	37
3.1.6	Transport time series extended by altimetry . . . . .	38
3.1.7	Uncertainty estimates . . . . .	38
3.2	Ekman transport from reanalysis data . . . . .	44
3.3	Transport time series obtained from model output . . . . .	45

<b>4 Trends and transport variability of the circulation in the subpolar eastern North Atlantic studied with inverted echo sounders</b>	<b>47</b>
4.1 Correlation between PIES and altimeter-derived SSH . . . . .	47
4.2 Transports . . . . .	50
4.2.1 PIES-derived transport in 2016 and 2017 . . . . .	50
4.2.2 PIES- and altimeter-derived transport in 1993 to 2017 . . . . .	54
4.2.3 Long-term trends . . . . .	57
4.2.4 Correlation between the meridional flow in the interior eastern and western basin and the transport across the MAR . . . . .	58
4.3 Summary and Discussion . . . . .	60
<b>5 The circulation in the subpolar eastern North Atlantic studied with model output</b>	<b>65</b>
5.1 Comparison of transports obtained from model data and observations . . . . .	65
5.1.1 Correlation between the meridional flow in the interior eastern and western basin, the transport across the MAR, and with the WBC . . . . .	73
5.2 Flow paths into the subpolar eastern North Atlantic . . . . .	74
5.2.1 Source regions and destination of particles seeded at the PIES transects	75
5.2.2 Exchange of particles between different regions . . . . .	90
5.2.3 Water mass transformation . . . . .	97
5.3 Summary and Discussion . . . . .	99
<b>6 Summary and Conclusion</b>	<b>103</b>
<b>7 Outlook</b>	<b>107</b>
<b>A Appendix</b>	<b>109</b>
<b>Bibliography</b>	<b>123</b>
<b>Listings</b>	<b>135</b>
List of Figures . . . . .	135
List of Tables . . . . .	138
<b>Abbreviations</b>	<b>141</b>
<b>Funding and Data Acknowledgment</b>	<b>147</b>





# 1 Introduction

The global ocean circulation includes a variety of major and minor currents in the surface layers and in the deep ocean. The possibly most famous and widely studied overarching circulation scheme is the Meridional Overturning Circulation (MOC), also referred to as the Great Ocean Conveyor Belt (Broecker, 1991), whose Atlantic part is the Atlantic Meridional Overturning Circulation (AMOC). It describes the zonally integrated flow in the ocean (Wunsch, 2002) and consists of many such major and minor currents. In a very simplified view, the main components of the AMOC are the wind-driven warm surface currents (the upper limb of the AMOC), a downward mass flux as a result of buoyancy loss, the flow of cold and dense deep waters (the lower limb of the AMOC), and wind-driven upwelling of deep waters (Kuhlbrodt et al., 2007; Stommel, 1961; Wunsch, 2002). As one of the dominating mechanisms behind the meridional heat transport towards the poles (Johns et al., 2011), the AMOC is an important component of the Earth's climate system which primarily also influences the climate in Northern Europe through the exchange of heat between the warm surface currents and the atmosphere (Buckley et al., 2016; Kuhlbrodt et al., 2007; Palter, 2015; Rhines et al., 2008; SROCC, 2019).

Being one of the few regions of the world oceans in which deep convection and formation of deep waters and hence of the source waters for the lower limb of the AMOC takes place (e.g. Petit et al., 2020; Pickart et al., 2003; Schmitz et al., 1993), the subpolar North Atlantic is one of the key climate relevant areas. The ocean currents within the subpolar North Atlantic, associated volume, heat, and freshwater fluxes, and their variability are thus of great interest, especially in the context of climate change.

Various studies exist that investigate and quantify the current branches in the Newfoundland Basin, i.e. the transition region between the subtropical and subpolar regime in the western North Atlantic. These are based on mooring devices and repeated ship surveys obtained from a survey line following the latitude of  $47^{\circ}/48^{\circ}\text{N}$  and output of high-resolution ocean models (among others Breckenfelder et al., 2017; Mertens et al., 2014; Rhein et al., 2011; Rhein et al., 2019; Roessler et al., 2015). However, studies concerning the meridional exchange of water between the subtropical and subpolar regime in the interior eastern basin are scarce. To close this gap, this study focuses on the meridional transport across the  $47^{\circ}/48^{\circ}\text{N}$  transect in the

interior eastern North Atlantic calculated from observational data and high resolution model output. To further examine the surrounding hydrographic and dynamic conditions and circulation patterns, sea surface height (SSH) fluctuations from observational data, model-based transports for the western basin and the Mid-Atlantic Ridge (MAR) region, and Lagrangian trajectories calculated from model velocity fields revealing amongst others regions for water mass transformation are presented complementary.

In the following, this chapter provides a more detailed introduction into the circulation in the subpolar North Atlantic. Moreover, the processes behind water mass transformation and the formation of deep waters which are pivotal for the AMOC (e.g. Bi et al., 2001; Gregory et al., 2005) are introduced. Additionally, the scope of this work as well as the research questions behind it are presented in more detail. As a first introduction into the study region, Figure 1.1 gives an overview of the subpolar North Atlantic highlighting important basins and names of several regional features referred to in different contexts throughout this study.

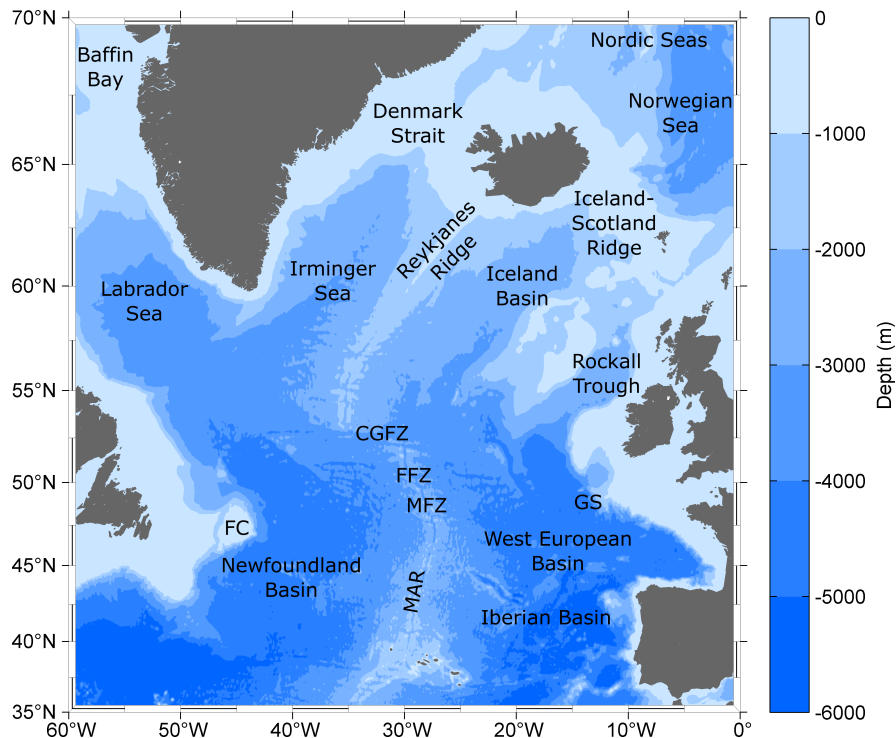


**Figure 1.1:** Map of the subpolar North Atlantic including the bathymetry and important names of basins and regional features this work refers to. Blue colors indicate the bathymetry in 1000 m steps. Abbreviations used in the map are FC (Flemish Cap), CGFZ (Charlie-Gibbs-Fracture-Zone), FFZ (Faraday-Fracture-Zone), MFZ (Maxwell-Fracture-Zone), MAR (Mid-Atlantic Ridge), GS (Goban Spur). Note: the Norwegian Sea is part of what is summarized under the term Nordic Seas. The map was created following Kieke (2005).

## 1.1 Main circulation in the subpolar North Atlantic

The main circulation pattern in the subpolar North Atlantic is the Subpolar Gyre (cf. Figure 1.2), a counter-clockwise current system including warm and salty near-surface currents and the flow of cold and dense waters in the deep ocean. The warm and salty surface currents of the Subpolar Gyre are the North Atlantic Current (NAC) which is the northward extension of the Gulf Stream, flowing in northeastward direction from the Canadian coast across the MAR into the eastern basin and partly following further downstream the bathymetry of the Reykjanes Ridge (cf. Figure 1.3a) and the East-Greenland Irminger Current following the coast of Greenland (Daniault et al., 2016; García-Ibáñez et al., 2015). Another inflow into the subpolar eastern Atlantic occurs through the Eastern Boundary Current (EBC) system, including the warm and salty outflow from the Mediterranean Sea that flows through the Strait of Gibraltar as well as the European slope current (e.g. González-Pola et al., 2019; González-Pola et al., 2005; Holliday et al., 2015; Iorga et al., 1999; Lozier et al., 2008; Reid, 1979; Stendardo et al., 2015). The East and West Greenland Current, and the Labrador Current fed by outflow of the Nordic Seas and Baffin Bay as well as the Deep Western Boundary Current (DWBC) which consists of cold and dense Labrador Sea Water (LSW) and overflow waters entering the Subpolar Gyre through Denmark Strait and via the Iceland-Scotland Ridge compose the cold and dense currents in the deep ocean (Daniault et al., 2016; García-Ibáñez et al., 2015).

### 1.1.1 The North Atlantic Current

The focus of this work is the NAC which, as the northward extension of the Gulf Stream, is the major oceanic artery to transport warm and saline water from the subtropics into the subpolar North Atlantic (Rossby, 1996). It contributes to the upper limb of the AMOC and as such plays an important role for regulating the global climate (IPCC, 2014; SROCC, 2019). Improving the knowledge regarding details on the various NAC pathways and quantification of the associated volume transport is thus of high importance in this context. The general course of the NAC is well known (Figure 1.3a). In the Newfoundland Basin, the NAC splits up into a recirculation (Bower et al., 2009; Mertens et al., 2014) and different branches that cross the MAR, e.g. via the Charlie-Gibbs- (CGFZ), Maxwell- (MFZ) and Faraday- (FFZ) Fracture-Zones (Bower et al., 2008; Rhein et al., 2011; Roessler et al., 2015). These branches subsequently flow eastward and continue into the Nordic Seas or they partly recirculate westward and feed the subpolar boundary current system, thus contributing to the Subpolar Gyre (Bower et al., 2002; Schott et al., 1999).

The NAC enters the Newfoundland Basin at a very high strength in the order of 100 Sv

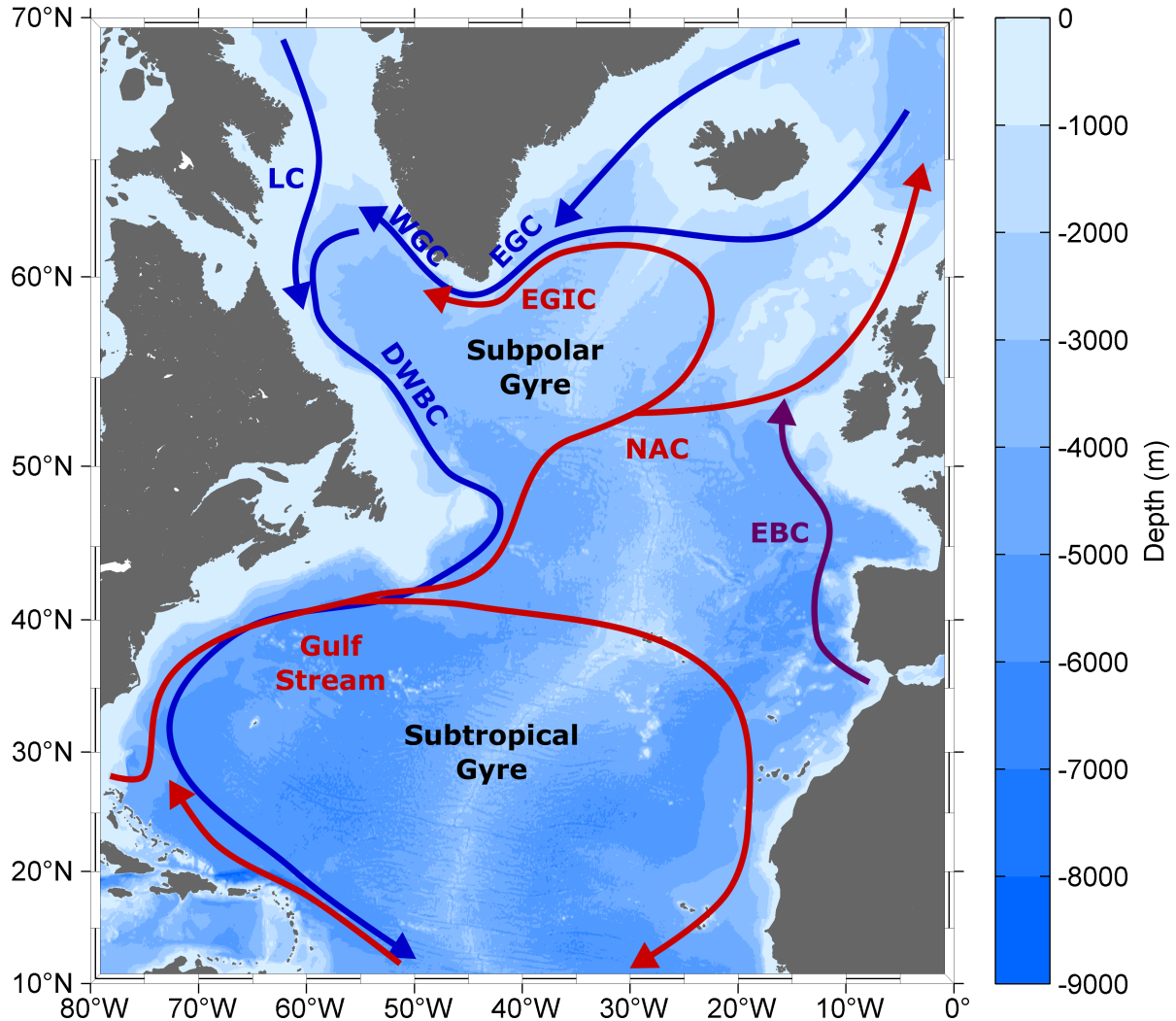


**Figure 1.2:** Simplified Circulation scheme of the North Atlantic including the Subpolar and Subtropical Gyre. The warm currents forming the main surface flow of the Subpolar and Subtropical Gyre are the Gulf Stream, the North Atlantic Current (NAC), and the East-Greenland Irminger Current (EGIC). Another inflow contributing to the Subpolar Gyre is the Eastern Boundary Current system (EBC). The cold and dense currents forming the deep flow of the gyres are the East (EGC) and West (WGC) Greenland Current, the Labrador Current (LC), as well as the Deep Western Boundary Current (DWBC). The surface currents (Gulf Stream, NAC, EGIC) are shown in red, the EBC including the salty outflow of the Mediterranean Sea in purple, and the deep currents (EGC, WGC, LC, and DWBC) in blue. The circulation scheme is based Daniault et al. (2016), García-Ibáñez et al. (2015), Lherminier et al. (2010), and Stendardo et al. (2015). Note: The flow paths of the currents as depicted here are very much simplified. A more detailed circulation scheme with the focus on the subpolar North Atlantic and the NAC is shown in Figure 1.3.

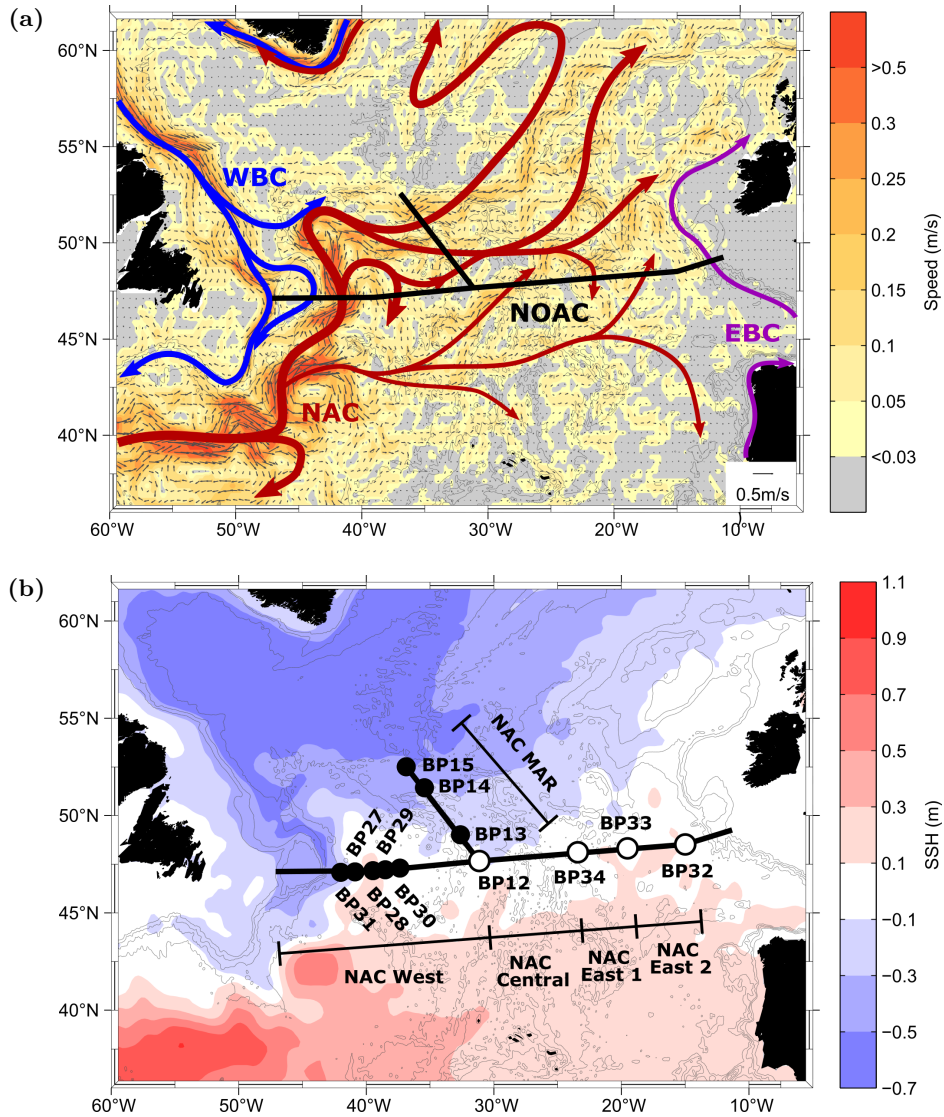


**Figure 1.3:** Panel (a) shows a simplified circulation scheme with a focus on the NAC and the location of the NOAC (North Atlantic Changes) array (e.g. Frajka-Williams et al., 2019). The colored contour plot in the background represents the mean satellite derived geostrophic surface velocity in 2016/2017, the arrows represent the direction and are scaled according to the velocity. The NAC circulation scheme is based on results of this study, previous studies (Daniault et al., 2016; Stendardo et al., 2020), and the satellite geostrophic velocity. The Western Boundary Current (WBC) as shown here combines the flow paths of the West Greenland Current, the Labrador Current and the Deep Western Boundary Current (Schneider et al., 2015). The Eastern Boundary Current (EBC) as shown here combines the flow paths of the Mediterranean Outflow Water and the slope current (Daniault et al., 2016; González-Pola et al., 2019; González-Pola et al., 2005; Holliday et al., 2015; Lozier et al., 2008; Stendardo et al., 2015). Panel (b) shows a detailed view of the NOAC array including the PIES locations shown as black and white circles, the PIES names (BPXX), and defined transport sections: *NAC MAR* ( $47^{\circ}40'N - 53^{\circ}30'N$ , transports analyzed in Roessler et al. 2015), *NAC West*/interior western basin ( $42^{\circ}W - 31^{\circ}08'W$ , transports analyzed in Rhein et al. 2019), *NAC Central* ( $31^{\circ}08'W-23^{\circ}25'W$ ), *NAC East 1* ( $23^{\circ}25'W-19^{\circ}32'W$ ) and *NAC East 2* ( $19^{\circ}32'W-15^{\circ}W$ ). The PIES represented by black circles are used in the SSH analysis. For the PIES represented by white circles, SSH and transports are analyzed. The colored contour plot represents the mean satellite SSH in 2016/2017. Both panels show the bathymetry with gray contour lines every 1000 m.

(Meinen, 2001; Meinen et al., 2000a; Meinen et al., 2000b), with peak velocities exceeding 100 cm/s. About half of the northward flow feeds a recirculation and a southward flow in close proximity east and west of the main NAC branch (Mertens et al., 2014; Rhein et al., 2019), about 28 Sv flow southward in the interior western basin east of 37°W (Rhein et al., 2019), and approximately 47 Sv flow into the Northwest Corner, a sharp topographic bend that basically follows the 4000 m isobath. Another southward flowing component of the circulation in the Newfoundland Basin is the western boundary current (WBC) system, exporting about 23 Sv of cold and fresh water southward across 47°/48°N (Rhein et al., 2019).

It is thought that the inflow of subtropical water into the eastern subpolar basin occurs through the zonal transport from the western basin across the MAR (e.g. García-Ibáñez et al., 2015; Lherminier et al., 2010; Schmitz et al., 1993; Schott et al., 2004). Combining pressure sensor equipped inverted echo sounder (PIES) and Argo data with satellite altimetry, Roessler et al. (2015) observed a total transport of about 32 Sv (updated time series in McCarthy et al., 2020) crossing the MAR north of 47°40'N, and estimated that about 60 % were of subtropical origin. The question whether and how much other warm and saline water pathways exist that for instance cross the MAR further south and enter the subpolar eastern Atlantic by crossing 47°/48°N in northward direction is still open to discussion.

Further east, several studies discuss the transport across the OVIDE repeat hydrography line that broadly connects Greenland and Portugal (Breckenfelder et al., 2017; Daniault et al., 2016; Mercier et al., 2015). Mercier et al. (2015) and Daniault et al. (2016) use repeat hydrographic and ADCP data collected between 1997 and 2012 to study the variability of the meridional overturning at the OVIDE line. Both studies present the cumulative sum of the depth-integrated transport across the transect and the more recent study from Daniault et al. (2016) reports a NAC related transport of about 42 Sv, approximately 10 Sv larger than the transport found by Roessler et al. (2015) and McCarthy et al. (2020) further upstream, suggesting that an additional NAC pathway south of 47°40'N exists that transports water from the subtropics into the subpolar eastern North Atlantic.

While the NAC is a swift and intense current in the Newfoundland Basin, reaching from top to bottom and exhibiting thus a barotropic structure, its properties are very different in the eastern basin. Based on repeated ship surveys conducted along 47°/48°N and high-resolution model output, Müller et al. (2017) and Müller et al. (2019) identified rather broad and weak current branches in the eastern basin (cf. Figure 1.4). Their clearest signature was located in the upper 1000 m range of the water column, and peak velocities were below 20 cm/s. However, with the focus on eddy analysis, they did not quantify the transport of the current branches. In order to shed more detail on the circulation at 47°/48°N, the mean meridional velocity in 2003 to 2017 obtained from repeat LADCP measurements is presented in Figure 1.4. The flow

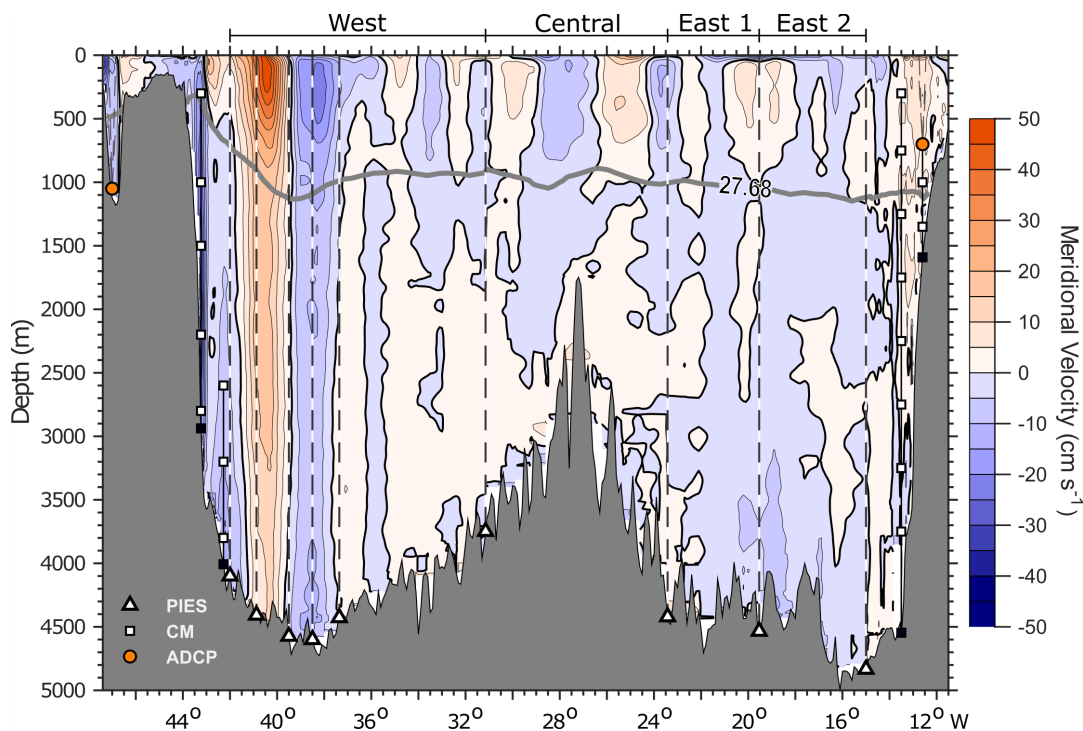


**Figure 1.4:** The NOAC array at 47°/48°N. Location of PIES (white triangles) and conventional deep-sea moorings at the western and eastern boundary with upward looking ADCPs (orange) and single point acoustic current meters (white squares). Colors denote the meridional velocities obtained from repeat LADCP measurements (2003 to 2017). The line on top indicates the region where transports obtained from PIES observations and model output are calculated and discussed, divided into a western, a central and two eastern segments. The gray line indicates the mean position of the isopycnal  $\sigma_\theta = 27.68 \text{ kg/m}^3$ . West of 44°W, the mean is calculated from on average 8 LADCP profiles, between 44°W and 31°W from on average 24, between 31°W and 15°W, from on average 8 profiles, and east of 15°W, from on average 4 profiles. Further information on the LADCP, western mooring, and PIES data can be found in Mertens et al. (2014) and Rhein et al. (2019).

is mainly surface intensified, with the strongest signals at the western boundary (Mertens et al., 2014; Rhein et al., 2019). In the eastern basin, the velocities are smaller, and, in contrast to the western basin, no permanent features can be discerned from the individual LADCP sections, which might be partly due to the much-reduced data coverage compared to the west. For later use, the transport study region is divided into a western, a central, and two eastern segments (Figure 1.4) and the MAR region (Figure 1.3).

### 1.1.2 Deep water formation in the subpolar North Atlantic

Linking the upper branches with the deep branches of the AMOC and impacting its strength (e.g. Bi et al., 2001; Gregory et al., 2005), the formation of deep waters is one of the key pro-

cesses impacting the global ocean circulation and thus inevitable to consider when studying large-scale ocean currents and circulation patterns such as the NAC or the flow with the Subpolar Gyre. Deep water formation takes place only in very few regions of the world oceans (e.g. Killworth, 1983; Pickart et al., 2003; Schmitz et al., 1993; Warren, 1983) with water masses summarized under the term North Atlantic Deep Water (NADW) being formed in the subpolar North Atlantic and in the Nordic Seas and the Antarctic Bottom Water (AABW) being formed in the Antarctic. As the focus of this work lies on the circulation in the subpolar North Atlantic, only the formation of NADW is introduced in the following, even though AABW, entering the Subpolar Gyre from the south, is also present in the subpolar North Atlantic and thus likewise part of the deep circulation in this region.

In the North Atlantic, the inflow of salty subtropical water via the NAC and Mediterranean Outflow Water (MOW), evaporation, buoyancy loss due to cooling, as well as deep convection set the condition for the formation of NADW. The water masses making up the NADW are Labrador Sea Water (LSW) which is the lightest component of NADW in the density range of  $27.68 \text{ kg/m}^3$  to  $27.8 \text{ kg/m}^3$ , Iceland-Scotland Overflow Water (ISOW) with densities between  $27.8 \text{ kg/m}^3$  and  $27.88 \text{ kg/m}^3$ , and Denmark Strait Overflow Water (DSOW) with densities below  $27.88 \text{ kg/m}^3$  (e.g. Rhein et al., 2015; Xu et al., 2018). The formation regions for ISOW and DSOW are the Nordic Seas and water that is flowing out of the Nordic Seas into the eastern North Atlantic either via the Iceland-Scotland Ridge or via Denmark Strait is named accordingly Iceland-Scotland Overflow Water or Denmark Strait Overflow Water. In the classical view, Labrador Sea Water is mainly formed in the Labrador Sea (e.g. Rhein et al., 2002; Schmitz et al., 1993). Other studies, however, identify also the Irminger Sea and Iceland Basin as important regions for the formation of LSW (Kieke et al., 2006; Lozier et al., 2019; Petit et al., 2020; Pickart et al., 2003) and debates concerning the importance of the contribution of the water formed in the different regions to the AMOC source waters are ongoing. The formation rates of the NADW water masses depend strongly on heat and freshwater fluxes and atmospheric forcing (e.g. Garcia-Quintana et al., 2019; Gerdes et al., 2006; Myers, 2005; Myers et al., 2008), i.e. on processes that are likely to change under global warming (IPCC, 2014). Generally, LSW is formed by preconditioning, i.e. the exposure of weakly stratified water masses with doming isopycnals beneath the thermocline to the surface, and deep convection occurring in winter time due to enhanced sea-air heat fluxes and accompanying buoyancy loss of the weakly stratified water masses (Lazier et al., 2002; Marshall et al., 1999). Whether this is also the main process being responsible for deep water formation in the Nordic Seas is still under debate and Eldevik et al. (2009) argue instead for a gradual transformation of inflowing Atlantic Water along the boundary currents into denser waters forming the deep waters in this region.

One of the major source waters for deep water masses are the Subpolar Mode Waters (SPMW) which are weakly stratified water masses close to the surface exhibiting nearly uniform properties (Brambilla et al., 2008b; Stendardo et al., 2015). Due to enhanced cooling accompanied by buoyancy loss, they are gradually transformed along their pathways in the subpolar North Atlantic into denser water masses with the transformation from waters with a potential density of  $27.5 \text{ kg/m}^3$  into waters with a potential density of  $27.7 \text{ kg/m}^3$  (i.e. a transformation into a water mass with the density of LSW, which is also analyzed in this work) mainly taking place east of the Reykjanes Ridge, in the Irminger Current, and in the East and West Greenland Current (Brambilla et al., 2008a). The properties of SPMW are impacted by ventilation and the circulation pattern in the subpolar North Atlantic as well as through inflowing water masses of subtropical origin (Stendardo et al., 2012; Stendardo et al., 2015). To what extent these different mechanisms contribute to the SPMW property change and how these are linked to the AMOC, however, has not been fully resolved yet. Further investigations of related processes such as water mass transformation are thus necessary and model studies such as the one presented in this work can contribute to broadening the knowledge concerning this topic.

## 1.2 Thesis objectives

The overarching goal of this work is to study the pathways and circulation in the subpolar North Atlantic with a focus on the interior eastern basin. For this purpose, observational data are used and complemented with data obtained from high resolution model output.

The first part of this study aims at elucidating the exchange of water between the subpolar and subtropical North Atlantic in the eastern basin, in particular the transport in the West European Basin across  $47^\circ/48^\circ\text{N}$  between  $31^\circ\text{W}$  and  $15^\circ\text{W}$ . To obtain volume transport time series, data from moored pressure sensor equipped inverted echo sounders (PIES) are combined with altimetry data and hydrographic data obtained from ship surveys and the international Argo program. The PIES deliver time series of bottom pressure fluctuations and travel times of an acoustic signal sent from the sea floor to the sea surface where it is reflected back to the sea floor. These data allow to infer barotropic and baroclinic SSH fluctuations and, using data of two PIES devices, barotropic and baroclinic transports. The moored sensors contribute to the eastern part of the North Atlantic Changes (NOAC) instrumental array deployed along  $47^\circ/48^\circ\text{N}$  between Flemish Cap in the west and Goban Spur in the east (e.g. Frajka-Williams et al., 2019). Figure 1.3b indicates that the  $47^\circ/48^\circ\text{N}$  section basically follows the transition zone between the subtropical and subpolar regimes, expressed by generally low levels of SSH elevations in the order of  $\pm 0.1 \text{ m}$ . Any noticeable meridional transport across this line is thus

interpreted as an exchange of water between the two regimes. The water which is transported northward across the eastern part of the measurement array presumably is to a large extent of subtropical origin. However, since it is not differentiated between the various water masses here, the exact amount cannot be quantified. The applied methods follow those described in Rhein et al. (2019) and Roessler et al. (2015) who used similar data to identify and quantify the various NAC branches in the Newfoundland Basin. For the western basin, Rhein et al. (2019) found a negative decadal trend in the meridional volume transport and argued for a compensating positive trend in the eastern basin which is also examined in this work. To further complete the picture, the transport time series calculated for the interior eastern basin are compared to the published transport time series from Mertens et al. (2014), Rhein et al. (2019), and Roessler et al. (2015). While Roessler et al. (2015) identify the baroclinic component of the flow as more relevant for the NAC related transport across the MAR, Rhein et al. (2019) find that both, the baroclinic and barotropic component, are of similar importance for the transport in the western basin. To unravel and analyze this difference, furthermore, a comparison of the different NAC regimes in terms of barotropic and baroclinic SSH fluctuations which highlights the differing characteristics of the three study regions (West, MAR and East, cf. Table 2.1) in this context is presented.

The second part of this work focuses on analyzing the representation of the circulation in the subpolar (eastern) North Atlantic in the ANHA12 configuration of the NEMO ocean model. In order to evaluate the accuracy of the model, the transport time series obtained from observational data are compared to volume transports calculated from model output. For this purpose, apart from the observation-based transport time series inferred for the eastern interior basin in this work, the published transport time series for the western basin and the MAR from Mertens et al. (2014), Rhein et al. (2019), and Roessler et al. (2015) are included in the analysis additionally. Furthermore, the Lagrangian trajectory tool ARIANE is used for calculating particle trajectories from the model velocity fields. About 770 000 particles were seeded along the NOAC array at the 47°/48°N transect between 43.5°W and 13°W and at the MAR between 48.7°N and 54°N. They were tracked with the ARIANE tool forward and backward in time for a maximum of five years between 2006 and 2017 in order to identify destinations and source regions of water crossing the NOAC array. Moreover, particle densities evolving along their flow paths in accordance with the surrounding model field are used to track the process of water mass transformation which is a key process indicator for a realistic representation of the ocean circulation in models (Heuzé, 2017).

In summary, the main questions in focus of this work are:

- How much water is exchanged in the interior eastern basin between 31°W and 15°W and how does it fit to other observations of volume transport in this region?

- Is there a trend in the meridional transport in the eastern basin that (partly) balances the negative decadal trend found by Rhein et al. (2019) for the western basin?
- How is the meridional inflow into the eastern basin related to the zonal inflow across the MAR?
- How well is the circulation scheme found from observations represented in the ANHA12 configuration of the NEMO model?
- What are the main pathways of water crossing the 47°/48°N and MAR NOAC array in the model?
- Where is water mass transformation taking place in the model?

This work is organized as follows: In Chapter 2, the different datasets used in this study are presented. In Chapter 3, the method used to convert PIES measurements of bottom pressure fluctuations and acoustic travel times into time series of barotropic and baroclinic SSH and transport fluctuations is explained and it is discussed how baroclinic transport time series inferred from PIES data are made absolute and are extended back to 1993 using satellite data. Additionally, uncertainty estimates concerning the calculated PIES transport time series are presented and the Ekman transport used to complete the transport calculations is derived in this chapter. Furthermore, it is explained how transport time series are obtained from model data. The next two chapters (Chapter 4 and 5) present and discuss the results obtained from observational data and high resolution model output following the underlying research questions of this work. Chapter 6 and 7 summarize the findings of this work and give an outlook on possible follow-up questions arising from this study. The results from Chapter 4 are already published in Nowitzki et al. (2021).



## 2 Data

### 2.1 Observational data

This study builds on a variety of different observational data obtained from single-point measurements by moored devices, repeated ship surveys and large-scale remote sensing that are outlined in the following.

#### 2.1.1 PIES

PIES are moored instruments, deployed at the seafloor, that measure bottom pressure and the vertical round trip travel time  $\tau$  of an acoustic signal sent out by the PIES at a frequency of 12 kHz. This signal travels to the sea surface where it is reflected, and back to the instrument which records its arrival time (Chaplin et al., 1984; Watts et al., 1977). Depending on the respective water depth at each instrument site, acoustic travel times are typically in the order of a few seconds. The bottom pressure is measured by each PIES once per half an hour, the acoustic travel time  $\tau$  is measured twelve times per half an hour. Daily mean values for bottom pressure and  $\tau$  are calculated as part of the instrument's internal routines as described in the Inverted Echo Sounder User Manual by University of Rhode Island (2015). Data retrieval either takes place via acoustic telemetry while the instrument remains in the water or after the instrument is recovered. During telemetry, only the daily mean values are transmitted whereas after the recovery of the instrument, the full resolution dataset can be downloaded from the instrument's hard disk. Here, only the daily mean values are used.

Throughout the past years, twelve locations in different regions of the North Atlantic have been equipped with PIES as part of the NOAC effort, with deployment periods ranging from annual to decadal times (Table 2.1). However, due to technical issues, and because not all locations were continuously equipped with an instrument, some of the obtained time series exhibit gaps.

	Name	Position	Depth	Deployment period
<b>PIES array western basin</b>	BP31	47°05.84'N / 41°59.94'W	4236 m	25 May 2014 – 19 Jun 2017
	BP27	47°05.84'N / 40°52.53'W	4486 m	1 Jun 2013 – 22 Apr 2016
	BP28	47°09.68'N / 39°30.06'W	4578 m	31 May 2013 – 28 Apr 2016
	BP29	47°12.52'N / 38°31.09'W	4607 m	31 May 2013 – 27 Apr 2016
	BP30	47°17.52'N / 37°21.47'W	4546 m	31 May 2013 – 22 Apr 2016
<b>PIES array MAR</b>	BP12*	47°39.91'N / 31°08.88'W	4090 m	7 Aug 2006 – 19 Apr 2018
	BP13*	49°01.15'N / 32°36.69'W	3968 m	7 Aug 2006 – 28 May 2013
	BP14*	51°25.76'N / 35°26.11'W	3631 m	8 Aug 2006 – 6 Jun 2015
	BP15	52°30.48'N / 36°51.63'W	3386 m	9 Aug 2006 – 16 May 2014
<b>PIES array eastern basin</b>	BP32	48°31.12'N / 15°00.22'W	4796 m	7 Apr 2016 – 6 Jun 2017
	BP33	48°18.50'N / 19°31.74'W	4560 m	8 Apr 2016 – 8 Jun 2017
	BP34	48°06.60'N / 23°25.32'W	4486 m	10 Apr 2016 – 10 Jun 2017

**Table 2.1:** Deployment positions, depths and deployment periods for the PIES. Whenever possible the position and depth were determined via trilateration. The deployment period does not necessarily correspond to the time period from which the data were analyzed. For positions that were equipped several times with an instrument, only the latest position/depth is shown. Details concerning the array in the western basin can be found in Rhein et al. (2019), details concerning the MAR array in Roessler et al. (2015).

\* Positions were not continuously equipped with instruments during the specified deployment period, and the time series exhibits gaps.

The measurements of the bottom pressure represent mass changes in the water column and are used to calculate the barotropic contribution to SSH and volume transport fluctuations. The measurements of the acoustic travel time represent density changes in the water column and are converted into the baroclinic contribution to SSH and volume transport fluctuations. Volume transports for the western part of the 47°/48°N section (west of 31°W) have been published by Rhein et al. (2019), transports across the western flank of the MAR by Roessler et al. (2015), updates in McCarthy et al. (2020) and Rhein et al. (2019). Distinguished time series of volume transport from the eastern basin are not yet available.

In order to provide this information, the focus of this study lies on the region between 31°W (BP12) and 15°W (BP32), for which PIES data from the period 2016 to 2017 are analyzed (Table 2.1) to calculate volume transports. Additionally, data from all twelve PIES stations (Figure 1.3b) are used to discuss the correlation between PIES inferred baroclinic and barotropic contributions to SSH fluctuations with satellite measured SSH, and to compare the calculated transport time series from the eastern basin to those obtained from the western basin and from the MAR region.

### 2.1.2 Hydrographic data

Hydrographic data of temperature, salinity, and pressure obtained from Argo floats and ship-board conductivity-temperature-depth (CTD) measurements are used to create a transfer function to convert the PIES-derived travel times  $\tau$  into water column profiles of specific volume anomalies (SVA), temperature, salinity, or potential density anomaly. This procedure is called Gravest Empirical Mode (GEM) method (Meinen et al., 2004; Meinen et al., 1998; Meinen et al., 2000a; Watts et al., 2001) and will be presented in more detail in the next section. From the reconstructed SVA profiles at each PIES position, baroclinic SSH fluctuations are calculated, and from the difference between two SVA profiles at two PIES positions, transport fluctuations are inferred. For the transfer function, data from several cruises between 2015 and 2018 are used (Table 2.2 and 2.3).

Research vessel	Cruise	Date	#	DOI / Reference
Maria S. Merian	MSM43	9 Jun – 12 Jun 2015	10	10.2312/cr_msm43
Maria S. Merian	MSM53	14 Apr – 21 Apr 2016	16	10.2312/cr_msm53
Celtic Explorer	CE17007	13 May 2017	1	Pers. comm. <sup>1</sup>
Maria S. Merian	MSM64	12 Jun – 13 Jun 2017	3	10.2312/cr_msm64
Maria S. Merian	MSM73	19 Apr – 17 May 2018	9	10.2312/cr_msm73

**Table 2.2:** Research cruises from which CTD data are used to create the transfer function for PIES BP12. The date refers to the time period in which the CTD data were taken, # indicates the respective number of CTD profiles included in the analysis.

Research vessel	Cruise	Date	#	DOI / Reference
Maria S. Merian	MSM53	6 Apr – 12 Apr 2016	20	10.2312/cr_msm53
Sarmiento de Gamboa	OVIDE 2016	30 Jun – 3 Jul 2016	9	10.20350/digitalCSIC/8513 (Perez et al., 2018)
Celtic Explorer	CE17007	15 May – 19 May 2017	15	Pers. comm. <sup>1</sup>
Maria S. Merian	MSM64	6 Jun – 11 Jun 2017	13	10.2312/cr_msm64
Maria S. Merian	MSM73	12 Apr – 14 Apr 2018	6	10.2312/cr_msm73
Thalassa	OVIDE 2018	23 Jun – 25 Jun 2018	9	10.17600/18000510 (Lherminier, 2018)

**Table 2.3:** Research cruises from which CTD data are used to create the transfer function for PIES BP32, BP33, and BP34. The date indicates the time period in which the CTD data were taken, # indicates the respective number of CTD profiles included in the analysis.

All cruises carried out with RV Maria S. Merian (2015 to 2018) followed the same survey line

<sup>1</sup>cruise report: [https://cchdo.ucsd.edu/data/14809/45CE20170427\\_do.pdf](https://cchdo.ucsd.edu/data/14809/45CE20170427_do.pdf)

along 47°/48°N. The RV Celtic Explorer cruise (2017) was on a similar track in the eastern basin but on a more southern track in the western basin. The RV Sarmiento de Gamboa cruise (2016) sampled the OVIDE line, which intersects the 47°/48°N array at about 20°W. Since the shipboard CTD data are limited in space and basically only stem from spring and early summer of the respective years, they cannot be used to assess any seasonal changes in the surface layers. The hydrographic dataset was therefore extended by including profile data obtained from the international Argo float program. The Argo float measurements generally cover the upper 2000 m range of the ocean. The measured profiles have been quality-controlled by Birgit Klein from the Federal Maritime and Hydrographic Agency (BSH) as described in Kieke et al. (2009). Only delayed mode Argo data with a quality flag 1 reaching as deep as at least 1900 dbar are considered. The Argo data stem from the time period January 2015 to July 2018, which is a compromise between using a sufficiently large dataset to create a robust transfer function and avoiding that the function is distorted by profiles representing a possible different hydrographic situation prevailing at another time. Rhein et al. (2019) estimated that transfer functions based on different five years of Argo/CTD data in the time period 1993 to 2018 could lead to mean transports for the whole time series that differ by  $\pm 10\%$ . The region from which the profiles are taken (Figure 2.1), is chosen by considering topographic constraints and different hydrographic realms (Figure 1.3).

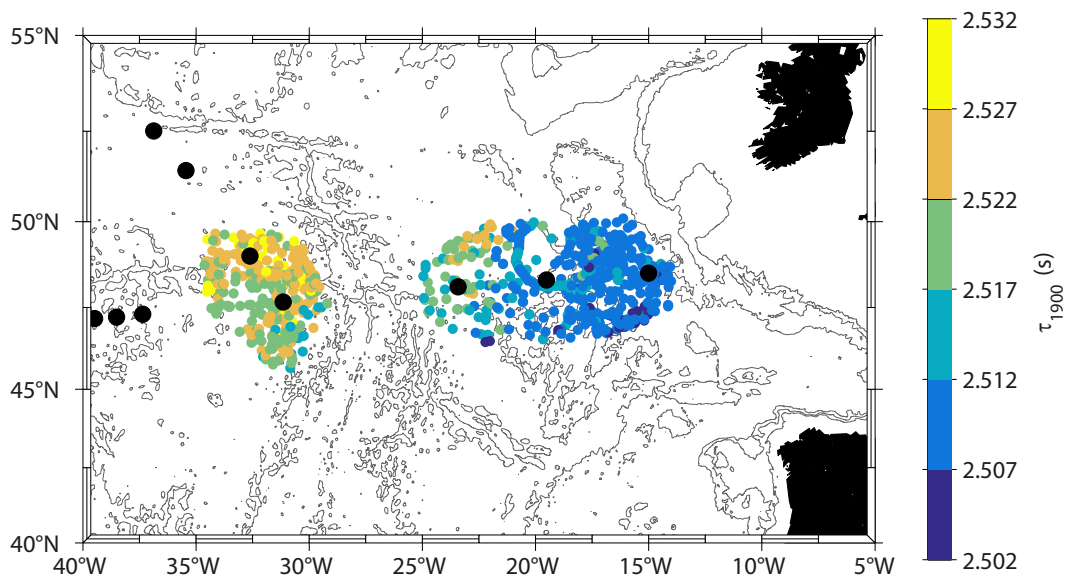


**Figure 2.1:** Locations of Argo float and shipboard CTD profiles used to calculate the transfer functions for PIES BP12 in the western basin and the three eastern PIES. Colors denote the acoustic travel time at 1900 dbar. The black dots show the locations of the PIES.

### 2.1.3 Satellite altimetry

In addition to the presented datasets that stem from measurements taken within the ocean body, this study uses satellite mapped absolute dynamic topography (MADT), in the following also addressed as satellite or altimeter SSH, and satellite absolute geostrophic surface velocities. The satellite data are provided by E.U. Copernicus Marine Environment Monitoring Service (CMEMS)<sup>1</sup>. They are available on a horizontal Cartesian grid of  $1/4^\circ \times 1/4^\circ$  resolution with global coverage and with a daily temporal resolution for the time period 1993 until 2020. In this study, data from the time period 1993 to 2017 are used.

The MADT data are derived from the satellite measurements as described in the CMEMS product user manual (Mertz et al., 2018). The satellite measurements give access to the instantaneous sea surface height ( $SSH_i$ ) above the reference ellipsoid. From these measurements, a temporal mean sea surface for a time period N ( $MSS_N$ ) is inferred. The dynamical part of the altimeter signal which is the sea level anomaly ( $SLA$ ) is obtained from the measured instantaneous sea surface height and the temporal mean as  $SLA_N = SSH_i - MSS_N$ . The temporal mean of the sea surface height above the geoid for a time period N is the mean dynamic topography (MDT) with  $MDT_N = MSS_N - geoid$ . The absolute dynamic topography ( $ADT$ ), used in this study as mapped version, is the dynamical part of the absolute signal and calculated from the SLA using a mean dynamic topography:  $ADT = SLA_N + MDT_N$ .

The satellite absolute geostrophic velocities ( $u$  and  $v$ ) are derived from the mapped absolute dynamic topography assuming geostrophic balance:

$$v = \frac{g}{f} \frac{\partial MADT}{\partial x}, \quad u = -\frac{g}{f} \frac{\partial MADT}{\partial y} \quad (2.1)$$

In the equations above,  $u$  and  $v$  are perpendicular to the MADT gradient respectively in meridional ( $\frac{\partial MADT}{\partial y}$ ) and zonal ( $\frac{\partial MADT}{\partial x}$ ) direction,  $g$  is the gravitational acceleration, and  $f$  the Coriolis parameter.

To classify the different NAC regimes and to analyze the relevance of the baroclinic and barotropic components for the SSH signal in the different regions, the satellite SSH is compared to the baroclinic and barotropic contributions to SSH fluctuations calculated from PIES data. Based on the results of this analysis, the satellite SSH is then used to calculate absolute transport time series for the deployment periods and to extend the baroclinic PIES transport time series backward in time until 1993. The absolute geostrophic velocities from the same dataset are used to analyze the mean surface flow east and west of the MAR crest in the *NAC Central* segment (cf. Figure 4.7).

<sup>1</sup>product identifier: SEALEVEL\_GLO\_PHY\_L4\_REP\_OBSERVATIONS\_008\_047

## 2.2 Model data

The results of this study which were obtained from observational data are complemented using output of the regional configuration ANHA12 (Arctic and Northern Hemisphere Atlantic,  $1/12^\circ$  horizontal resolution) of the Nucleus for European Modeling of the Ocean (NEMO) model, version 3.4. The NEMO model is a state of the art modeling framework used for oceanographic research, operational oceanography, seasonal forecasting and climate studies (Madec et al., 2008). The model simulation used in this study to analyze the PIES sections in terms of cross-section velocities and transports was carried out by the Ocean Modeling Group of the University of Alberta (Hu et al., 2018). Model output is available up from 2002, however, in this study, only output from the years 2006 to 2017 is used and the time span from 2002 to 2006 is considered as model spin-up time and thus excluded from the analysis.

In the following, the ANHA12 model configuration of the NEMO model and the Lagrangian model ARIANE (Blanke et al., 1999; Blanke et al., 1997), an offline trajectory tool used to calculate three-dimensional trajectories from the velocity field provided from the ocean component of the NEMO model, are presented.

### 2.2.1 ANHA12 model configuration of the NEMO model

The NEMO model consists of three major components making up the model which are the blue ocean (ocean dynamics and thermodynamics), the white ocean (sea-ice dynamics and thermodynamics), and the green ocean (biogeochemistry). Additionally, it includes two numerical tools which are an adaptive mesh refinement software allowing for higher resolution regions nested within coarser grids, and an assimilation tool allowing for re-forecasts and model constraining. Details can be found at <https://www.nemo-ocean.eu/>. This section focuses on the physics behind the blue ocean component which is the model component used in this study and the ANHA12 configuration and setup of the simulation.

#### The blue ocean component of the NEMO model

The blue ocean component of the NEMO model was developed from the primitive equation model Océan PARallélisé (OPA) described in Madec et al. (1998). Prognostic variables of the model are the three-dimensional velocity field as well as temperature and salinity (Madec et al., 1998). In the following, the primitive equations making up the model, the curvilinear coordinate system, and the discretization in space and time are described.

**Primitive equations:**

The ocean as a fluid can be fairly well described by the primitive equations, a set of coupled equations representing the conservation of momentum, mass, thermal energy, and salt, along with a nonlinear equation of state coupling the two active tracers temperature and salinity to the fluid velocity, and the following assumptions originating from scale considerations (Madec et al., 2008):

1. Spherical Earth approximation: The geopotential surfaces are assumed to be spheres so that the vertical gravity vector is always directed to the Earth's center and gravitational acceleration  $g$  is set to  $9.8 \text{ m s}^{-2}$ .
2. Thin-shell approximation: The ocean depth is neglectable compared to the Earth's radius.
3. Turbulent closure hypothesis: Turbulent fluxes are parametrized and expressed in terms of large-scale features.
4. Boussinesq approximation: Density variations are neglected except in their contribution to the buoyancy force.
5. Hydrostatic hypothesis: The vertical momentum equation is reduced to a balance between the vertical pressure gradient and the buoyancy force, i.e. convective processes must be parametrized.
6. Incompressibility hypothesis: Seawater is assumed to be incompressible.

To derive the equations which make up the model as described by Madec et al., 2008, it is useful to introduce an orthogonal set of unit vectors ( $\mathbf{i}, \mathbf{j}, \mathbf{k}$ ) linked to the Earth's geometry with  $\mathbf{k}$  being aligned with gravity and  $\mathbf{i}$  and  $\mathbf{j}$  being orthogonal to the vertical vector  $\mathbf{k}$ . The three-dimensional velocity vector is given by  $\mathbf{U} = \mathbf{U}_h + \omega \mathbf{k}$  with  $\mathbf{U}_h = (U, V)$  representing the horizontal flow components and  $\omega$  the vertical velocity in  $\mathbf{k}$  direction. The six equations are:

Horizontal conservation of momentum, i.e. Navier-Stokes equation:

$$\frac{\partial \mathbf{U}_h}{\partial t} = - \underbrace{\left[ (\nabla \times \mathbf{U}) \times \mathbf{U} + \frac{1}{2} \nabla (\mathbf{U}^2) \right]_h}_{\text{inertial term}} \underbrace{- f \mathbf{k} \times \mathbf{U}_h}_{\text{Coriolis term}} - \underbrace{\frac{1}{\rho_0} \nabla_h p}_{\text{pressure gradient}} + \mathbf{D}^U + \mathbf{F}^U \quad (2.2)$$

Vertical momentum balance, originating from the hydrostatic balance:

$$\frac{\partial \rho}{\partial z} = -\rho g \quad (2.3)$$

Conservation of mass, represented by the continuity equation:

$$\frac{\partial \rho}{\partial t} + \nabla \cdot [\rho \mathbf{v}] = 0 \quad \xrightarrow{\rho = \text{const.}} \quad \nabla \cdot \mathbf{v} = 0 \quad (2.4)$$

Conservation of heat:

$$\frac{\partial T}{\partial t} = -\nabla \cdot (T\mathbf{U}) + D^T + F^T \quad (2.5)$$

Conservation of salt:

$$\frac{\partial S}{\partial t} = -\nabla \cdot (S\mathbf{U}) + D^S + F^S \quad (2.6)$$

Equation of state:

$$\rho = \rho(T, S, p) \quad (2.7)$$

The variables used in these equations are  $f = 2\boldsymbol{\Omega} \cdot \mathbf{k}$  as Coriolis parameter with  $\boldsymbol{\Omega}$  being the Earth's angular velocity vector,  $\rho$  as in situ and  $\rho_0$  as reference density,  $p$  as pressure,  $g$  as the gravitational acceleration,  $T$  and  $S$  as temperature and salinity,  $\mathbf{D}^U$ ,  $D^T$ , and  $D^S$  as parametrizations for small-scale physics, and  $\mathbf{F}^U$ ,  $F^T$ , and  $F^S$  as surface forcing terms.

### Boundary conditions:

The complex boundaries of the ocean including coastlines, bathymetry and the air-sea and ice-sea interfaces can be defined by two surfaces represented by  $z = -H(i, j)$  and  $z = \eta(i, j, k, t)$  with  $H$  being the depth of the ocean and  $\eta$  being the SSH as described in Madec et al. (2008). Both,  $H$  and  $\eta$  are referenced to the mean sea surface  $z = 0$  (Figure 2.2).

Via these boundaries, the ocean exchanges momentum, heat, salt, and fresh water with the land, the solid earth, the sea-ice, and the atmosphere. Examples for processes leading to such exchange across the boundaries are river runoff, precipitation, evaporation, or wind stress. In the ocean model, the boundary processes are set up using the coupling to a sea-ice model, open boundary conditions, atmospheric forcing, and a runoff climatology. A more detailed description of the simulation setup and datasets used in this context is provided below.

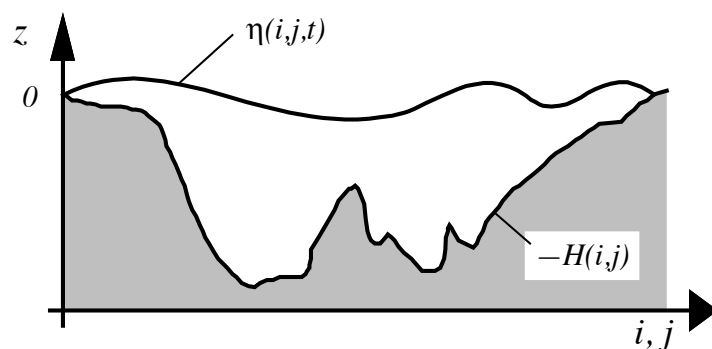


**Figure 2.2:** Sketch of the two surfaces  $z = -H(i, j)$  and  $z = \eta(i, j, t)$  representing the oceanic boundaries with  $H$  being the depth of the ocean and  $\eta$  being the SSH. Figure is taken from Madec et al. (2008).

### Curvilinear coordinate system and spatial discretization:

The model domain covers the whole North Atlantic and Arctic with two open boundaries, one at  $20^\circ\text{S}$  and one close to Bering Strait (Hu et al., 2018). In Figure 2.3, the ANHA12 horizontal mesh grid, including the open boundaries, is shown.

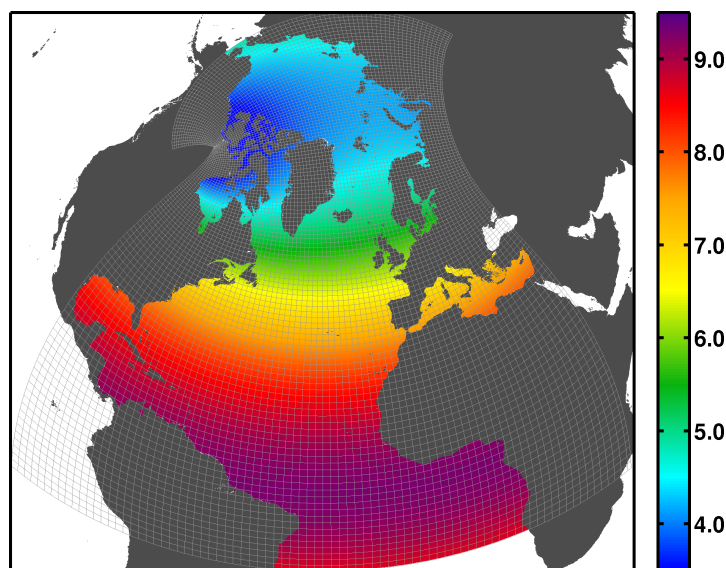


**Figure 2.3:** ANHA12 (Arctic and Northern Hemisphere Atlantic configuration of the NEMO model with  $1/12^\circ$  horizontal resolution) horizontal mesh with open boundaries at  $20^\circ\text{S}$  and close to Bering Strait and with the poles shifted over land to avoid a singularity within the ocean domain. Colors denote resolution in km. Only every 20th grid line is plotted. Figure is from Xianmin Hu and taken from <http://knossos.eas.ualberta.ca/>.

The model uses a curvilinear coordinate system with  $(\mathbf{i}, \mathbf{j}, \mathbf{k})$  being a set of orthogonal unit vectors linked to the Earth's geometry such that  $\mathbf{k}$  is the local upward pointing vector aligned with the gravitational acceleration, and the two horizontal vectors  $(\mathbf{i}, \mathbf{j})$  are tangential to the geopotential surfaces of the Earth (cf. Figure 2.4a). Instead of having  $(\mathbf{i}, \mathbf{j})$  aligned with the

latitudes and longitudes of the standard geographical grid, the model grid converges at poles shifted over land via coordinate transformation (Murray, 1996) to avoid a singularity (a point that cannot be easily treated in a global model without filtering) within the ocean domain as described in Madec et al. (2008) (cf. Figure 2.3).

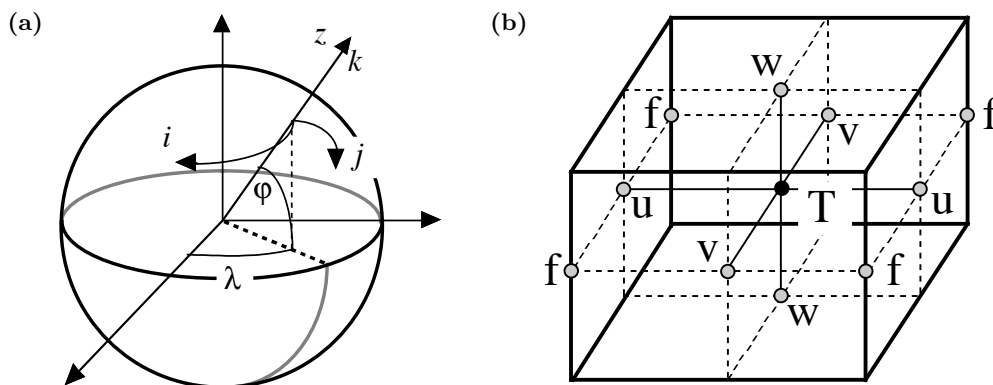


**Figure 2.4:** Panel (a) shows the curvilinear coordinate system used in the NEMO model with  $(i, j, k)$  being a set of orthogonal unit vectors linked to the Earth’s geometry such that  $k$  is the local upward pointing vector aligned with the gravitational acceleration, and the two horizontal vectors  $(i, j)$  are tangential to the geopotential surfaces of the Earth. The figure is taken from Madec et al. (2008). Panel (b) shows the arrangement of variables within the Arakawa C grid (Mesinger et al., 1976) used in the model. The scalar variables  $T$  and  $S$  are located at the center of the grid cell ( $T$ -point), the vector variables ( $u$ -/ $v$ -/ $w$ -points) are located at the center of the cell faces, and vorticity is located between the  $u$ - and  $v$ -points at the center of the edge of a grid cell ( $f$ -point). The figure is taken from Madec et al. (2008).

In the vertical direction parallel to the local vector  $k$ , the ocean component of the model has 50 levels with exponentially increasing cell thicknesses reaching from about 1 m at the top level to about 450 m at the lowest level. Furthermore, a partial step representation of the bottom topography is used (Bernard et al., 2006) with a variable depth of the cell closest to the seafloor which is adjustable to the real depth of the ocean (Adcroft et al., 1997).

The arrangement of variables within the model grid is the same in all directions. The NEMO model uses an Arakawa C grid (Mesinger et al., 1976) with the scalar variables  $T$  and  $S$  for temperature and salinity located at the center of the grid cell ( $T$ -point), vector variables located at the center of the cell faces ( $u$ -/ $v$ -/ $w$ -points), and vorticity located at the  $f$ -point between the  $u$ - and  $v$ -points at the center of the edge of a grid cell (Figure 2.4b). The grid cell size is defined by its height, width, and length and processes on smaller scales cannot be resolved and must be parametrized.

### Time discretization:

The model time-steps are 180 s and output is saved every 5 days starting in 2002. The model

uses a three level time stepping scheme (Equation 2.8) which is different for non-diffusive and diffusive processes (Madec et al., 2008).

$$x^{t+\Delta t} = x^{t-\Delta t} + 2\Delta t \mathbf{RHS}_x^{t-\Delta t, t, t+\Delta t} \quad (2.8)$$

In the above equation,  $x$  represents the variables  $u$ ,  $v$ ,  $T$ , or  $S$ , and  $\Delta t$  is the time step. **RHS** is the right-hand-side of the corresponding time evolution equation whose terms are evaluated at a specific time step which depends on the physics behind the processes associated with the variable represented by  $x$  (Madec et al., 2008).

The time stepping procedure for non-diffusive processes is the Leapfrog scheme (Mesinger et al., 1976). Classically, this means that the forcing applied to  $x$  is time-stepped over a  $2\Delta t$ -period, i.e. the variable at a certain time  $t$  depends on its value two time steps before. As this scheme allows for the existence of a non-physical numerical mode since a divergence of even and odd time steps may occur, the leapfrog scheme usually is applied together with a Robert-Asselin time filter (Equation 2.9) that mixes even and odd time steps (Asselin, 1972; Madec et al., 2008; Robert, 1966):

$$x_F^t = x^t + \gamma \left[ x_F^{t-\Delta t} - 2x^t + x^{t+\Delta t} \right] \quad (2.9)$$

In the above equation,  $F$  denotes filtered values and  $\gamma$  the Asselin coefficient.

For diffusive processes, a forward (to resolve horizontal diffusion, cf. Equation 2.10) or backward (to resolve vertical diffusion, cf. Equation 2.11) time-stepping scheme is used:

$$x^{t+\Delta t} = x^{t-\Delta t} + 2\Delta t D_x^{t-\Delta t} \quad (2.10)$$

$$x^{t+\Delta t} = x^{t-\Delta t} + 2\Delta t \mathbf{RHS}_x^{t+\Delta t} \quad (2.11)$$

In the above equation,  $D_x$  represents the diffusive term.

### Simulation setup

As described above, to initialize and set up the ocean model, initial and open boundary conditions, atmospheric forcing, and runoff have to be provided. For the simulation used in this study, the model is set up as described in Hu et al. (2018). Both, the initial conditions, including the three-dimensional ocean fields of zonal and meridional velocity, temperature and salinity, and the two-dimensional SSH and sea-ice fields, as well as the open boundary conditions, including temperature, salinity and horizontal velocities, are provided by the Global Ocean Reanalysis and Simulations (GLORYS2v3) product by Mercator Ocean (Masina et al.,

2017). The exchange of momentum, heat, and salt between the ocean and sea-ice is achieved via coupling of the ocean component to the Louvain-la-Neuve sea-ice model (LIM2) (Fichefet et al., 1997) which includes dynamical and thermodynamical processes. As bottom topography, the ETOPO1 dataset (Amante et al., 2009) is used. Atmospheric forcing is provided from the Canadian Meteorological Center (CMC) Global Deterministic Prediction System (GDPS) reforecasts (CGRF) dataset (Smith et al., 2014) which consists of wind speeds at 10 m, air temperature at 2 m, humidity, downwelling, longwave radiation flux, and precipitation. Monthly river runoff data is provided by Dai et al. (2009) and Greenland meltwater discharge by Bamber et al. (2012). The river runoff data is available until 2007, the meltwater runoff until 2010. After these years, the runoff forcing of the previous year is repeated each individual year until the end of the simulation.

### 2.2.2 The Lagrangian model ARIANE

The offline Lagrangian trajectory tool ARIANE (Blanke et al., 1999; Blanke et al., 1997) is used to calculate particle trajectories using the velocity fields from the output of the above described ANHA12 simulation. Along their pathways, the particles change their properties (salinity, temperature, and density) according to the Eulerian model fields (Lique et al., 2010). In this study, particle trajectories are used for the description of major pathways of water into and within the subpolar eastern basin and particle densities are used for studying the changing properties of the particles along their way.

#### Lagrangian and Eulerian perspective

As stated above, the trajectory tool ARIANE is a mathematical tool with a Lagrangian perspective of the flow while the model itself provides Eulerian model fields. The difference between the two perspectives lies in the position of the observer and is most conveniently formulated by introducing a control volume element (the particles seeded by the ARIANE tool can be considered as such). While in the Eulerian perspective the control element is fixed in space, in the Lagrangian scheme it moves with the flow (cf. Figure 2.5).

In the ARIANE tool, the particles represent Lagrangian floating elements with conserved infinitesimal volume which means that mass transport between two sections can be determined (Hu et al., 2013). The properties of each particle, i.e. temperature, salinity, or density, are determined by the surrounding Eulerian model fields and evolve along the computed trajectories (Lique et al., 2010) thus water mass transformation can be studied (Hu et al., 2013).

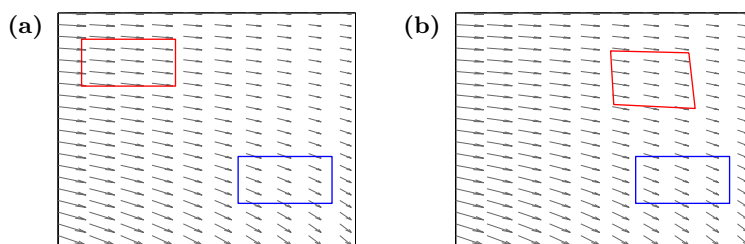


**Figure 2.5:** Sketch (not to scale) of Lagrangian and Eulerian perspectives depicted by a control element with conserved volume in an arbitrary flow field. The blue rectangle corresponds to the Eulerian control element which is fixed in space, the red rectangle corresponds to the Lagrangian control element which moves with the flow. Panel (a) corresponds to the time step  $t$  and panel (b) to the time step  $t + \Delta t$ .

### ARIANE setup

The ARIANE tool can be set up using a forward and backward mode. In the forward mode, particle trajectories are tracked forward in time, while in the backward mode, particle trajectories are tracked backward in time, i.e. the source region of a particle can be determined. In this study, the forward as well as the backward mode of ARIANE are used. To determine major pathways of water into the eastern subpolar North Atlantic across the sections spanned at  $47^\circ/48^\circ\text{N}$  and the MAR by the PIES, a specific number of particles was seeded four times per year in the period 2006 to 2017 in five different boxes (Figure 2.6 and Table 2.5).

The initial positions (latitude/longitude/depth) of the particles are distributed randomly over the model grid indices  $(i, j, k)$  as shown in Figure 2.6. As described in the previous section, the vertical extent of the model grid cells increases with increasing depths of the cells. Consequently, the initial depths of the particles have a bias towards the upper ocean (Figure 2.6b and 2.6c).

Initial positions are the same for all for starting times, and for both, the forward and backward mode. The numbers of particles seeded in the different boxes four times per year and in total are listed in Table 2.4. In the forward mode, the particles were seeded at the beginning of a five-day model output while in the backward mode, the last day of the five-day model output was used as initial time. The four dates per year at which the particles were seeded are for the forward mode: 31st of January, 1st of May, 30th of July, and 2nd of November. For the backward mode, the corresponding dates are: 30th of January, 30th of April, 29th of July, and 1st of November.

From 2006 to 2017, each year the same amount of particles was seeded. In the forward as well as in the backward mode, the particles were tracked over the whole time of the simulation (2006 to 2017). In this study, the focus lies on regions in relative close proximity to the PIES transects. Therefore, particle trajectories are analyzed for a maximum of five years.

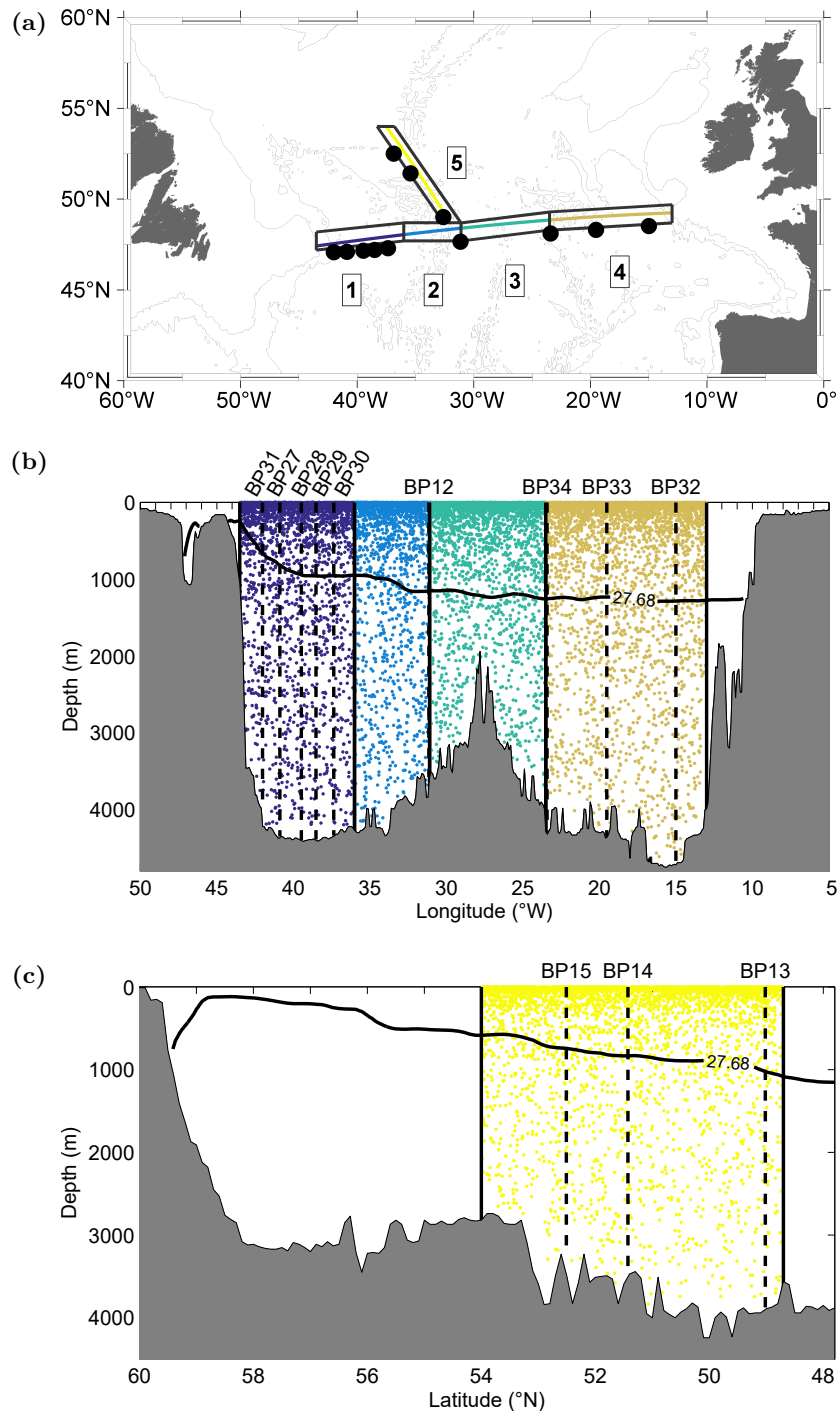


**Figure 2.6:** Initial positions and depths of particles tracked with the Lagrangian trajectory tool ARIANE along the 47°/48° and MAR PIES transects. Different colors represent different regions defined by five boxes in which the particles were seeded. Panel (a) shows the initial position of the particles in terms of latitude and longitude, the horizontal extent of the five boxes, and the PIES positions. The depth distribution of particles is shown in panel (b) for the 47°/48°N PIES transect and in panel (c) for the MAR PIES transect. Additionally, the PIES positions (dashed lines), box limits (solid lines), and the 27.68-isopycnal from the mean model field in 2016/2017 which is used in the analysis as approximate separation between the upper and lower ocean are plotted.

	# each time	total
<b>Box 1</b>	2975	142 800
<b>Box 2</b>	1928	92 544
<b>Box 3</b>	3014	144 672
<b>Box 4</b>	4038	193 824
<b>Box 5</b>	4052	194 496

**Table 2.4:** Number of particles seeded in the different boxes four times per year in each year from 2006 to 2017 and the total number of seeded particles. Initial positions are the same for forward and backward mode and thus the seeded particles in the different boxes amount to the same numbers for both modes.

<b>Box 1</b>	43.5°W/47.2°N	36°W/47.7°N	36°W/48.7°N	43.5°W/48.2°N
<b>Box 2</b>	31.1°W/47.7°N	36°W/47.7°N	36°W/48.7°N	31.1°W/48.7°N
<b>Box 3</b>	23.5°W/49.3°N	31.1°W/48.7°N	31.1°W/47.7°N	23.5°W/48.3°N
<b>Box 4</b>	13°W/48.7°N	23.5°W/48.3°N	23.5°W/49.3°N	13°W/49.7°N
<b>Box 5</b>	31.1°W/48.7°N	36.8°W/54°N	38.3°W/54°N	32.6°W/48.7°N

**Table 2.5:** Horizontal extent of boxes 1 to 5 used in the ARIANE analysis.

## 2.3 Reanalysis data

As already described in the previous section, reanalysis data providing gridded parameters which represent atmospheric and oceanographic conditions are used to set up and force the model. Reanalysis data are a combination of historic observations with state-of-the-art forecast systems. By periodically feeding an unchanging forecast scheme with all available observational data, global datasets with consistent temporal and spatial coverage are produced for the past until present.

In addition to the reanalysis data used in the context of the NEMO model, another reanalysis dataset is used in this study which is the NCEP/NCAR Reanalysis 1 surface flux data (Kalnay et al., 1996) provided by NOAA/OAR/ESRL PSL, Boulder, Colorado, USA <sup>1</sup>. The data are gridded onto a T62 Gaussian grid with  $192 \times 94$  datapoints which corresponds to a horizontal spacing of about  $2^\circ$ . It includes daily mean values of meridional and zonal wind stress up from 1948 to present from which the mean Ekman transport across the PIES transects is calculated.

<sup>1</sup><https://psl.noaa.gov/data/gridded/data.ncep.reanalysis.surfaceflux.html>, access date 11 June 2020



## 3 Methodology

### 3.1 Sea surface height fluctuations and volume transport obtained from PIES data

To infer time series of SSH fluctuations and volume transport from the PIES data, several preparatory steps are necessary. In a first step, the telemetric transmitted PIES data have to be prepared for further analysis. In a next step, a transfer function has to be created to convert the PIES measurements of the acoustic round trip travel time into water column profiles of SVA from which the SSH fluctuations and transports are calculated. Furthermore, the whole process has to be quality controlled and estimates for the uncertainties have to be quantified. The individual steps are outlined in more detail the following. Moreover, this section describes how satellite data is used to convert the PIES transport into time series of absolute volume transport and how these time series are extended backwards in time until the beginning of the satellite data record.

#### 3.1.1 Pre-processing of PIES data obtained by telemetry

The telemetric transferred PIES data consist of the year day, and daily mean values of the acoustic round trip travel time  $\tau$  and the bottom pressure  $p$ . Depending on the ambient conditions during the data retrieval process, the transferred time series may exhibit sporadic gaps. Furthermore, some of the measured time series include singular spikes which are removed from the time series leaving also some gaps. PIES data that stem from the same location but different deployment periods are combined to longer time series, a procedure which naturally leads to additional (longer) gaps in the time series due to the time that passed between instrument recovery and re-deployment. The gaps in the time series either arising from incomplete data transmission, spike removal, or from the combination of time series from several deployment periods are closed with linear interpolation. Data gaps lasting longer than ten days are not closed but the time series are in this case considered as two separate time series.

Additionally, the unknown drift of the PIES pressure sensor (Watts et al., 1990) has to be removed prior to the analysis. The procedure of drift removal follows the description of Roessler et al. (2015) and Watts et al. (1990). As a consequence, only bottom pressure fluctuations are taken into account for the data analysis.

### 3.1.2 Transfer of PIES measured travel times into specific volume anomaly

The transfer function (Figure 3.1) used to convert the PIES travel time measurements into water column profiles of e.g. SVA is created following Meinen et al. (2004), Meinen et al. (1998), Meinen et al. (2000a), Roessler et al. (2015), and Watts et al. (2001). Owing to the different hydrographic conditions in the western and the eastern basins, the transfer function for PIES BP12 located on the western flank of the MAR differs from the one used for the three PIES located in the eastern Atlantic (Figure 2.1 and 3.1).

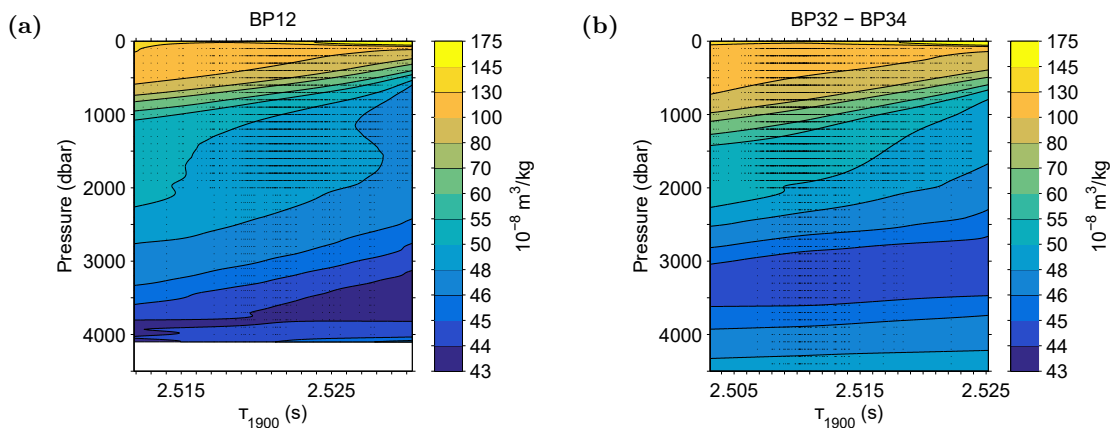


**Figure 3.1:** Transfer function between the SVA calculated from the Argo float and shipboard CTD profiles shown in Figure 2.1 and the acoustic travel time at the reference pressure level of 1900 dbar for PIES BP12 in the western basin (a) and the PIES BP32 – 34 in the eastern basin (b). The black dots represent the Argo float and shipboard CTD profiles shown in Figure 2.1.

The PIES travel time is transferred into an SVA profile at each PIES site using Argo float and shipboard CTD profiles (Figure 2.1). All Argo float and shipboard CTD profiles are combined and gridded in 10 dbar intervals down to a maximum depth of 4500 dbar in case of the three eastern PIES BP32 – BP34 and down to 4100 dbar for BP12. The two pressure levels 4500 dbar and 4100 dbar correspond to the approximate water depths at the PIES positions (Table 2.1) and are thus chosen as depth limits for the transfer function. For each hydrographic temperature and salinity profile, the acoustic travel time is calculated and corrected for the different latitudes of the Argo float and shipboard CTD data, i.e. the calculated travel time

is referenced to a common gravitational acceleration  $g = 9.8 \text{ m/s}^2$  (Meinen et al., 1998; Watts et al., 2001). Then, the potential density anomaly and SVA are calculated for each profile. The seasonal signal in  $\tau$ -space is removed for the upper 250 dbar so that the transfer function can be used for all PIES measurements irrespective of the date at which the measurement was taken. The profiles are sorted according to  $\tau$  at 1900 dbar and cubic smoothing splines are applied horizontally at each pressure level over all  $\tau$  values. In  $\tau$  ranges where no deep reaching shipboard CTD data are available, the dataset is vertically extrapolated and afterwards vertical splines are applied over the whole depth range. Furthermore, a cubic smoothing spline is applied between 1600 dbar and 2400 dbar to smooth the transition to depths below 2000 dbar where considerably fewer measurements are available due to the lack of Argo data. As the Argo float and shipboard CTD profiles, the acoustic travel time measured by the PIES is also corrected for different latitudes by referencing to  $g = 9.8 \text{ m/s}^2$ . To use the transfer function to convert PIES measurements into water column profiles of SVA, it is necessary to reference the travel time measurements onto a common reference pressure level (1900 dbar). The pressure level of 1900 dbar is chosen as common reference because each profile used to create the transfer function reaches down to at least this limit. For referencing the travel time measurement onto 1900 dbar, two steps are necessary. First, CTD data at the PIES positions from the deployment and recovery cruises are used to convert the PIES measured  $\tau$  into a  $\tau_{4500}$  (eastern PIES BP32 – 34) and  $\tau_{4100}$  (BP12), i.e. the travel time relative to 4500 dbar and 4100 dbar, which corresponds to the respective pressure limits of the two transfer functions. This step is necessary because the PIES positions are not exactly at depths of 4500 dbar or 4100 dbar. In a next step, the converted  $\tau$  values are referenced to a common  $\tau_{1900}$  at 1900 dbar with the following equation from Meinen et al. (1998, Equation B1):

$$\tau_{P_1} = A \times \tau_{P_2} + B \tag{3.1}$$

In order to determine the coefficients A and B of Equation 3.1, all of the deep reaching CTD data included in the transfer function have been used. The converted  $\tau$  values are corrected for seasonality in  $\tau$ -space, and with the help of the transfer function, time series of SVA profiles are reconstructed from the PIES data.

The barotropic contribution to the SSH fluctuation  $\eta'_{bt}$  is calculated as shown in Equation 3.2 from the bottom pressure fluctuations  $p'_{PIES}$ , the density of the water at the sea floor  $\rho_{bottom}$  (obtained from the reconstructed profiles), and the gravitational acceleration at the PIES position  $g(\lambda, H)$  depending on latitude  $\lambda$  and the instrument depth H (Teague et al., 1995).  $\eta'_{bt}$  is converted into the barotropic contribution to the travel time  $\tau_{bt}$  using the sound speed in water  $c_{sound}$  calculated with the Del Grosso equation (Del Grosso, 1974) from the reconstructed

temperature and salinity water column profiles (Equation 3.3).  $\tau_{bt}$  is then removed from the measured  $\tau_{PIES}$  (Equation 3.4) to get the baroclinic contribution to  $\tau$ . The baroclinic contribution  $\tau_{bc}$  to the measured travel time  $\tau_{PIES}$  is then used for reconstructing new time series of water column profiles as described before.

$$\eta'_{bt} = \frac{p'_{PIES}}{\rho_{bottom} \cdot g(\lambda, H)} \quad (3.2)$$

$$\tau_{bt} = 2 \frac{\eta'_{bt}}{c_{sound}} \quad (3.3)$$

$$\tau_{bc} = \tau_{PIES} - \tau_{bt} \quad (3.4)$$

### Seasonal model

To use the transfer function to convert the PIES measurements into water column profiles, the seasonal signal in the  $\tau$ -measurements is removed as described in the previous section. To conserve the seasonal signal in the data nonetheless, a seasonal model is constructed which is added to the reconstructed water profiles. The seasonal model (Figure 3.2) is calculated from the residuals of the measured shipboard and Argo float CTD profiles and the transfer function (Roessler et al., 2015). It includes for each year day a specific seasonal SVA water profile for the upper 250 dbar, a limit below which the seasonal cycle is negligible in terms of its effect on the volume transport.

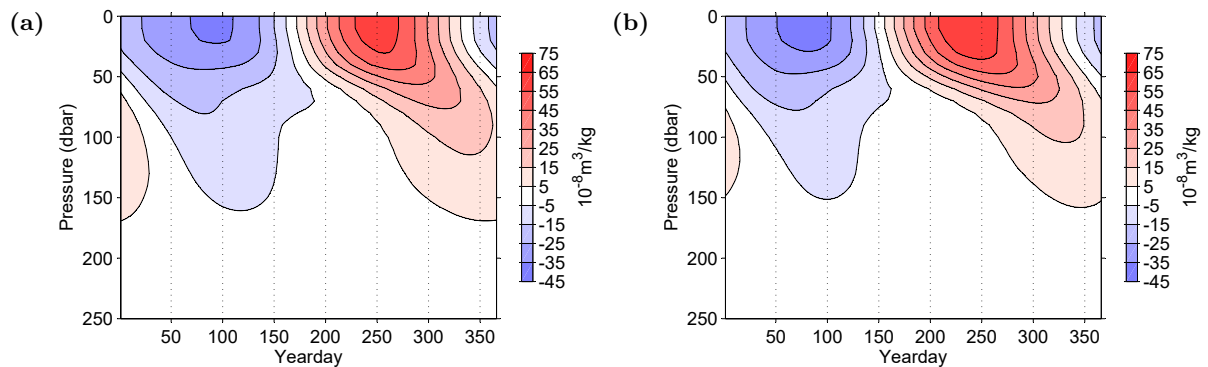


**Figure 3.2:** Seasonal model for SVA calculated from the residuals of the measured shipboard and Argo float CTD profiles and the transfer function (Roessler et al., 2015). For each year day, a specific seasonal SVA water profile is provided which is added to the reconstructed water column profiles. Panel (a) shows the seasonal model for the reconstructed data from PIES BP12, panel (b) shows the seasonal model for the reconstructed data from PIES BP32, BP33 and BP34.

### Quality control of GEM method

To assess the goodness of the transfer function obtained from the GEM method, several quality control measures are performed following Roessler et al. (2015). The first step is to ensure an unambiguous relation between the travel time and water column profiles. For this, the geopotential anomaly (GPA) integrated between 250 dbar and 1900 dbar plotted against the travel time for 1900 dbar is explored (Figure 3.3).

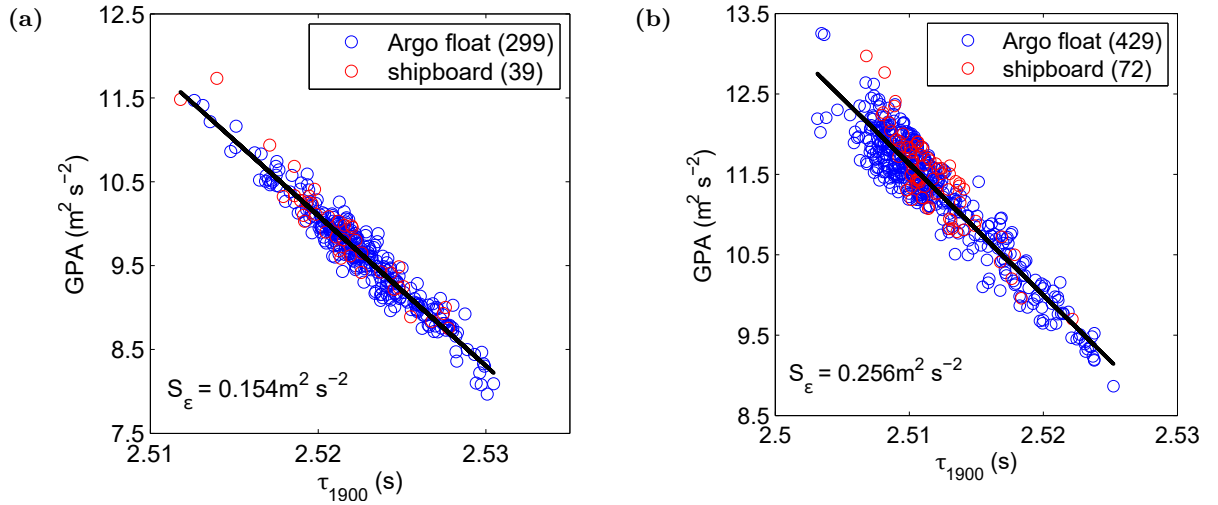


**Figure 3.3:** Correlation between acoustic travel time and GPA integrated between 250 dbar and 1900 dbar for the transfer function for PIES BP12 (a) and the three eastern PIES (b).  $S_\epsilon$  denotes the standard error of the fit. Note the different x- and y-scales. Numbers in brackets indicate number of Argo float and shipboard CTD profiles.

The profiles exhibit a linearly decreasing relation between the integrated GPA and the travel time at 1900 dbar. This is an indicator for an unambiguous relation between the water column profiles at the respective locations in general and the travel time. The acoustic travel times smaller than 2.51 s show larger deviations from the linear correlation in the eastern Atlantic (Figure 3.3b). This is presumably caused by the presence of the relatively warm and saline Mediterranean Outflow Water (MOW) at intermediate depths, that is not observed in the western basin. Furthermore, travel times that small are mostly not present in the western basin. Indeed, the deviations between both transfer functions are largest in the depth range of the MOW between about 600 m and 900 m depth (Figure 3.4). Nonetheless, the correlation between travel time and integrated GPA is good enough (goodness of fit expressed by standard error  $S_\epsilon$  of the fit) to apply the GEM method also in the eastern basin.

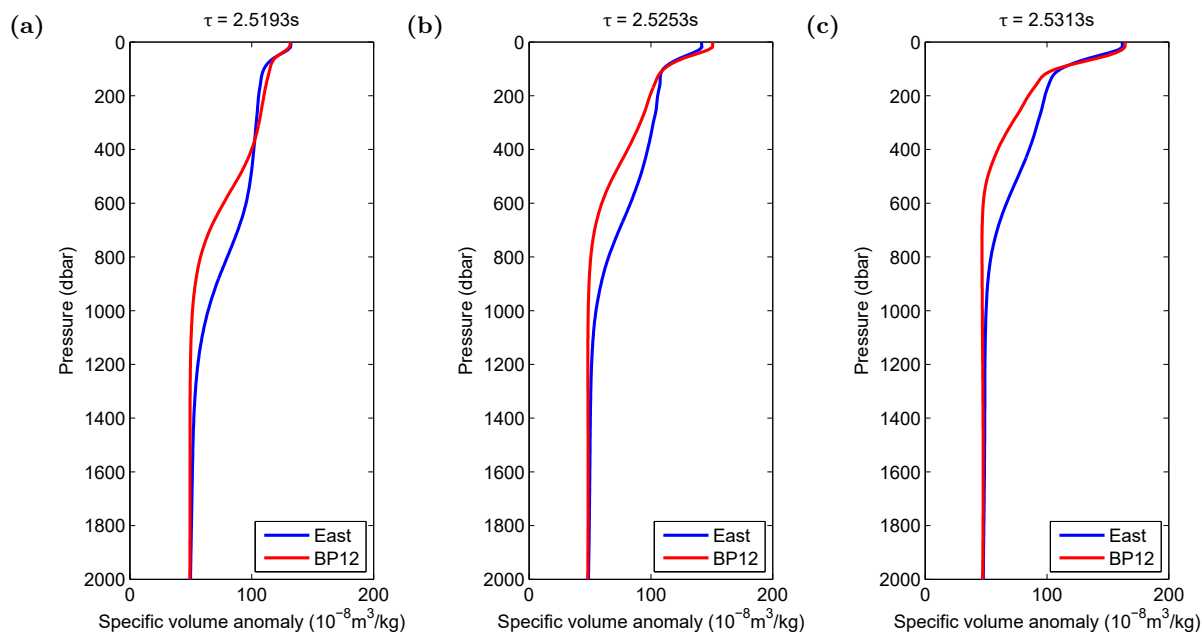


**Figure 3.4:** SVA profiles for different acoustic travel times (listed on top) reconstructed from the transfer function for BP12 (red) and for the three eastern basin PIES BP32 – BP34 (blue).

In a second step, the reconstructed sections are compared to the measured cruise section from 2016 (Figure 3.5 and 3.6). To do this, the transfer function is calculated without using the hydrographic data from this particular cruise. Even though small-scale features cannot be resolved with the GEM technique due to the necessary smoothing and filtering of the data, the general features of the measured and the reconstructed section look quite similar. Overall, the differences are small compared to the signal itself, which justifies the use of the GEM method and the choice of the Argo and shipboard CTD data shown in Figure 2.1. Both transfer functions can be used to reconstruct the observed SVA between the two GEM regimes (Figure 3.6), i.e. the region which is kept gray in Figure 3.5, as the deviations between observations and reconstructions are not larger than for the regions for which the GEM transfer functions were calculated.

### 3.1.3 Barotropic and baroclinic sea surface height fluctuations

In order to analyze the different study regions in terms of baroclinic and barotropic contributions to the SSH fluctuations and to reveal different NAC regimes, the correlation between PIES inferred SSH fluctuations and satellite measured SSH is discussed.

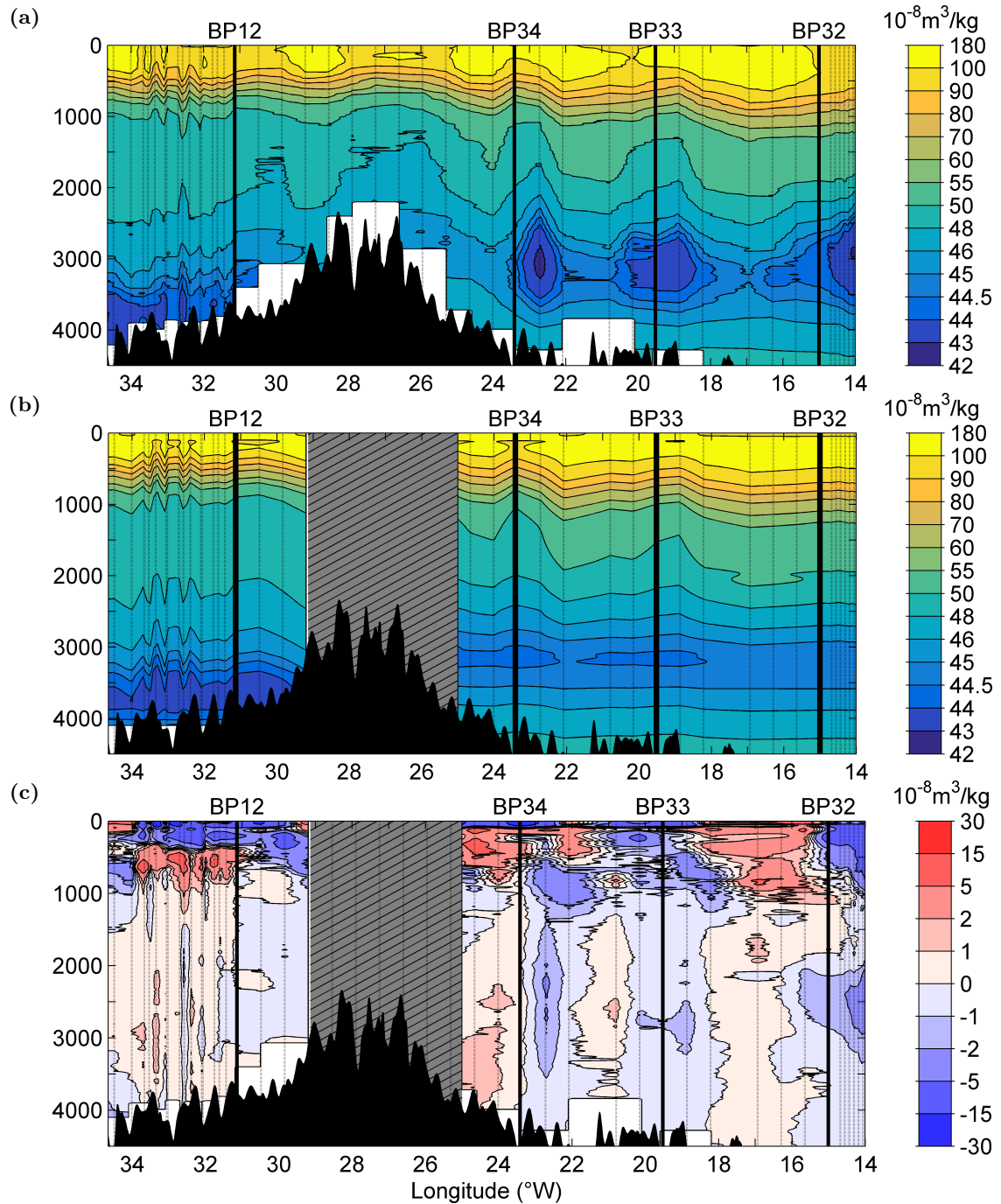


**Figure 3.5:** SVA from (a) CTD measurements from cruise MSM53 in 2016, (b) SVA based on the GEM reconstructed CTD profiles of this cruise, and (c) the difference between the CTD and GEM reconstructed section. Dashed lines indicate CTD stations, solid thick lines indicate PIES positions. The hatched gray area indicates the transition region between the transfer function for PIES BP12 west of the MAR and the PIES BP32 – BP34 east of the MAR (cf. Figure 2.1 and 3.6).

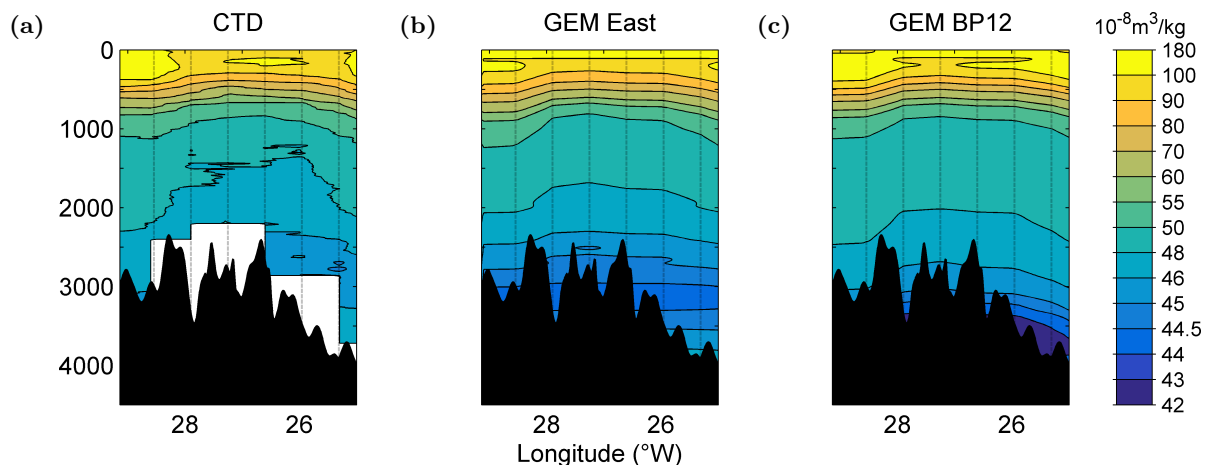


**Figure 3.6:** Transition area between the region of the GEM transfer function for PIES BP12 and for the eastern PIES BP32 – BP34. (a) SVA from CTD measurements, (b) SVA reconstructed from the GEM transfer function for the eastern PIES BP32 – BP34, (c) SVA reconstructed from the GEM transfer function for PIES BP12.

The barotropic (bt) contribution to PIES inferred SSH fluctuations  $\eta'_{bt}$  is calculated following Equation 3.2. The baroclinic (bc) contribution  $\eta'_{bc}$  is determined from  $\tau_{bc}$  which was corrected for the barotropic component (Equation 3.4) by calculating the GPA as an integral over the reconstructed SVA (Hallock, 1987; He et al., 1998):

$$GPA = \int_0^p SVA dp \quad (3.5)$$

with  $p$  being the pressure at the PIES position. With  $GPA = \overline{GPA} \pm GPA'$ , the baroclinic contribution to the SSH variability  $\eta'_{bc}$  becomes:

$$\eta'_{bc} = \frac{GPA'}{g(\lambda, H)} \quad (3.6)$$

with  $g(\lambda, H)$  as the gravitational acceleration at the PIES position.

### 3.1.4 Barotropic and baroclinic transport fluctuations

In order to complement the analysis with meridional transport calculations at the NOAC array, data from the PIES BP12 (west of the MAR) and the three eastern PIES BP32 – 34 is used. From respectively two PIES measurements a barotropic and baroclinic contribution to the velocity profile and thus the transport between these two PIES is inferred.

The barotropic contribution to the velocity profile  $v'_{bt}$  is calculated from the bottom pressure fluctuations of two PIES, the mean density  $\bar{\rho}$  calculated from the reconstructed water column

profiles at the PIES positions, the mean Coriolis parameter  $f(\lambda)$  of the two locations, and the distance between the two PIES:

$$v'_{bt} = \frac{\Delta p'_{PIES}}{\bar{\rho} \cdot f(\lambda) \cdot distance} \quad (3.7)$$

From the reconstructed SVA water column profiles at two PIES positions, the geostrophic velocity relative to a reference level at 4500 dbar (transport between BP32 and BP33 and between BP33 and BP34) or 4100 dbar (transport between BP12 and BP34) is calculated. The obtained velocity profiles are defined as the baroclinic contribution. The barotropic velocity component is added and both together are defined as the total relative PIES-derived velocity. In order to calculate the transport between two PIES, the velocity profile has to be multiplied with the area of the cross-section spanned by the two PIES. Obviously, this area is not exactly rectangular, especially not in the case of the cross-section between BP12 and BP34 which includes the MAR. To account for the topography in the calculation of the area of the cross-section, the ETOPO1 topography dataset (Amante et al., 2009) is used. The velocity profiles are extrapolated down to the sea floor in cases where the seafloor is below the GEM pressure limit of 4500 dbar / 4100 dbar or cut off at the respective pressure level in cases where the sea floor is above the GEM pressure limit. From these extrapolated or truncated velocity profiles which are multiplied with the area of the cross-section, the total relative PIES-derived transport between two PIES is calculated. However, since the barotropic contribution is only a transport fluctuation and the baroclinic contribution is calculated to a reference level of no motion, without further known reference level (cf. Section 3.1.5), the resulting time series represents only a relative transport.

### 3.1.5 Absolute PIES transport time series

For all transport sections, a high correlation between the geostrophic surface velocities calculated from the satellite SSH and the baroclinic PIES transports is found (all correlation coefficients are above 0.85). The geostrophic velocity between two PIES is calculated from the satellite SSH ( $MADT$ ), the mean Coriolis parameter  $f$  and the mean gravitational acceleration  $g$  for the involved PIES positions as:

$$v = \frac{g \Delta MADT}{f \cdot distance} \quad (3.8)$$

The  $MADT$  values used in this context are the ones from the grid points that are closest to the PIES positions.

The PIES-derived barotropic transport fluctuation varies independently from the baroclinic transport and also exhibits a smaller variability compared to the baroclinic signal. It is thus not imprinted well on the altimeter signal and for all transport sections the correlation between the satellite geostrophic surface velocities and the barotropic PIES transports is not significant at the 95 % confidence limit. These findings are very similar to and supported by the results of the analysis of the different NAC regimes in terms of SSH fluctuations presented and discussed in Section 4.1.

Using the high correlation between the satellite record and the PIES data, absolute baroclinic PIES-derived transport time series are obtained following Rhein et al. (2019). The PIES-derived baroclinic velocities which are relative to an assumed reference level are referenced to the geostrophic velocities calculated from the satellite SSH to obtain absolute PIES-derived baroclinic velocity profiles and consequently transport time series.

In a last step, the PIES-derived barotropic transport fluctuations are added to the absolute PIES-derived baroclinic transport time series to obtain the total PIES-derived daily transport for the period 2016 to 2017.

#### **3.1.6 Transport time series extended by altimetry**

To extend the transport time series back to 1993 the absolute baroclinic transports are regressed on the altimeter surface velocity field. In contrast to the flow field in the western basin west of 37°W (see also Figure 4.1 and 4.2), the barotropic part of the flow between the four PIES considered here is not correlated well with altimetry as stated above. Consequently, a daily baroclinic transport time series for the period 1993 to 2017 is obtained with the barotropic component representing an uncertainty in the interpretation of the altimeter signal as proxy for the transport.

#### **3.1.7 Uncertainty estimates**

In the following, the different sources for uncertainties in the transport time series are discussed. For this, the baroclinic and barotropic transport time series from PIES are treated separately from the long-term transport time series obtained by regression on the altimeter data.

### Uncertainties in the barotropic and baroclinic PIES transport time series

First, the uncertainty for the time series with daily resolution is calculated followed by the uncertainty for yearly mean values obtained by scaling the daily error with the effective number of independent observations (effective degree of freedom, Bayley et al., 1946; Garrett et al., 1981; Rhein et al., 2019; Roessler et al., 2015). The effective degree of freedom is given in Table 3.1, the uncertainties are given in Table 3.2. The combined uncertainties for the baroclinic time series with daily resolution range from 7.5 Sv to 8.8 Sv, for the annual mean values from 2.6 Sv to 2.9 Sv. The uncertainty in the barotropic time series related to the pressure measurement ranges from 1.2 Sv to 1.7 Sv for the daily values and from 0.03 Sv to 0.06 Sv for the annual mean values.

	Central	East 1	East 2
<b>Baroclinic transport</b>	15	17	14
<b>Barotropic transport</b>	40	27	26
<b>Altimeter-based transport</b>	11	11	11

**Table 3.1:** Effective degrees of freedom for the individual time series, used to estimate yearly uncertainties.

		Central	East 1	East 2
<b>Barotropic transport</b>		1.2 / 0.03	1.6/0.06	1.7 / 0.06
<b>Baroclinic transport</b>	$\tau$ Sea roughness/rain	1.3 / 0.08	1.1 / 0.06	1.1 / 0.08
	Scatter from lin. fit	4.6 / 0.3	5.8 / 0.3	5.8 / 0.4
	CTD Calibration	1.8 / -	2.0 / -	2.0 / -
	Removal of bt. part	0.007 / 0.0004	0.006 / 0.0003	0.006 / 0.0004
	<b>Total</b>	7.2 / 2.6	8.8 / 2.9	8.7 / 2.8
	GEM profile choice	0.003 / -	0.002 / -	0.002 / -
	Coriolis parameter	2.1 / 0.1	0.02 / 0.0009	0.02 / 0.001
	<b>Total</b>	7.5 / 2.6	8.8 / 2.9	8.7 / 2.8
<b>Altimeter-based extended transp.</b>		2.2 / 0.2	2.2 / 0.2	2.3 / 0.2
<b>Total</b>		7.8 / 2.6	9.1 / 2.9	9.0 / 2.9

**Table 3.2:** Summary of the estimated daily (1st value) and, if applicable, yearly (2nd value) uncertainties which are obtained by scaling the daily value with the effective degree of freedom for the individual sections (cf. Table 3.1). The uncertainties due to the CTD calibration and the GEM profile choice are not scaled with the effective degree of freedom thus the yearly uncertainty estimate corresponds to the daily uncertainty estimate (Roessler et al., 2015). Uncertainties are given in Sverdrup.

### Uncertainty in the barotropic PIES transport related to the pressure measurements

The uncertainty for the individual half-hourly pressure measurement related to the de-drifting routine is less than 0.02 dbar (Watts et al., 1990). To convert this value into an uncertainty in

the barotropic transport fluctuation, it is scaled with the effective degrees of freedom ( $n = 48$ ), for a measurement period of 24 h, since the de-drifted and de-tided statistically independent daily mean values are used in the calculations, and multiplied by  $\sqrt{2}$ , since data from two PIES are used to calculate the transport for a section. This results in an uncertainty of 1.2 Sv to 1.7 Sv for the daily values and for the yearly mean values of 0.03 Sv to 0.06 Sv (scaled with the effective degree of freedom from Table 3.1).

#### **Uncertainties in the baroclinic PIES transport**

The uncertainties in the baroclinic transport are caused by several independent sources. As described in Chidichimo et al. (2014), Meinen et al. (2004), and Roessler et al. (2015), they originate from:

1. uncertainties in the  $\tau$  measurements caused by
  - a. scatter in the measurements due to sea roughness and rain, i.e. the measurement accuracy,
  - b. scatter from the linear relation between the Fofonoff potential and  $\tau_{1900}$  (Figure 3.7),
  - c. calibration of the measured  $\tau$  into  $\tau_{1900}$  via CTD measurements,
  - d. removal of the barotropic component from the travel time measurement,
2. uncertainties due to the choice of Argo float and shipboard CTD profiles used to create the GEM transfer function,
3. uncertainties due to latitudinal differences between the PIES positions.

To determine uncertainties for the yearly mean transports of the PIES measurement record, the daily uncertainty for the measurement accuracy of  $\tau$ , the scatter from the linear fit (cf. Figure 3.7), the removal of the barotropic component in  $\tau$ , and the error due to different latitudes are scaled with the effective degrees of freedom. The uncertainties resulting from the choice of GEM profiles and from the calibration of  $\tau$  represent biases and are thus not scaled by the effective degrees of freedom (Roessler et al., 2015). The uncertainties for the mean baroclinic transports are given in Table 3.1. Uncertainties range from 7.5 Sv to 8.8 Sv for the daily values and 2.6 Sv to 2.9 Sv for the yearly mean values.

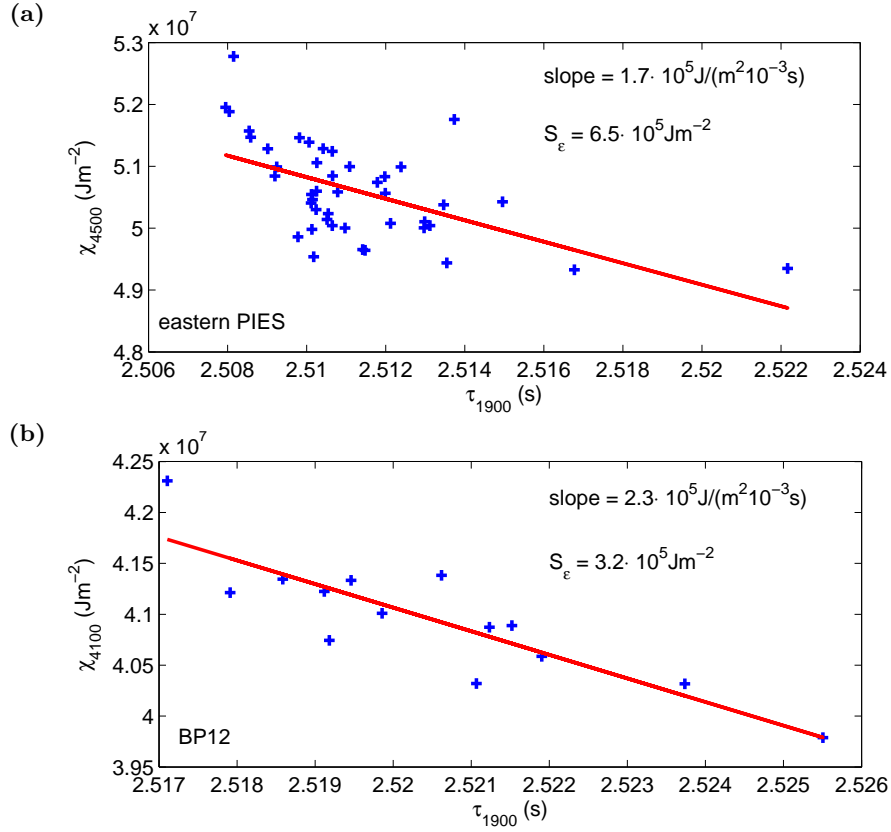


**Figure 3.7:** Fofonoff potential for CTD profiles used to create the transfer function with corresponding  $\tau_{1900}$  values for (a) eastern basin PIES and (b) BP12. The Fofonoff potential  $\chi$  represents the potential energy anomaly and is defined as  $\chi = g^{-1} \int p \cdot SVA dp$  (with  $g$  being gravitational acceleration,  $p$  pressure and  $SVA$  specific volume anomaly), The scatter of the linear relation is expressed as the standard error  $S_\epsilon$  of the fit. The slope of the fit is used to convert uncertainties in  $\tau$  into uncertainties in Sverdrup (Meinen et al., 2004; Roessler et al., 2015).

#### Uncertainties in the $\tau$ measurements:

1a) Uncertainties due to sea roughness and rain: According to the manufacturer, for instrument depths of around 4500 m, the standard deviation of a 24-ping sample is typically below 2.2 ms at wind speeds of 25 knots and in heavy rain around 3.5 ms (University of Rhode Island, 2015). Using the larger value of 3.5 ms, this leads to a standard deviation of 0.7 ms for the daily mean travel times (Chidichimo et al., 2014; Roessler et al., 2015; University of Rhode Island, 2015). Combined with the slope of the fit of the Fofonoff potential in Figure 3.7, this translates into an uncertainty between 1.1 Sv and 1.3 Sv for the daily values and between 0.06 Sv to 0.08 Sv for yearly mean values.

1b) The scatter from the linear relation between the Fofonoff potential  $\chi$  and  $\tau_{1900}$  is represented by the standard error  $S_\epsilon$  of the linear fit (Figure 3.7) which is for the daily values  $3.2 \times 10^5 \text{ J/m}^2$

for BP12 and  $6.5 \times 10^5 \text{ J/m}^2$  for the eastern PIES corresponding to error estimates ranging from 4.6 Sv to 5.8 Sv for the daily values and from 0.3 Sv to 0.4 Sv for the yearly mean values.

1c) The uncertainty originating in the CTD calibration procedure of the measured  $\tau$  into  $\tau_{1900}$  includes uncertainties originating from i) the conversion of the measured  $\tau$  into  $\tau_{1900}$  and ii) the determination of the PIES depth.

- i) For every PIES, the standard deviations of the correction factor used to convert the measured  $\tau$  into  $\tau_{4500}$  and  $\tau_{4100}$  is calculated. Then, the standard error of the fit is used as an estimator of the scatter of the fit translating into the uncertainty due to the conversion of  $\tau_{4500}$  and  $\tau_{4100}$  into  $\tau_{1900}$ .
- ii) The uncertainty in the determination of the instrument depth is calculated via error propagation from the standard deviation of the determined pressure at the instrument's depth.

The square root of the summed up squared individual uncertainties is then used as the total uncertainty related to the calibration procedure. The uncertainties range from 1.8 Sv to 2 Sv for the daily and yearly mean values since in this case the daily uncertainty is not scaled with the effective degree of freedom.

1d) The uncertainty in the baroclinic transport which results from the removal of the barotropic component of the travel time is estimated by taking into account the measurement accuracy of the half-hourly individual pressure measurements related to the removal of the drift in the pressure sensor procedure as described by Watts et al. (1990) who find an uncertainty of less than 0.02 dbar for de-drifted pressure time series that are at least a year long. Since the pressure time series used for this analysis consists of de-drifted and de-tided statistically independent daily mean values, the uncertainty of 0.02 dbar is divided by the effective degrees of freedom ( $n = 48$ ) of a 24 h pressure record. This value is then converted into an equivalent of the acoustic travel time of 0.004 ms (for all PIES). The uncertainties range from 0.006 Sv to 0.007 Sv for the daily values and 0.0003 Sv to 0.0004 Sv for the yearly mean values.

For the total  $\tau$  related transport uncertainty, all four uncertainties are combined by taking the square root of the sum of the individual squared uncertainties and multiplying the result with  $\sqrt{2}$  since data from two PIES are used to two calculate the transport for a section. The total uncertainty for the baroclinic transports ranges from 7.2 Sv to 8.8 Sv for the daily values and 2.6 Sv to 2.9 Sv for the yearly mean values.

#### **Uncertainties in the creation of the GEM transfer function:**

The uncertainty of the calculated transports based on choice and availability of Argo float

and shipboard CTD profiles is estimated through a bootstrapping analysis following Roessler et al. (2015). From the set of Argo float and shipboard CTD profiles that is used to create the GEM transfer function, the same number of profiles were drawn randomly with replacement. This procedure was repeated 1000 times. For every new set of profiles, a transfer function and transports were calculated. The mean of the standard deviation at each time step was calculated and used as an uncertainty estimate. The estimates range from 0.002 Sv to 0.003 Sv for the daily and yearly mean values since this uncertainty also represents a bias error and is not scaled with the effective degree of freedom.

**Uncertainties due to latitudinal differences between the PIES positions:**

The uncertainties resulting from the different latitudes of the deployment sites are estimated following Roessler et al. (2015): The difference between the maximal and minimal  $\tau$  measured for each section is multiplied by the slope of the fit from Figure 3.7 divided by the mean density and the two different values for the Coriolis parameter respectively. This results in a maximal transport estimate due to the maximal difference in  $\tau$  combined with an estimate for the impact of the change in the Coriolis parameter. The standard deviation of these two transport estimates represents the maximal and thus threefold standard deviation since it is based on the maximal  $\tau$  difference. It is therefore divided by three to be comparable with the other estimated uncertainties. The resulting uncertainty estimates range from 0.02 Sv to 2.1 Sv for the daily values and from 0.0009 Sv to 0.1 Sv for the yearly mean values.

**Total uncertainty:**

To summarize, the total uncertainty estimates for the baroclinic transport are calculated from the square root of the sum of the squared individual errors for the uncertainty in  $\tau$ , the GEM profile choice, and the latitudinal differences. They range from 7.5 Sv to 8.8 Sv for the daily values and from 2.6 Sv to 2.9 Sv for the yearly averages.

**Uncertainties in the altimeter-based extended transport time series**

Following Roessler et al. (2015), the uncertainty in the daily altimeter-based extended transport is calculated from the mean standard deviation of the residuals between the altimeter-based absolute baroclinic transport time series and the absolute baroclinic transport calculated from the PIES (2.2 Sv to 2.3 Sv for the daily values). To obtain an estimate of the uncertainty of the annual means, the uncertainty for the daily values is scaled with the effective degree of freedom calculated from the integral time scale. Typical integral time scales for the altimeter-based

expanded time series for one year of data are in the range of 16 to 32 days. To not underestimate the decorrelation time scale, the maximal time of 32 days for scaling the uncertainty of the daily values is chosen and an uncertainty estimate for the annual mean values of 0.2 Sv for all sections is obtained. Combined with the uncertainties in the PIES transports this yields a total uncertainty of 7.8 Sv to 9.1 Sv for the daily transport times series and 2.6 Sv to 2.9 Sv for the yearly time series (Table 3.2).

### 3.2 Ekman transport from reanalysis data

To calculate Ekman transport, i.e. water transported by wind, across the 47°/48°N PIES transect, the wind stress of the NCEP/NCAR reanalysis data provided in meridional and zonal direction is used. Both components of the wind stress ( $\tau_{wind,meridional}$  and  $\tau_{wind,zonal}$ ) are combined and projected onto the transect spanned between two neighboring PIES to calculate the wind stress parallel to the PIES transect (referred to as  $\tau_{wind,PIES}$ ).

$$\tau_{wind,PIES} = \tau_{wind,meridional} \cdot \sin \alpha + \tau_{wind,zonal} \cdot \cos \alpha \quad (3.9)$$

In this context,  $\alpha$  is the angle between a line of constant latitude and the line spanned by two PIES.

The wind stress  $\tau_{wind}$  is defined as  $\tau_{wind} = \rho_{air} C_D U_{10}^2$  where  $\rho_{air}$  is the density of air,  $C_D$  the drag coefficient which depends of the wind speed, and  $U_{10}$  is the wind speed 10 m above the sea surface. By balancing friction and Coriolis force and integrating the resulting equation, the Ekman transport expressed as volume transport  $Q_E$  can be inferred.

$$Q_E = -\frac{\tau_{wind,PIES}}{\rho_{sw} f} \cdot distance \quad (3.10)$$

In the equations above,  $Q_E$  and  $\tau_{wind,PIES}$  are perpendicular to each other. The density of sea water  $\rho_{sw}$  is set to 1027.7 kg/m<sup>3</sup> which corresponds to the mean density calculated from the reconstructed water column profiles (cf. previous section). The Coriolis parameter is  $f = 2\Omega \cdot \sin \varphi$  with  $\Omega$  being the Earth's angular velocity and  $\varphi$  the mean latitude of two neighboring PIES positions while *distance* refers to the distance between the two PIES.

The mean Ekman transport across the whole PIES transect from BP12 to BP32 was found to be -1 Sv in 2016/2017 and -1.5 Sv in 1993-2017 (Table 3.3).

	2016/2017		1993 - 2017	
	Mean (Sv)	Std. (Sv)	Mean (Sv)	Std. (Sv)
<b>Central</b>	-0.6	1.1	-0.7	1.3
<b>East 1</b>	-0.2	0.6	-0.4	0.7
<b>East 2</b>	-0.2	0.6	-0.4	0.8
<b>Central + East 1 + 2</b>	-1.0	2.2	-1.5	1.6

**Table 3.3:** Mean Ekman transport and corresponding standard deviation (Std.) in 2016/2017 and 1993 - 2017 across the different PIES transects.

### 3.3 Transport time series obtained from model output

To compare the PIES- and altimeter-inferred transport time series to model output, transports across several model sections corresponding approximately to the PIES sections are calculated. For obtaining the total volume transport across a transport section, the transport across the face of each grid cell (Figure 2.4b) included in the defined section (Figure 3.8) is calculated. The calculated transports for each grid cell are summed up vertically from top to bottom and then combined either in *i*- or in *j*-direction, depending on the position and orientation of the defined section.

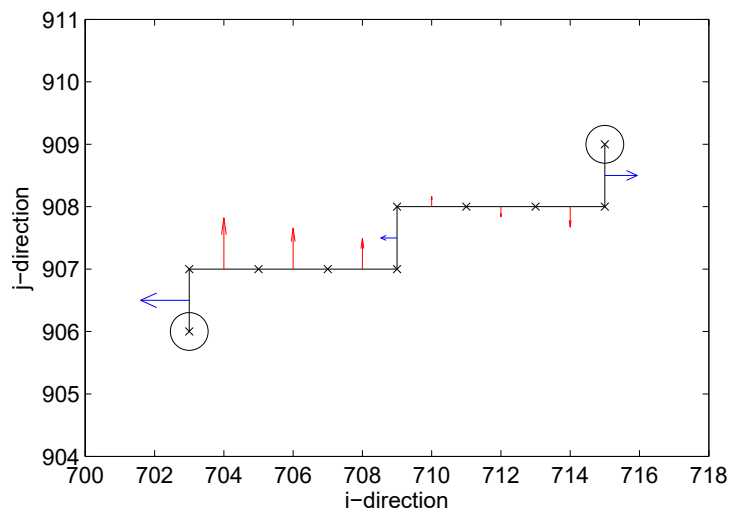


**Figure 3.8:** Sketch explaining the calculation of volume transport across a defined section in the model. The section is seen from atop. The points defining the end of the section in horizontal (*i*- and *j*-) direction are shown as black circles. Instead of directly connecting the end points with a straight line, the model transport section follows the horizontal mesh grid of the model, i.e. it exhibits a stepwise shape. The corners of each grid cell of the horizontal mesh which are included in the defined section are represented by a black x. Blue arrows denote top-to-bottom transport in *i*-, and red arrows top-to-bottom transport in *j*-direction. Direction, arrow size and grid cell indices are arbitrarily chosen and do not correspond to any specific model section. To calculate the total volume transport across the section, the individual transports in *i*- and *j*-direction are summed up.

In a first step, the individual transports across the faces of the grid cells at the position  $(i, j)$  are summed up vertically from top to bottom (Equation 3.11 and 3.12):

$$Q_{v,i,j} = \sum_k v_{i,j,k} \cdot e_{1,i,j,k} \cdot e_{3,i,j,k} \quad (3.11)$$

$$Q_{u,i,j} = \sum_k u_{i,j,k} \cdot e_{2,i,j,k} \cdot e_{3,i,j,k} \quad (3.12)$$

In the equations above,  $Q_{v,i,j}$  and  $Q_{u,i,j}$  are the top-to-bottom transport in  $u$ - (parallel to  $\mathbf{i}$ ) or  $v$ -direction (parallel to  $\mathbf{j}$ ) at the location defined by the indices  $(i, j)$  of the horizontal model grid.  $v_{i,j,k}$  and  $u_{i,j,k}$  are the velocities at the grid cell of the position  $(i, j, k)$  and  $e_{1,i,j,k}$ ,  $e_{2,i,j,k}$ , and  $e_{3,i,j,k}$  represent the grid cell length in  $\mathbf{i}$ -,  $\mathbf{j}$ -, and  $\mathbf{k}$ -direction respectively.

In a next step, the top-to-bottom transport at each horizontal location  $(i, j)$  is combined and summed up in  $\mathbf{i}$ - and  $\mathbf{j}$ -direction along the defined section:

$$Q_v = \sum_i Q_{v,i,j} \quad (3.13)$$

$$Q_u = \sum_j Q_{u,i,j} \quad (3.14)$$

$Q_v$  and  $Q_u$  are the total transport in  $\mathbf{j}$ - and  $\mathbf{i}$ -direction whose sum represents as  $Q = Q_v + Q_u$  the total transport across the defined section.

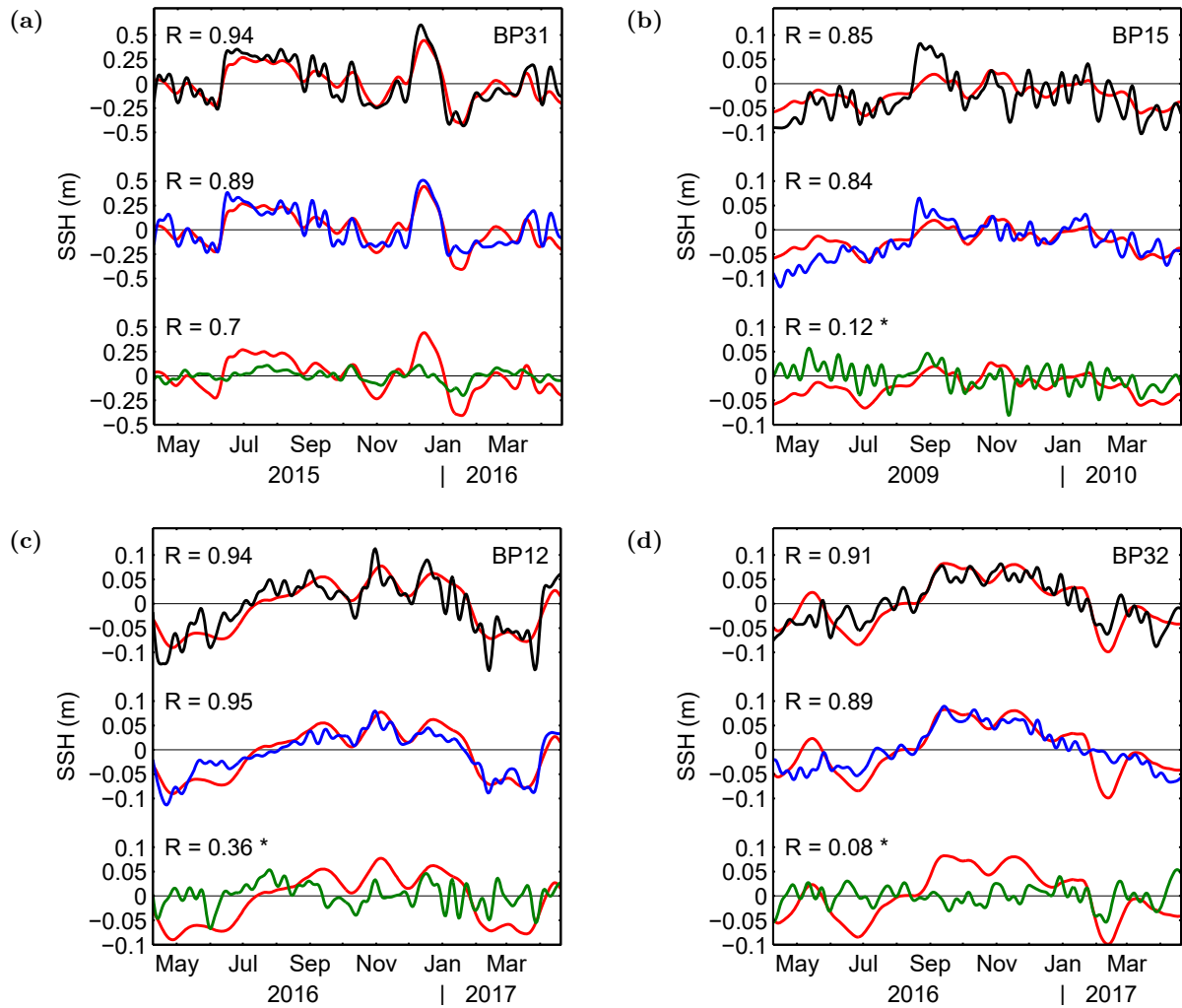
## 4 Trends and transport variability of the circulation in the subpolar eastern North Atlantic studied with inverted echo sounders

This chapter focuses on the analysis of the observational data regarding the circulation in the subpolar North Atlantic, especially in the eastern basin. PIES- and satellite-derived SSH data are compared to each other and the first PIES-derived transport time series for the eastern basin across  $47^{\circ}/48^{\circ}\text{N}$  are presented and discussed. Using satellite data, the PIES-derived transport time series are extended into decadal time series and are put into relation with corresponding time series from the western basin and the MAR region (cf. Figure 1.3).

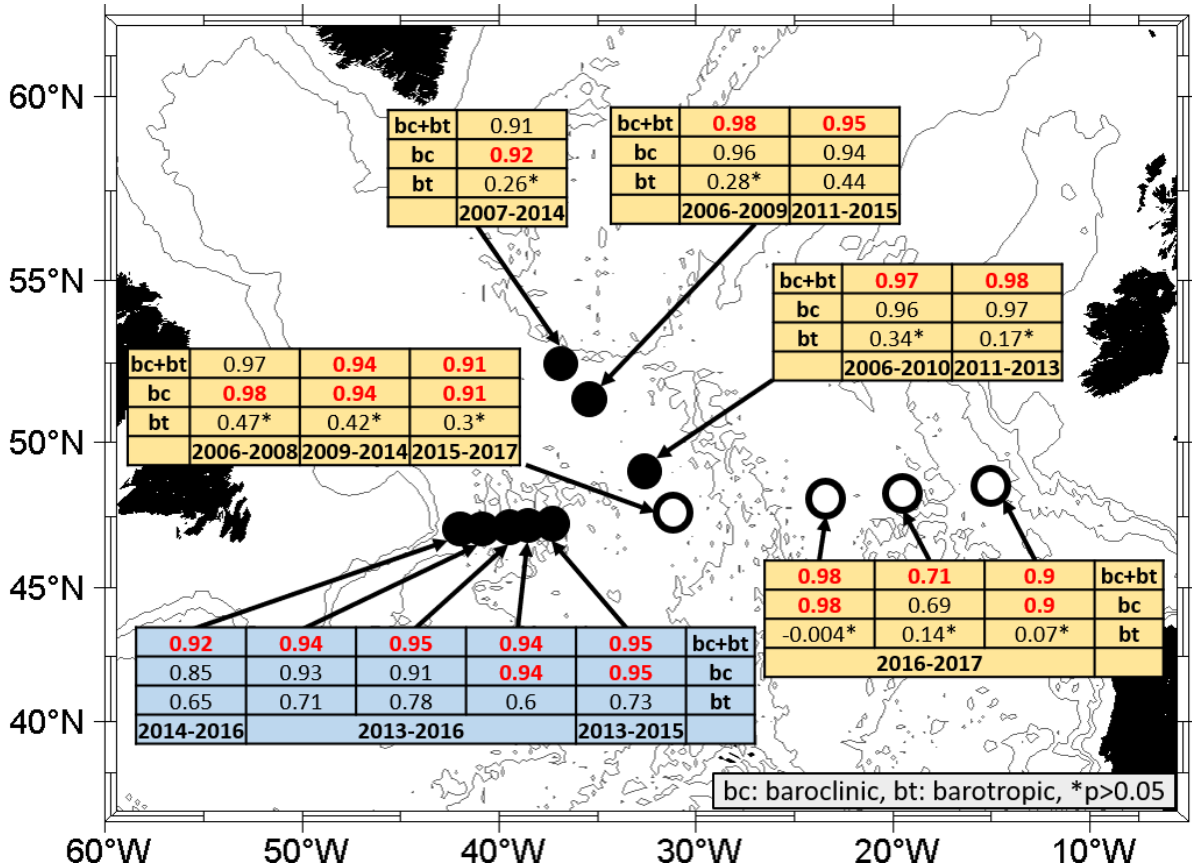
### 4.1 Correlation between PIES and altimeter-derived SSH

Figure 4.1 shows a comparison of selected PIES positions representing the western, central and eastern NAC regimes regarding the baroclinic and barotropic contributions to the SSH fluctuation. Each PIES time series is compared to the satellite-derived SSH signal and correlation coefficients are calculated for each comparison. The time series are shortened to show the same time period in each panel. Figure 4.2 summarizes for each PIES site all calculated correlation coefficients for the comparison of baroclinic and barotropic contributions to the PIES-derived SSH fluctuation with the satellite-derived SSH. The correlation coefficients reveal different dynamical regimes: In the western Atlantic, west of  $37^{\circ}\text{W}$ , the barotropic as well as the baroclinic contribution to the PIES-derived SSH signal is highly correlated with the altimeter signal, while at the MAR and in the eastern Atlantic, the correlation of the satellite-derived SSH with the barotropic SSH signal is for most cases not significant and therefore negligible when considering the total signal (Figure 4.2). West of  $37^{\circ}\text{W}$ , the flow has thus a strong barotropic signal (Figure 4.1a) with top-bottom averaged mean velocities of the order of tenths of  $\text{cm/s}$  (Rhein et al., 2019), while at the MAR (Roessler et al., 2015) and in the

4 Trends and transport variability of the circulation in the subpolar eastern North Atlantic studied with inverted echo sounders



**Figure 4.1:** Comparison of time series of barotropic (green), baroclinic (blue) and barotropic + baroclinic (black) SSH fluctuations to satellite SSH fluctuations (red) from (a) PIES BP31 (western endpoint of 47°/48°N-array), (b) PIES BP15 (northern endpoint of MAR array), (c) PIES BP12 (located at the midpoint connecting the MAR- and 47°/48°N-array), and (d) PIES BP32 (eastern endpoint of 47°/48°N-array). For each comparison, the corresponding correlation coefficient  $R$  is given. The asterisk marks non-significant correlations at the 95% confidence limit ( $p > 0.05$ ). Note the different years on the x-axes and different scales on the y-axes in each figure. To compare time series of the same length and times of the year, the time series were shortened. Correlation coefficients for the unshortened time series are given in Figure 4.2.



**Figure 4.2:** Correlation between the PIES-derived barotropic (bt), baroclinic (bc) and baroclinic + barotropic (bc+bt) contribution to the SSH variability and the satellite-derived SSH signal at the PIES positions. Numbers denote the correlation coefficients with the highest correlation marked in bold red. P-values > 0.05 indicate that the correlation is not significant at the 95% confidence limit. Table colors indicate the different dynamic regimes: In the western basin (blue) the barotropic PIES signal is imprinted well on the altimeter SSH signal, whereas in the eastern basin and the MAR region (yellow), only the baroclinic PIES signal is strongly correlated with the altimeter signal. The correlation is calculated under consideration of the decorrelation time for each 10-day low pass filtered time series. The decorrelation time scale is calculated as twice the integral of the lagged autocorrelation function (Bayley et al., 1946; Garrett et al., 1981; Rhein et al., 2019; Roessler et al., 2015). For the altimeter-derived SSH fluctuation, the decorrelation time is in the range of 16 to 109 days, for the barotropic PIES-derived SSH fluctuation, it is in the range of 7 to 35 days, for the baroclinic PIES-derived SSH fluctuation, it is in the range of 19 to 86 days, and for the sum of the baroclinic and barotropic PIES-derived SSH fluctuation, it is in the range of 15 to 82 days.

eastern Atlantic, the variability of the barotropic signals is smaller with a very weak imprint on the SSH (Figure 4.1b, c, and d).

## 4.2 Transports

In this section, the PIES-derived transport time series for meridional transports across  $47^\circ/48^\circ\text{N}$  in the eastern basin from 2016 to 2017 are presented, including the total top-to-bottom transport as well as the transport in upper and lower layers. Furthermore, the reconstructed long-term time series (1993 to 2017) which were obtained using satellite altimetry data are presented and analyzed in terms of long-term trends. Additionally, the time series for the eastern basin are compared and correlated to published transport time series from the western basin and the MAR region.

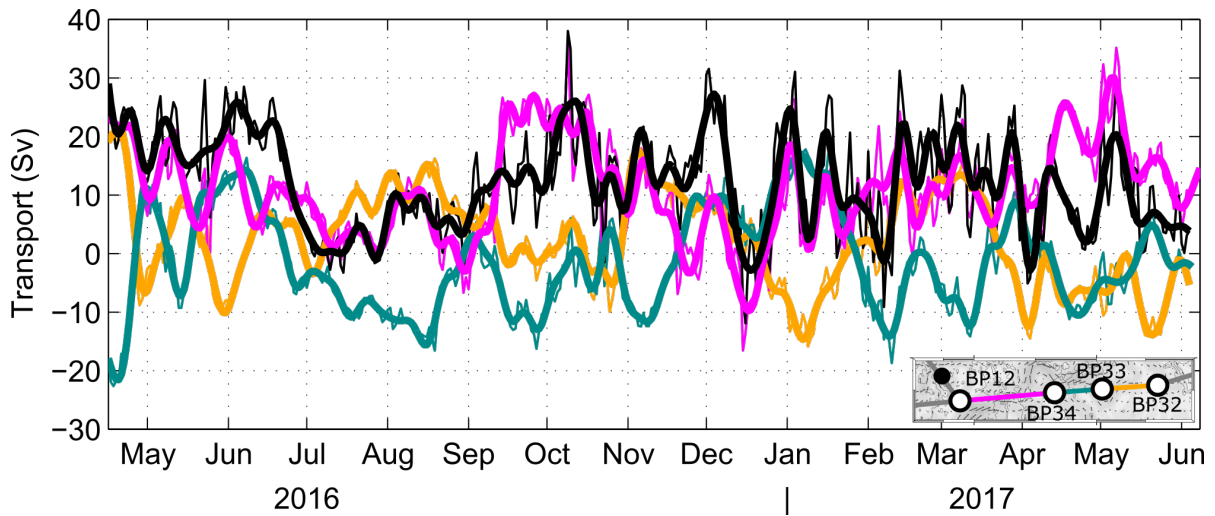
### 4.2.1 PIES-derived transport in 2016 and 2017

Figure 4.3 shows the PIES-derived transport time series for meridional transports across  $47^\circ/48^\circ\text{N}$  in the eastern basin from 2016 to 2017 with the corresponding mean values, standard errors of the mean, standard deviations, effective degrees of freedom, and decorrelation time scales summarized in Table 4.1. Figure 4.4 shows the transport time series in the eastern basin from 2016 to 2017 separated into upper ocean and deep ocean transport.

	<b>Central</b>	<b>East 1</b>	<b>East 2</b>	<b>Sum</b>
<b>Mean (Sv)</b>	+11.1	-1.4	+2.5	+12.2
<b>Standard error of mean (Sv)</b>	1.7	1.8	1.7	1.4
<b>Standard deviation (Sv)</b>	8.6	8.6	7.9	8.7
<b>Degrees of freedom</b>	26	24	23	39
<b>Decorrelation time (days)</b>	16	17	18	11

**Table 4.1:** Mean values, standard error of the mean, standard deviation, effective degrees of freedom, and decorrelation time scale for the PIES transport time series, April 2016 - June 2017 (cf. Figure 4.3). The standard error of the mean is used as a measure of uncertainty for the calculated mean transports.

For the measurement period 2016 to 2017, the largest mean northward transport ( $+11.1\text{ Sv} \pm 1.7\text{ Sv}$ ) is found in the *NAC Central* segment, a smaller mean southward transport in the *NAC East 1* part ( $-1.4\text{ Sv} \pm 1.8\text{ Sv}$ ) and a smaller mean northward flow in the easternmost segment *NAC East 2* ( $+2.5\text{ Sv} \pm 1.7\text{ Sv}$ ). Even if the transports are scaled with the distance between the PIES, the mean meridional transport across the *NAC Central* segment is more



**Figure 4.3:** Total (absolute baroclinic + barotropic) PIES derived transport as daily values (thin lines) and 10-day low pass filtered (thick lines) in the period April 2016 to June 2017. The Ekman transport is not included. Positive values: northward transport, negative values: southward transport. *NAC Central* segment: magenta, *NAC East 1* segment: green, *NAC East 2* segment: yellow, sum of all three segments: black. For mean transports cf. Table 4.1.

than twice as high as in the *NAC East 2* part and almost four times larger than the *NAC East 1* segment. All three transport time series exhibit a high variability with the standard deviations between 7.9 Sv (*NAC East 2*) and 8.6 Sv (*NAC Central* and *NAC East 1*) being of the same order of magnitude and larger than the mean signal. The maximum transport across the central segment is of the order of +30 Sv and the maximum transport lasting longer than a month of +25 Sv (Figure 4.3). Furthermore, in some time periods with a rather large or small flow across the *NAC Central* segment, the transport across the two eastern segments changes as well and compensates the transport across the *NAC Central* segment. For example, in October 2016, the unusual large northward transport across the *NAC Central* segment (about +25 Sv) corresponds to a time period with a small northward transport in the *NAC East 1* and *NAC East 2* segments (between -10 Sv and 0 Sv). In contrast to that, in August and September 2016, the transport across the *NAC Central* was rather small (between 0 Sv and +10 Sv) whereas the northward transport across the *NAC East 2* segment was unusually large (about +10 Sv or more). Moreover, also for the two easternmost time series, a compensating behavior among each other is found. For most times of a larger northward transport across the *NAC East 2* segment, the transport across the *NAC East 1* segment is larger in southward direction (e.g. in August and September 2016 or February and March 2017) and vice versa (e.g. in January 2017). This implies a negative correlation between the transports in the eastern basin suggesting a meandering of currents between the segments which will be addressed in

Section 4.2.4. To what extent these 14 months of data are representative of the mean flow and the observed variability will be further explored when analyzing the reconstructed decadal time series in Section 4.2.2.

### Upper and deep ocean PIES-derived transport

The velocity section in Figure 1.4 based on ADCP measurements suggests that east of the main NAC branch in the western basin, including the recirculation and what is defined by Rhein et al. (2019) as southward flow west of the NAC, the flow at depth is sometimes opposite to the flow in the upper layers. In order to address this difference, the flow at depth and in the upper layers is therefore calculated separately in addition to the total top-to-bottom transport (Figure 4.4). The isopycnal  $\sigma_\theta = 27.68 \text{ kg/m}^3$  representing the upper limit of Labrador Sea Water, the lightest water component of North Atlantic Deep Water, was chosen as a separation between the flow at depth and in the upper layers. It corresponds in average to a pressure level of 1030 dbar (averaged over all three sections, *NAC Central*, *NAC East 1* and *NAC East 2*, and the time period from 2016 to 2017). The transport of water denser than  $27.68 \text{ kg/m}^3$  is defined here as the flow in the deep ocean or lower layers, the transport of water lighter than  $27.68 \text{ kg/m}^3$  is defined as flow in the upper ocean or upper layers.

For the *NAC Central* segment, for the upper ocean (+6.9 Sv) as well as for the deep ocean (+4.2 Sv), a mean northward transport is found. In contrast to that, for the *NAC East 1* and *NAC East 2* segments, the transport in the upper layers is in both cases in northward direction (even though very close to zero in case of the *NAC East 1* segment) but in the deep ocean in southward direction. The largest difference between the upper and lower layer transport is found for the *NAC East 2* segment. Here, the northward transport in the upper layer (+5 Sv) is almost as high as the one found for the *NAC Central* segment (+6.9 Sv). In the deep layer, however, the *NAC East 2* segment transport is southward (-2.5 Sv), while in the *NAC Central* segment it is northward (+4.2 Sv). For the *NAC East 1* segment, the smallest mean transports as well as the smallest difference between the mean transports in the upper (+0.2 Sv) and lower (-1.6 Sv) layers are found. The net northward transport in the upper layers summed up for all three segments (+12.1 Sv) is as large as the summed up net top-to-bottom northward transport for these segments (+12.2 Sv). Furthermore, for all three segments, the northward transport across each segment is larger than the northward transport in the deep layer across the segment (cases of southward flow are considered for this statement as negative northward flow).

In the *NAC Central* segment, the mean transport in the upper layer amounts to about 62 % of the total top-to-bottom transport. This is comparable to the flow across the MAR (where the upper layer transport amounts to about 60 % of the total transport) as reported by Roessler

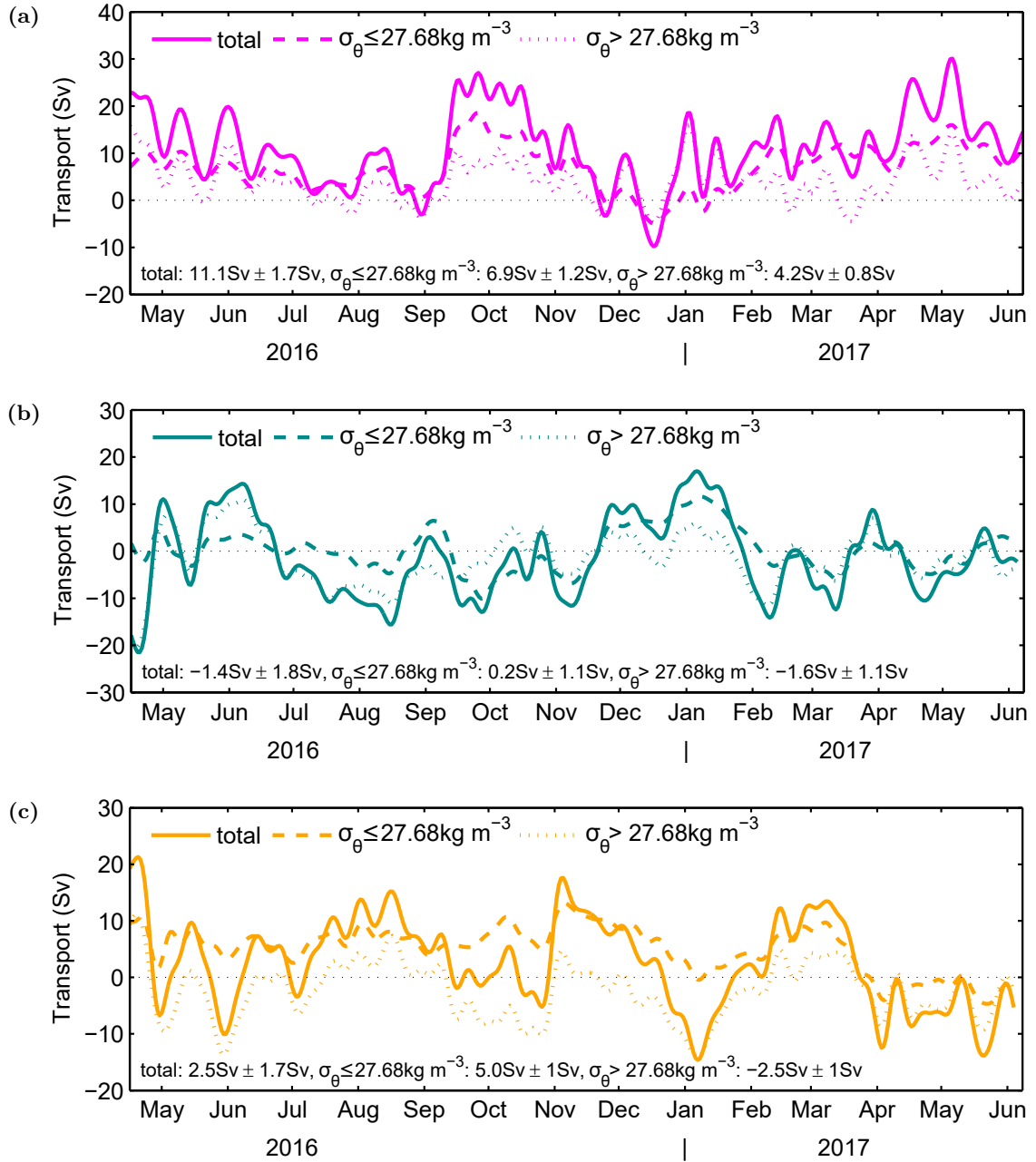


**Figure 4.4:** Total top-to-bottom transport (solid line) and transport below (dotted line) and above (dashed line) the  $27.68 \text{ kg/m}^3$  potential density isoline for the segments *NAC Central* (a), *NAC East 1* (b) and *NAC East 2* (c). Transports are 10-day low pass filtered. Numbers represent mean transports and standard errors of the mean for the total transport section and are given in each panel for the total transport and the transport below and above the chosen isoline. Positive values: northward transport, negative values: southward transport. The chosen isoline for separating between upper and lower transports corresponds to an average pressure level of 1030 dbar.

et al. (2015). Due to the high variability of the flow field, however, the amount of subtropical water cannot be inferred from this because, in contrast to Roessler et al. (2015), subtropical and recirculated water cannot clearly be separated from each other. Furthermore, because of the relatively short mooring period for the PIES in the eastern basin, this result is not extrapolated to the time period 1993 to 2017.

#### 4.2.2 PIES- and altimeter-derived transport in 1993 to 2017

Figure 4.5 shows the reconstructed long-term time series (1993 to 2017) which were obtained using satellite altimetry data for the three sections as well as for their sum. Furthermore, a dashed line indicates the decadal trend which was found for the transport time series summed up over all three segments and which will be discussed in Section 4.2.3. Table 4.2 summarizes the mean transports, standard errors of the mean, standard deviations, effective degrees of freedom, and decorrelation time scales for the extended time series.

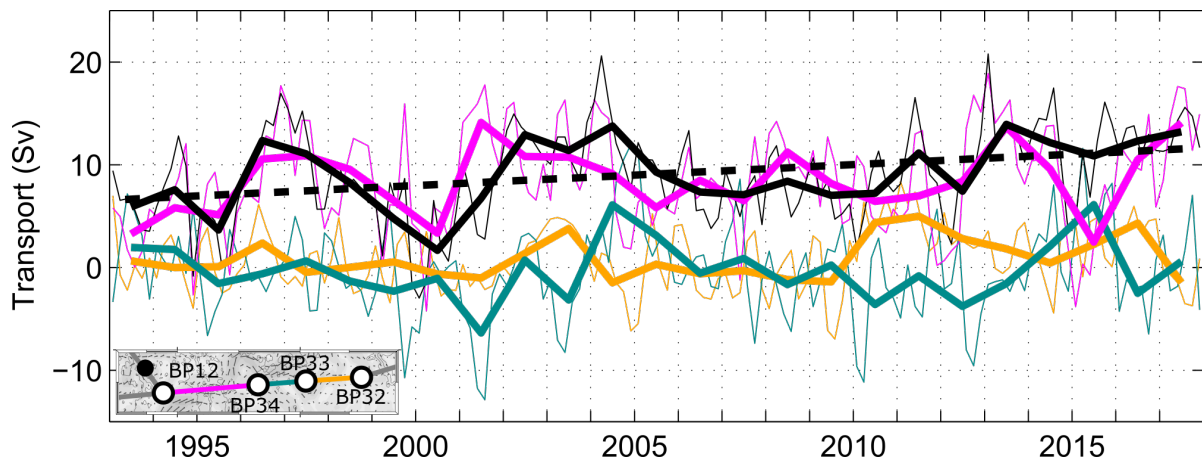


**Figure 4.5:** Absolute baroclinic PIES transport expanded with satellite altimetry (1993 - 2017). Solid thin lines: bi-monthly means, solid thick lines: annual means, dashed line: decadal trend for the sum of all segments. Colors as in Figure 4.3. The Ekman transport is not included. For mean transports cf. Table 4.2. Significant decadal trend for all segments together  $+2\text{ Sv} \pm 1.5\text{ Sv}$  ( $p = 0.01$ ).

Over the time period from 1993 to 2017 (Figure 4.5), the mean pattern is very similar to the short PIES-derived time series from 2016 to 2017 (Figure 4.3). The annual mean transport obtained from the decadal time series (Table 4.2) is northward (overall mean:  $+9.1\text{ Sv} \pm 0.8\text{ Sv}$ ) and dominated by the almost permanent northward flow in the *NAC Central* segment (overall mean:  $+8.5\text{ Sv} \pm 0.6\text{ Sv}$ ). The eastern segments *NAC East 1* and *NAC East 2* generally show a near zero flow with tendency to a southward flow for the *NAC East 1* segment (overall mean:

$-0.3\text{ Sv} \pm 0.6\text{ Sv}$ ) and a tendency to a northward flow for the *NAC East 2* segment (overall mean:  $+0.9\text{ Sv} \pm 0.4\text{ Sv}$ ). The exceptions are 2005 for the *NAC East 1* segment ( $+7\text{ Sv}$ ) and 2011 ( $+6\text{ Sv}$ ) for the *NAC East 2* segment. The former is correlated with a relatively small transport in the central segment, indicating an eastward shift of the flow regime and a meandering and shifts of the currents. A similar pattern was also observed in 2015, when the northward transport in the *NAC Central* segment decreased from  $+16\text{ Sv}$  to  $+2\text{ Sv}$  from 2013 to 2015 and the southward flow in the *NAC East 1* segment with  $-4\text{ Sv}$  in 2013 turned into a northward flow with  $+3\text{ Sv}$  in 2015.

	<b>Central</b>	<b>East 1</b>	<b>East 2</b>	<b>Sum</b>
<b>Mean (Sv)</b>	8.5	-0.3	0.9	9.1
<b>Standard error of mean (Sv)</b>	0.6	0.6	0.4	0.8
<b>Standard deviation (Sv)</b>	5.5	5.1	3.5	4.8
<b>Degrees of freedom</b>	75	76	68	36
<b>Decorrelation time (days)</b>	122	120	133	256

**Table 4.2:** Mean values, standard error of the mean, standard deviation, degrees of freedom, and decorrelation time scale for the PIES- and altimeter-based transport time series 1993 - 2017 (Figure 4.5). The standard error of the mean is used as a measure of uncertainty for the calculated mean transports.

### Preferred flow paths derived from satellite data

To address the hypothesis of meandering currents with a focus on the *NAC Central* segment, satellite-derived absolute geostrophic velocities are used to complement the analysis of the volume transports.

Figure 4.6 shows the mean absolute geostrophic velocities averaged over the time periods with a larger and smaller northward transport within the *NAC Central* segment in 2016 to 2017. A larger/smaller northward transport is defined here as a transport larger/smaller than the mean PIES transport across the *NAC Central* segment of  $+11.1\text{ Sv}$  plus/minus the standard deviation of  $8.6\text{ Sv}$  (cf. Figure 4.3 and Table 4.1). To reveal a potentially preferred flow path east or west of the MAR crest within the *NAC Central* segment, Figure 4.7 shows the satellite-derived absolute geostrophic velocities across the *NAC Central* transect from 1993 to 2017, separated into the region west and east of the crest of the MAR.

The analysis of the surface geostrophic velocities in times of larger and smaller transport across the *NAC Central* segment reveals that for the PIES region in general preferred flow paths exist. Figure 4.6 shows that, while still being visible in times of higher northward transport across the *NAC Central* segment, during times of lower northward transport, a more pronounced branch detaching from the NAC main branch at about  $43^\circ\text{N}$  is found, flowing northeastward,

and crossing the MAR south of the 47°/48°N line. In times of lower northward transport in the *NAC Central* segment, this branch tends to cross the 47°/48°N line further east than in times of higher northward transport.

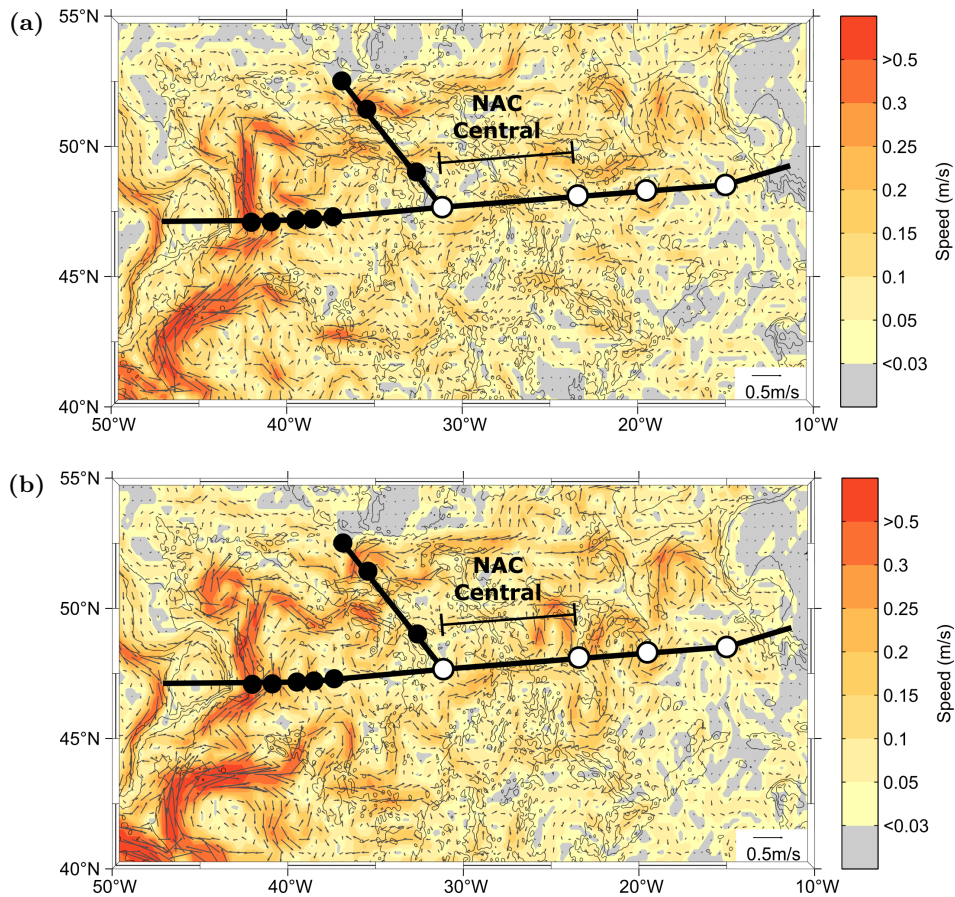


**Figure 4.6:** Mean geostrophic velocities in 2016/2017 averaged over time periods with a (a) larger northward and (b) smaller transport across the *NAC Central* segment. A larger northward transport is defined as transport larger than the mean PIES transport across the *NAC Central* segment (+11.1 Sv) plus the standard deviation (8.6 Sv) and smaller transport is defined as transport below the mean PIES transport minus the standard deviation (cf. Figure 4.3 and Table 4.1). Colors and arrows as in Figure 1.3a, black and white circles represent PIES positions, the lines show the location of the NOAC array.

However, no pronounced pathway within the *NAC Central* segment at the eastern or western flank of the MAR can be inferred from Figure 4.7. Instead, this figure also supports the assumption of meandering currents within this segment and presumably also out of this segment since for some time periods, the mean velocities are negatively correlated and a higher northward surface velocity in the western part corresponds to a smaller northward surface velocity in the eastern part of the segment or vice versa (e.g. from 1997 to 2000), but for other time

periods, both, the velocities at the western and eastern flank are similarly large (e.g. in 2002 or in 2013) or small (e.g. in 2016).

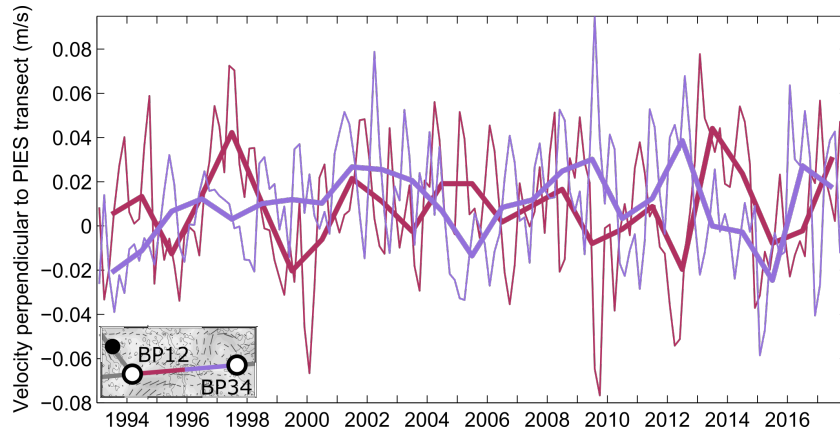


**Figure 4.7:** Bi-monthly (thin lines) and annual mean (thick lines) altimeter-derived surface velocities (absolute geostrophic velocities) perpendicular to the *NAC Central* segment for the period 1993 to 2017. Data are averaged between PIES BP12 and the MAR crest (red) and the MAR crest and BP 34 (purple). Mid of transect ( $27^{\circ}17.06'W$ ) is defined as separation.

### 4.2.3 Long-term trends

Table 4.3 summarizes the calculated trends for the eastern basin and the results of the trend analysis for the western basin from Rhein et al. (2019).

Segment	Trends (Sv/decade)	Mean transports (Sv)
Central	+1.2 Sv $\pm$ 1.4 Sv	+8.5 Sv $\pm$ 0.6 Sv
East 1	+0.1 Sv $\pm$ 1.3 Sv	-0.3 Sv $\pm$ 0.6 Sv
East 2	+0.7 Sv $\pm$ 0.8 Sv	+0.9 Sv $\pm$ 0.4 Sv
Central + East 1 + East 2	<b>+2.0 Sv <math>\pm</math> 1.5 Sv</b>	+9.1 Sv $\pm$ 0.8 Sv
West*	<b>-6.0 Sv <math>\pm</math> 5.7 Sv</b>	+19.3 Sv $\pm$ 3.3 Sv
West* + WBC*	<b>-7.1 Sv <math>\pm</math> 3.9 Sv</b>	-3.8 Sv $\pm$ 2.6 Sv

**Table 4.3:** Long-term trends (Sv/decade) and mean transports in 1993 to 2017 (Sv). The transport errors are summarized in Table 3.2 and standard errors of the mean in Table 4.1 and 4.2.

Bold: trend significant with  $p < 0.05$ . \* from Rhein et al. (2019), time series 1993 to 2018.

For the overall interior eastern basin between PIES BP12 and PIES BP32 (see also Figure 4.5), a significant positive decadal trend of  $+2.0 \text{ Sv} \pm 1.5 \text{ Sv}$  is found. The individual segments,

however, do not exhibit any significant trend. The positive trend found for the eastern basin is opposite to the negative decadal trend of  $-6.0 \text{ Sv} \pm 5.7 \text{ Sv}$  (or  $-7.1 \text{ Sv} \pm 3.9 \text{ Sv}$  if the WBC is included) found by Rhein et al. (2019) for the interior western basin and compensates about 30% of it.

#### 4.2.4 Correlation between the meridional flow in the interior eastern and western basin and the transport across the MAR

As suggested in the previous subsections, the individual transport time series show in some cases similar patterns suggesting a positive or negative correlation. To address this hypothesis, correlation coefficients were calculated for the annual mean transport from 1993 to 2017 across the *NAC Central* and the two easternmost segments *NAC East 1* + *NAC East 2*, but also for the comparison with the transport from Rhein et al. (2019) for the interior western basin, and from Roessler et al. (2015) for the *NAC MAR* section. The correlation coefficients are presented in Table 4.4. Figure 4.8 shows the considered transport time series for the *NAC Central* segment, the summed up transport across the *NAC East 1* and *NAC East 2* segments, and the time series for the interior western basin (*NAC West*) and across the MAR.

Transport time series 1	Transport time series 2	R
Central	East 1 + East 2	<b>-0.5</b>
Central	MAR	<b>-0.6</b>
Central	West	<b>-0.5</b>
East 1 + East 2	MAR	-0.1
East 1 + East 2	West	+0.2
Central + East 1 + East 2	MAR	<b>-0.7</b>
Central + East 1 + East 2	West	<b>-0.4</b>
MAR	West	<b>+0.6</b>

**Table 4.4:** Correlation coefficients between annual mean flow components at  $47^\circ/48^\circ\text{N}$  and across the MAR (Figure 4.8). Bold: Correlation coefficient is significant at the 95% confidence level. *NAC MAR*: updated transport time series from Roessler et al. (2015), *NAC West*: from Rhein et al. (2019, their Figure 9b).

As becomes apparent from Figure 4.8 and the calculated correlation coefficients, the transport time series discussed here – especially the one representing the *NAC Central* segment - indeed show some patterns that are also observed in the interior western basin and in the transport across the MAR. There is a positive significant correlation between the interior western basin (*NAC West*) and the *NAC MAR* transport ( $R = +0.6$ ). In contrast to that, the *NAC*

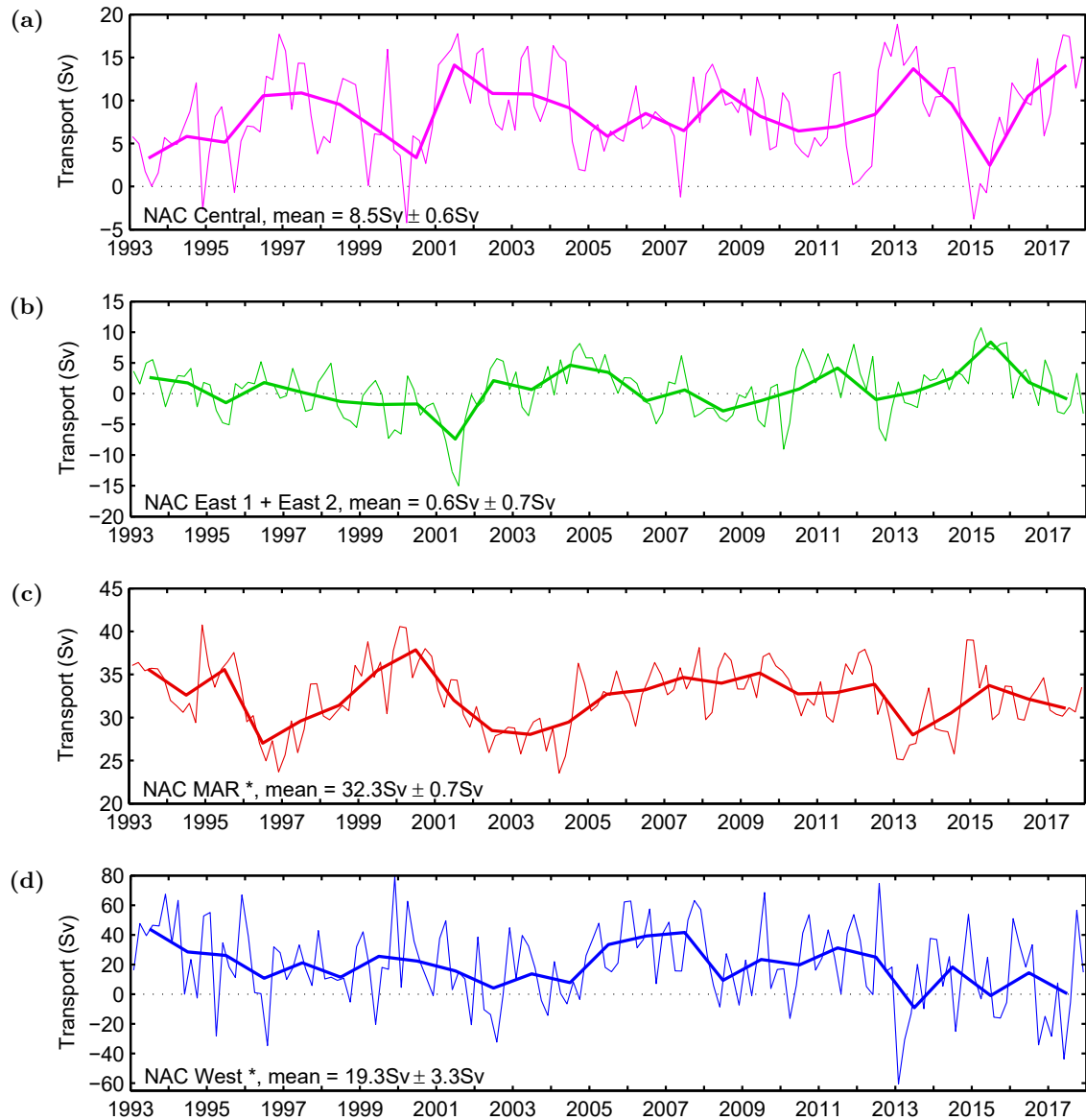


**Figure 4.8:** Bi-monthly (thin) and annual mean (bold) transport time series (Sv) at the NOAC site (Ekman transport not included) between 1993 and 2017, (a) the *NAC Central* segment between  $31^\circ\text{W}$  and  $23^\circ\text{W}$ , (b) the sum of the eastern segments (*NAC East 1* and *NAC East 2*) between  $23^\circ\text{W}$  and  $15^\circ\text{W}$ , (c) *NAC MAR*: across Mid-Atlantic Ridge between  $47^\circ\text{N}$  and  $53^\circ\text{N}$  (update from Roessler et al., 2015), and (d) *NAC West*: meridional flow in the interior western basin between  $42^\circ\text{W}$  and  $31^\circ\text{W}$  (from Rhein et al., 2019). Numbers indicate mean transport and standard error of the mean for the respective transport section.

\* values from Rhein et al. (2019), note: time series are only shown until end of 2017 but in the calculation of the mean values and standard errors also data from the year 2018 are used.

MAR transport ( $R = -0.7$ ) and NAC West transport ( $R = -0.4$ ) are both significantly anti-correlated to the flow between  $31^\circ\text{W}$  and  $15^\circ\text{W}$  (*NAC Central* + *NAC East 1* + *NAC East 2*). In general, a larger northward transport into the interior western basin (*NAC West*) leads to a larger transport across the MAR into the eastern basin, while the northward transport in the eastern interior basin between  $31^\circ\text{W}$  and  $15^\circ\text{W}$  is smaller. The *NAC MAR* transport and northward transport across  $47^\circ/48^\circ\text{N}$  between  $31^\circ\text{W}$  and  $15^\circ\text{W}$  thus partly compensate each other leading to a smaller variability for the input of subtropical water into the eastern basin than observed in the individual transport time series. The significance of the correlation of the transport between  $31^\circ\text{W}$  and  $15^\circ\text{W}$  with the *NAC MAR* transport and with the *NAC West* transport is mainly owed to the *NAC Central* segment, where most of the meridional transport occurs (Figure 4.5 and 4.8).

### 4.3 Summary and Discussion

In this chapter, the PIES- and altimeter-derived SSH and transport time series were presented and analyzed with a focus on the interior eastern basin.

PIES-derived SSH time series were calculated for the interior western basin, the MAR region and the interior eastern basin. From the comparison of the PIES-derived SSH time series with the altimeter-derived SSH, two different dynamic regimes were revealed. One is the interior western basin where the flow exhibits both, a strong barotropic and baroclinic signal, and the other one is the PIES MAR region and the interior eastern basin for which the barotropic contribution to the total SSH signal is negligible.

The volume transports were calculated for the interior eastern basin across three defined segments (*NAC Central*, *NAC East 1*, and *NAC East 2*) between  $31^\circ\text{W}$  and  $15^\circ\text{W}$ . The main results from the transport analysis including mean transport values for the western basin (Mertens et al., 2014; Rhein et al., 2019), the MAR region (Roessler et al., 2015), and the OVIDE line further northeast (Daniault et al., 2016), to which the transports for the eastern basin are compared, are summarized in Figure 4.9.

The PIES-derived transport time series for the time period 2016 to 2017 shows a mean top-to-bottom northward flow of  $+12.2\text{ Sv} \pm 1.4\text{ Sv}$  with the signal being dominated by the almost permanent northward flow in the *NAC Central* segment between  $31^\circ\text{W}$  and  $23^\circ\text{W}$  with a mean of  $+11.1\text{ Sv} \pm 1.7\text{ Sv}$ . Dividing the PIES-derived transport into transport in the upper and deep ocean (separated from each other by the isopycnal  $\sigma_\theta = 27.68\text{ kg/m}^3$ ) showed that the total flow for all three segments is dominated by the flow in the upper layers as the net northward transport in the upper layers summed up for all three segments is as large as the summed

up net top-to-bottom transport. Furthermore, for the *NAC Central* segment, the flow in the upper ocean makes up about 62 % of the top-to-bottom flow, a number comparable to the 60 % found by Roessler et al. (2015) for the *NAC MAR* segment.

To extend the PIES-derived transports backward in time until the beginning of available satellite data, the correlation between the satellite SSH signal and the baroclinic PIES-inferred transport time series was used. For the long-term satellite-derived transport time series between 1993 and 2017, similar patterns as for the shorter PIES-derived transport were found. The annual mean transports obtained from the decadal time series is northward (overall mean:  $+9.1 \text{ Sv} \pm 0.8 \text{ Sv}$ ) and dominated by the almost permanent northward flow in the *NAC Central* segment (overall mean:  $+8.5 \text{ Sv} \pm 0.6 \text{ Sv}$ ). As satellite-derived geostrophic velocities suggest, the transport across the *NAC Central* segment can be interpreted as another pathway of subtropical water into the eastern subpolar North Atlantic, even though it is also evident from the analysis that not all water crossing the transect in northward direction is of subtropical origin but also consists of recirculating water. This agrees with Stendaro et al. (2020) who find branches splitting from the NAC south of the NOAC array and transporting water directly into the eastern subpolar North Atlantic without following the pronounced NAC branch in the western basin and with Kwon et al. (2005) who use profiling floats to monitor the circulation in the North Atlantic and observe a float entering the subpolar eastern North Atlantic after crossing the  $47^\circ/48^\circ\text{N}$  transect east of the MAR. Further analysis of satellite-derived geostrophic velocities suggests moreover that a meandering of the currents and even eastward shifts out of the *NAC Central* segment into the neighboring segments occur. This is supported by the results of the correlation analysis as for the transport time series for the *NAC Central* segment a negative correlation with the two easternmost segments is found. Apart from that, the correlation analysis reveals a significant negative correlation between the meridional transport in the interior eastern basin and the meridional transport in the interior western basin as well as the zonal transport across the MAR. The variability of the total inflow of subtropical water into the eastern basin is thus damped. In general, the mean annual transport estimates with significant high (anti-)correlations have one common feature: They include  $31^\circ\text{W}$  (PIES BP12) as one of their bounds. The variability at the other end points of the transport sections seems to have a smaller influence on the correlations. That is somewhat surprising, since the variability at the western boundary is much larger than in the interior (Figure 4.1).

Roessler et al. (2015) analyzed the inflow from the western into the eastern subpolar basin between  $47^\circ\text{N}$  and  $53^\circ\text{N}$  across the MAR. The updated mean (1993 to 2018) transport of  $+32.3 \text{ Sv}$  (McCarthy et al., 2020) and the northward flow into the eastern Atlantic across  $47^\circ/48^\circ\text{N}$  ( $+9.1 \text{ Sv}$ ) sum up to  $+41.4 \text{ Sv}$ , with the latter contributing 22 % to the total flow. At the OVIDE line further northeast, repeat ship-based hydrographic and velocity measurements

(Mercier et al., 2015) resulted in a total NAC related transport across that line of +41.8 Sv, i.e. significantly larger than the MAR inflow reported by Roessler et al. (2015). Therefore, Daniault et al. (2016) postulated that part of the NAC enters the Subpolar Gyre directly in the eastern basin without the detour through the Newfoundland basin, while Rhein et al. (2011) and Roessler et al. (2015) assumed that this southernmost branch of the NAC remains in the subtropical region. To make the NAC transport across the MAR and the OVIDE line compatible, a northward flow across 47°/48°N of the order of +9.5 Sv is needed. This number is comparable to the mean observed inflow through the *NAC Central* segment of +8.5 Sv  $\pm$  0.6 Sv or to the mean inflow over the central and eastern segments of +9.1 Sv  $\pm$  0.8 Sv found in this study.

The roughly 41 Sv entering the eastern subpolar basin are partly transported into the Nordic Seas (8.0 Sv, Østerhus et al., 2019), but the main flow, about 33 Sv (a number comparable to the observations of Daniault et al., 2016), is to the west, north of the study region, and forms the northern branch of the Subpolar Gyre. The NOAC array does not support a southward transport across 47°/48°N east of 31°W (Daniault et al., 2016), but this is most likely due to the too northward location of the array missing the subtropical pathways.

In the western basin, Rhein et al. (2019) observe a NAC related northward flow of +105.9 Sv, a southward flow west of 41°W of -29 Sv (SWF), a southward flow further west with the WBC of -23.1 Sv, a recirculation in the Newfoundland Basin of -29.8 Sv (NBR), and a southward flow east of 37°W of -27.8 Sv. As discussed in Rhein et al. (2019), the WBC transport of -23.1 Sv misses part of the flow east of 42°W because per definition it is included in the southward flow west of 41°W. The mean WBC transport as reported by Mertens et al. (2014) is -37.3 Sv and includes also the WBC related southward transport east of 42°W. For further comparison of the transports and discussion of the circulation, this value is therefore used in the following. To make the mean WBC transport compatible with the meridional flow in the interior western basin observed by Rhein et al. (2019), consequently, also a larger mean transport (+61.3 Sv instead of +47.1 Sv for NAC+SWF+NBR) is assumed for the net northward flow across 47°/48°N between 42°W and 37°W. In summary, the northward transport of +61.3 Sv and the southward transport of -27.8 Sv in the interior western basin yield a net northward transport in the interior western basin of +33.5 Sv which is comparable to the updated zonal transport across the MAR found by Roessler et al. (2015).

The overall meridional top-to-bottom transport west of 31°W, including the main part of the Newfoundland shelf region and the Ekman transport, was reported to be -9.8 Sv during 1993 to 2018 (Rhein et al., 2019). The mean Ekman transport across the whole transect from BP12 to BP32 was found to be -1 Sv in 2016 to 2017 and -1.5 Sv in 1993 to 2017 (calculated from NCEP/NCAR reanalysis data, Kalnay et al., 1996). The mean top-to-bottom transports in

interior eastern Atlantic in 1993 to 2017 (including the segments *NAC Central*, *NAC East 1* and *NAC East 2* and Ekman transport) sum up to +7.6 Sv and thus compensate about 78 % of the flow in the western basin. Assuming mass balance across the whole section, a northward transport of +2.2 Sv is left for the eastern boundary and the eastern shelf. This number is in the range of former transport estimates of the Eastern Boundary Current between +1.5 Sv and +4.7 Sv (Ellett et al., 1973; Huthnance, 1986; van Aken et al., 1996).

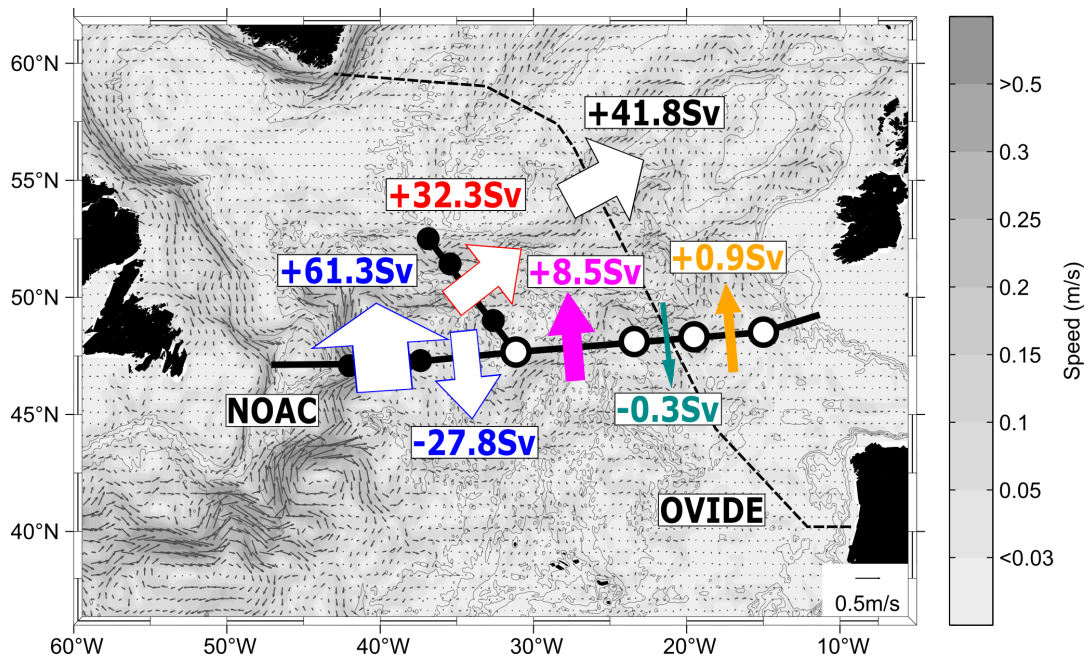


**Figure 4.9:** Interior circulation scheme (boundary currents are excluded) at the NOAC array combining results from this study with results from the western basin from Mertens et al. (2014) and Rhein et al. (2019), with the updated transport time series at the MAR, following Roessler et al. (2015), and with results from the OVIDE array (Daniault et al., 2016). In the western basin, the big white northward pointing arrow represents the net northward transport (+61.3 Sv) which is calculated from the NAC transport of +105.9 Sv (Rhein et al., 2019) and the southward flows east and west of the NAC (SWF+NBR) of  $-58.8$  Sv (Rhein et al., 2019) of which  $-14.2$  Sv are attributed to the WBC transport to match the results from Mertens et al. 2014. The big white southward pointing arrow represents the southward flow east of  $37^\circ\text{W}$  of  $-27.8$  Sv (Rhein et al., 2019). At the OVIDE line, the NAC related northeastward transport between  $46.14^\circ\text{N}$  and  $57.17^\circ\text{N}$  from Daniault et al. (2016) is shown. Arrow widths representing the mean top-to-bottom transports across the sections are not to scale. In the background, the mean geostrophic velocity field is shown (as in Figure 1.3a).

For the interior western basin and the period 1993 to 2018, Rhein et al. (2019) found a negative decadal transport trend of  $-6.0 \text{ Sv} \pm 5.7 \text{ Sv}$  ( $-7.1 \text{ Sv} \pm 3.9 \text{ Sv}$  when the WBC is included), dominated by the trend in the region between  $37^\circ\text{W}$  and  $31^\circ\text{W}$  ( $-4.4 \text{ Sv} \pm 3.7 \text{ Sv}$ ). The trends are related to the significant positive SSH trends at the western boundary with no or negligible trends in the interior (Rhein et al., 2019, their Figure 11). Following the ocean heat content

trends from Häkkinen et al. (2016), Rhein et al. (2019) attributed the positive SSH trends at the western and eastern boundary with none or small (mostly insignificant) trends in the interior to be responsible for the long-term transport trends in the western basin and argued for a positive trend in the eastern basin. The decadal transport trend in the eastern basin found in this study is indeed positive and significant ( $+2 \text{ Sv} \pm 1.5 \text{ Sv}$ ), compensating about 30% of the transport trend found in the western Atlantic. The trend is dominated by the transport in the *NAC Central* segment (Table 4.3).

One would expect that the long-term positive trend in the transport across  $47^\circ/48^\circ\text{N}$  east of  $31^\circ\text{W}$  would lead to a slow salinification of the eastern subpolar basin, and this is somewhat inconsistent with the observed freshening in the time period 2012 to 2016 (Holliday et al., 2020). On the other hand, the strong inter- and multiannual variability of the transport time series might override the trend. For instance, in 2012-2016, the NAC transport across the MAR was lower than average (mean in 2012-2016:  $+31.6 \text{ Sv}$ , mean in the five years before (2007-2011):  $+33.9 \text{ Sv}$ , cf. Figure 4.8c). Holliday et al. (2020) attributed the freshening to a slowing of the NAC in the western basin - which is confirmed by the lower *NAC West* transports at  $47^\circ/48^\circ\text{N}$  (Figure 4.8d) and across the MAR at that time period (Figure 4.8c) - and to a higher than normal Arctic freshwater contribution from the western boundary into the eastern basins. Apparently, only a part is compensated by the anomalous high transport across  $47^\circ/48^\circ\text{N}$  east of  $31^\circ\text{W}$ . But since the analysis in this work does not include the characteristics of the water masses, it is also possible that this branch of the circulation might also be fresher than usual. Another point to consider is the possibility that the main transport in the *NAC Central* segment follows different pathways in 2012 to 2016. The mean satellite geostrophic velocities across the *NAC Central* transect (Figure 4.7) show indeed that after 2012 and approximately until 2016, the northward pointing surface velocities in the eastern part decreased and even changed direction from northward to southward.

## 5 The circulation in the subpolar eastern North Atlantic studied with model output

This chapter focuses on the circulation in the subpolar North Atlantic studied with model output of the ANHA12 configuration of the NEMO model and with output from the ARIANE trajectory tool, a Lagrangian model using the velocity fields of the ANHA12 simulation. Firstly, volume transports calculated from the ANHA12 model output are compared to the findings obtained from observational data which were presented in the previous chapter. In the second part of this chapter, three-dimensional trajectories of particles provided by the Lagrangian trajectory tool ARIANE are studied to track the pathways of water in the subpolar North Atlantic with a focus on the eastern basin and complement the results of the volume transport analysis.

### 5.1 Comparison of transports obtained from model data and observations

To compare volume transports calculated from model output to observational data, the overall circulation pattern of the model has to be studied beforehand and linked to the circulation pattern found from observations.

In Figure 5.1, the mean model-derived surface velocities in 2016/2017 are compared to the mean satellite-derived geostrophic velocities from the same time period. The direct comparison of the differently obtained mean surface velocities shows a good agreement in the overall circulation pattern as pointed out in the following. Both, satellite and model data, exhibit a strong northward flowing NAC at about 40°W to 42°W which is also in good agreement with the findings from repeat LADCP measurements (Figure 1.4) and with the cross-section of mean meridional model velocities at 47°/48°N (Figure 5.2). However, the comparison of the mean surface velocities suggests a more pronounced northward flow in the model data in this region at 47°/48°N. Also the southward flowing WBC is very similar in its pathway for both datasets

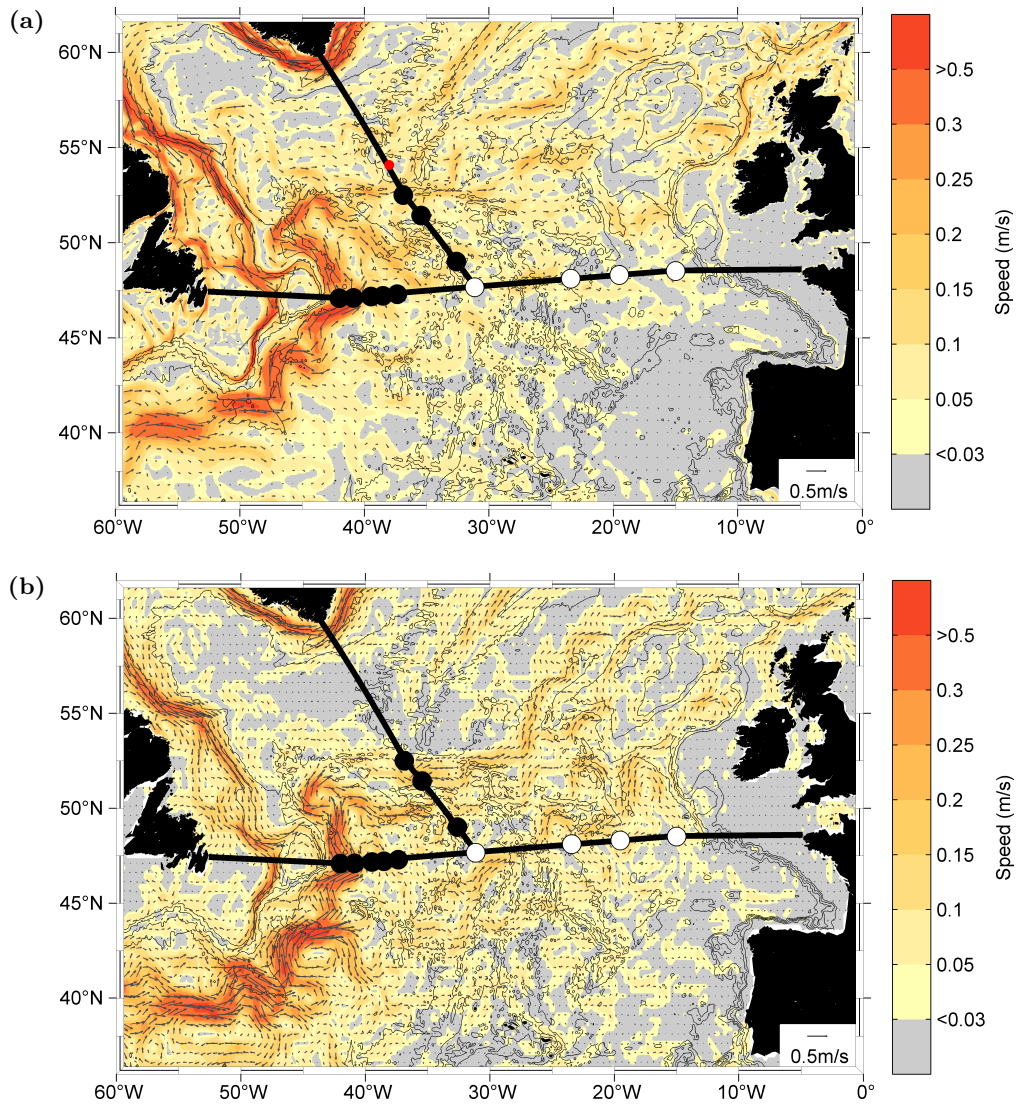


**Figure 5.1:** Panel (a) shows the mean model-derived surface velocities from 2016/2017, the arrows represent the direction and are scaled according to the speed. The PIES locations are shown as white and black circles and the black line indicates the section for which the cross-section velocities obtained from model data are shown in Figure 5.2. The red dot indicates the location until which the *NAC MAR* section is extended for the model transport calculation. Panel (b) shows the mean satellite-derived geostrophic surface velocities in 2016/2017. Arrows represent direction and speed, PIES locations and black lines as for panel (a). Note: For panel (a), only every tenth arrow is shown, whereas for panel (b), due to the coarser spatial resolution of the dataset, every second arrow is shown.

but more pronounced in the model. The main zonal inflow into the eastern basin as seen in the satellite data occurs south of the northernmost PIES BP15 and even distinct pathways of water flowing from the western into the eastern basin south of  $47^{\circ}/48^{\circ}\text{N}$  are visible (a finding which is also supported by the results of the PIES data analysis presented in the previous chapter). In contrast to that, for the model data, the flow field is shifted further north compared to the flow field from the satellite data so that a substantial part of the zonal inflow into the eastern basin occurs north of PIES BP15. The zonal inflow south of  $47^{\circ}/48^{\circ}\text{N}$  into the eastern basin in the model exhibits a less pronounced structure which is also more confined to regions near  $47^{\circ}/48^{\circ}\text{N}$  and close to the eastern side of the MAR compared to the satellite data for which the zonal inflow also reaches as far east as the easternmost PIES and fills a substantial part of the West European Basin south of  $47^{\circ}/48^{\circ}\text{N}$ .

Figure 5.2 and 5.3 show the mean cross-section velocities and standard deviations at the PIES  $47^{\circ}/48^{\circ}\text{N}$  section and at the MAR (sections as indicated in Figure 5.1). For the  $47^{\circ}/48^{\circ}\text{N}$  section (Figure 5.2), the flow field in the western basin including the northward flowing NAC, the recirculation east and west of it, as well as the WBC, is very similar to the mean velocities calculated from LADCP measurements (Figure 1.4). However, the magnitude of the velocities, especially for the upper ocean in the region of the NAC, differs between the model and the observations which might partly be owed to the different time spans from which the mean velocities are calculated. Moreover, the standard deviation in the same area (Figure 5.2b) whose magnitude is in the same order as the signal itself (Figure 5.2a) hints at an overall strong variability of the currents in this region. Further east along the  $47^{\circ}/48^{\circ}\text{N}$  section, the current flow field in the model becomes less pronounced with the standard deviation being for most areas of the same magnitude as the mean flow. Especially for the PIES sections east of BP12, no features indicating a considerable permanent net north- or southward flow can be depicted as already suggested by the flow field pattern seen from atop as shown in Figure 5.1. For the PIES MAR section, the most striking difference between model data and observations is the northward shift of the model flow field in comparison to the observations which became already apparent in the comparison of the surface velocities from model and satellite data in Figure 5.1. Such a shift was also observed in other high resolution ocean models (e.g. Breckenfelder et al., 2017). For comparing volume transport across the MAR section calculated from model output with the one calculated from observational data, the model MAR section is therefore extended further north until approximately  $54^{\circ}\text{N}$  to also include the northeastward transport north of PIES BP15 (cf. Figure 5.3). The northern limit of the section at about  $54^{\circ}\text{N}$  was chosen considering the surface velocities from Figure 5.1, the mean velocities at the MAR cross-section from Figure 5.2a and the standard deviation of the mean from Figure 5.2b.

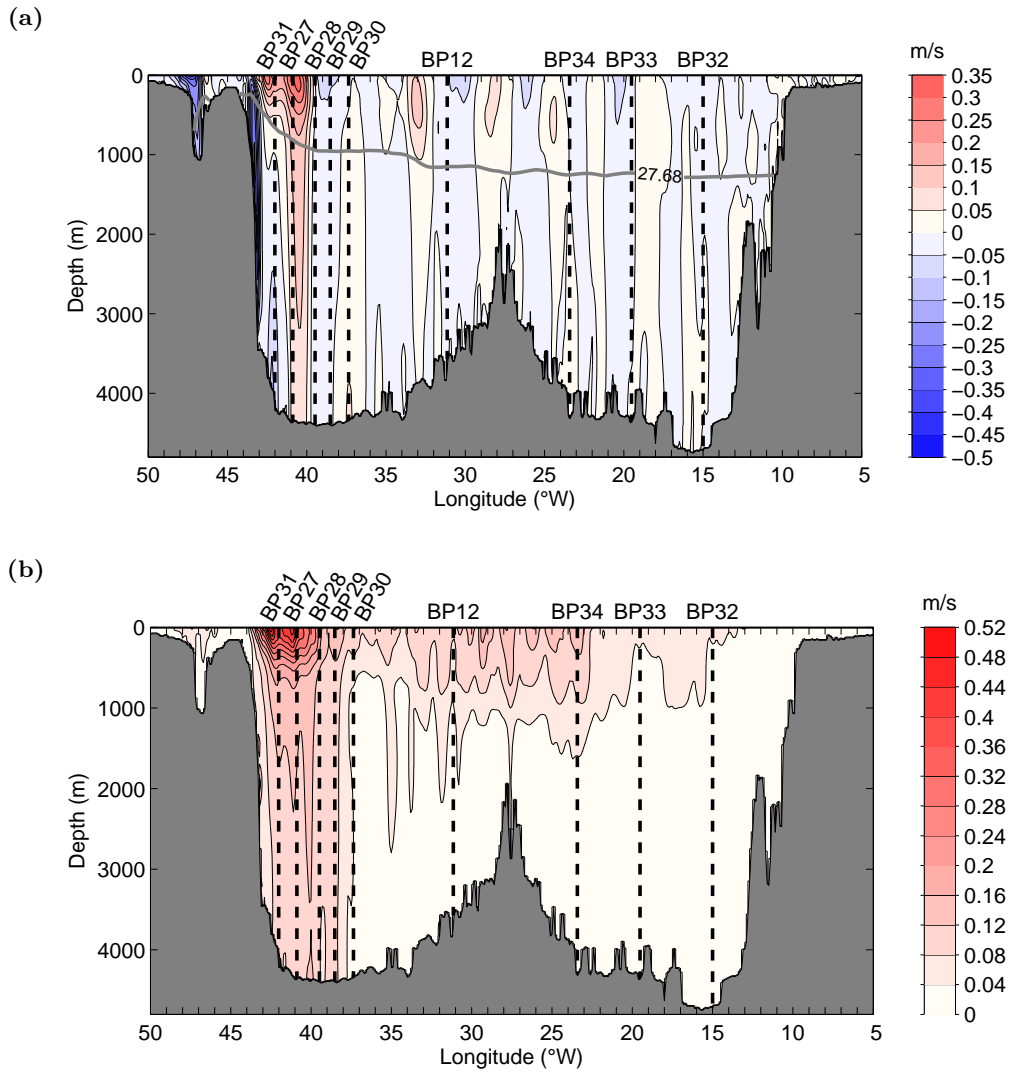


**Figure 5.2:** Panel (a) shows the mean meridional model velocities across the  $47^\circ/48^\circ\text{N}$  section as indicated in Figure 5.1 in 2006 to 2017. Blueish colors denote a southward transport, reddish colors denote a northward transport. The gray line indicates the mean position of the isopycnal  $\sigma_\theta = 27.68 \text{ kg/m}^3$ . Panel (b) shows the respective standard deviation of the mean model velocities across the  $47^\circ/48^\circ\text{N}$  section in 2006 to 2017. For both panels, the PIES locations are shown as dashed lines.

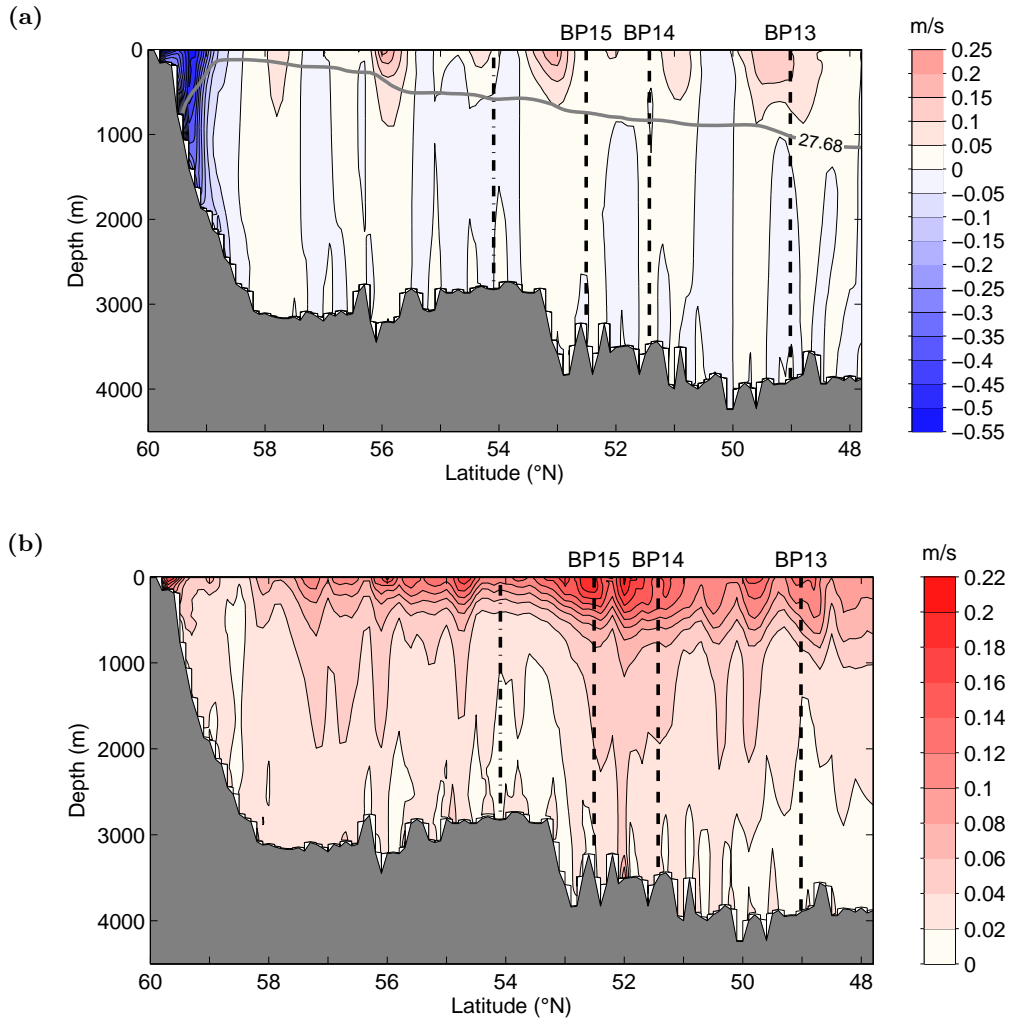


**Figure 5.3:** Panel (a) shows the mean model velocities perpendicular to the PIES MAR section as indicated in Figure 5.1b in 2006 to 2017. Blueish colors denote a southwest transport, reddish colors denote a northeast transport. The gray line indicates the mean position of the isopycnal  $\sigma_\theta = 27.68 \text{ kg/m}^3$ . Panel (b) shows the respective standard deviation of the mean model velocities across the PIES MAR section in 2006 to 2017. For later use in the calculation of volume transport across the MAR from model data (Figure 5.4b), the northward extension at about 54°N of the PIES MAR section is shown in both panels as a dashed-dotted line.

In addition to the mean flow field at the PIES sections, for later use, both figures (Figure 5.2a and 5.3a) also show the mean position of the potential density isoline  $\sigma_\theta = 27.68 \text{ kg/m}^3$  which is the upper limit of the Labrador Sea Water found from observations but also applies to the model data (Courtois et al., 2020; Garcia-Quintana et al., 2019). This isoline is chosen as separation between the flow in the upper and deep ocean and will be used in the following section for studying water mass transformation with the ARIANE trajectory tool.

In Figure 5.4, a comparison of the volume transport time series obtained from observational data (cf. Chapter 4 of this work, Roessler et al. 2015, Rhein et al. 2019) and model output is shown. Visual analysis of the time series already indicates that the transports obtained from model output and observations differ significantly from each other not only in their mean values but also in terms of variability. The calculation of correlation coefficients between the model and the observational time series indeed confirms this assumption: None of the model time series from Figure 5.4 is significantly correlated with the observational data.

Figure 5.4a shows the time series for the volume transport in the interior eastern basin including the summed up transport across the sections *NAC Central*, *NAC East 1* and *NAC East 2* which is based on the PIES and altimeter data between 1993 and 2017 and the model transport across the section between BP12 and BP32 between 2006 and 2017. As already suggested by the mean surface velocities (Figure 5.1) and the mean cross-section velocities (Figure 5.2), both time series differ from each other in terms of magnitude, variability, and even in direction. The observational data show a net northward transport for almost every time with a mean northward transport of  $+9.1 \text{ Sv} \pm 0.8 \text{ Sv}$  while the mean transport obtained from the model data is closer to zero and in the mean ( $-2.4 \text{ Sv} \pm 0.9 \text{ Sv}$ ) in southward direction. The most prominent feature of this model time series is the period from approximately 2012 to 2016 in which the net annual mean transport is constantly very close to zero corresponding also to a time period of smaller transport in northeast direction across the MAR and suggesting a negative correlation between the two transport time series. For the interior western basin (Figure 5.4c), the model data transport is in the mean ( $+49.5 \text{ Sv} \pm 2.4 \text{ Sv}$ ) by about 20 Sv higher than the transport from observational data ( $+19.3 \text{ Sv} \pm 3.3 \text{ Sv}$ ), while for the MAR transect (Figure 5.4b), the model transport in northeastward direction is significantly smaller (in the mean  $+26.6 \text{ Sv} \pm 1.4 \text{ Sv}$ ) than the transport from observational data ( $+32.3 \text{ Sv} \pm 0.7 \text{ Sv}$ ). This suggests a weaker coupling between the interior western and eastern basin at these latitudes in the model than proposed by the observations. To understand where the surplus inflow of water in the interior western basin across  $47^\circ/48^\circ\text{N}$  goes to (as mass balance is required), the comparison in Figure 5.4 includes also the southward transport with the WBC at  $47^\circ/48^\circ\text{N}$  (Figure 5.4d) with the observational data taken from Rhein et al. (2019). Indeed, this comparison shows that in the model, the southward transport with the WBC ( $-38.9 \text{ Sv} \pm 2.1 \text{ Sv}$ ), defined as the

## 5.1 Comparison of transports obtained from model data and observations

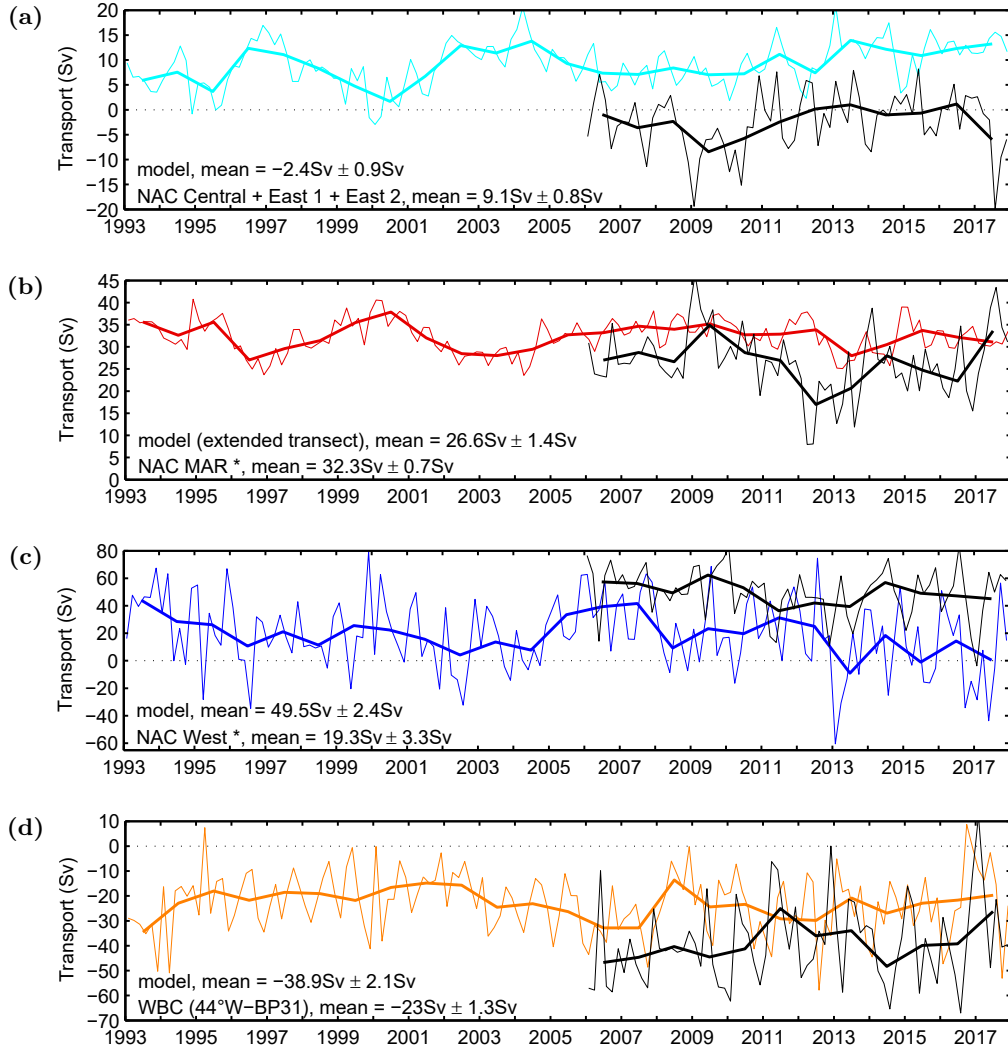


**Figure 5.4:** Bi-monthly (thin) and annual mean (bold) transports at the NOAC site from observations (1993 - 2017) and model output (2006 - 2017). PIES transports are shown in colors, model transports in black. Panel (a) shows the transport in the interior eastern basin across the *NAC Central*, *NAC East 1* and *NAC East 2* segments between BP12 at about  $31^\circ\text{W}$  and BP32 at about  $15^\circ\text{W}$ , panel (b) the transport across the Mid-Atlantic Ridge between BP12 at about  $47^\circ\text{N}$  and BP15 at about  $53^\circ\text{N}$  (observations, update from Roessler et al. 2015) and between BP12 at about  $47^\circ\text{N}$  and approximately  $54^\circ\text{N}$  (model output), panel (c) the meridional flow in the interior western basin between BP31 at about  $42^\circ\text{W}$  and BP12 at about  $31^\circ\text{W}$  (Rhein et al., 2019), and panel (d) the meridional transport between BP31 at about  $42^\circ\text{W}$  and  $44^\circ\text{W}$  (Rhein et al., 2019) defined as Western Boundary Current transport. Numbers indicate mean transport and standard error of the mean for the respective transport section.

\* Values from Rhein et al. (2019), note: time series are only shown until end of 2017 but in the calculation of the mean values and standard errors also data from the year 2018 are used.

net transport between 44°W and PIES BP31, is significantly stronger than the one obtained from observational data ( $-23.1 \text{ Sv} \pm 1.3 \text{ Sv}$ , Rhein et al. 2019). However, as discussed by Rhein et al. (2019), the actual mean WBC transport presumably is larger than the  $-23.1 \text{ Sv}$  which were presented in Figure 5.4 as the calculated transport time series strongly depends on the mooring location (cf. Chapter 4). Other observation-based studies find WBC related transports closer to what is calculated from the model: Zantopp et al. (2017) find a WBC transport at 53°N of  $-30.2 \text{ Sv} \pm 6.6 \text{ Sv}$  and Mertens et al. (2014) observe a WBC transport of  $-37.3 \text{ Sv} \pm 3.0 \text{ Sv}$ . Both values agree well with the transport found from model data in this study and thus, as in the previous chapter, the mean WBC transport of  $-37.3 \text{ Sv}$  (Mertens et al., 2014) is used for further comparison of the transports and discussion of the circulation. Consequently, to make the mean WBC transport compatible with the meridional flow from Rhein et al. (2019) for the interior western basin, a larger mean northward transport of  $+33.5 \text{ Sv}$  is assumed here for the flow across 47°/48°N between BP31 at 42°W and BP12 at 31°W as well.

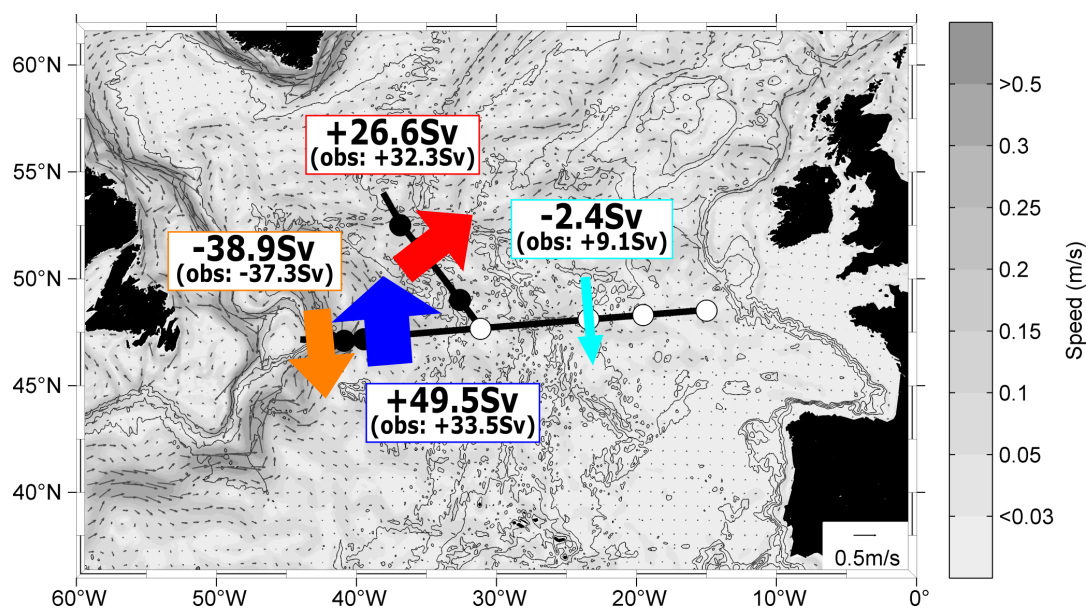


**Figure 5.5:** Circulation scheme at the NOAC array combining results from observational data with the results from model data as presented in this chapter. The net transport in the eastern basin (cyan) refers to the mean transport between PIES BP31 at about 31°W and PIES BP32 at about 15°W. The transport section at the MAR (red) for the model-based transport reaches until 54°N while for the PIES-based transport from McCarthy et al. (2020) and Roessler et al. (2015) it reaches only until PIES BP15 at about 52°N. The mean values for the interior western basin (blue) refer to the net transport between PIES BP12 at about 31°W and PIES BP31 at about 42°W for the model-based transport and to the mean net transport calculated from Mertens et al. (2014) and Rhein et al. (2019) as described in Figure 4.9. The WBC related values (orange) refer to the net transport between 44°W and PIES BP31 at about 42°W for the model-based transport and to the mean transport found by Mertens et al. (2014) in case of the observation-based transport. Arrow widths representing the mean top-to-bottom transports across the sections are not to scale. In the background, the mean geostrophic velocity field is shown (as in Figure 5.1a).

Figure 5.5 summarizes the mean transports calculated from model output for the interior eastern basin, the MAR, the interior western basin, and the WBC. For comparison, also the mean transport values for the respective transport sections based on observational data from this study and from McCarthy et al. (2020), Mertens et al. (2014), Rhein et al. (2019), and Roessler et al. (2015) are shown in this figure. The strongest discrepancies between the model- and observation-based mean transports are the inflow in the subpolar eastern basin which is in total in the model about +24.2 Sv and in the observations +41.4 Sv and the meridional inflow in the western basin which is in the model about +49.5 Sv and in the observations +33.5 Sv. The transport with the WBC is in both cases very similar (−38.9 Sv in the model and −37.3 Sv in the observations) even though the definitions for the WBC related flow are different. While for the observations, the net meridional northward flow in the western basin corresponds roughly to the mean transport observed for the zonal transport across the MAR, for the model-based transports these two values are substantially different as the meridional flow across 47°/48°N of about +49.5 Sv is by about 23 Sv larger than the zonal transport across the MAR of about +26.6 Sv. This requires additional pathways of water either flowing north of 54°N into the eastern basin or directly southward across 47°/48°. Further investigation of the model transport are thus necessary to fully close the transport budget and to complete the circulation scheme.

### 5.1.1 Correlation between the meridional flow in the interior eastern and western basin, the transport across the MAR, and with the WBC

To further analyze the coupling between the eastern and western subpolar North Atlantic basin in the model and the link between the transports across the different transport sections, the correlation coefficient  $R$  was calculated at the 95 % confidence level for each pair of the sections *interior eastern basin*, *interior western basin*, *MAR*, and *WBC* (Table 5.1). The section *interior eastern basin* reaches from PIES BP12 at about 31°W to PIES BP32 at about 15°W, the section *interior western basin* reaches from PIES BP12 to PIES BP31 at about 42°W, the section *MAR* reaches from PIES BP12 to about 38°W/54°N, and the *WBC* section is defined as the transport between PIES BP31 and 44°W. The integral time scales for the individual time series reach from  $n = 8$  to  $n = 19$  model time steps which corresponds to 40 to 95 days. Thus, as for the calculation of the correlation coefficients the time series of the annual mean values are used, the individual annual mean values can be considered as independent observations.

For the comparison of the meridional transport in the interior eastern basin with the zonal transport across the MAR section, a significant negative correlation is found with  $R = -0.9$ . This coincides with the results of the PIES data analysis in the previous chapter: The more water is transported into the eastern basin across the MAR, the less water water is transported northward across  $47^\circ/48^\circ\text{N}$  in the interior eastern basin. Furthermore, as for the observational data, the time series for the meridional transport in the interior western basin and the zonal transport across the MAR are positively correlated with  $R = 0.5$ , however, only at the 90 % confidence level. A stronger transport across  $47^\circ/48^\circ\text{N}$  in the western basin leads hence to a higher zonal transport from the western into the eastern basin across the MAR, yet with a smaller confidence level as for the observational data supporting the hypothesis of a weaker coupling between the western and eastern basin in the model compared to the observations. To strengthen this argument, for the model data, the correlation between the WBC related transport and the transports across the other sections was analyzed additionally and indeed, for the comparison of WBC related meridional transport and the transport in the interior western basin, a significant negative correlation between the two time series was found. This shows the strong connection between the northward flow in the interior western basin with the southward flow further west with the WBC: The more water is transported northward between  $42^\circ\text{W}$  and  $31^\circ\text{W}$ , the more water is transported southward between  $44^\circ\text{W}$  and  $42^\circ\text{W}$ .

Transport time series 1	Transport time series 2	R
interior eastern basin	MAR	<b>-0.9</b>
interior eastern basin	interior western basin	-0.5
interior eastern basin	WBC	-0.002
MAR	interior western basin	+0.6 *
MAR	WBC	-0.1
interior western basin	WBC	<b>-0.9</b>

**Table 5.1:** Correlation coefficients between annual mean flow components at  $47^\circ/48^\circ\text{N}$  and across the MAR (Figure 5.4). Bold: Correlation coefficient is significant at the 95 % confidence level.

\* Correlation is significant at the 90 % confidence level with  $p = 0.056$

## 5.2 Flow paths into the subpolar eastern North Atlantic

To study the flow paths and origin of water in the subpolar North Atlantic, particle trajectories were calculated from the model velocity fields using the Lagrangian trajectory tool ARIANE. The particles were seeded at the  $47^\circ/48^\circ\text{N}$  transect and the MAR as described in Section 2.2.2

and trajectories were either calculated in forward or in backward mode. For better comparability with the results of the transport analysis, five boxes were defined whose horizontal extent is in accordance with the PIES positions and sections defined for transport calculations (Table 2.5). Box 1 and 2 correspond approximately to the interior western basin even though box 1 also includes part of the WBC as it reaches as far west as 43.5°W. Box 3 and 4 correspond to the interior eastern basin with a longitudinal extent from PIES BP12 to 13°W which is slightly further east than PIES BP32. Box 5 covers the MAR region from PIES BP12 until 54°N. The latitudinal and longitudinal extent of the boxes are listed in Table 2.5.

For each of the boxes, the trajectories of the particles seeded in the respective box are analyzed for a maximum of five years. As the focus of this study lies on the subpolar (eastern) North Atlantic in close proximity to the PIES positions, these five years of travel time are a sufficiently long time span for the region of interest to be crossed by the particles (Figure 5.7 to 5.16). Firstly, all particle trajectories were analyzed regardless of the particle depth or density. For further analysis, they were subdivided according to their initial seeding depths and either assigned to the upper ocean flow (initial depth between 200 m and 900 m) or the flow in the deep ocean (initial depth below 1100 m).

To track water mass transformation, particles were additionally subdivided according to their initial densities into particles above and below the isopycnal  $\sigma_\theta = 27.68 \text{ kg/m}^3$  which represents the upper limit of Labrador Sea Water and is chosen as a separation between the upper and deep ocean. For the eastern basin and also for the southern part of the MAR section, the mean depth of this isopycnal is at about 1000 m. The depth limits of 900 m and 1100 m chosen for the analysis can thus be considered as limit between the upper and deep ocean, excluding the depth level of 900 m to 1100 m from the analysis as a transition region. For the western side of box 1 (western basin), the isopycnal is inclined and its depth decreases towards the west (Figure 5.2a) so that for this region, the separation of particles according to their initial densities might be the more adequate choice. The same applies to the northern part of the MAR section where the depth of the isopycnal also continuously decreases (Figure 5.3a).

### 5.2.1 Source regions and destination of particles seeded at the PIES transects

In the following, the trajectories of particles seeded in the boxes 1 to 5 are discussed. Complementing the visualization of individual trajectories, the probabilities of particles to cross grid cells of an artificially defined horizontal mesh with a  $1/4^\circ \times 1/4^\circ$  spatial resolution were calculated and are presented additionally.

## Trajectories of particles seeded in the western basin

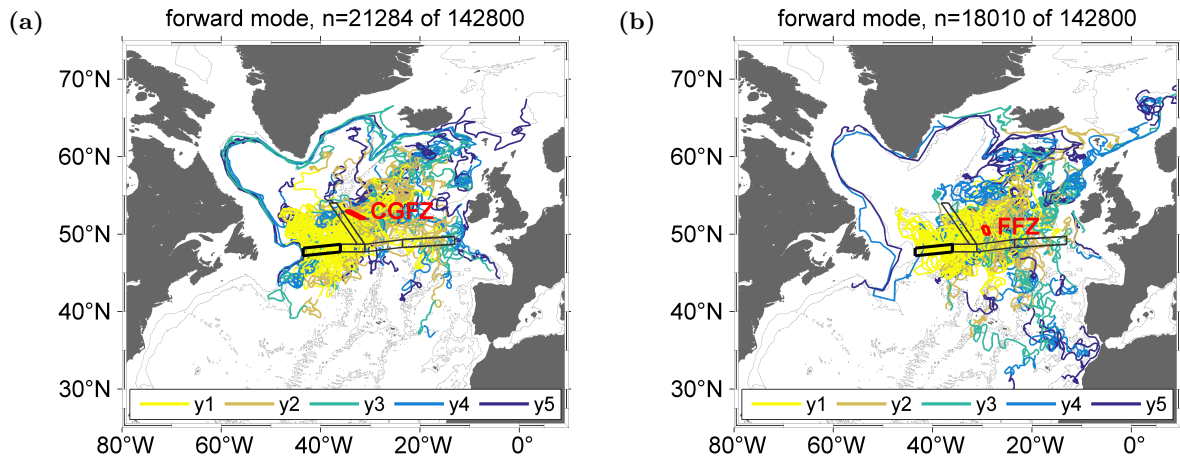
### Box 1:

Figure 5.7 shows the trajectories of particles seeded in box 1 and tracked in forward and backward mode regardless of the seeding depths (Figure 5.7a and 5.7b), with initial depths in the upper ocean between 200 m and 900 m (Figure 5.7c and 5.7d), and in the deep ocean below 1100 m (Figure 5.7e and 5.7f). Figure 5.8 shows the probability of particles to cross grid cells of the horizontal  $1/4^\circ \times 1/4^\circ$  mesh grid for the forward and backward mode and the different starting depths.

The figures show that most of the particles seeded in box 1 and tracked in forward mode stay for the first years in the Subpolar Gyre. After two or three years of travel time, particles seeded in the upper ocean between 200 m and 900 m partly feed the boundary current system from where they either are exported south of the  $47^\circ/48^\circ\text{N}$  PIES line or they recirculate and remain in the Subpolar Gyre. Furthermore, some are exported into the Nordic Seas following a route south of Iceland. In contrast to that, particles seeded in the deep ocean below 1100 m mostly remain in close proximity to box 1 in the interior western basin, only a few particles reach the interior of the Labrador Sea, or even cross the MAR into the eastern basin. Moreover, a significant amount of particles is directly exported southward across  $47^\circ/48^\circ\text{N}$  which suggests a westward turn and recirculation of the particles in the model and supports the hypothesis of a strong southward flow with the WBC that balances the surplus inflow in northward direction in the western basin formulated in the previous section. However, the partial inclusion of the WBC in box 1 distorts the unambiguous interpretation of the signal in this context. The trajectories of particles seeded in the upper ocean and tracked in backward mode show that most of them are imported from the subtropics or the boundary current system and the probability plots show that some, flowing through Baffin Bay, even have their origin in the Arctic. Particles seeded in the deep ocean mainly stem from the Subpolar Gyre and boundary currents.

To further analyze the zonal inflow of water into the eastern basin, Figure 5.6 shows particle trajectories of particles which have been seeded in box 1 and which cross either the Charlie-Gibbs-Fracture-Zone (CGFZ) or the Faraday-Fracture-Zone (FFZ) on their way. The fracture zones are indicated by red boxes in Figure 5.6 and defined according to the ETOPO1 bottom topography used in the model. About 15 % of the particles seeded in box 1 cross the CGFZ, about 13 % cross the FFZ which identifies the flow through both fracture zones as major routes from the interior western into the interior eastern basin. Further downstream on their route, the particles feed the boundary current system or flow into the Nordic Seas with particles passing the CGFZ preferably crossing the Iceland Basin and particles passing the FFZ mainly flowing northeastward via the Rockall Trough. Furthermore, some particles, especially those passing

the FFZ beforehand, are exported southeastward across  $47^\circ/48^\circ\text{N}$  into the West European and the Iberian Basin.

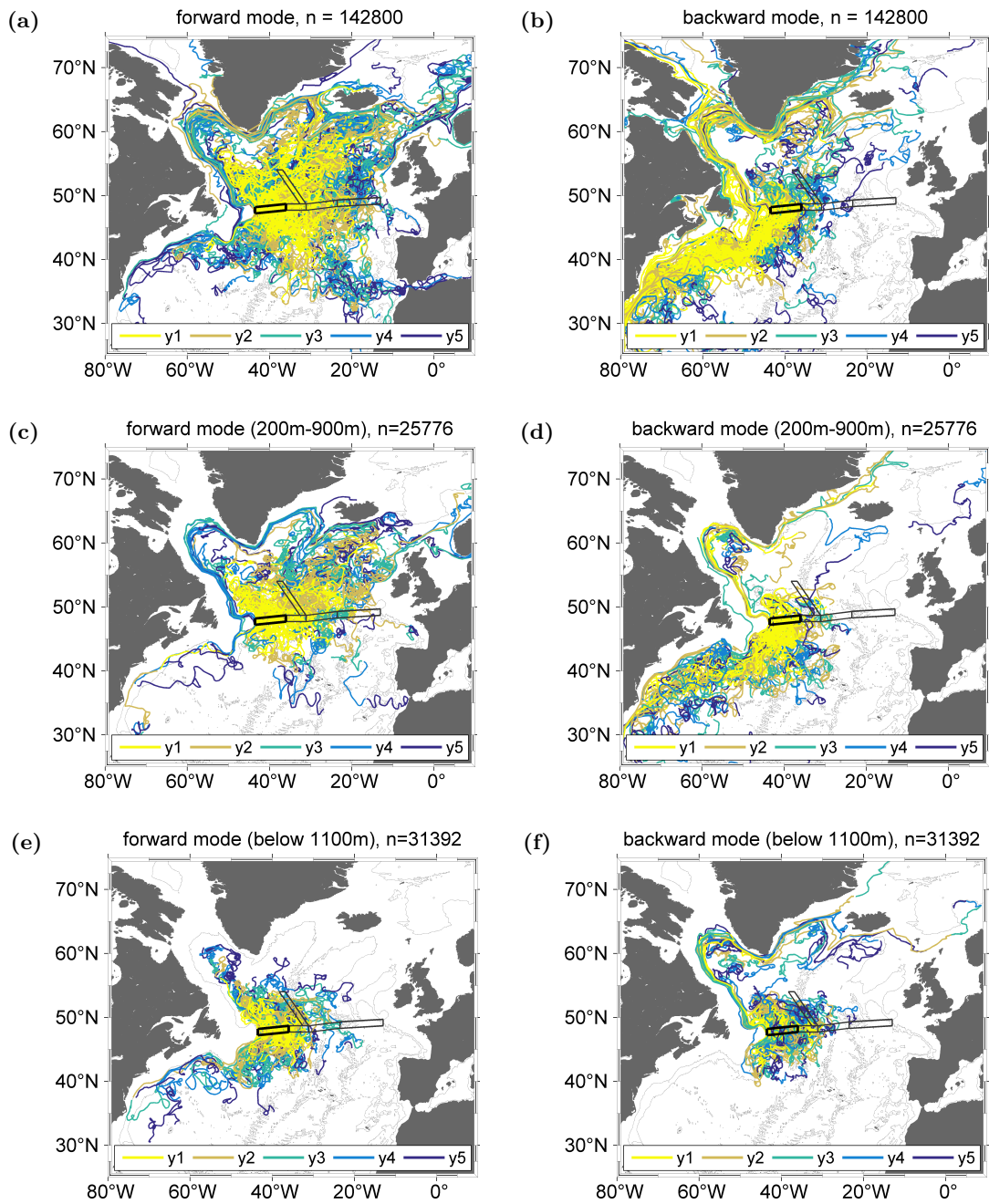


**Figure 5.6:** Trajectories of particles (forward mode) that have been seeded in box 1 and crossed (a) the Charlie-Gibbs-Fracture-Zone (CGFZ) and (b) Faraday-Fracture-Zone (FFZ). Gray contour lines show the bathymetry every 2000m. The different colors denote the different years of the five years (maximum) travel time. The horizontal extent of the different boxes is indicated by black lines, with the bold line highlighting box 1.

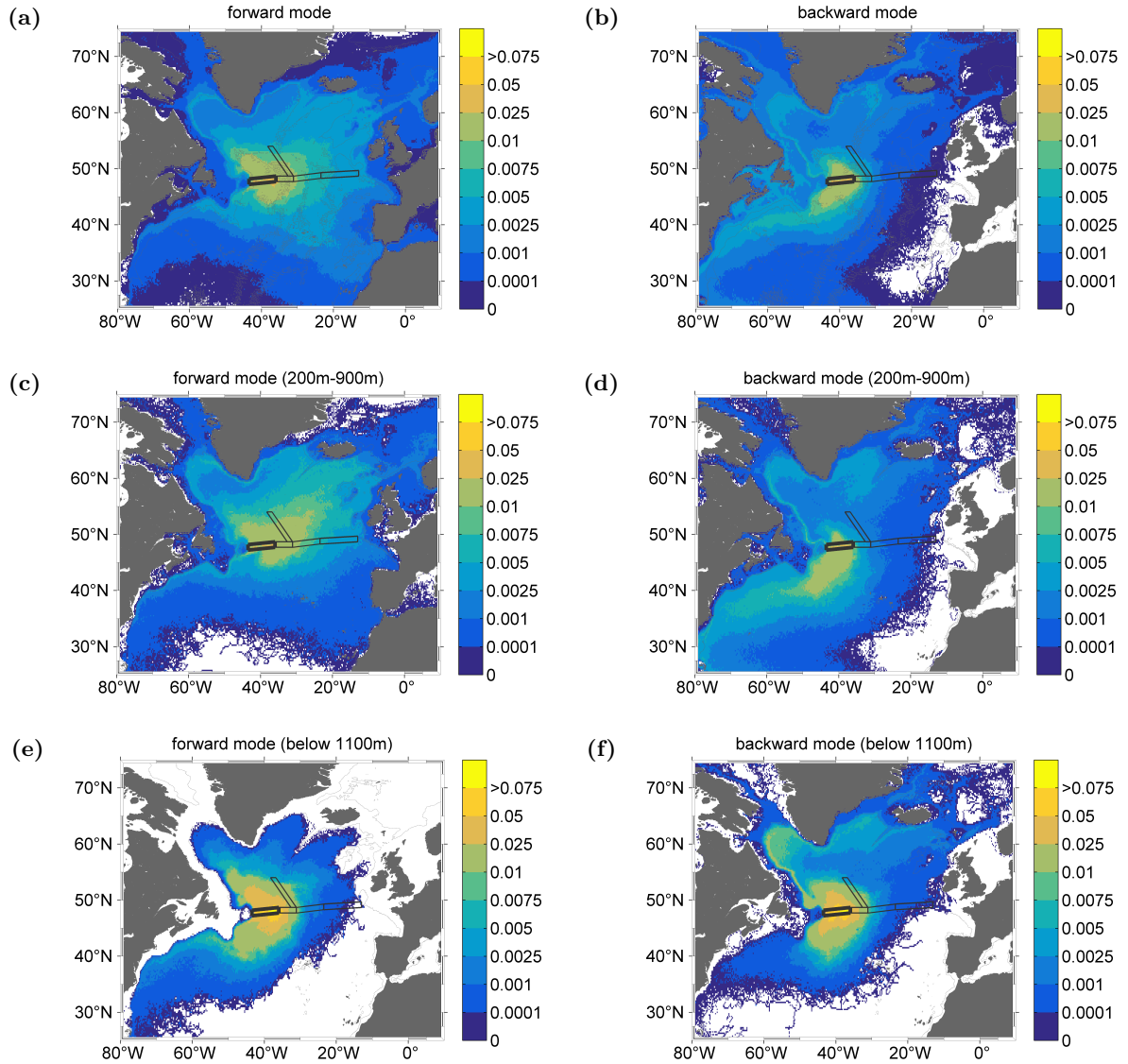
### Box 2:

Figure 5.9 shows the trajectories of particles seeded in box 2 and tracked in forward and backward mode regardless of the seeding depths (Figure 5.9a and 5.9b), with initial depths in the upper ocean between 200 m and 900 m (Figure 5.9c and 5.9d), and in the deep ocean below 1100 m (Figure 5.9e and 5.9f). Figure 5.10 shows the corresponding probabilities of particles to cross grid cells of the defined horizontal grid after their placement in box 2.

In contrast to the particles seeded in box 1, the trajectories for the particles seeded in box 2 and tracked in forward mode (shown in Figure 5.9a, Figure 5.9c, and Figure 5.9e) indicate a stronger connection, especially of the upper ocean, with the eastern basin. Particles seeded in the upper layers have a high probability to flow into the eastern basin north of  $47^\circ/48^\circ\text{N}$  and, contrary to particles seeded in box 1, no pathway into the interior of the Labrador Sea is found. Particles seeded in the deep ocean are more confined to the western basin and only a few also flow into the eastern basin north or south of  $47^\circ/48^\circ\text{N}$ . Particles ending up in box 2 in the upper ocean and tracked in backward mode mainly have their origin in the Gulf Stream but also in the WBC and some particles even represent Arctic water flowing out of the Arctic through Baffin Bay. Particles ending up in the deep ocean in box 2 mostly have their origin in the Subpolar Gyre and the boundary currents.



**Figure 5.7:** Trajectories of particles seeded in box 1. Panel (a) shows trajectories of particles seeded throughout the whole water column and tracked in forward mode. Panel (b) shows trajectories of particles seeded throughout the whole water column and tracked in backward mode. Panel (c) - (f) show trajectories of particles separated by the seeding depths (panel (c) and (d): seeding depths between 200 m and 900 m, panel (e) and (f): seeding depths below 1100 m, panel (c) and (e): forward mode, panel (d) and (f): backward mode). The particles were seeded in 2006 to 2017 and tracked for a maximum of five years. The different colors denote the different years of the five years (maximum) travel time. For panel (a) and (b), only every 1000th trajectory is plotted, for panels (c) - (f), every 500th trajectory is plotted. Gray contour lines show the bathymetry every 2000m. n is the total number of trajectories. The horizontal extent of the different boxes is indicated by black lines, with the bold line highlighting box 1.



**Figure 5.8:** Probabilities of particles to cross grid cells of a horizontal mesh with a  $1/4^\circ \times 1/4^\circ$  spatial resolution after having been seeded in box 1. Panel (a) shows probabilities for particles seeded throughout the whole water column and tracked in forward mode. Panel (b) shows probabilities for particles seeded throughout the whole water column and tracked in backward mode. Panel (c) - (f) show probabilities for particles separated by the seeding depths (panel (c) and (d): seeding depths between 200 m and 900 m, panel (e) and (f): seeding depths below 1100 m, panel (c) and (e): forward mode, panel (d) and (f): backward mode). Gray contour lines show the bathymetry every 2000m. Numbers are in percent (counts of particles that crossed the grid cell relative to total number of counts). The horizontal extent of the different boxes is indicated by black lines, with the bold line highlighting box 1.

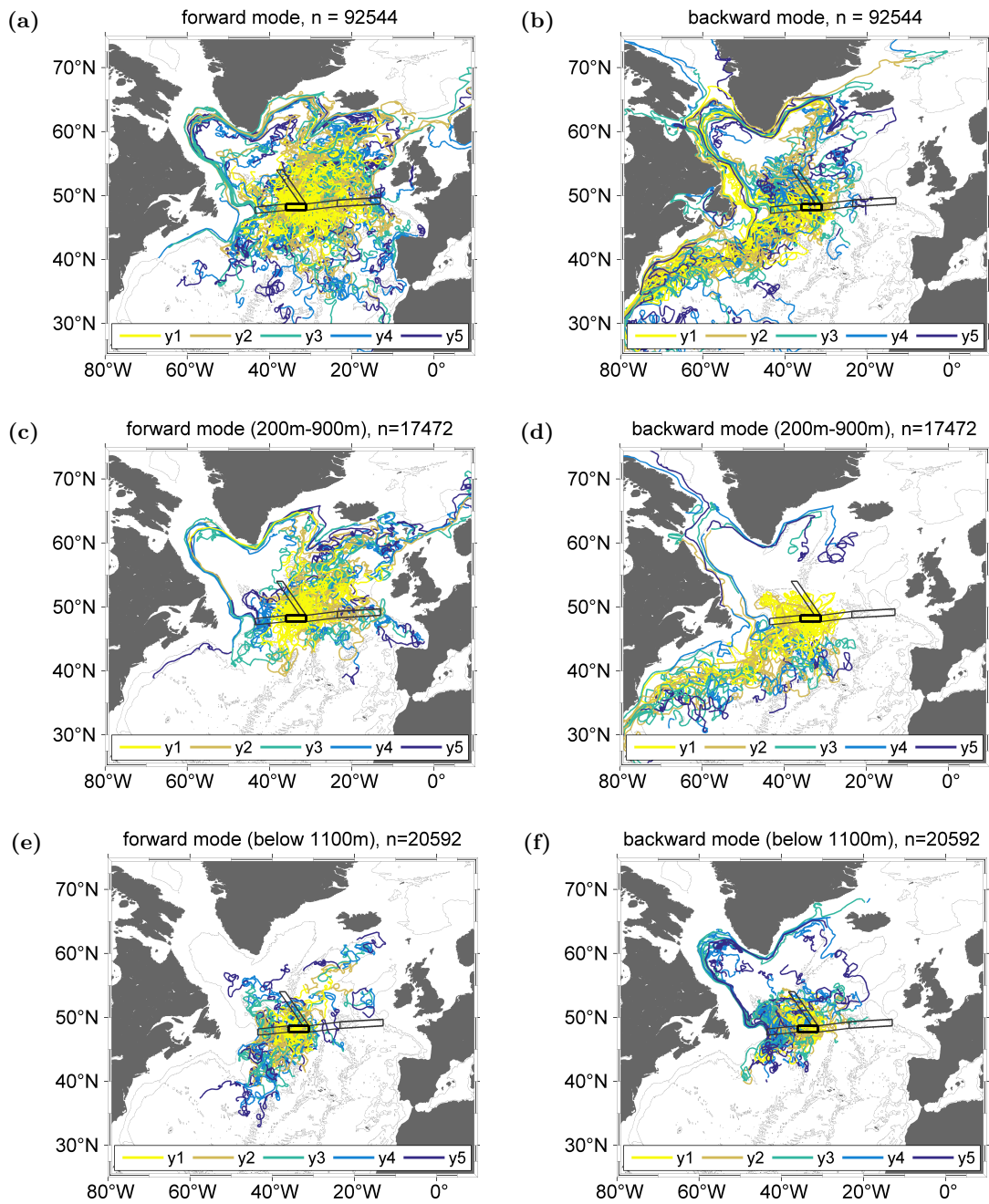


**Figure 5.9:** Trajectories of particles seeded in box 2. Panel (a) shows trajectories of particles seeded throughout the whole water column and tracked in forward mode. Panel (b) shows trajectories of particles seeded throughout the whole water column and tracked in backward mode. Panel (c) - (f) show trajectories of particles separated by the seeding depths (panel (c) and (d): seeding depths between 200 m and 900 m, panel (e) and (f): seeding depths below 1100 m, panel (c) and (e): forward mode, panel (d) and (f): backward mode). The particles were seeded in 2006 to 2017 and tracked for a maximum of five years. The different colors denote the different years of the five years (maximum) travel time. For panel (a) and (b), only every 1000th trajectory is plotted, for panels (c) - (f), every 500th trajectory is plotted. Gray contour lines show the bathymetry every 2000m. n is the total number of trajectories. The horizontal extent of the different boxes is indicated by black lines, with the bold line highlighting box 2.

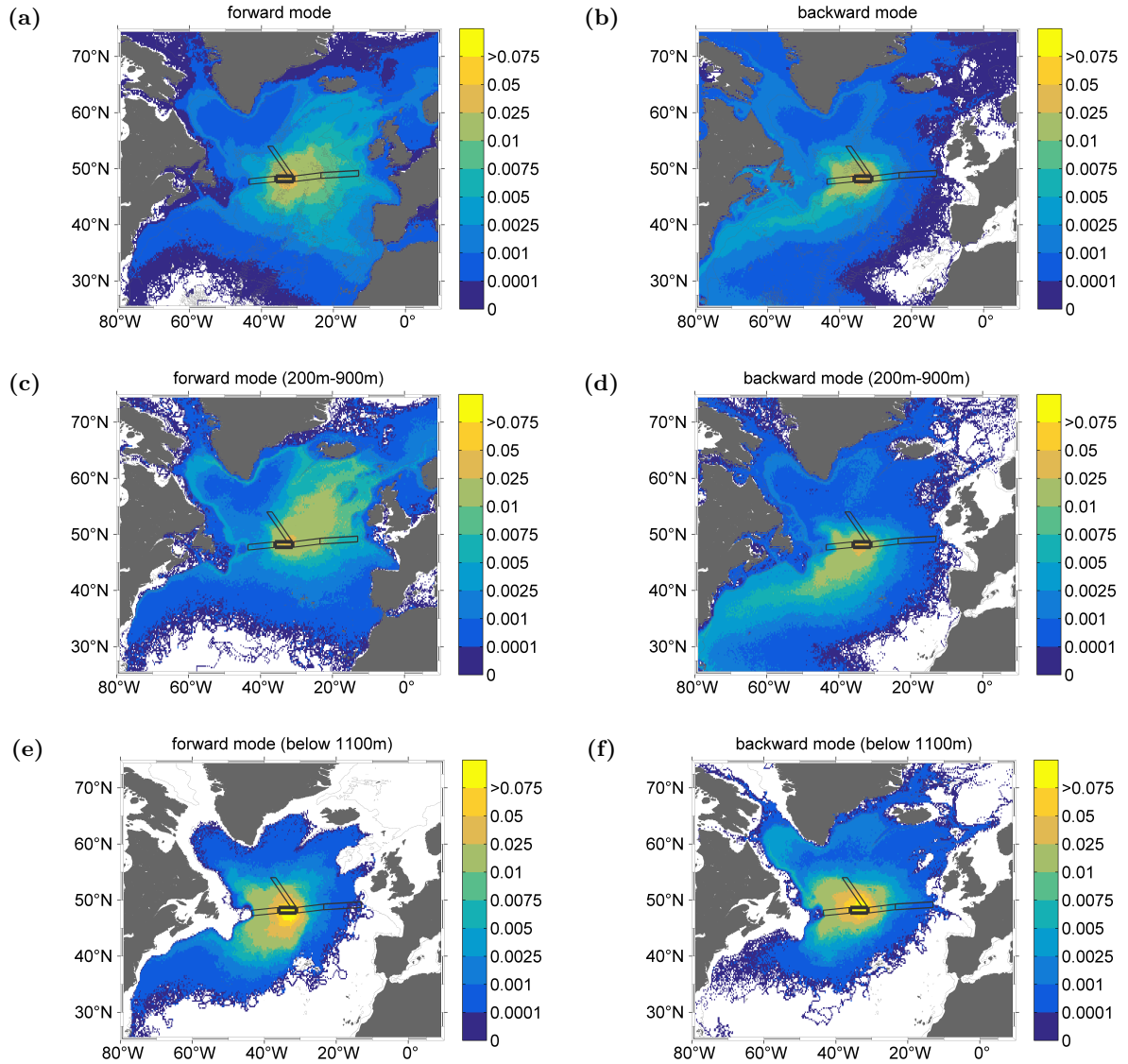


**Figure 5.10:** Probabilities of particles to cross grid cells of a horizontal mesh with a  $1/4^\circ \times 1/4^\circ$  spatial resolution after having been seeded in box 2. Panel (a) shows probabilities for particles seeded throughout the whole water column and tracked in forward mode. Panel (b) shows probabilities for particles seeded throughout the whole water column and tracked in backward mode. Panel (c) - (f) show probabilities for particles separated by the seeding depths (panel (c) and (d): seeding depths between 200 m and 900 m, panel (e) and (f): seeding depths below 1100 m, panel (c) and (e): forward mode, panel (d) and (f): backward mode). Gray contour lines show the bathymetry every 2000m. Numbers are in percent (counts of particles that crossed the grid cell relative to total number of counts). The horizontal extent of the different boxes is indicated by black lines, with the bold line highlighting box 2.

### **Trajectories of particles seeded in the eastern basin**

#### **Box 3:**

Figure 5.11 shows the trajectories of particles seeded in box 3 and Figure 5.12 the corresponding probabilities of the particles to cross grid cells of the defined horizontal  $1/4^\circ \times 1/4^\circ$  mesh grid after their placement. For the upper ocean, one of the main pathways is the export of water into the Nordic Seas either via the Iceland Basin and directly south of Iceland or, for most of the particles, via the more western route through Rockall Trough. Another major pathway is the flow following the bathymetry along the Reykjanes Ridge and contributing to the boundary current system. In contrast to that, particles seeded in the deep ocean stay rather close to their origins within the studied five years and also have their source regions mostly close to box 3 which conforms to the observations revealing only weak currents in this area (Müller et al., 2017; Müller et al., 2019). As for the boxes in the western basin, for the particles ending up in the upper ocean in box 3, the Gulf Stream and thus subtropical waters are one of the major source regions. Another source region is the Subpolar Gyre and WBC, however, of less importance than for the particles in the deep ocean. Moreover, the trajectory plots (Figure 5.11d and 5.11f) reveal an export pathway from the interior of the Labrador Sea into the eastern basin, possibly via the CGFZ, as is also found in observations (e.g. Sy et al., 1997; Talley et al., 1982) even though, as shown by the probability plots (Figure 5.12d and 5.12f), followed by a few particles only.

#### **Box 4:**

The trajectories and corresponding probability plots for particles seeded in box 4 are presented in Figure 5.13 and 5.14. Particles seeded in the upper ocean mainly are exported into the Nordic Seas or feed the boundary currents but most of the particles remain rather close to their origins for the first years of travel time which is, as for box 3, to be expected since no strong currents are known in this area. Particles which are exported into the Nordic Seas either cross on their way the Iceland basin and follow the route directly south of Iceland or flow northeastward via the Rockall Trough which is, as for box 3, the preferred pathway (Figure 5.13c and 5.14c). The trajectory plots for the backward mode (Figure 5.13d and 5.13f) show, in contrast to the previously discussed boxes, that only very few particles have their origin in the boundary current system, at least for the discussed five years of travel time, but they mostly stem from the Gulf Stream region in case of the upper ocean or from the surrounding waters of box 4 where they stayed for the studied five years.

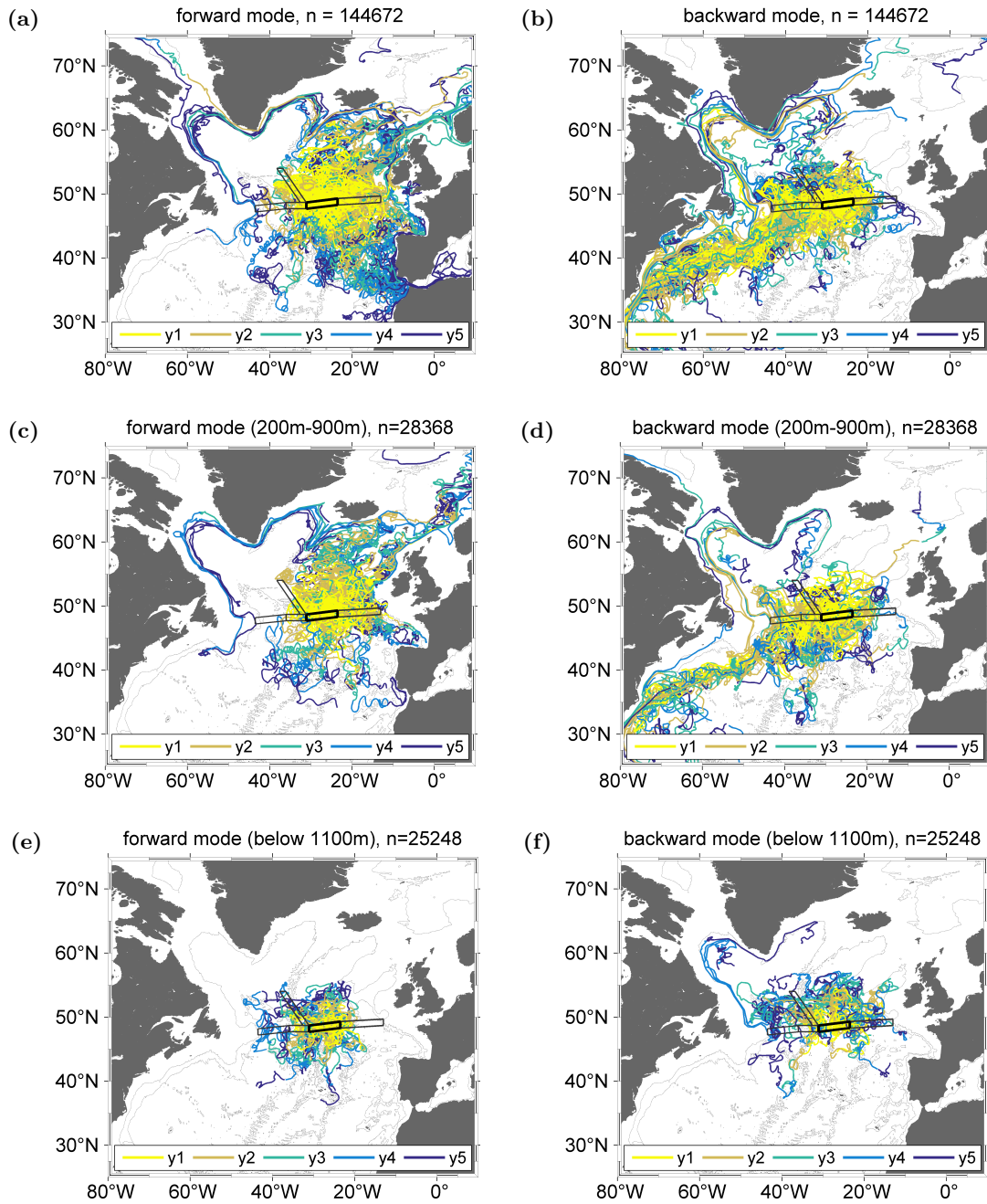


**Figure 5.11:** Trajectories of particles seeded in box 3. Panel (a) shows trajectories of particles seeded throughout the whole water column and tracked in forward mode. Panel (b) shows trajectories of particles seeded throughout the whole water column and tracked in backward mode. Panel (c) - (f) show trajectories of particles separated by the seeding depths (panel (c) and (d): seeding depths between 200 m and 900 m, panel (e) and (f): seeding depths below 1100 m, panel (c) and (e): forward mode, panel (d) and (f): backward mode). The particles were seeded in 2006 to 2017 and tracked for a maximum of five years. The different colors denote the different years of the five years (maximum) travel time. For panel (a) and (b), only every 1000th trajectory is plotted, for panels (c) - (f), every 500th trajectory is plotted. Gray contour lines show the bathymetry every 2000m. n is the total number of trajectories. The horizontal extent of the different boxes is indicated by black lines, with the bold line highlighting box 3.

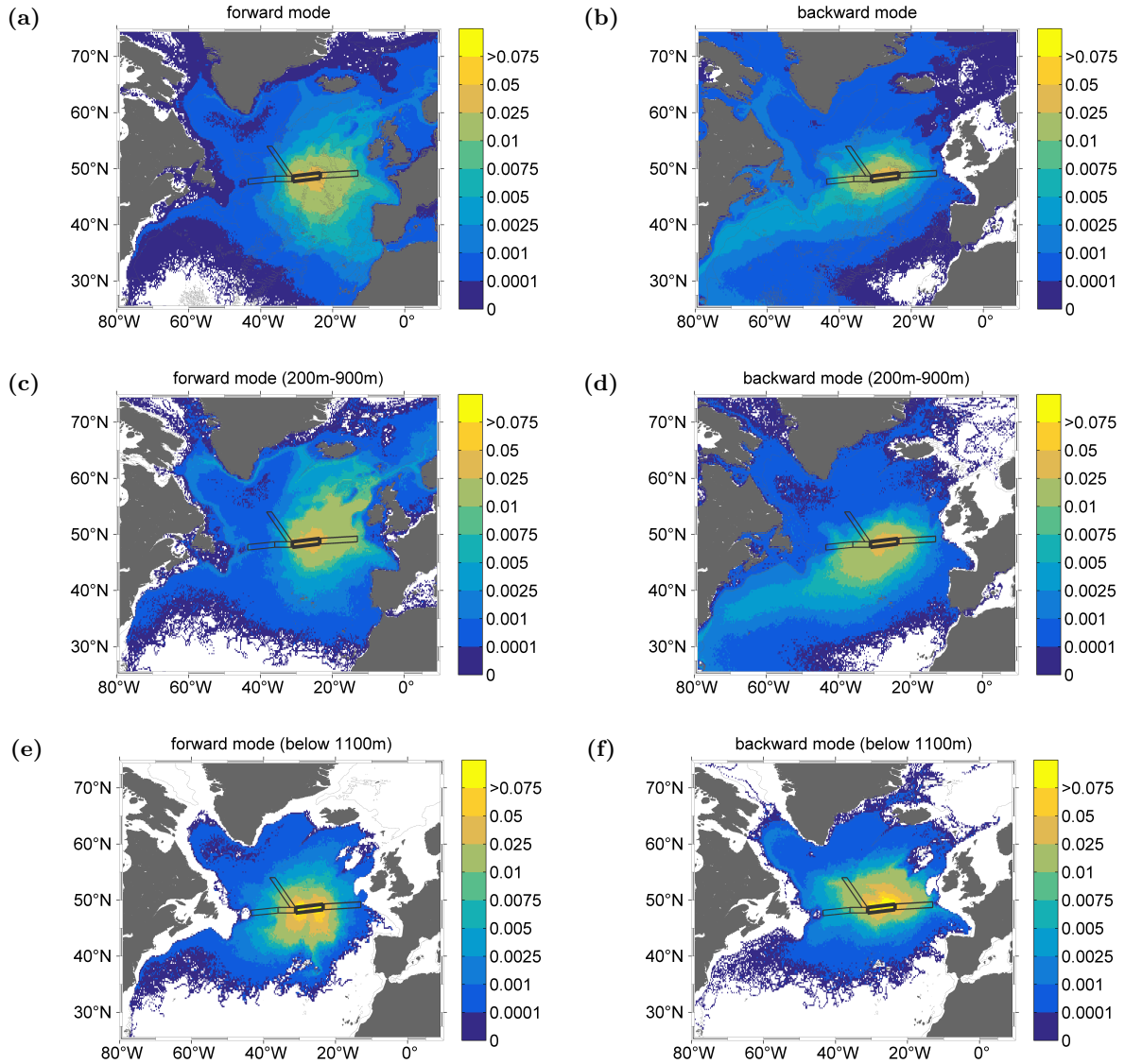


**Figure 5.12:** Probabilities of particles to cross grid cells of a horizontal mesh with a  $1/4^\circ \times 1/4^\circ$  spatial resolution after having been seeded in box 3. Panel (a) shows probabilities for particles seeded throughout the whole water column and tracked in forward mode. Panel (b) shows probabilities for particles seeded throughout the whole water column and tracked in backward mode. Panel (c) - (f) show probabilities for particles separated by the seeding depths (panel (c) and (d): seeding depths between 200 m and 900 m, panel (e) and (f): seeding depths below 1100 m, panel (c) and (e): forward mode, panel (d) and (f): backward mode). Gray contour lines show the bathymetry every 2000m. Numbers are in percent (counts of particles that crossed the grid cell relative to total number of counts). The horizontal extent of the different boxes is indicated by black lines, with the bold line highlighting box 3.

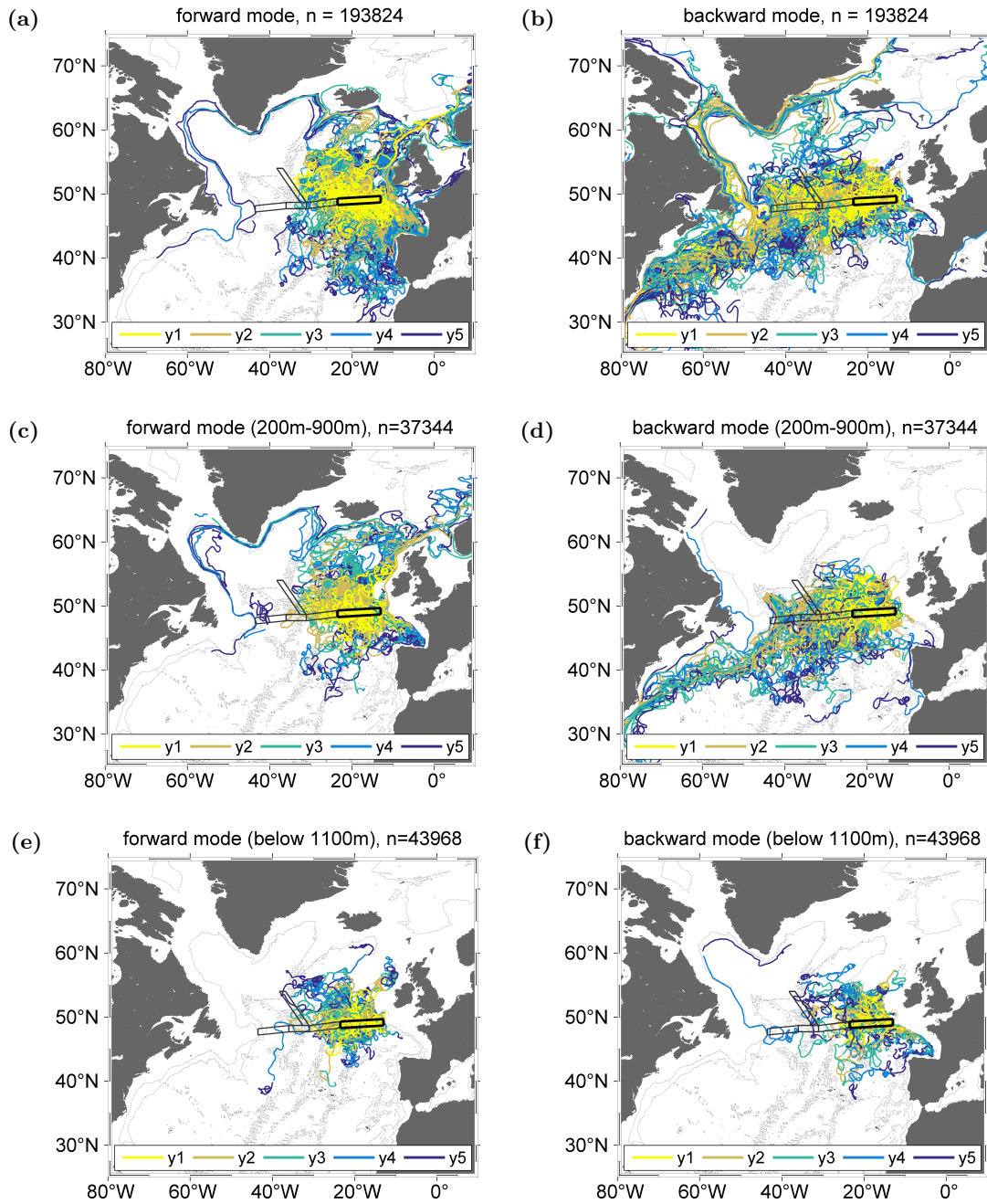


**Figure 5.13:** Trajectories of particles seeded in box 4. Panel (a) shows trajectories of particles seeded throughout the whole water column and tracked in forward mode. Panel (b) shows trajectories of particles seeded throughout the whole water column and tracked in backward mode. Panel (c) - (f) show trajectories of particles separated by the seeding depths (panel (c) and (d): seeding depths between 200 m and 900 m, panel (e) and (f): seeding depths below 1100 m, panel (c) and (e): forward mode, panel (d) and (f): backward mode). The particles were seeded in 2006 to 2017 and tracked for a maximum of five years. The different colors denote the different years of the five years (maximum) travel time. For panel (a) and (b), only every 1000th trajectory is plotted, for panels (c) - (f), every 500th trajectory is plotted. Gray contour lines show the bathymetry every 2000m. n is the total number of trajectories. The horizontal extent of the different boxes is indicated by black lines, with the bold line highlighting box 4.

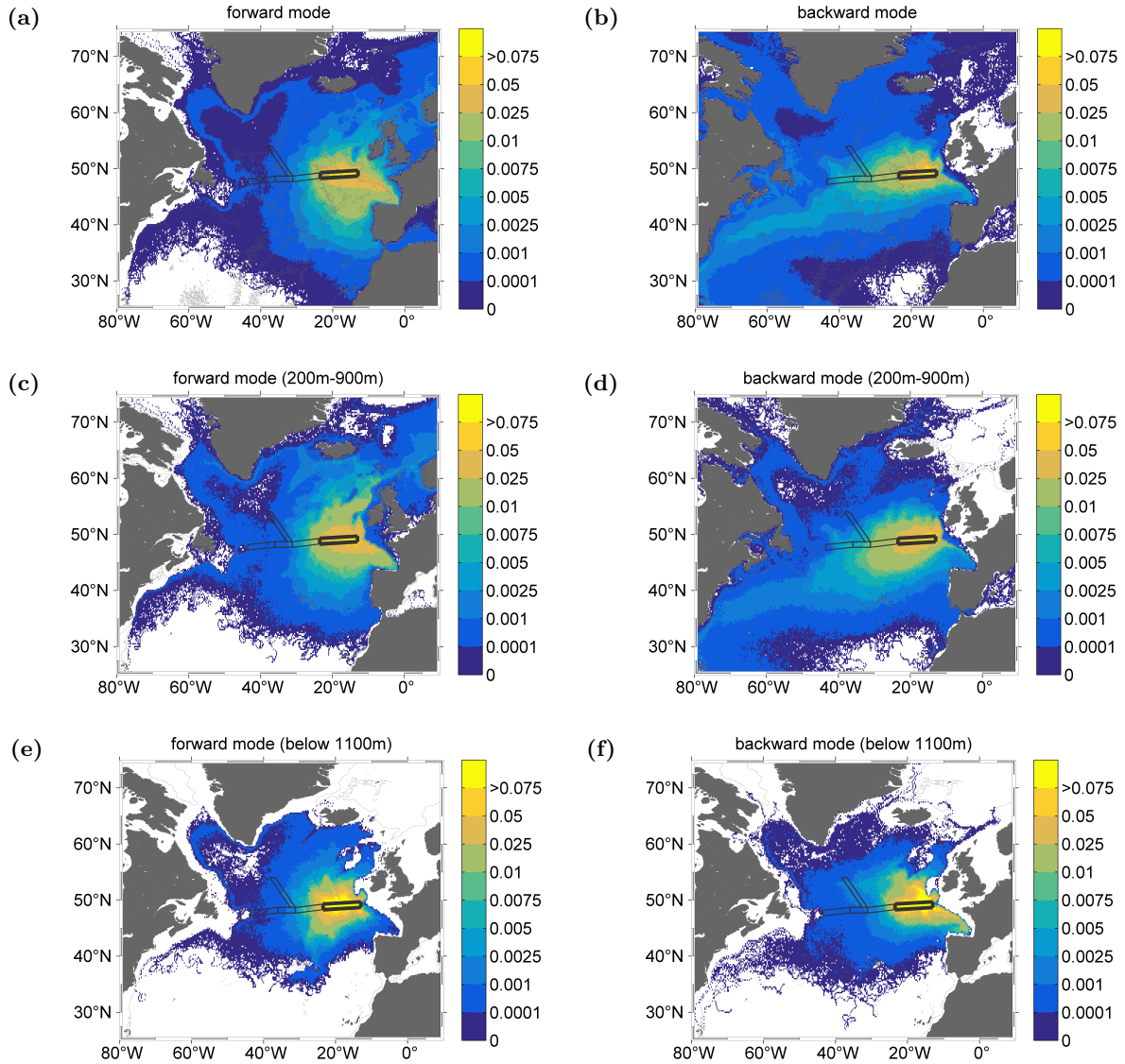


**Figure 5.14:** Probabilities of particles to cross grid cells of a horizontal mesh with a  $1/4^\circ \times 1/4^\circ$  spatial resolution after having been seeded in box 4. Panel (a) shows probabilities for particles seeded throughout the whole water column and tracked in forward mode. Panel (b) shows probabilities for particles seeded throughout the whole water column and tracked in backward mode. Panel (c) - (f) show probabilities for particles separated by the seeding depths (panel (c) and (d): seeding depths between 200 m and 900 m, panel (e) and (f): seeding depths below 1100 m, panel (c) and (e): forward mode, panel (d) and (f): backward mode). Gray contour lines show the bathymetry every 2000m. Numbers are in percent (counts of particles that crossed the grid cell relative to total number of counts). The horizontal extent of the different boxes is indicated by black lines, with the bold line highlighting box 4.

### Trajectories of particles seeded at the MAR

#### Box 5:

The MAR north of 47°/48°N represents the gateway between the interior western and eastern North Atlantic. As such, the pathways of particles starting or ending in box 5 are of special interest for studying the exchange of water between the western and eastern basin. Even though the volume transport across the MAR was found to be substantially smaller in the model than the one obtained from observational data (Figure 5.4), the trajectories (Figure 5.15) and probability plots (Figure 5.16) underline what is meant by gateway between the two basins: Particles seeded in box 5 and tracked in the forward mode (Figure 5.15a and 5.16a) mainly flow into the eastern basin, especially those seeded in the upper ocean (Figure 5.15c and 5.16c), whereas particles tracked in the backward mode mostly stem from the western basin (Figure 5.15b and 5.16b). Beyond that, a majority of the particles seeded in the upper ocean stays in the Subpolar Gyre within the studied five years and feeds the boundary current system, only a few are exported into the Nordic Seas with an enhanced pathway via the Iceland Basin. Particles seeded in the deep ocean tend to stay closer to their origin but also are exported south of 47°/48°N in the western basin as their depths presumably prevent them from crossing the MAR. The source regions of the particles seeded in box 5 mainly lies, apart from the interior western basin, in the boundary currents, and, for upper ocean particles, in the region of the Gulf Stream.

#### Comparison of the circulation scheme known from observations to the main flow paths identified in the model

Overall, the model data and particle trajectories agree well with the currents and pathways identified through observations at the 47°/48°N and PIES transect. The main inflow into the subpolar North Atlantic is the NAC which is fed by water from the subtropics flowing northward with the Gulf Stream along the continental slope. The NAC crosses 47°/48°N within the borders of box 1 and turns eastward further north before crossing box 5 and the MAR with an enhanced flow through the fracture zones. Beyond the flow into the interior eastern basin, two major routes were identified: One follows the bathymetry of the Reykjanes Ridge and feeds the boundary current system and one is the export pathway into the Nordic Seas either via the Iceland Basin or via Rockall Trough. Particles which follow the boundary currents along the coastline of Greenland, around the Labrador Sea, and southward along the Canadian coast either recirculate and stay in the Subpolar Gyre or are exported south of 47°/48°N. Apart from that, also a pathway from the interior of the Labrador Sea via the MAR into the eastern

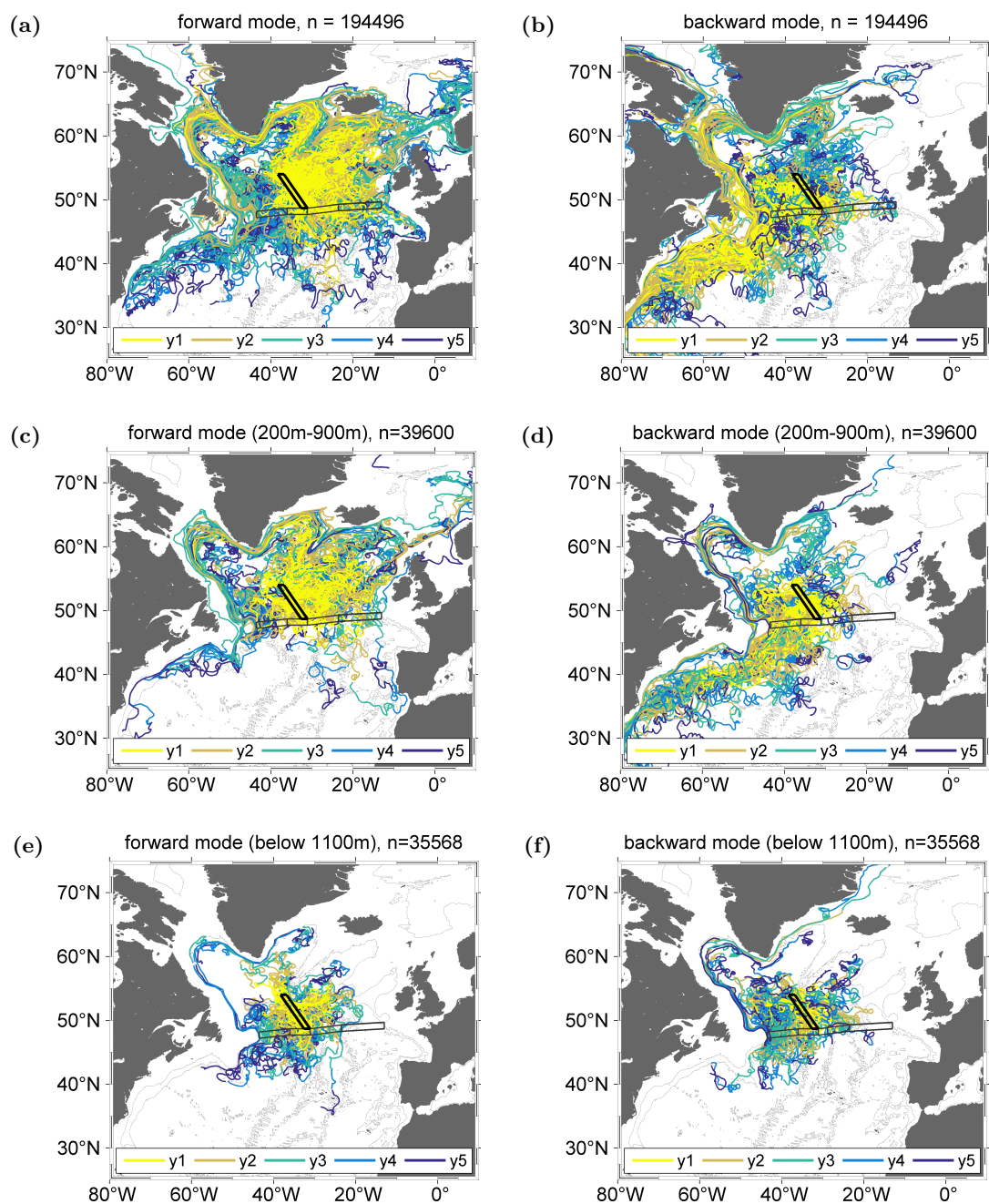


**Figure 5.15:** Trajectories of particles seeded in box 5. Panel (a) shows trajectories of particles seeded throughout the whole water column and tracked in forward mode. Panel (b) shows trajectories of particles seeded throughout the whole water column and tracked in backward mode. Panel (c) - (f) show trajectories of particles separated by the seeding depths (panel (c) and (d): seeding depths between 200 m and 900 m, panel (e) and (f): seeding depths below 1100 m, panel (c) and (e): forward mode, panel (d) and (f): backward mode). The particles were seeded in 2006 to 2017 and tracked for a maximum of five years. The different colors denote the different years of the five years (maximum) travel time. For panel (a) and (b), only every 1000th trajectory is plotted, for panels (c) - (f), every 500th trajectory is plotted. Gray contour lines show the bathymetry every 2000m.  $n$  is the total number of trajectories. The horizontal extent of the different boxes is indicated by black lines, with the bold line highlighting box 5.

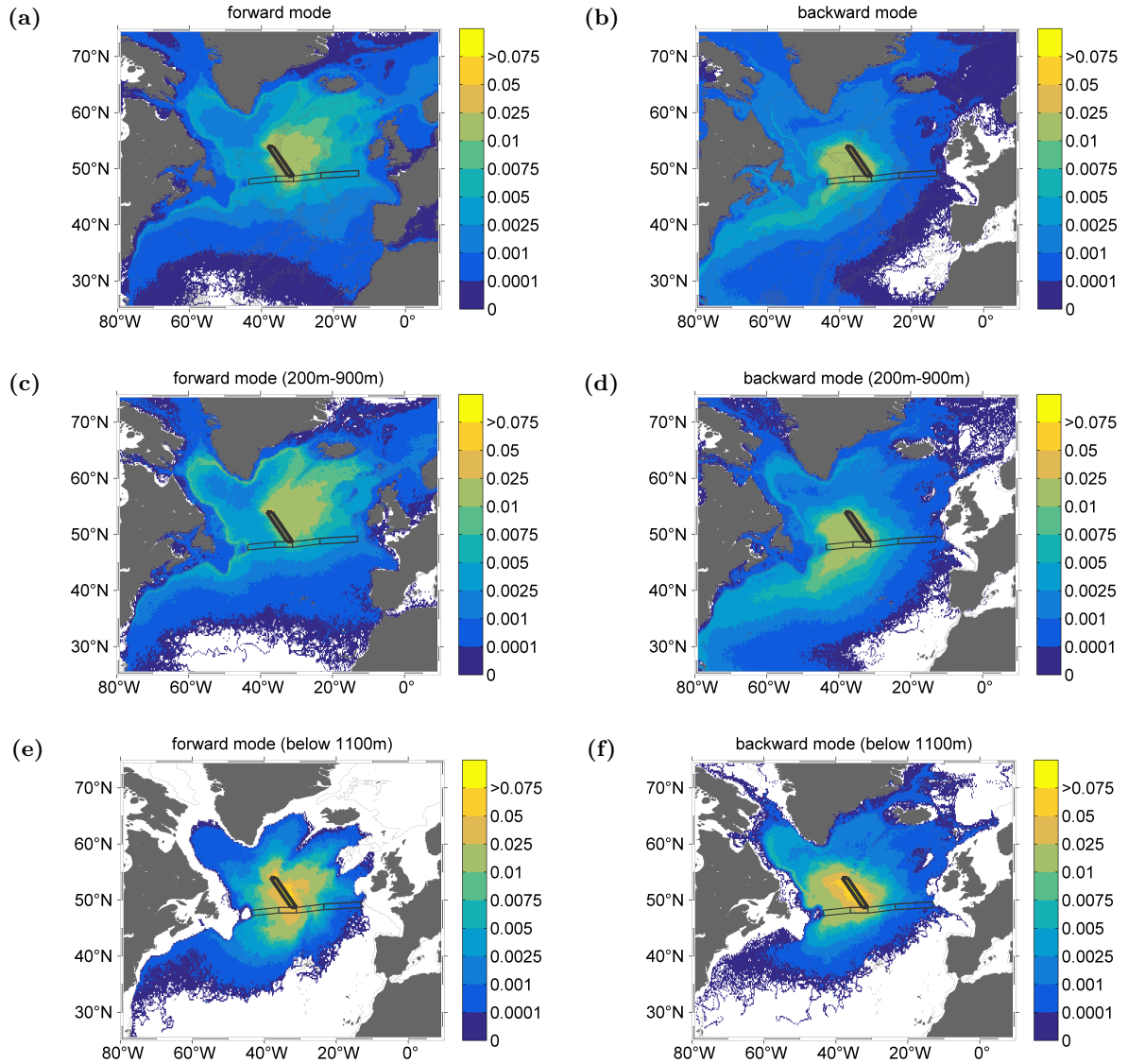


**Figure 5.16:** Probabilities of particles to cross grid cells of a horizontal mesh with a  $1/4^\circ \times 1/4^\circ$  spatial resolution after having been seeded in box 5. Panel (a) shows probabilities for particles seeded throughout the whole water column and tracked in forward mode. Panel (b) shows probabilities for particles seeded throughout the whole water column and tracked in backward mode. Panel (c) - (f) show probabilities for particles separated by the seeding depths (panel (c) and (d): seeding depths between 200 m and 900 m, panel (e) and (f): seeding depths below 1100 m, panel (c) and (e): forward mode, panel (d) and (f): backward mode). Gray contour lines show the bathymetry every 2000m. Numbers are in percent (counts of particles that crossed the grid cell relative to total number of counts). The horizontal extent of the different boxes is indicated by black lines, with the bold line highlighting box 5.

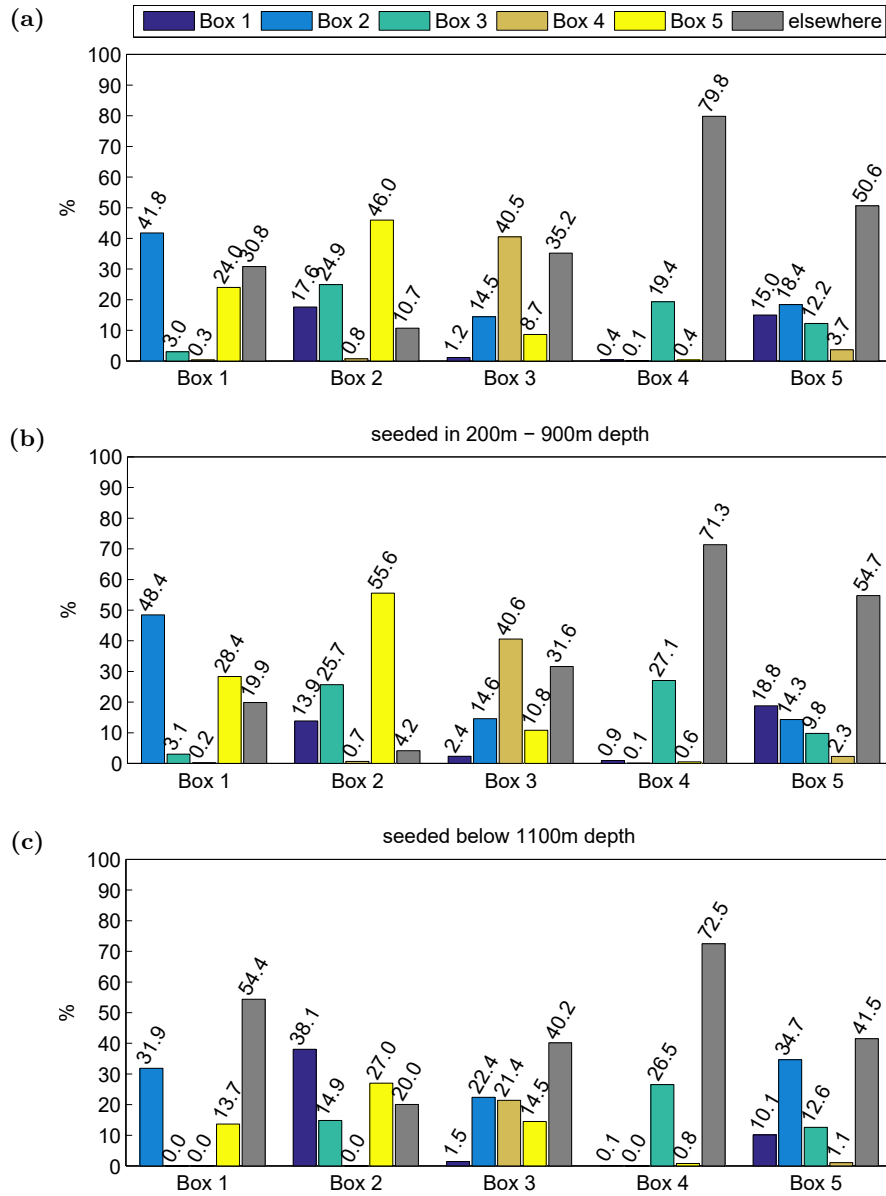
basin was identified which is also found in observations. As already suggested from the volume transport calculations in the previous section, there is presumably a strong connection of the interior western basin with the WBC, even though the choice of the longitudinal extent of box 1 which includes partly the WBC hinders the unambiguous interpretation of the trajectories. For the eastern basin, the trajectories and probability plots suggest only weak currents which fits to the results of the volume transport calculations revealing a net meridional mean transport close to zero in this region.

### 5.2.2 Exchange of particles between different regions

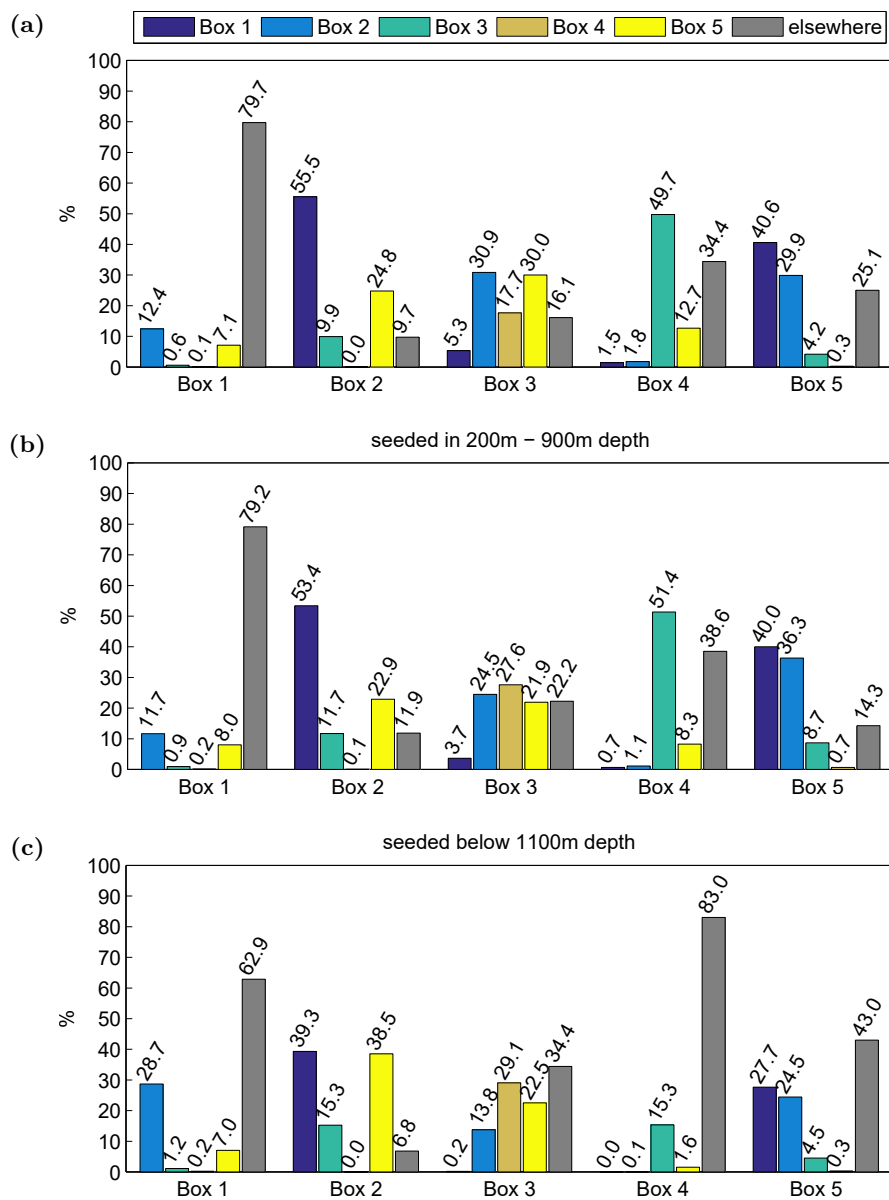
While the previous subsection focused on the qualitative description of the general flow paths and of origins and source regions of the particles seeded in the different boxes, this subsection quantitatively examines the exchange of water between the different boxes in order to identify major routes within the studied region. Furthermore the amount of particles having their origin in the subtropics and of those flowing out of the subpolar North Atlantic into the Nordic Seas are calculated.

Figure 5.17 and 5.18 illustrate with numbers in percent the direct exchange of particles between the boxes, i.e. the numbers describe how many particles of  $n$  particles seeded in box  $X$  cross afterwards box  $Y$  or how many have crossed it before. Figure 5.17a and 5.18a show the percentages for particles seeded throughout the whole water column, Figure 5.17b and 5.18b show the percentages for the exchange of particles seeded in the upper ocean between 200 m and 900 m, and Figure 5.17c and 5.18c show the corresponding percentages for the exchange of particles seeded below 1100 m.

For both tracking modes, the most noticeable feature are the numbers representing particles which do not cross any other box than the one they were seeded in within the studied five years of travel time. For the forward mode (Figure 5.17), about 70 % to 80 % of the particles seeded in the upper and deep ocean in box 4 do not cross any of the other boxes on their route but, as the trajectory plots show, presumably continue their way into northeastward direction or are exported further south. Also about 50 % of the particles seeded in box 5, do not cross any other box but supposedly leave the PIES region into northeastward direction, only about 10 % flow southeastward towards box 3 or 4, and about 30 % to 40 % flow south-westward towards box 1 or 2. For the backward mode (Figure 5.18), the most outstanding numbers are the 60 % to 80 % of the particles ending up in box 1 and the about 80 % of the particles ending up in the deep ocean in box 4 without having crossed any of the other boxes before in neither of the cases. Apart from that, water is generally mainly exchanged between two neighboring boxes and along the well-studied pathway of the NAC flowing northward across 47°/48°N in the



**Figure 5.17:** Bar plots showing the percentages of particles exchanged in forward mode between the five boxes relative to the total number of particles seeded in the boxes. On the x-axis, the boxes in which the particles were seeded are shown and the colored bars represent the amount of particles crossing box 1 (dark blue), box 2 (light blue), box 3 (green), box 4 (gold), and box 5 (yellow) afterwards or none of them (gray). The first bar, for example, with 41.8%, represents the particles which were seeded in box 1 and crossed afterwards box 2. Panel (a) shows the percentages for particles that were seeded throughout the whole water column. Panel (b) shows the percentages for particles seeded in the upper ocean between 200 m and 900 m. Panel (c) shows the corresponding percentages for particles seeded below 1100 m. All particles were tracked for a maximum of five years.



**Figure 5.18:** Bar plots showing the percentages of particles exchanged in backward mode between the five boxes relative to the total number of particles seeded in the boxes. On the x-axis, the boxes in which the particles were seeded are shown and the colored bars represent the amount of particles crossing box 1 (dark blue), box 2 (light blue), box 3 (green), box 4 (gold), or box 5 (yellow) before or none of them (gray). The first bar, for example, with 12.4%, represents the particles which ended up in box 1 and crossed before box 2. Panel (a) shows the percentages for particles that were seeded throughout the whole water column. Panel (b) shows the percentages for particles seeded in the upper ocean between 200 m and 900 m. Panel (c) shows the corresponding percentages for particles seeded below 1100 m. All particles were tracked for a maximum of five years.

western basin and turning eastward afterwards before crossing the MAR. Particles starting in the western basin in the upper ocean in box 1 or 2 and tracked in forward mode, for example, mainly cross box 5 on their way (about 30 % for box 1 and about 55 % for box 2) and particles ending in box 5 in most cases crossed boxes 1 or 2 the western basin before (up to in total 70 %). This highlights also retrospectively the importance of the fracture zones as gateways into the eastern basin as it was found that about 15 % of the particles starting in box 1 cross the CGFZ and 13 % cross the FFZ on their way into the eastern basin which are about half of the particles flowing from box 1 to box 5. Another substantial amount of particles is exchanged between the two boxes in the western basin (about 30 % to 50 % of the particles starting in the upper ocean in box 1 cross box 2 afterwards and about 40 % to 55 % of the particles ending in box 2 crossed box 1 before). In contrast to that, particles starting in the eastern basin and tracked in forward mode mostly remain in the eastern basin and the highest numbers are found for the exchange within the eastern basin between the boxes 3 and 4. Even though box 3 also shows a connection with box 2 in the western basin, especially particles seeded in box 4 nearly exclusively follow pathways going towards or coming from box 3 (about 20 % for the forward mode and about 50 % for the upper ocean and backward mode) and only a minority stems from the MAR region (about 10 % for upper ocean). Due to the slow and undefined currents in the eastern basin, however, the maximal travel time of five years which is considered here, presumably also plays a role in setting those numbers and further analysis of longer travel times could increase these.

Figure 5.19 shows the trajectories of particles seeded in box 1 to 5 which crossed before a box spanning the entire Atlantic at about 40°N. These particles are defined in this context as particles which have their origin in the subtropics. Figure 5.20 shows the trajectories of particles seeded in box 1 to 5 which cross afterwards a box spanned across Denmark Strait and the Iceland-Scotland Ridge. These particles are defined in this context as particles flowing out of the subpolar North Atlantic into the Nordic Seas. The corresponding percentages for each of the cases are given in Table 5.2.

This further analysis of particle trajectories shows that about 59 % of the particles seeded at the 47°/48°N transect in the boxes 1 to 4, about 65 % of the particles seeded in the western basin at 47°/48°N in the boxes 1 and 2, about 55 % of the particles seeded in the eastern basin at 47°/48°N in the boxes 3 and 4, and about 61 % of the particles seeded at the MAR section stem from the subtropics. Moreover, about 10 % of the particles seeded at 47°/48°N in the boxes 1 to 4, about 11 % of the particles seeded in the western basin at 47°/48°N, in the boxes 1 and 2, about 9 % of the particles seeded in the eastern basin at 47°/48°N in the boxes 3 and 4, and about 15 % of the particles seeded at the MAR continue their pathways into the Nordic Seas.

5 The circulation in the subpolar eastern North Atlantic studied with model output

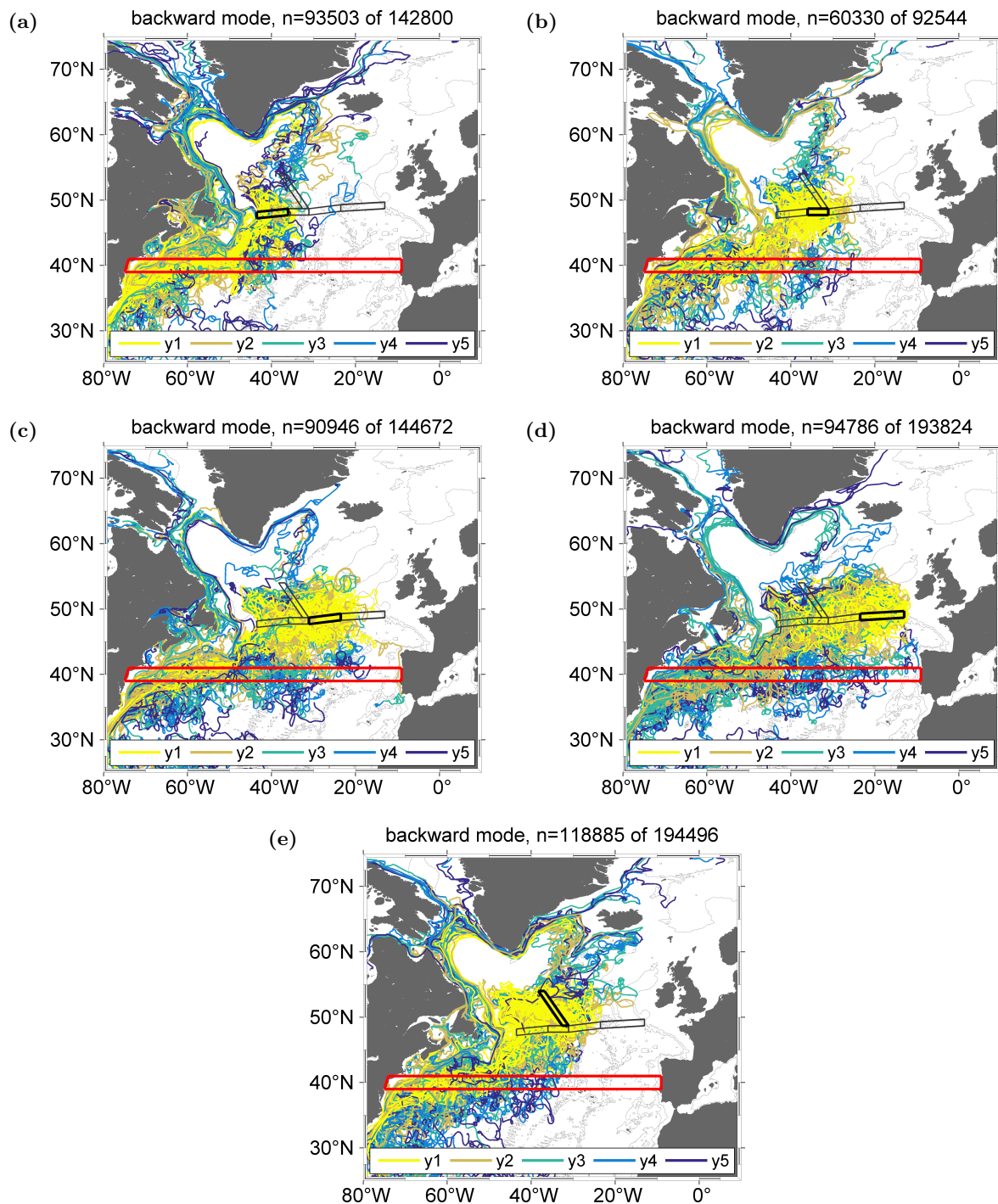


**Figure 5.19:** Trajectories for boxes 1 to 5 of particles having their origin in the subtropics. The different panels show the same plot for the different starting boxes. Particles were tracked for a maximum of five years in backward mode. Numbers indicate how many of the total number of particles seeded in the respective boxes crossed the red box (representing the subtropical origin) before. The different colors denote the different years of the five years (maximum) travel time. Only every 500th trajectory of the in total n particles is shown. Gray contour lines show the bathymetry every 2000m.

## 5.2 Flow paths into the subpolar eastern North Atlantic

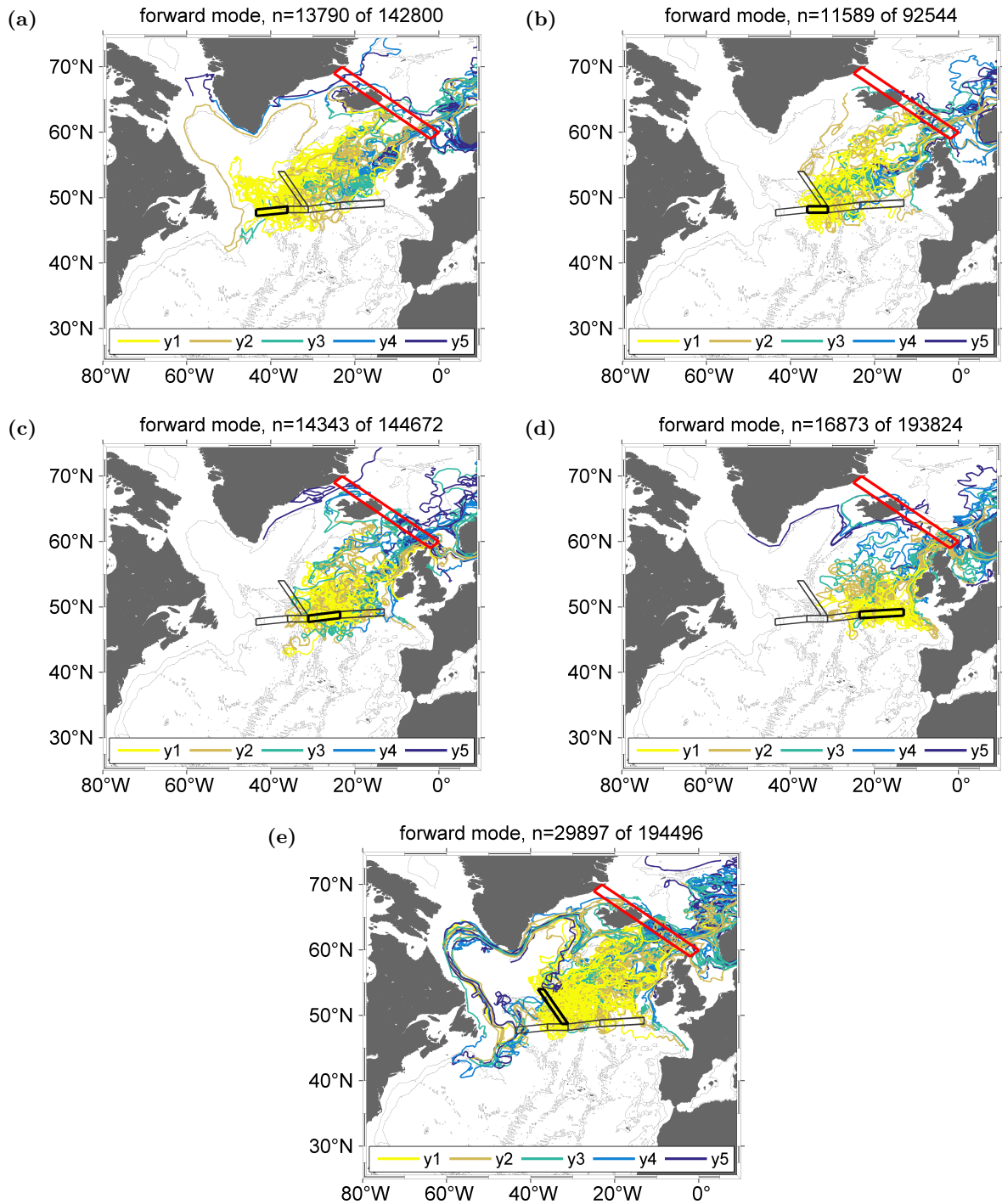


**Figure 5.20:** Trajectories for boxes 1 to 5 of particles flowing into the Nordic Seas. The different panels show the same plot for the different starting boxes. Particles were tracked for a maximum of five years in forward mode. Numbers indicate how many of the total number of particles seeded in the respective boxes cross the red box (representing the flow into the Nordic Seas). The different colors denote the different years of the five years (maximum) travel time. Only every 500th trajectory of the in total  $n$  particles is shown. Gray contour lines show the bathymetry every 2000m.

	<b>Subtropics</b>	<b>Nordic Seas</b>
Box 1	65 %	10 %
Box 2	65 %	13 %
Box 3	63 %	10 %
Box 4	49 %	9 %
Box 5	61 %	15 %
47°/48°N (Box 1 to 4)	59 %	10 %
Western basin (Box 1+2)	65 %	11 %
Eastern basin (Box 3+4)	55 %	9 %
Eastern basin + MAR (Box 3 to 5)	57 %	11 %

**Table 5.2:** Amount of particles in % seeded in boxes 1 to 5 which originate in the subtropics or flow into the Nordic Seas. To determine the amount of particles originating in the subtropics, the particles were tracked for a maximum of five years in backward mode. To determine the amount of particles flowing into the Nordic Seas, the particles were tracked for a maximum of five years in forward mode.

The numbers calculated here for the inflow from the subtropics into the subpolar North Atlantic compare well with literature and the observational part of this study. Roessler et al. (2015) estimate for the PIES MAR transect that about 60 % of the water transported across the MAR into the eastern basin is of subtropical origin which agrees with the 61 % which are found here. Breckenfelder et al. (2017) and Mertens et al. (2014) find for the western basin at 47°N that about 40 % to 45 % of the NAC related northward flow is water which is lighter than  $27.68 \text{ kg/m}^3$ . However, since the longitudinal ranges used for the transport calculations differ from the horizontal extents of the boxes used in the analysis here, the numbers cannot be compared directly. For the interior eastern basin, it was calculated in this study (cf. Chapter 4) that the upper ocean transport above the  $27.68 \text{ kg/m}^3$  isopycnal corresponds in 2016 to 2017 to about 62 % of the total meridional transport which compares relatively well to the about 55 % found here, especially when considering the weaker coupling between the western and eastern basin as well as the net southward transport across 47°/48°N found for the model. For the inflow into the Nordic Seas, Østerhus et al. (2019) find a mean transport based on observations of about 8 Sv. This corresponds to about 19 % of the inflow into the eastern subpolar North Atlantic found from the combination of the PIES-based results from this study (cf. Chapter 4) with the results of McCarthy et al. (2020) and Roessler et al. (2015). This value is considerably larger than the 11 % found for the combined numbers from boxes 3 to 5 but only slightly larger than the 15 % found here when considering only the zonal inflow across the MAR and might thus be owed to the model specific small meridional flow in the interior eastern basin. Consequently, further analysis of travel times longer than five years, might lead

to increased numbers related to the flow into the Nordic Seas. This is also indicated by the color coding of the travel time in Figure 5.20 since most particles flowing into the Nordic Seas do so only after two or even three years.

In summary, the quantification of the particle exchange between the individual boxes supports what was also concluded from the trajectory and probability plots: The overall circulation scheme in the model agrees well with observations and particles are mainly exchanged between two neighboring boxes and along the well-studied pathway of the NAC. The weaker coupling between the western and eastern basin as well as the smaller northward inflow in the eastern basin, however, became also apparent. The bar plots show that particles seeded in the deep ocean are less likely to cross any other box within the studied five years of travel time than particles seeded in the upper ocean with box 5 being the exception for the forward mode and boxes 1 and 2 for the backward mode. As the trajectory plots suggest, the reason for this probably lies in the bathymetry representing an obstacle for deeper particles forcing them on different pathways or hindering their advance, but also, especially in the eastern basin, in rather slow and undefined currents as were found in the model volume transports. Further analysis included two additional boxes, one at 40°N to track particles of subtropical origin and one further northeast between Greenland and Scotland to track particles flowing into the Nordic Seas. From this analysis it was inferred that about 60 % of the particles seeded at 47°/48°N and the MAR transect are of subtropical origin and that about 11 % to 15 % of the particles flow into the Nordic Seas.

### 5.2.3 Water mass transformation

In addition to the separation of particles according to their seeding depths in the upper and deep ocean roughly defined by the mean depth of the potential density anomaly isoline  $\sigma_\theta = 27.68 \text{ kg/m}^3$  which is the upper limit of the Labrador Sea Water, this subsection focuses on the analysis of the trajectories in relation to their dynamically changing potential density anomaly. Of special interest here is the transformation of lighter particles into particles denser than  $27.68 \text{ kg/m}^3$  as this process of water mass transformation is one of the key components of the AMOC and the subpolar North Atlantic is one of the main regions for this process to happen (e.g. Killworth, 1983; Rhein et al., 2011; Talley et al., 1982).

Figure 5.21 shows for boxes 1 to 5 all trajectories of particles whose potential density anomaly changed from lighter to denser than  $27.68 \text{ kg/m}^3$ . The figure reveals three main regions in which the water mass transformation happens in the model with a bias depending on the boxes where the particles were seeded in: West and east of Greenland in the Labrador Sea and the Irminger Sea including the boundary currents, and (south-)east of Iceland including

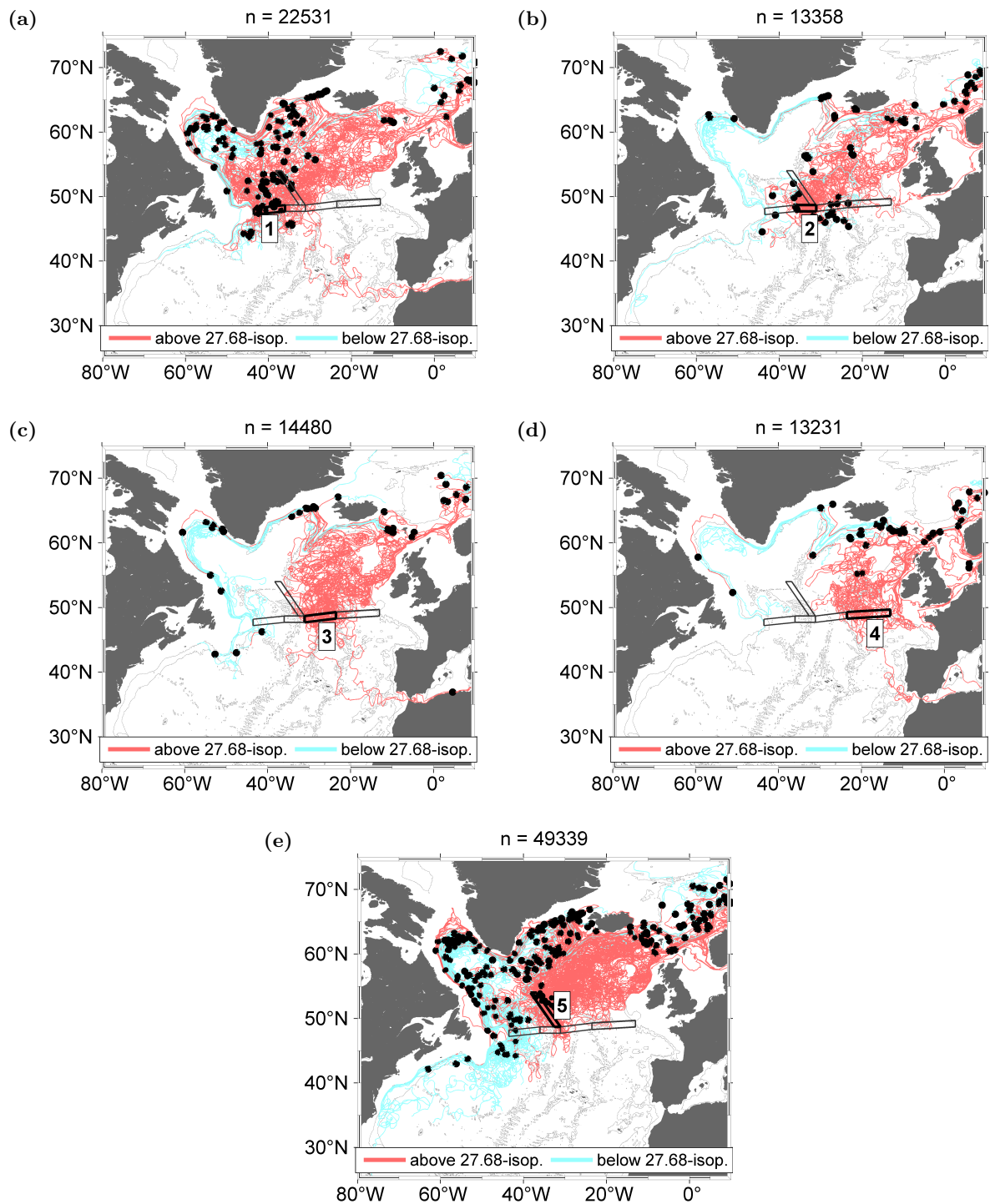


**Figure 5.21:** Trajectories of particles for boxes 1 to 5 which were transformed from lighter (shown as red trajectories) into denser (shown as blue trajectories) water. Black dots indicate where the density of the particle changes from lighter to denser than  $27.68 \text{ kg/m}^3$ . The different panels show the same plot for the different starting boxes. Particles were tracked for a maximum of five years in forward mode. Only every 500th trajectory of the in total  $n$  particles is shown. Gray contour lines show the bathymetry every 2000m.

the Iceland Basin and the Norwegian Sea. These regions are also found in studies based on observational data (e.g. Brambilla et al., 2008a; Brambilla et al., 2008b; Petit et al., 2020; Schmitz et al., 1993) even though their contribution to the source waters of the AMOC is rated differently (Petit et al., 2020).

Particles seeded in box 1 mainly are transformed in the Irminger and Labrador Sea. Particles starting in box 2 mainly are transformed southeast and east of Iceland and along the Reykjanes Ridge. Particles starting in box 3 are transformed southeast and east of Iceland and in the boundary currents east and west of Greenland but not in the interior of the basins. Particles starting in box 4 mostly are transformed southeast and east of Iceland. And lastly, particles starting in box 5 at the MAR are transformed into denser water in all of the named regions. Furthermore, in some cases, particles are also transformed further south in the interior western basin, presumably through the entrainment of the southward flowing denser waters into the interior basin, a process that is also described in Kieke et al. (2009), Mertens et al. (2014), and Rhein et al. (2002).

### 5.3 Summary and Discussion

In this chapter, model output was used to calculate volume transports across the  $47^{\circ}/48^{\circ}\text{N}$  and MAR sections defined by the PIES locations. The model-based transport time series were compared to the PIES-derived transport for the interior eastern basin calculated in this study, and to the transport time series for the interior western basin (Rhein et al., 2019), the WBC (Mertens et al., 2014; Rhein et al., 2019), and the MAR section (update from Roessler et al., 2015). The analysis was complemented by the comparison of model surface velocities to satellite-derived geostrophic velocities.

In general, the overall circulation scheme in the model is very similar to the one found from observations even though some deviations were found which impact the amount of water transported across the studied sections. For the interior western basin, a surplus inflow across  $47^{\circ}/48^{\circ}\text{N}$  was found which is in the mean by about 16 Sv larger than the one found from observations while the mean transport of the southward flowing WBC further west is very similar in the model ( $-38.9\text{ Sv}$ ) and observations ( $-37.3\text{ Sv}$ , Mertens et al. 2014). In contrast, the main zonal model flow across the MAR segment, which is shifted further to the north compared to the observations, is substantially smaller than the one found from observations (even after the extension of PIES MAR section until  $54^{\circ}\text{N}$  to also capture the more norther NAC branch visible in the model data). While the mean observation-based transport across the MAR ( $+32.3\text{ Sv}$ , McCarthy et al. 2020; Roessler et al. 2015) roughly corresponds to the mean

observation-based meridional inflow in the interior western basin (+33.5 Sv, Mertens et al. 2014; Rhein et al. 2019), the mean model-based transport across the MAR of about +26.6 Sv is substantially smaller than the mean model-based meridional inflow in the interior western basin of about +49.5 Sv. Thus, additional pathways - for example an increased southward transport west of Flemish Cap as indicated from the surface velocities (cf. Figure 5.1) - are required to balance this surplus inflow into the western basin. Also for the meridional flow in the interior eastern basin, smaller mean transports are found (roughly  $-2.4$  Sv in the model and  $+9.1$  Sv in observations) suggesting even weaker currents in the model in this region than found from observations and also a weaker coupling between the western and eastern basin. Overall, a total inflow into the subpolar eastern North Atlantic of +24.2 Sv was found from the model which is considerably smaller than the one found from observations (about +41.4 Sv). From the correlation analysis, no significant correlation between the transport time series calculated from model data and from observations was found. Additionally, the comparison of the mean transports revealed the sensitivity of these values to latitudinal and longitudinal bounds used in the transport calculation. Both findings highlight the importance of transport definitions and thorough analysis of the model- and observation-based flow field, especially when model data are used to complement observation-based transport time series.

Furthermore, as for the observational data, the correlations between the individual transport time series were calculated and analyzed. For the meridional flow in the interior eastern basin between  $31^{\circ}\text{W}$  and  $15^{\circ}\text{W}$  and the transport across the extended MAR segment, a significant negative correlation ( $R = -0.9$ ) was found which is comparable to the one found in the observational data ( $R = -0.7$ ) yielding in a smaller variability of the total inflow of subtropical water into the interior eastern basin. Moreover, the meridional flow in the interior western basin is also significantly correlated with the WBC transport ( $R = -0.9$ ). As for the observational data, also a positive correlation between the interior western transport and the transport across the MAR is found, however, at a smaller confidence level. Overall, the correlation between the individual transport time series also suggests a weaker coupling between the western and eastern basin in the model as was already concluded from the corresponding mean transports and comparison of model surface velocities to satellite data.

In a second part of this chapter, trajectories of particles calculated from the model velocity field with the Lagrangian trajectory tool ARIANE were analyzed. The particles were seeded along the  $47^{\circ}/48^{\circ}\text{N}$  transect and the MAR in five different boxes. The analysis of the trajectories confirmed an overall good agreement for the overall circulation scheme between the model and observations. The northward flowing NAC represents the main import pathway of subtropical water into the subpolar North Atlantic. It splits into different branches crossing the MAR further north and then either feeding the boundary currents and contributing thus

to the Subpolar Gyre or flowing into the Nordic Seas via the Iceland Basin or the Rockall Trough. For the eastern basin, the trajectory analysis revealed rather slow undefined currents which also compares well to observations.

As part of the trajectory analysis, the amount of particles originating in the subtropics or flowing into the Nordic Seas was quantified. About 60 % of the total number of particles seeded at the 47°/48°N transect and at the MAR originate in the subtropics. Moreover, about 15 % of the particles seeded at the MAR or about 11 % of the particles seeded at the MAR and in the eastern basin flow into the Nordic Seas. Combining those numbers with the mean model-based transports calculated in this chapter yields in a transport from the MAR into the Nordic Seas of roughly 2.7 Sv (11 % of the +24.4 Sv inflow into the subpolar eastern North Atlantic). This is considerably smaller than what is found from observations (8 Sv, Østerhus et al. 2019) but might be partly owed to the too short travel time considered here. About 21.7 Sv are left for the main return flow with the Subpolar Gyre into the western basin north of 54°N. In the interior western basin, the meridional transport across 47°/48°N is about 23 Sv larger than the zonal flow across the MAR into the eastern basin. Combining this number with the return flow yields a mean transport which is in the order of the WBC related southward flow. However, further analysis and additional model-based transport calculations are necessary to fully close this circulation scheme as other in- and outflows into and from the subpolar North Atlantic, such as the EBC coming from the south, the outflow of the Nordic Seas and Baffin Bay, or the southward flow west of Flemish Cap, were not considered here.

Apart from the presented analysis which only considered the position and depth of a particle, particle densities evolving along their trajectories were studied additionally to identify major regions of water mass transformation. Three main regions were revealed in which water mass transformation takes place in the model: The Labrador Sea and Irminger Sea (including the boundary currents along the coastline of Greenland), and the region southeast and east of Iceland in the Iceland Basin and the Norwegian Sea. Studies based on observational data confirm these results (e.g. Brambilla et al., 2008a; Brambilla et al., 2008b; Petit et al., 2020; Schmitz et al., 1993) even though they rate their contribution to the source waters of the AMOC differently. Classically, the dense water formed in the Labrador Sea is considered to be one of the major sources for the deep water masses of the AMOC (Schmitz et al., 1993). In contrast to that, Petit et al. (2020), using a different definition of the deep AMOC branches, identify the Irminger Sea and the Iceland Basin as major source regions for the deep AMOC waters. Moreover, Stendardo et al. (pers. comm.) find a high spatial interannual variability for the formation regions of subpolar mode waters, which are homogenous water masses representing source waters for e.g. the LSW. This highlights the sensitivity of conclusions based on observational data which are fixed in space (e.g. mooring arrays) to their capability of capturing

a signal and also supports the findings from this study which proposed that all of the named regions are source regions for deep water formation. Also in this context, the model data thus provide a valuable tool to complement the picture obtained from observational data.

## 6 Summary and Conclusion

Long-term (1993 to 2017) transport time series at the boundary ( $47^{\circ}/48^{\circ}\text{N}$ ) between the eastern subtropical and Subpolar Gyre in the eastern North Atlantic were calculated using PIES, Argo float and shipboard CTD data and their relation to the dynamic topography measured with satellite altimetry – a method which was already successfully applied to the western basin of the North Atlantic (Rhein et al., 2019) and to the flow across the MAR in the central subpolar North Atlantic (McCarthy et al., 2020; Roessler et al., 2015). The measurements presented in this study confirmed two pathways into the eastern subpolar basin: the zonal flow across the MAR between  $47^{\circ}\text{N}$  and  $53^{\circ}\text{N}$  of  $+32.3\text{ Sv}$  of which about 60 % is of subtropical origin (McCarthy et al., 2020; Roessler et al., 2015) and a more direct pathway across  $47^{\circ}/48^{\circ}\text{N}$  coming from the south (Figure 4.9). The latter contributes with  $+9.1\text{ Sv} \pm 0.8\text{ Sv}$  about 22 % to the total flow of  $+41.4\text{ Sv}$  which is compatible to the NAC related transport of  $+41.8\text{ Sv}$  across the Greenland-Portugal OVIDE line (Daniault et al., 2016; Mercier et al., 2015). While Roessler et al. (2015) assumed that most of the eastward NAC transport is of subtropical origin, in this work, recirculated water cannot be clearly separated from water that followed the direct pathway from the subtropics into the eastern North Atlantic.

The pathways into the eastern Atlantic are significantly anticorrelated ( $R = -0.7$ ), i.e. a stronger MAR transport corresponds to a weaker transport from the south and vice versa. The transport in the interior western basin ( $42^{\circ}\text{W} - 31^{\circ}\text{W}$ ) is also significantly anticorrelated with the transport in the eastern basin between  $31^{\circ}\text{W}$  and  $23^{\circ}\text{W}$  ( $R = -0.5$ ). Additionally, both time series exhibit opposite decadal trends, i.e. the observed transport decline in the western basin is partly compensated by an increase of the northward flow east of  $31^{\circ}\text{W}$ .

The mean transport imbalance at the  $47^{\circ}/48^{\circ}\text{N}$  section from Newfoundland to  $15^{\circ}\text{W}$  was found to be  $-2.2\text{ Sv}$ . This imbalance is most likely compensated by the Eastern Boundary Current. This is encouraging for the application of the PIES / altimetry method for future AMOC estimates at this latitude.

To complement the results obtained in this study from observational data, model output of the ANHA12 configuration of the NEMO model was used. Volume transport time series based on the model velocity field were calculated for the interior eastern basin, the interior western

basin, an extended MAR section, and additionally for the WBC. The model transport time series revealed major differences between the model and observations with respect to mean transports across the different segments. While the meridional transport in the interior eastern basin ( $-2.4\text{ Sv}$ ) is significantly smaller than the one found in this study (and most of the time, in contrast to the observations, even directed southward), the meridional northward transport in the interior western basin ( $+49.5\text{ Sv}$ ) is considerably higher than the one found by Rhein et al. (2019). The model flow across the MAR ( $+26.6\text{ Sv}$ ), however, is substantially smaller than the one observed by Roessler et al. (2015), even with the model section being extended further north to capture more of the zonal inflow into the eastern basin which is located further north in the model compared to the observed flow. The total inflow into the eastern subpolar North Atlantic amounts to  $+24.2\text{ Sv}$ . Further analysis revealed that 60 % of the water at  $47^\circ/48^\circ\text{N}$  and the MAR originates in the subtropics and about 11 % of the water crossing MAR and the  $47^\circ/48^\circ\text{N}$  transect in the eastern basin flows into the Nordic Seas even though the second number presumably is too small due to the rather short travel time of five years analyzed here.

Additionally calculated correlation coefficients comparing the individual model time series to each other support the suggested weaker coupling of the western and eastern basin in the model found already from the comparison of the mean volume transports: Only between the interior western basin transport and the WBC as well as between the zonal MAR transport and the interior eastern basin transport significant negative correlations are found at a 95 % confidence level.

From the qualitative analysis of particle trajectories seeded at the  $47^\circ/48^\circ\text{N}$  and MAR sections, an overall good agreement between the model flow field and the observational data was found. Tracking the densities of the particles revealed, moreover, three major regions for water mass transformation in the model: The Labrador Sea and Irminger Sea including the boundary currents and the regions southeast and east of Iceland which is in accordance of what is proposed by literature (e.g. Brambilla et al., 2008a).

Even though the overall circulation pattern and the major pathways of the NAC in the model are very similar to the observations, the transport time series, corresponding correlation coefficients, and the trajectory analysis revealed also significant differences between the model and observational flow field. While in the model, the flow in the interior western basin is strongly coupled to the flow with the WBC, the interior western and eastern basin are so only weakly. Moreover, the meridional flow in the eastern basin is smaller in the model and sometimes even directed opposite to the observations. This points out that complementing observational data with model data is a difficult process which has to be carried out carefully and requires thorough testing of the accuracy of the specific model for each individual application and might not

---

be feasible in all cases. However, as observational data is often very much limited in space and time, for some applications, as for example in the discussed case of identifying regions where water mass transformation takes place, the use of model data seems to be an appropriate and promising additional tool. Furthermore, another study shows encouraging first results also for the complementation of the transport time series east of 15°W with high resolution model data from another ocean model (Wett, pers. comm.).



## 7 Outlook

To further investigate the circulation in the subpolar North Atlantic beyond the research questions of this thesis, several additional aspects could be examined. Some ideas for this are presented in the following including the observational part of this study as well as the model part.

To fully close the budget concerning the meridional exchange of water across the  $47^{\circ}/48^{\circ}\text{N}$  transect calculated from observational data, transport time series east of  $15^{\circ}\text{W}$  are needed (Moritz et al., in review). With a fully closed budget, estimations concerning the strength of the overturning at these latitudes are possible as well which will be subject of a future study (Wett, pers. comm.). The same is valid for the model-based circulation scheme for which also additional information related to further inflow and outflow into and from the subpolar North Atlantic is needed in order to provide a closed budget at  $47^{\circ}/48^{\circ}\text{N}$  and further north.

As this study has revealed some substantial differences between flow paths found from observations and in the model, for acquiring certain information such as volume transports across a specific section, it might be necessary not only to look at latitudinal and longitudinal bounds from an observational point of view, but to adjust the latitudinal and longitudinal bounds according to the model characteristics to better represent the study area in the model. In the specific case presented here, the use of a higher resolution model run, or a high resolution nest upstream of the region of interest, shows furthermore also promising results in terms of a more realistic representation of the circulation pattern in this region (Myers et al., pers. comm. Wett, pers. comm.).

Generally, the use of model data opens up a variety of possibilities for many additional studies. Especially of interest with respect to the results obtained in this work would be the further exploitation of the trajectories calculated with the ARIANE tool. On the one hand, it is possible to use these data also for additional quantitative studies, for example to directly calculate volume transports. Complementing the already existing time series with transport values describing the exchange of water between the different boxes defined in this study would thus be one interesting aspect allowing further insights into the model circulation. Moreover, as the debate about the importance of the different deep water formation regions in terms of their

contribution to the AMOC source waters is still ongoing, further examination of the process of water mass transformation from a model perspective would be useful, especially since measurement arrays often are very limited in space and time and may not capture a signal which is rather confined in space such as for example deep convection occurring on scales of 1 km (Marshall et al., 1999). Apart from that, previous studies have shown a dependence of the flow with the NAC on the North Atlantic Oscillation (NAO) (e.g. Breckenfelder et al., 2017; Roessler et al., 2015). From this work, a bias concerning the different regions for water mass transformation depending on the initial starting position of the tracked particles was inferred. Examining the process of water mass transformation also in terms of its relation with the different NAO phases seems therefore another plausible next step.

## A Appendix

The figures presented in the appendix of this work support the results of the ANHA12 model data and Lagrangian trajectory analysis and might also provide ideas for future studies. The detailed analysis of the figures, however, is beyond the scope of this work.

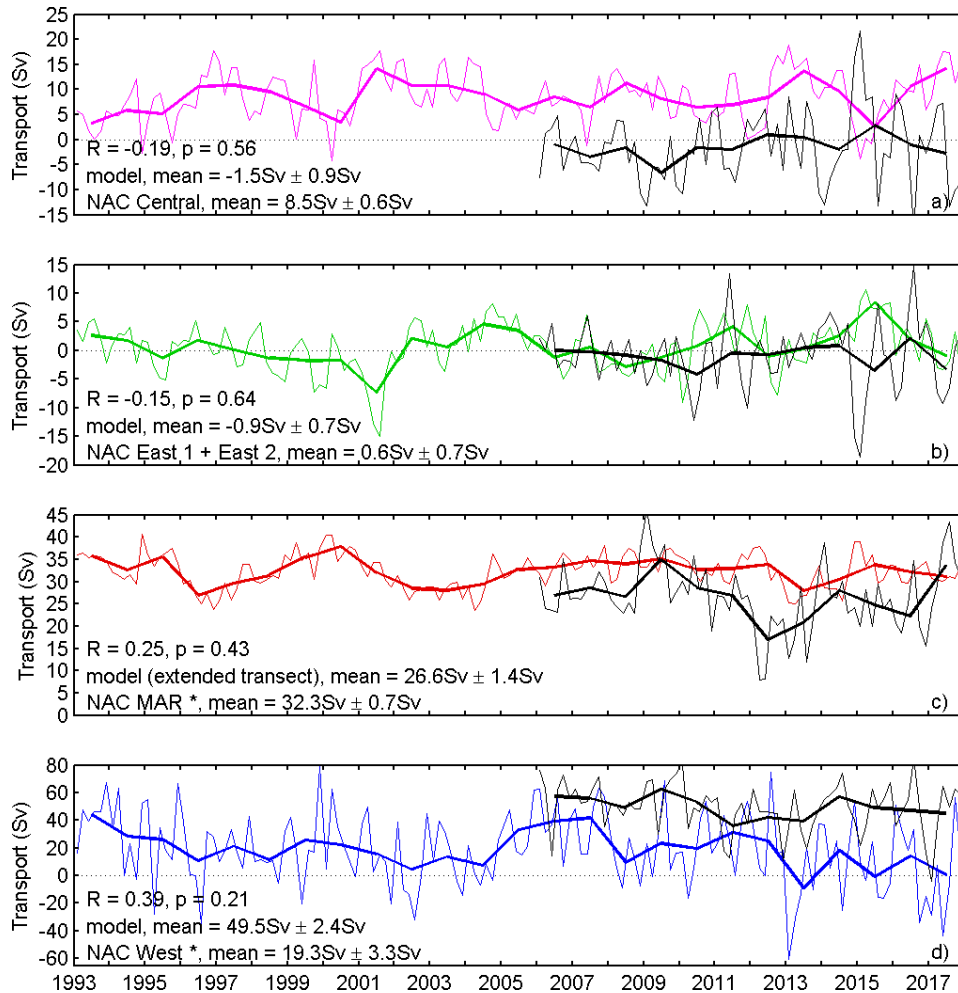
Figure A.1 shows the volume transport comparison between model and observational data as discussed in this work similar to Figure 5.4 with the transport across the *NAC Central* segment being separated from the transport across the *NAC East 1* and *NAC East 2* segments.

Figure A.2 shows the trajectories of particles (tracked in forward mode of the ARIANE tool) that have been seeded in box 1 and crossed (a) the Charlie-Gibbs-Fracture-Zone (CGFZ) and (b) the Faraday-Fracture-Zone (FFZ) compared to trajectories of particles that did not cross the fracture zones. Figure A.3 shows the trajectories of particles (tracked in forward mode) that have been seeded in box 1 and crossed the Maxwell-Fracture-Zone (MFZ) further downstream on their pathway.

Figure A.4 shows the probability of particles seeded in the boxes 3 and 4 (tracked for an extended time span of ten years in backward mode) to cross grid cells of the horizontal  $1/4^\circ \times 1/4^\circ$  mesh grid. The extended time span of ten years was chosen to find out whether Mediterranean Outflow Water plays a substantial role for water crossing the boxes 3 and 4.

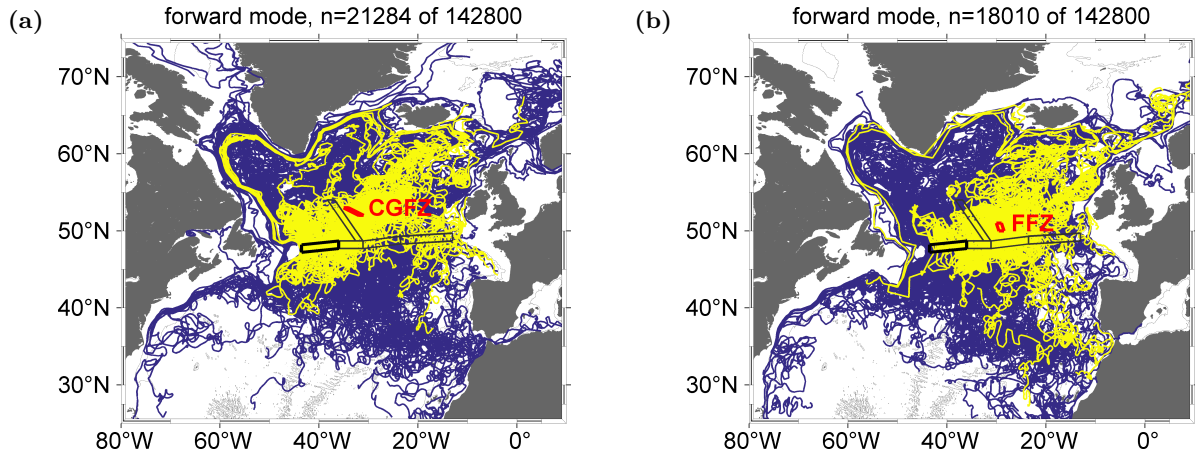
Figure A.5 shows the percentages for the exchange of particles between two boxes relative to the total number of particles seeded in the boxes as in Figure 5.17. Figure A.6 to A.10 show the corresponding trajectories of particles. In these figures, only the second box that was crossed by the particles was considered and it is possible that the particles cross other boxes further downstream on their pathway (forward mode) or that they have crossed other boxes before (backward mode). Only those routes are shown for which the amount of particles following the route is higher than 5% in at least one of the directions.

Figure A.11 shows the percentages of particles following the different major routes relative to the total number of particles in the initial boxes. Figure A.11 to A.12 show the corresponding trajectories of particles for routes ending either in box 3 or 4 to illustrate major pathways into the eastern North Atlantic. In these figures, only those routes are shown for which the amount of particles following the route is higher than 5%.



**Figure A.1:** Bi-monthly (thin) and annual mean (bold) transports at the NOAC site from observations (1993 - 2017) and model output (2006 - 2017). PIES transports are shown in colors, model transports in black. Transport time series are shown for the interior eastern basin across the *NAC Central* segment between BP12 at about  $31^\circ\text{W}$  and BP34 at about  $23^\circ\text{W}$ , across the *NAC East 1* and *NAC East 2* segments between BP34 and BP32 at about  $15^\circ\text{W}$ , for the transport across the Mid-Atlantic Ridge between BP12 at about  $47^\circ\text{N}$  and BP15 at about  $53^\circ\text{N}$  (observations, update from Roessler et al. 2015) and between BP12 at about  $47^\circ\text{N}$  and approximately  $54^\circ\text{N}$  (model output), and for the meridional flow in the interior western basin between BP31 at about  $42^\circ\text{W}$  and BP12 at about  $31^\circ\text{W}$  (Rhein et al., 2019). Numbers indicate mean transport and standard error of the mean for the respective transport section.

\* Values from Rhein et al. (2019), note: time series are only shown until end of 2017 but in the calculation of the mean values and standard errors also data from the year 2018 are used.



**Figure A.2:** Trajectories of particles (tracked in forward mode for a maximum of five years) that have been seeded in box 1 and crossed (a) the Charlie-Gibbs-Fracture-Zone (CGFZ) and (b) Faraday-Fracture-Zone (FFZ) afterwards compared to trajectories of particles that did not cross the fracture zones. Gray contour lines show the bathymetry every 2000m. The different color separate particles crossing the fracture zones (yellow) from particles that did not cross the fracture zones (blue). The horizontal extent of the different boxes is indicated by black lines, with the bold line highlighting box 1. Note: only every 500th trajectory is shown.

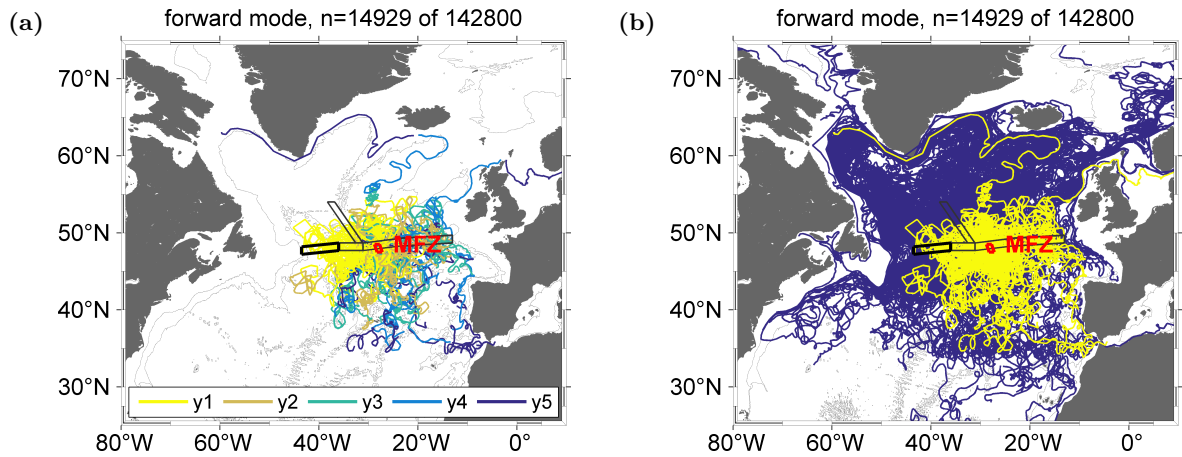


**Figure A.3:** Trajectories of particles (tracked in forward mode) that have been seeded in box 1 and crossed (a) the Maxwell-Fracture-Zone (MFZ) and (b) particles which crossed the MFZ compared to trajectories of particles that did not cross the MFZ. Gray contour lines show the bathymetry every 2000m. The different colors denote (a) the different years of the five years (maximum) travel time and (b) separate particles crossing the MFZ (yellow) from particles that did not cross the MFZ (blue). The horizontal extent of the different boxes is indicated by black lines, with the bold line highlighting box 1. Note: only every 500th trajectory is shown.

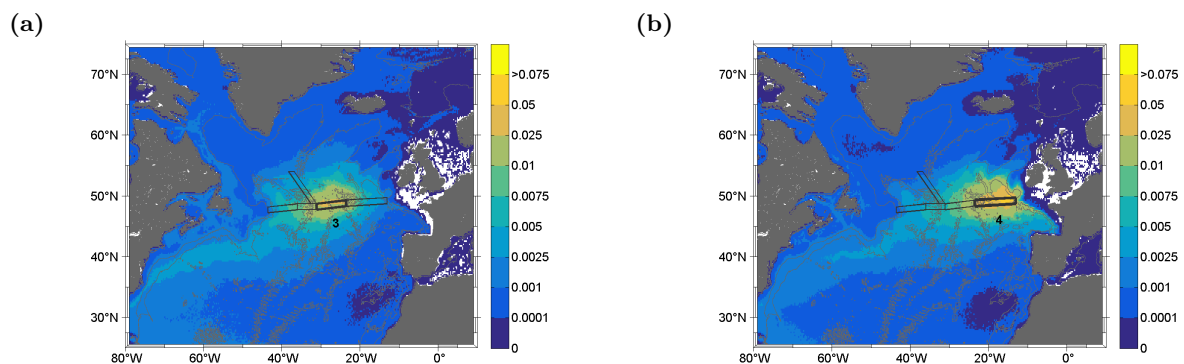


**Figure A.4:** Probabilities of particles seeded in box 3 (a) or 4 (b), tracked in backward mode for ten years, to cross grid cells of a horizontal mesh with a  $1/4^\circ \times 1/4^\circ$  spatial resolution. The extended time span of ten years was chosen to find out whether Mediterranean Outflow Water plays a substantial role for water crossing the boxes 3 and 4. Gray contour lines show the bathymetry every 2000m. Numbers are in percent (counts of particles that crossed the grid cell relative to total number of counts). The horizontal extent of the different boxes is indicated by black lines, with the bold lines highlighting box 3 and 4.

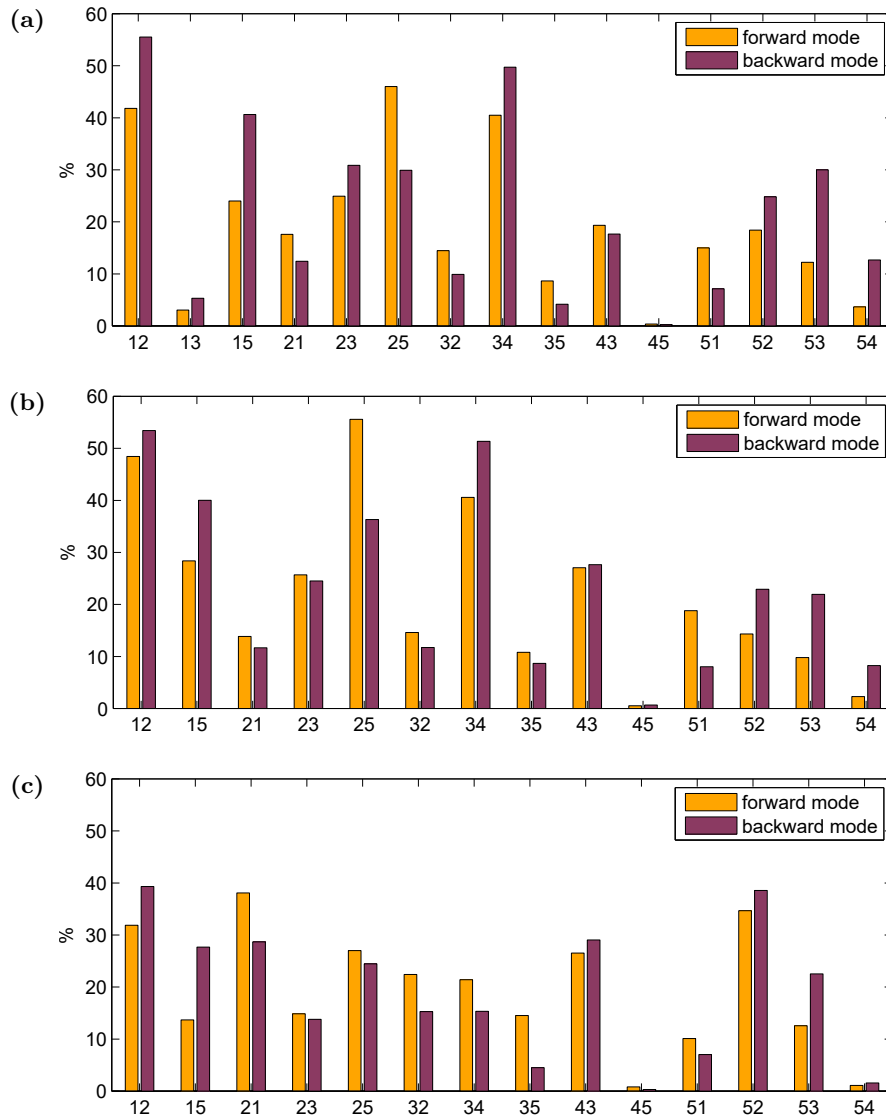


**Figure A.5:** Bar plots illustrating the exchange of particles between two boxes. Numbers represent percentages of particles following the different routes relative to the total number of particles in the initial boxes as in Figure 5.17. Panel (a) shows the percentages for the forward and backward mode considering particles seeded throughout the whole water column, panel (b) shows the percentages for particles seeded into the upper layers (200-900m), and panel (c) shows the percentages for particles seeded in the lower layers (below 1100m). Only those routes are shown for which the amount of particles following the route is higher than 5%.

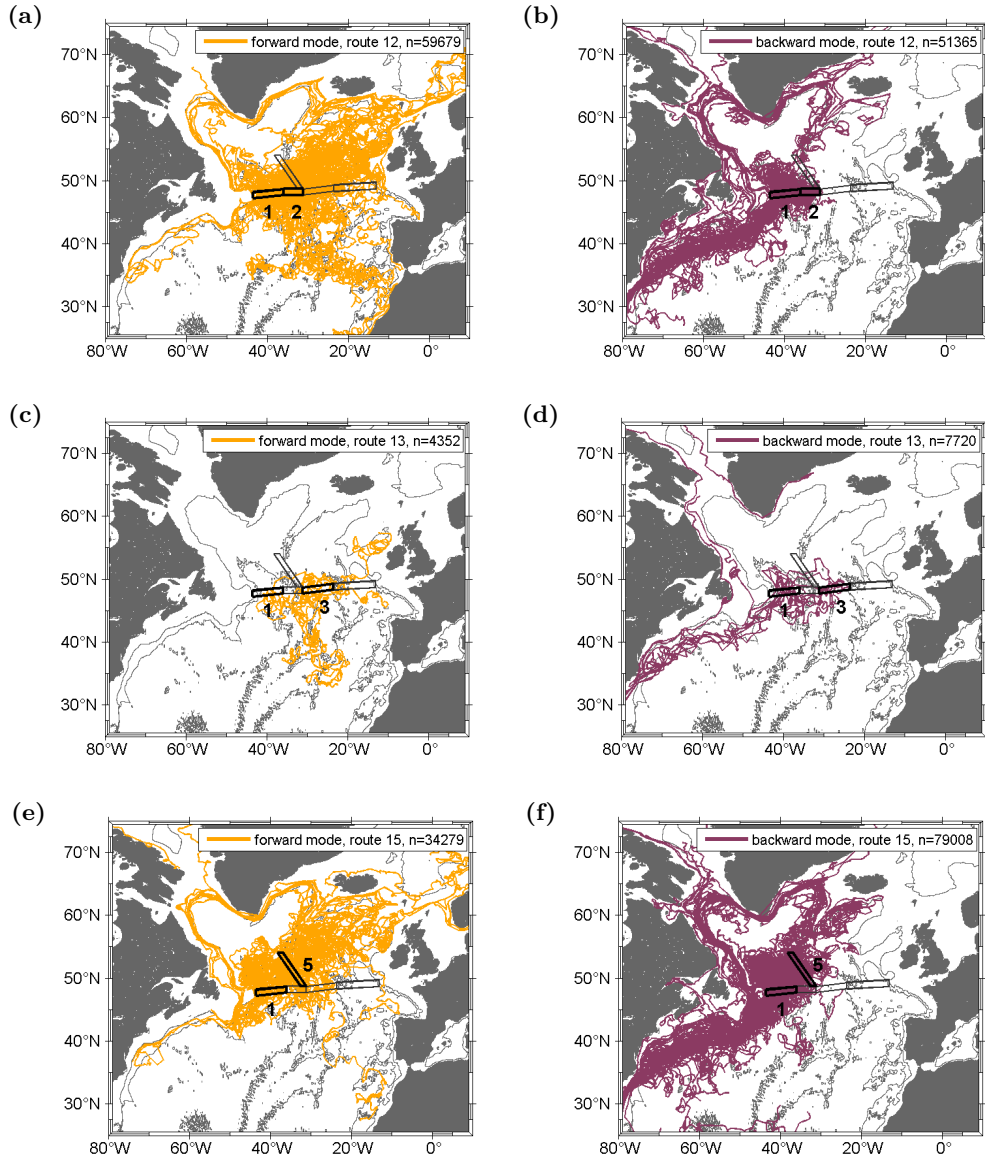


**Figure A.6:** Trajectories of particles seeded throughout the whole water column. Panel (a) shows trajectories of particles seeded in box 1, crossing box 2 afterwards, panel (b) shows trajectories of particles seeded in box 2, crossing box 1 before. Panel (c) shows trajectories of particles seeded in box 1, crossing box 3 afterwards, panel (d) shows trajectories of particles seeded in box 3, crossing box 1 before. Panel (e) shows trajectories of particles seeded in box 1, crossing box 5 afterwards, panel (f) shows trajectories of particles seeded in box 5, crossing box 1 before. Gray contour lines show the bathymetry every 2000m. n is the total number of particles following the indicated routes. The horizontal extent of the different boxes is indicated by black lines. Note: only every 1000th trajectory is shown.

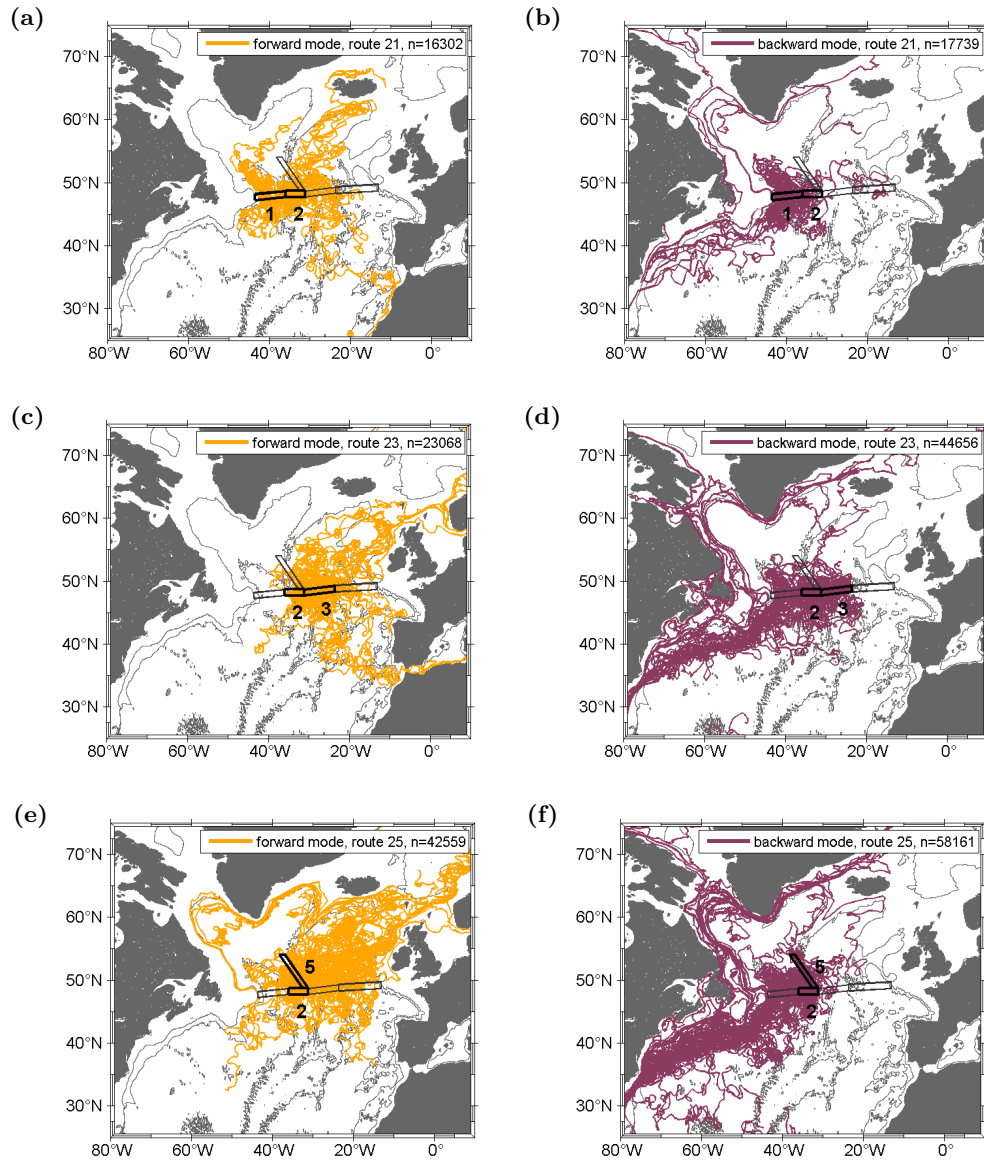


**Figure A.7:** Trajectories of particles seeded throughout the whole water column. Panel (a) shows trajectories of particles seeded in box 2, crossing box 1 afterwards, panel (b) shows trajectories of particles seeded in box 1, crossing box 2 before. Panel (c) shows trajectories of particles seeded in box 2, crossing box 3 afterwards, panel (d) shows trajectories of particles seeded in box 3, crossing box 2 before. Panel (e) shows trajectories of particles seeded in box 2, crossing box 5 afterwards, panel (f) shows trajectories of particles seeded in box 5, crossing box 2 before. Gray contour lines show the bathymetry every 2000m.  $n$  is the total number of particles following the indicated routes. The horizontal extent of the different boxes is indicated by black lines. Note: only every 1000th trajectory is shown.

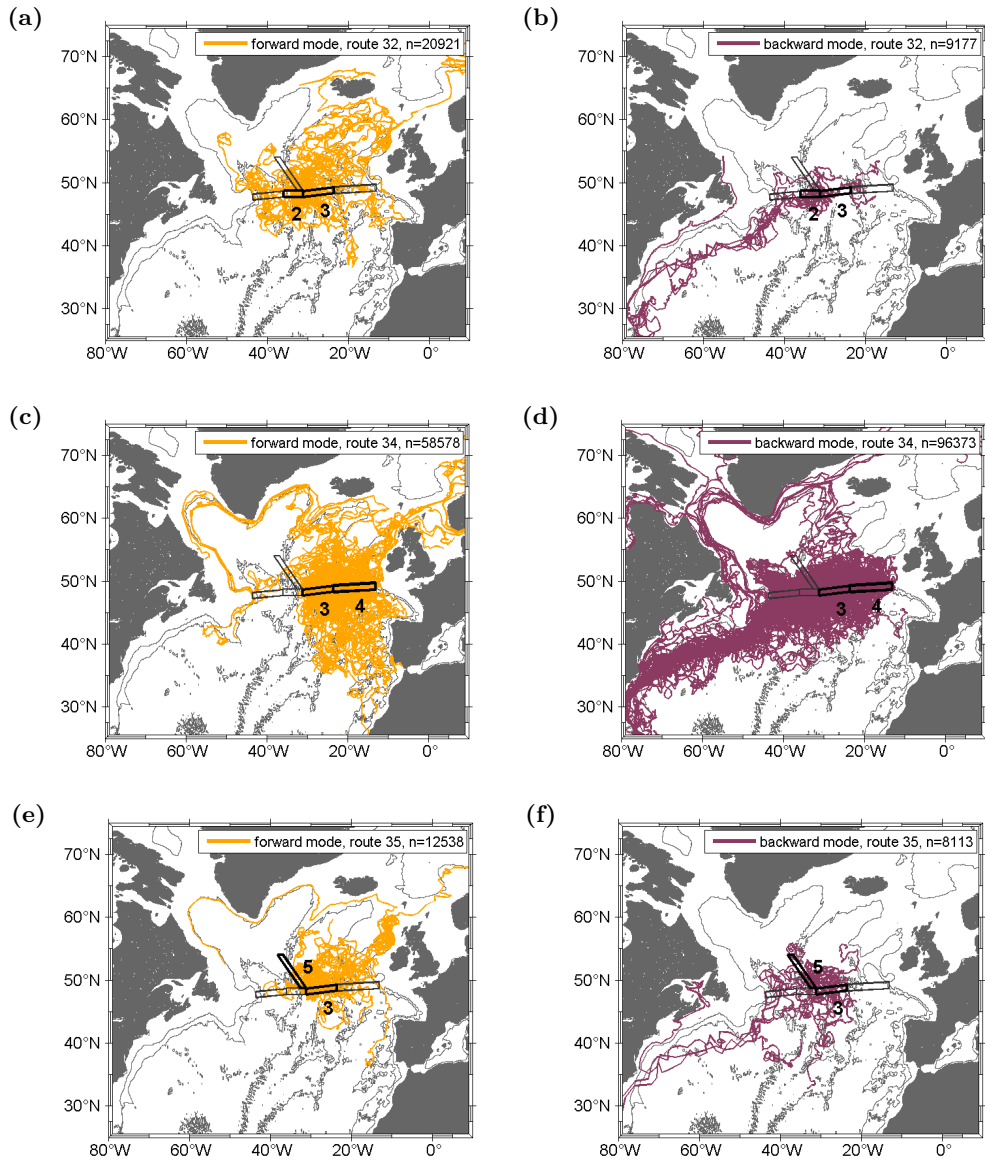


**Figure A.8:** Trajectories of particles seeded throughout the whole water column. Panel (a) shows trajectories of particles seeded in box 3, crossing box 2 afterwards, panel (b) shows trajectories of particles seeded in box 2, crossing box 3 before. Panel (c) shows trajectories of particles seeded in box 3, crossing box 4 afterwards, panel (d) shows trajectories of particles seeded in box 4, crossing box 3 before. Panel (e) shows trajectories of particles seeded in box 3, crossing box 5 afterwards, panel (f) shows trajectories of particles seeded in box 5, crossing box 3 before. Gray contour lines show the bathymetry every 2000m. n is the total number of particles following the indicated routes. The horizontal extent of the different boxes is indicated by black lines. Note: only every 1000th trajectory is shown.

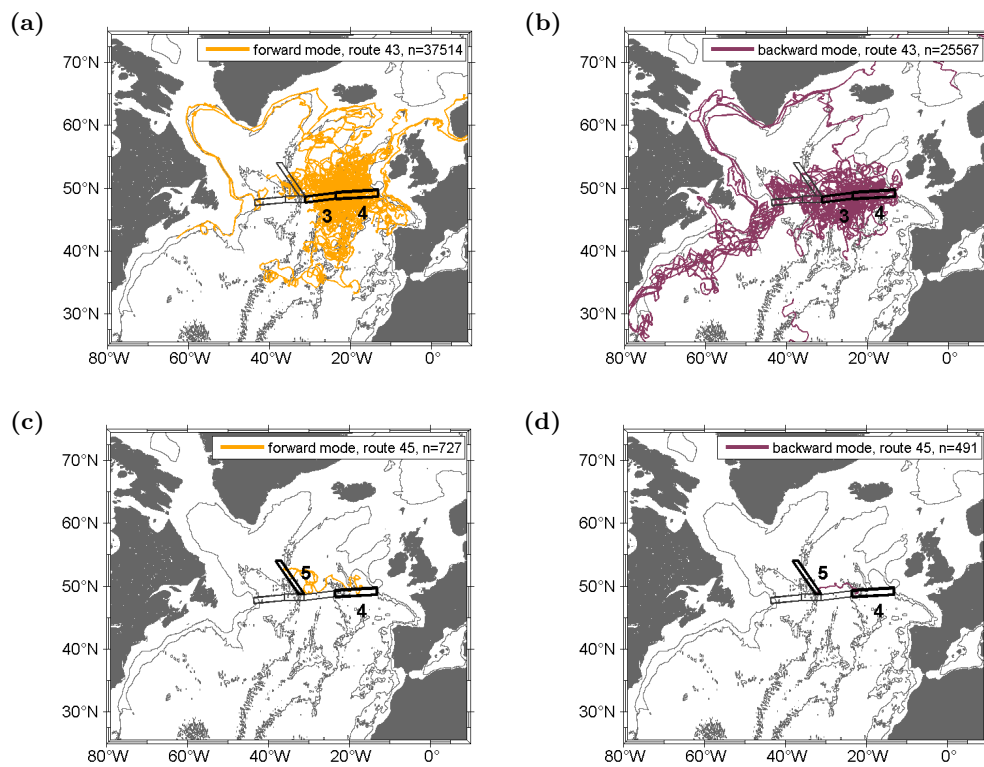


**Figure A.9:** Trajectories of particles seeded throughout the whole water column. Panel (a) shows trajectories of particles seeded in box 4, crossing box 3 afterwards, panel (b) shows trajectories of particles seeded in box 3, crossing box 4 before. Panel (c) shows trajectories of particles seeded in box 4, crossing box 5 afterwards, panel (d) shows trajectories of particles seeded in box 5, crossing box 4 before. Gray contour lines show the bathymetry every 2000m.  $n$  is the total number of particles following the indicated routes. The horizontal extent of the different boxes is indicated by black lines. Note: only every 1000th trajectory is shown.

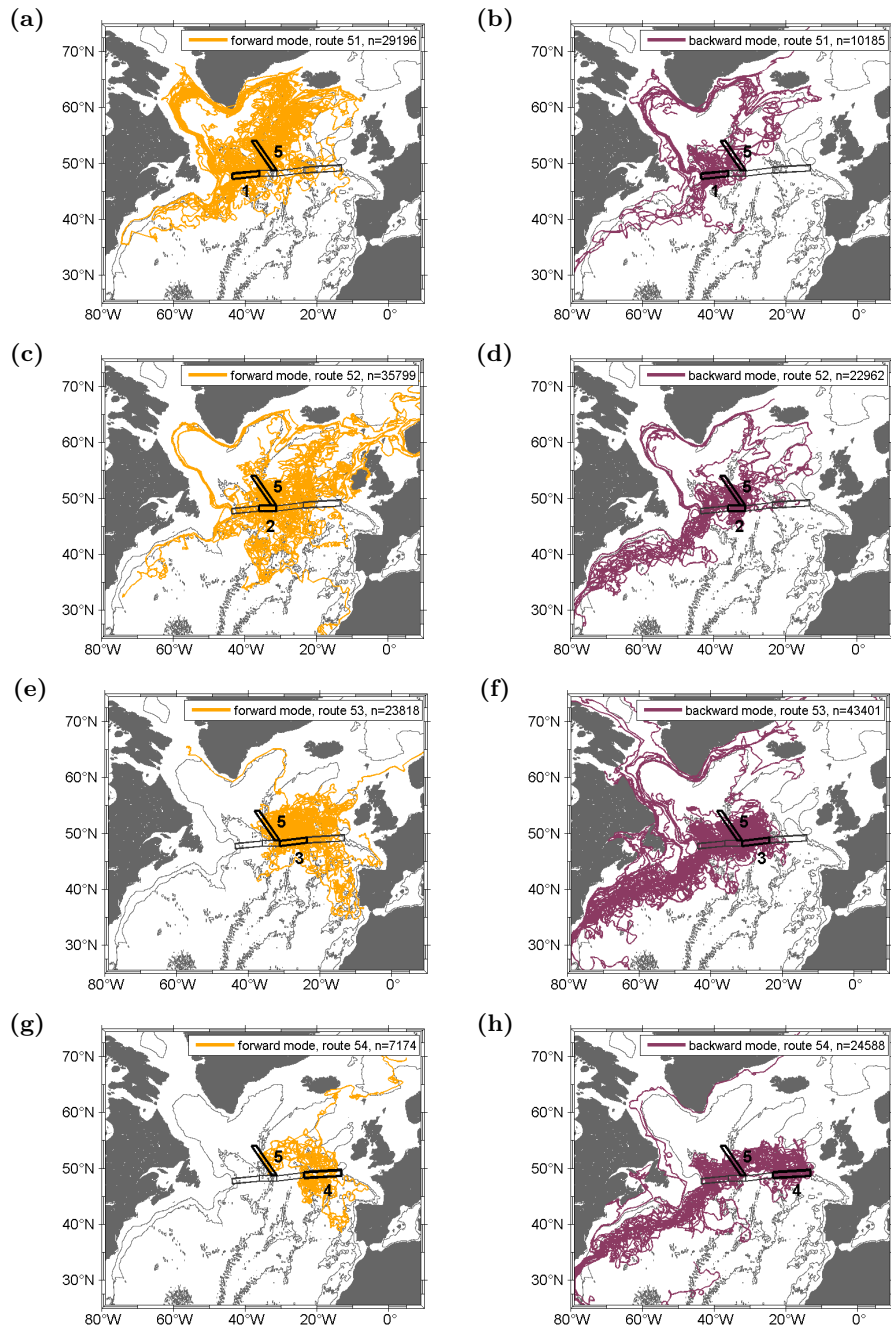


**Figure A.10:** Trajectories of particles seeded throughout the whole water column. Panel (a) shows trajectories of particles seeded in box 5, crossing box 1 afterwards, panel (b) shows trajectories of particles seeded in box 1, crossing box 5 before. Panel (c) shows trajectories of particles seeded in box 5, crossing box 2 afterwards, panel (d) shows trajectories of particles seeded in box 2, crossing box 5 before. Panel (e) shows trajectories of particles seeded in box 5, crossing box 3 afterwards, panel (f) shows trajectories of particles seeded in box 3, crossing box 5 before. Panel (g) shows trajectories of particles seeded in box 5, crossing box 4 afterwards, panel (h) shows trajectories of particles seeded in box 4, crossing box 5 before. Gray contour lines show the bathymetry every 2000m. n is the total number of particles following the indicated routes. The horizontal extent of the different boxes is indicated by black lines. Note: only every 1000th trajectory is shown.

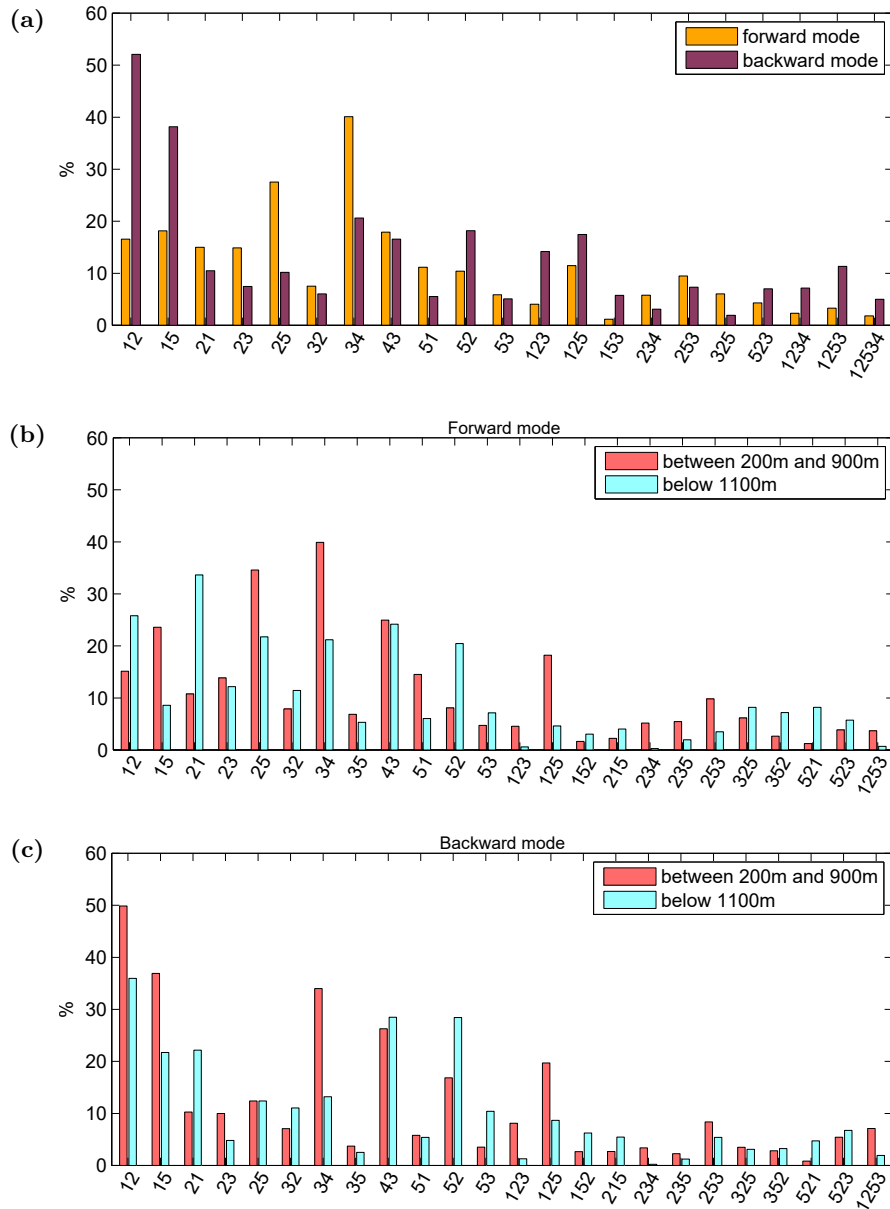


**Figure A.11:** Bar plots illustrating the major routes of particles. Numbers represent percentages of particles following the different routes relative to the total number of particles in the initial boxes. Panel (a) shows the percentages for the forward and backward mode considering particles seeded throughout the whole water column, panel (b) shows the percentages for particles tracked in the forward mode and treats particles seeded into the upper layers (200-900m), and lower layers (below 1100m) of the water column separately, and panel (c) shows the percentages for particles tracked in the backward mode and treats particles seeded into the upper layers (200-900m), and lower layers (below 1100m) of the water column separately. Only those routes are shown for which the amount of particles following the route is higher than 5% in one of the cases. Note: each trajectory is counted only once, i.e. all particles following the route '123' are neither counted for route '12' nor for route '13' and particles are traced for a maximum of five years.

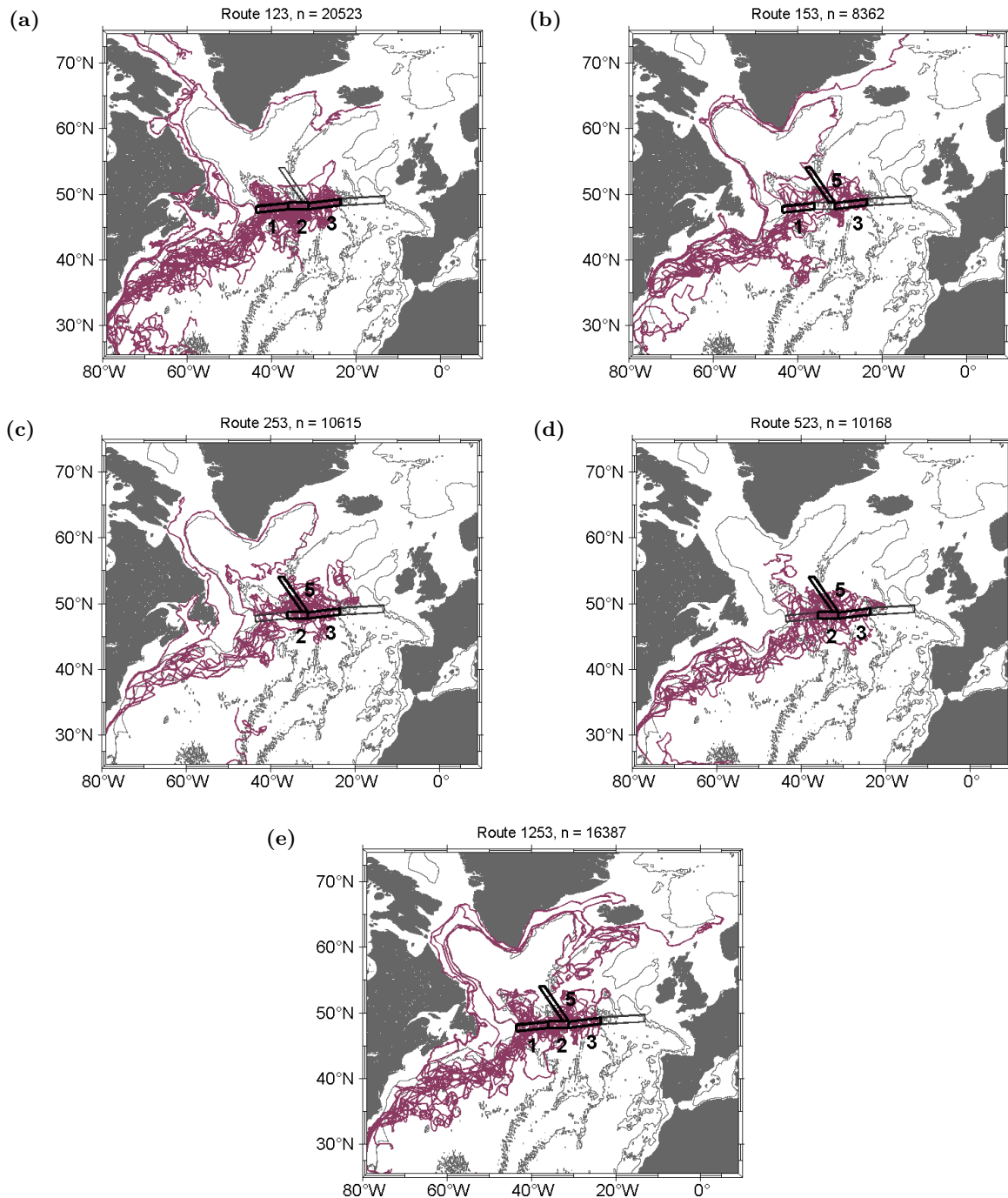


**Figure A.12:** Major routes from Figure A.11 (major = more than 5% of particles followed the route) of particles ending in box 3 (tracked in backward mode). Every 1000th trajectory is plotted.

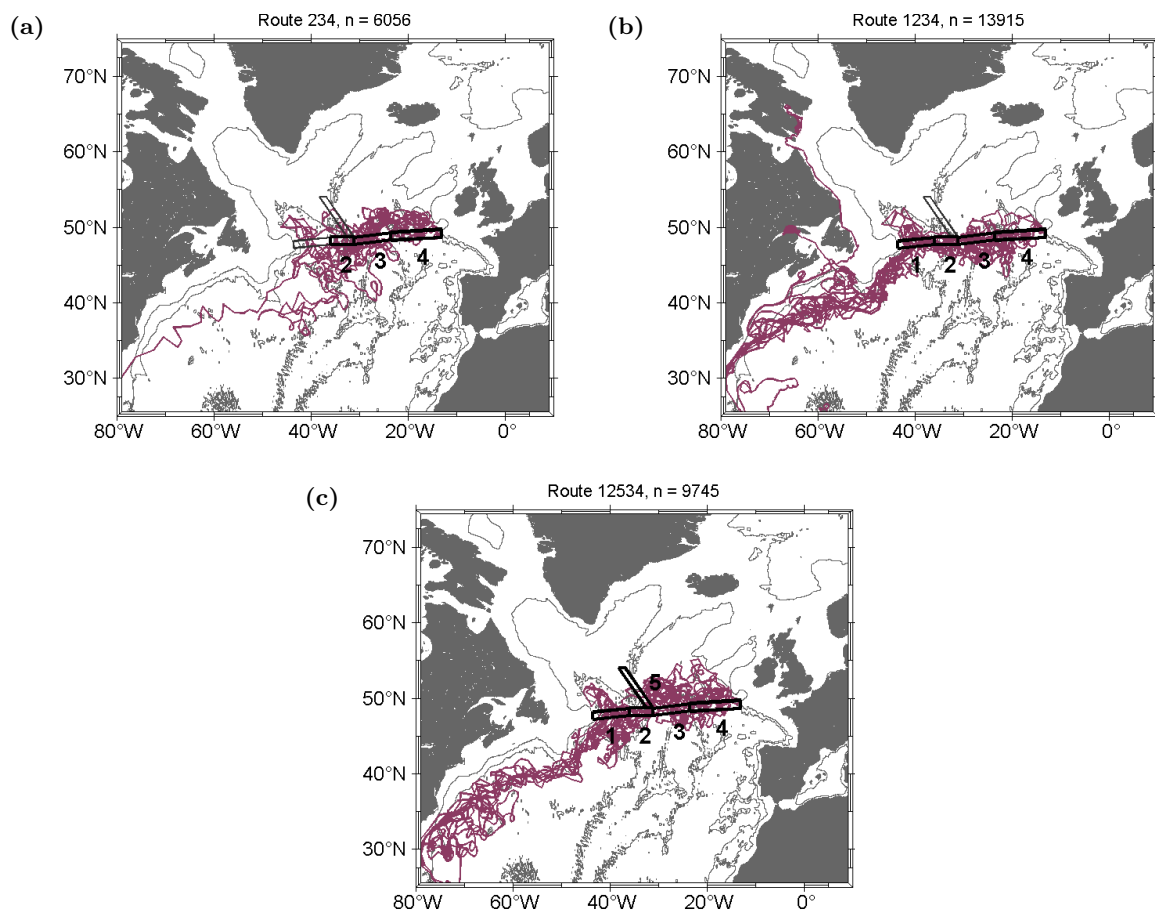


**Figure A.13:** Major routes from Figure A.11 (major = more than 5% of particles followed the route) of particles ending in box 4 (tracked in backward mode). Every 1000th trajectory is plotted.



## Bibliography

- Adcroft, A., C. Hill, and J. Marshall (1997). 'Representation of topography by shaved cells in a height coordinate ocean model'. In: *Monthly Weather Review* 125.9, pp. 2293–2315. DOI: 10.1175/1520-0493(1997)125<2293:R0TBSC>2.0.CO;2.
- Amante, C. and B. W. Eakins (2009). 'ETOPO1 1 Arc-Minute Global Relief Model: Procedures, Data Sources and Analysis'. In: *NOAA Technical Memorandum NESDIS NGDC-24. National Geophysical Data Center, NOAA*, [access date: 29 Nov 2018]. DOI: 10.7289/V5C8276M.
- Argo (2002). 'Argo float data and metadata from Global Data Assembly Centre (Argo GDAC). SEANOE.' In: DOI: 10.17882/42182.
- Asselin, R. (1972). 'Frequency filter for time integrations'. In: *Monthly Weather Review* 100.6, pp. 487–490. DOI: 10.1175/1520-0493(1972)100<0487:FFFTI>2.3.CO;2.
- Bamber, J., M. van Den Broeke, J. Ettema, J. Lenaerts, and E. Rignot (2012). 'Recent large increases in freshwater fluxes from Greenland into the North Atlantic'. In: *Geophysical Research Letters* 39.19. DOI: 10.1029/2012GL052552.
- Bayley, G. V. and J. M. Hammersley (1946). 'The "Effective" Number of Independent Observations in an Autocorrelated Time Series'. In: *Supplement to the Journal of the Royal Statistical Society* 8.2, pp. 184–197. DOI: 10.2307/2983560.
- Bernard, B., G. Madec, T. Penduff, J. Molines, A. Treguier, J. Le Sommer, A. Beckmann, A. Biastoch, C. Böning, J. Dengg, C. Derval, E. Durand, S. Gulev, E. Remy, C. Talandier, Theetten S., Maltrud M., J. McClean, and B. De Cuevas (2006). 'Impact of partial steps and momentum advection schemes in a global ocean circulation model at eddy-permitting resolution'. In: *Ocean dynamics* 56.5, pp. 543–567. DOI: 10.1007/s10236-006-0082-1.
- Bi, D., W. F. Budd, A. C. Hirst, and X. Wu (2001). 'Collapse and reorganisation of the Southern Ocean overturning under global warming in a coupled model'. In: *Geophysical Research Letters* 28.20, pp. 3927–3930. DOI: 10.1029/2001GL013705.
- Blanke, B., M. Arhan, G. Madec, and S. Roche (1999). 'Warm water paths in the equatorial Atlantic as diagnosed with a general circulation model'. In: *Journal of Physical Oceanography* 29.11, pp. 2753–2768. DOI: 10.1175/1520-0485(1999)029<2753:WWPITE>2.0.CO;2.

- Blanke, B. and S. Raynaud (1997). ‘Kinematics of the Pacific Equatorial Undercurrent: An Eulerian and Lagrangian Approach from GCM Results’. In: *Journal of Physical Oceanography* 27.6, pp. 1038–1053. DOI: 10.1175/1520-0485(1997)027<1038:KOTPEU>2.0.CO;2.
- Bower, A. S. and W.-J. von Appen (2008). ‘Interannual Variability in the Pathways of the North Atlantic Current over the Mid-Atlantic Ridge and the Impact of Topography’. In: *Journal of Physical Oceanography* 38.1, pp. 104–120. DOI: 10.1175/2007JP03686.1.
- Bower, A. S., B. Le Cann, T. Rossby, W. Zenk, J. Gould, K. Speer, P. L. Richardson, M. D. Prater, and H. M. Zhang (2002). ‘Directly measured mid-depth circulation in the northeastern North Atlantic Ocean’. In: *Nature* 419.6907, pp. 603–607. DOI: 10.1038/nature01078.
- Bower, A. S., M. S. Lozier, S. F. Gary, and C. W. Böning (2009). ‘Interior pathways of the North Atlantic meridional overturning circulation’. In: *Nature* 459.7244, pp. 243–247. DOI: 10.1038/nature07979.
- Brambilla, E. and L. D. Talley (2008a). ‘Subpolar Mode Water in the northeastern Atlantic: 1. Averaged properties and mean circulation’. In: *Journal of Geophysical Research: Oceans* 113.C4. DOI: 10.1029/2006JC004062.
- Brambilla, E., L. D. Talley, and P. E. Robbins (2008b). ‘Subpolar mode water in the northeastern Atlantic: 2. Origin and transformation’. In: *Journal of Geophysical Research: Oceans* 113.C4. DOI: 10.1029/2006JC004063.
- Breckenfelder, T., M. Rhein, A. Roessler, C. W. Böning, A. Biastoch, E. Behrens, and C. Mertens (2017). ‘Flow paths and variability of the North Atlantic Current: A comparison of observations and a high-resolution model’. In: *Journal of Geophysical Research: Oceans* 122, pp. 2686–2708. DOI: 10.1002/2016JC012444.
- Broecker, W. S. (1991). ‘The great ocean conveyor’. In: *Oceanography* 4.2, pp. 79–89. DOI: 10.5670/oceanog.1991.07.
- Buckley, M. W. and J. Marshall (2016). ‘Observations, inferences, and mechanisms of the Atlantic Meridional Overturning Circulation: A review’. In: *Reviews of Geophysics* 54.1, pp. 5–63. DOI: 10.1002/2015RG000493.
- Chaplin, G. F. and D. R. Watts (1984). ‘Inverted Echo Sounder Development’. In: *Oceans Conference Record (IEEE)*, pp. 249–253. DOI: 10.1109/OCEANS.1984.1152347.
- Chidichimo, M. P., K. A. Donohue, D. R. Watts, and K. L. Tracey (2014). ‘Baroclinic Transport Time Series of the Antarctic Circumpolar Current Measured in Drake Passage’. In: *Journal of Physical Oceanography* 44.7, pp. 1829–1853. DOI: 10.1175/JPO-D-13-071.1.
- Courtois, P., Y. Garcia-Quintana, X. Hu, and P. G. Myers (2020). ‘Kinematic Subduction Rate Of Labrador Sea Water From an Eddy-Permitting Numerical Model’. In: *Journal of Geophysical Research: Oceans* 125.7. DOI: 10.1029/2019JC015475.

- Dai, A., T. Qian, K. E. Trenberth, and J. D. Milliman (2009). ‘Changes in continental fresh-water discharge from 1948 to 2004’. In: *Journal of climate* 22.10, pp. 2773–2792. DOI: 10.1175/2008JCLI2592.1.
- Daniault, N., H. Mercier, P. Lherminier, A. Sarafanov, A. Falina, P. Zunino, F. F. Pérez, A. F. Ríos, B. Ferron, T. Huck, V. Thierry, and S. Gladyshev (2016). ‘The northern North Atlantic Ocean mean circulation in the early 21st century’. In: *Progress in Oceanography* 146, pp. 142–158. DOI: 10.1016/j.pocean.2016.06.007.
- Del Grosso, V. A. (1974). ‘New equation for the speed of sound in natural waters (with comparisons to other equations)’. In: *Journal of the Acoustical Society of America* 56.4, pp. 1084–1091. DOI: 10.1121/1.1903388.
- Eldevik, T., J. E. Ø. Nilsen, D. Iovino, K. A. Olsson, A. B. Sandø, and H. Drange (2009). ‘Observed sources and variability of Nordic seas overflow’. In: *Nature Geoscience* 2.6, pp. 406–410. DOI: 10.1038/ngeo518.
- Ellett, D. J. and J. H. A. Martin (1973). ‘The physical and chemical oceanography of the Rockall channel’. In: *Deep Sea Research and Oceanographic Abstracts* 20.7. DOI: 10.1016/0011-7471(73)90030-2.
- Fichefet, T. and M. A. M. Maqueda (1997). ‘Sensitivity of a global sea ice model to the treatment of ice thermodynamics and dynamics’. In: *Journal of Geophysical Research: Oceans* 102.C6, pp. 12609–12646. DOI: 10.1029/97JC00480.
- Frajka-Williams, E., I. J. Ansorge, J. Baehr, H. L. Bryden, M. P. Chidichimo, S. A. Cunningham, G. Danabasoglu, S. Dong, K. A. Donohue, S. Elipot, P. Heimbach, N. P. Holliday, R. Hummels, L. C. Jackson, J. Karstensen, M. Lankhorst, I. A. Le Bras, M. S. Lozier, E. L. McDonagh, C. S. Meinen, H. Mercier, B. I. Moat, R. C. Perez, C. G. Piecuch, M. Rhein, M. A. Srokosz, K. E. Trenberth, S. Bacon, G. Forget, G. Goni, D. Kieke, J. Koelling, T. Lamont, G. D. McCarthy, C. Mertens, U. Send, D. A. Smeed, S. Speich, M. van den Berg, D. Volkov, and C. Wilson (2019). ‘Atlantic Meridional Overturning Circulation: Observed Transport and Variability’. In: *Frontiers in Marine Science* 6.260. DOI: 10.3389/fmars.2019.00260.
- García-Ibáñez, M. I., P. C. Pardo, L. I. Carracedo, H. Mercier, P. Lherminier, A. F. Ríos, and F. F. Pérez (2015). ‘Structure, transports and transformations of the water masses in the Atlantic Subpolar Gyre’. In: *Progress in Oceanography* 135, pp. 18–36. DOI: 10.1016/j.pocean.2015.03.009.
- Garcia-Quintana, Y., P. Courtois, X. Hu, C. Pennelly, D. Kieke, and P. G. Myers (2019). ‘Sensitivity of Labrador Sea Water formation to changes in model resolution, atmospheric forcing, and freshwater input’. In: *Journal of Geophysical Research: Oceans* 124.3, pp. 2126–2152. DOI: 10.1029/2018JC014459.

- Garrett, C. and B. Petrie (1981). ‘Dynamical Aspects of the Flow Through the Strait of Belle Isle’. In: *Journal of Physical Oceanography* 11, pp. 376–393. DOI: 10.1175/1520-0485(1981)011<0376:DAOTFT>2.0.CO;2.
- Gerdes, R., W. Hurlin, and S. M. Griffies (2006). ‘Sensitivity of a global ocean model to increased run-off from Greenland’. In: *Ocean Modelling* 12.3-4, pp. 416–435. DOI: 10.1016/j.ocemod.2005.08.003.
- González-Pola, C., K. M. H. Larsen, P. Fratantoni, and A. Beszczynska-Möller (eds.) (2019). *ICES Report on Ocean Climate 2018. ICES Cooperative Research Report No. 349*. Tech. rep., 122 pp. DOI: 10.17895/ices.pub.5461.
- González-Pola, C., A. Lavín, and M. Vargas-Yáñez (2005). ‘Intense warming and salinity modification of intermediate water masses in the southeastern corner of the Bay of Biscay for the period 1992-2003’. In: *Journal of Geophysical Research: Oceans* 110.5, pp. 1–14. DOI: 10.1029/2004JC002367.
- Gregory, J. M., K. W. Dixon, R. J. Stouffer, A. J. Weaver, E. Driesschaert, M. Eby, T. Fichefet, H. Hasumi, A. Hu, J. H. Jungclaus, I. V. Kamenkovich, A. Levermann, M. Montoya, S. Murakami, S. Nawrath, A. Oka, A. P. Sokolov, and R. B. Thorpe (2005). ‘A model intercomparison of changes in the Atlantic thermohaline circulation in response to increasing atmospheric CO<sub>2</sub> concentration’. In: *Geophysical Research Letters* 32.12. DOI: 10.1029/2005GL023209.
- Häkkinen, S., P. B. Rhines, and D. L. Worthen (2016). ‘Warming of the global ocean: Spatial Structure and Water-Mass Trends’. In: *Journal of Climate* 29.13, pp. 4949–4963. DOI: 10.1175/JCLI-D-15-0607.1.
- Hallock, Z. R. (1987). ‘Regional Characteristics for Interpreting Inverted Echo Sounders (IES) Observations’. In: *Journal of Atmospheric and Oceanic Technology* 4, pp. 298–304. DOI: 10.1175/1520-0426(1987)004<0298:RCFIIE>2.0.CO;2.
- He, Y., D. R. Watts, and K. L. Tracey (1998). ‘Determining geostrophic velocity shear profiles with inverted echo sounders’. In: *Journal of Geophysical Research* 103.C3, pp. 5607–5622. DOI: 10.1029/97JC03439.
- Heuzé, C. (2017). ‘North Atlantic deep water formation and AMOC in CMIP5 models’. In: *Ocean Science* 13.4, pp. 609–622. DOI: 10.5194/os-13-609-2017.
- Holliday, N. P., M. Bersch, B. Berx, L. Chafik, S. Cunningham, C. Florindo-López, H. Hátún, W. Johns, S. A. Josey, K. M. H. Larsen, S. Mulet, M. Oltmanns, G. Reverdin, T. Rossby, V. Thierry, H. Valdimarsson, and I. Yashayaev (2020). ‘Ocean circulation causes the largest freshening event for 120 years in eastern subpolar North Atlantic’. In: *Nature Communications* 11.1. DOI: 10.1038/s41467-020-14474-y.
- Holliday, N. P., S. A. Cunningham, C. Johnson, S. F. Gary, C. Griffiths, J. F. Read, and T. Sherwin (2015). ‘Multidecadal variability of potential temperature, salinity and transport in

- the eastern subpolar North Atlantic'. In: *Journal of Geophysical Research: Oceans* 120. DOI: 10.1002/2015JC010762.
- Hu, X. and P. G. Myers (2013). 'A Lagrangian view of Pacific water inflow pathways in the Arctic Ocean during model spin-up'. In: *Ocean Modelling* 71, pp. 66–80. DOI: 10.1016/j.oceomod.2013.06.007.
- Hu, X., J. Sun, T. O. Chan, and P. G. Myers (2018). 'Thermodynamic and dynamic ice thickness contributions in the Canadian Arctic Archipelago in NEMO-LIM2 numerical simulations'. In: *The Cryosphere* 12.4, pp. 1233–1247. DOI: 10.5194/tc-12-1233-2018.
- Huthnance, J. (1986). 'The Rockall slope current and shelf-edge processes'. In: *Proceedings of the Royal Society of Edinburgh. Section B. Biological Sciences* 88, pp. 83–101. DOI: 10.1017/S0269727000004486.
- Iorga, M. C. and M. S. Lozier (1999). 'Signatures of the Mediterranean outflow from a North Atlantic climatology 1. Salinity and density fields'. In: *Journal of Geophysical Research: Oceans* 104.C11, pp. 26011–26029. DOI: 10.1029/1999JC900115.
- IPCC (2014). *Climate Change 2014: Synthesis Report. Contribution of Working Groups I, II and III to the Fifth Assessment Report of the Intergovernmental Panel on Climate Change [Core Writing Team, R.K. Pachauri and L.A. Meyer (eds.)]. IPCC, Geneva, Switzerland.* DOI: 10.1017/CB09781107415324.
- Johns, W. E., M. O. Baringer, L. M. Beal, S. A. Cunningham, T. Kanzow, H. L. Bryden, J. J. M. Hirschi, J. Marotzke, C. S. Meinen, B. Shaw, and R. Curry (2011). 'Continuous, array-based estimates of Atlantic Ocean heat transport at 26.5 N'. In: *Journal of Climate* 24.10, pp. 2429–2449. DOI: 10.1175/2010JCLI3997.1.
- Kalnay, E., M. Kanamitsu, R. Kistler, W. Collins, D. Deaven, L. Gandin, M. Iredell, S. Saha, G. White, J. Woollen, Y. Zhu, M. Chelliah, W. Ebisuzaki, W. Higgins, J. Janowiak, K. C. Mo, C. Ropelewski, J. Wang, A. Leetmaa, R. Reynolds, Roy Jenne, and Dennis Joseph (1996). 'The NCEP/NCAR 40-Year Reanalysis Project'. In: *Bulletin of the American Meteorological Society* 77, pp. 437–472. DOI: 10.1175/1520-0477(1996)077<0437:TNYRP>2.0.CO;2.
- Kieke, D. (2005). 'Water Mass Circulation and Variability in the Subpolar North Atlantic'. Universität Bremen.
- Kieke, D., B. Klein, L. Stramma, M. Rhein, and K. P. Koltermann (2009). 'Variability and propagation of Labrador Sea Water in the southern subpolar North Atlantic'. In: *Deep-Sea Research I* 56, pp. 1656–1674. DOI: 10.1016/j.dsr.2009.05.010.
- Kieke, D. and M. Rhein (2006). 'Variability of the Overflow Water Transport in the Western Subpolar North Atlantic, 1950-97'. In: *Journal of Physical Oceanography* 36.3, pp. 435–456. DOI: 10.1175/JPO2847.1.

- Killworth, P. D. (1983). ‘Deep convection in the world ocean’. In: *Reviews of Geophysics* 21.1, pp. 1–26. DOI: 10.1029/RG021i001p00001.
- Kuhlbrodt, T., A. Griesel, M. Montoya, A. Levermann, M. Hofmann, and S. Rahmstorf (2007). ‘On the driving processes of the Atlantic meridional overturning circulation’. In: *Reviews of Geophysics* 45.2. DOI: 10.1029/2004RG000166.
- Kwon, Y. O. and S. C. Riser (2005). ‘General circulation of the western subtropical North Atlantic observed using profiling floats’. In: *Journal of Geophysical Research C: Oceans* 110.10, pp. 1–22. DOI: 10.1029/2005JC002909.
- Lazier, J., R. Hendry, A. Clarke, I. Yashayaev, and P. Rhines (2002). ‘Convection and re-stratification in the Labrador Sea, 1990–2000’. In: *Deep Sea Research Part I: Oceanographic Research Papers* 49.10, pp. 1819–1835. DOI: 10.1016/S0967-0637(02)00064-X.
- Lherminier, P. (2018). ‘OVIDE 2018 cruise, RV Thalassa’. In: DOI: 10.17600/18000510.
- Lherminier, P., H. Mercier, T. Huck, C. Gourcuff, F. F. Perez, P. Morin, A. Sarafanov, and A. Falina (2010). ‘The Atlantic Meridional Overturning Circulation and the subpolar gyre observed at the A25-OVIDE section in June 2002 and 2004’. In: *Deep-Sea Research Part I: Oceanographic Research Papers* 57.11, pp. 1374–1391. DOI: 10.1016/j.dsr.2010.07.009.
- Lique, C., A. Treguier, B. Blanke, and N. Grima (2010). ‘On the origins of water masses exported along both sides of Greenland: A Lagrangian model analysis’. In: *Journal of Geophysical Research: Oceans* 115.C5. DOI: 10.1029/2009JC005316.
- Lozier, M. S., F. Li, S. Bacon, F. Bahr, A. S. Bower, S. A. Cunningham, M. F. de Jong, L. de Steur, B. deYoung, J. Fischer, S. F. Gary, B. J. W. Greenan, N. P. Holliday, A. Houk, L. Houpert, M. E. Inall, W. E. Johns, H. L. Johnson, C. Johnson, J. Karstensen, G. Koman, I. A. Le Bras, X. Lin, N. Mackay, D. P. Marshall, H. Mercier, M. Oltmanns, R. S. Pickart, A. L. Ramsey, D. Rayner, F. Straneo, V. Thierry, D. J. Torres, R. G. Williams, C. Wilson, J. Yang, I. Yashayaev, and Zhao J. (2019). ‘A sea change in our view of overturning in the subpolar North Atlantic’. In: *Science* 363.6426, pp. 516–521. DOI: 10.1126/science.aau6592.
- Lozier, M. S. and N. M. Stewart (2008). ‘On the temporally varying northward penetration of mediterranean overflow water and eastward penetration of Labrador sea water’. In: *Journal of Physical Oceanography* 38.9, pp. 2097–2103. DOI: 10.1175/2008JP03908.1.
- Madec, G., P. Delecluse, M. Imbard, and C. Levy (1998). *OPA 8 ocean general circulation model reference manual*.
- Madec, G. and NEMO System Team (2008). *NEMO ocean engine*. Notes Du Pôle De Modélisation. Institut Pierre-Simon Laplace (IPSL), France, No 27. Zenodo. DOI: 10.5281/zenodo.1464816.
- Marshall, J. and F. Schott (1999). ‘Open-ocean convection: Observations, theory, and models’. In: *Reviews of geophysics* 37.1, pp. 1–64. DOI: 10.1029/98RG02739.

- Masina, S., A. Storto, N. Ferry, M. Valdivieso, K. Haines, M. Balmaseda, H. Zuo, M. Drevillon, and L. Parent (2017). ‘An ensemble of eddy-permitting global ocean reanalyses from the MyOcean project’. In: *Climate Dynamics* 49.3, pp. 813–841. DOI: 10.1007/s00382-015-2728-5.
- McCarthy, G. D., P. J. Brown, C. N. Flagg, G. Goni, L. Houpert, C. W. Hughes, R. Hummels, M. Inall, K. Jochumsen, K. M. H. Larsen, P. Lherminier, C. S. Meinen, B. I. Moat, D. Rayner, M. Rhein, A. Roessler, C. Schmid, and D. A. Smeed (2020). ‘Sustainable Observations of the AMOC : Methodology and Technology’. In: *Reviews of Geophysics* 58. DOI: 10.1029/2019RG000654.
- Meinen, C. S. (2001). ‘Structure of the North Atlantic Current in stream-coordinates and the circulation in the Newfoundland basin’. In: *Deep-Sea Research Part I: Oceanographic Research Papers* 48.7, pp. 1553–1580. DOI: 10.1016/S0967-0637(00)00103-5.
- Meinen, C. S., S. L. Garzoli, W. E. Johns, and M. O. Baringer (2004). ‘Transport variability of the Deep Western Boundary Current and the Antilles Current off Abaco Island, Bahamas’. In: *Deep-Sea Research I* 51, pp. 1397–1415. DOI: 10.1016/j.dsr.2004.07.007.
- Meinen, C. S. and D. R. Watts (1998). ‘Calibrating Inverted Echo Sounders Equipped with Pressure Sensors’. In: *Journal of Atmospheric and Oceanic Technology* 15, pp. 1339–1345. DOI: 10.1175/1520-0426(1998)015<1339:CIESEW>2.0.CO;2.
- Meinen, C. S. and D. R. Watts (2000a). ‘Vertical structure and transport on a transect across the North Atlantic Current near 42°N: Time series and mean’. In: *Journal of Geophysical Research: Oceans* 105.C9, pp. 21869–21891. DOI: 10.1029/2000JC900097.
- Meinen, C. S., D. R. Watts, and R. A. Clarke (2000b). ‘Absolutely referenced geostrophic velocity and transport on a section across the North Atlantic Current’. In: *Deep-Sea Research Part I: Oceanographic Research Papers* 47.2, pp. 309–322. DOI: 10.1016/S0967-0637(99)00061-8.
- Mercier, H., P. Lherminier, A. Sarafanov, F. Gaillard, N. Daniault, D. Desbruyères, A. Falina, B. Ferron, C. Gourcuff, T. Huck, and V. Thierry (2015). ‘Variability of the meridional overturning circulation at the Greenland-Portugal OVIDE section from 1993 to 2010’. In: *Progress in Oceanography* 132, pp. 250–261. DOI: 10.1016/j.pocean.2013.11.001.
- Mertens, C., M. Rhein, M. Walter, C. W. Böning, E. Behrens, D. Kieke, R. Steinfeldt, and U. Stöber (2014). ‘Circulation and transports in the Newfoundland Basin, western subpolar North Atlantic’. In: *Journal of Geophysical Research: Oceans* 119, pp. 7772–7793. DOI: 10.1002/2014JC010019.
- Mertz, F., M. Pujol, and Y. Faugère (2018). *CMEMS Product User Manual for Sea Level SLA products, Issue 1.5*. EU Copernicus Marine Service.

- Mesinger, F. and A. Arakawa (1976). ‘Numerical methods used in atmospheric models’. In: *Global Atmospheric Research Programme (GARP) Publications Series 17*.
- Moritz, M., K. Jochumsen, D. Kieke, B. Klein, H. Klein, M. Köllner, and M. Rhein (in review). ‘Volume transport time series and variability of the North Atlantic Eastern Boundary Current at Goban Spur’. In: *Journal of Geophysical Research: Oceans*.
- Müller, V., D. Kieke, P. G. Myers, C. Pennelly, and C. Mertens (2017). ‘Temperature flux carried by individual eddies across 47°N in the Atlantic Ocean’. In: *Journal of Geophysical Research: Oceans* 122. DOI: 10.1002/2016JC012175.
- Müller, V., D. Kieke, P. G. Myers, C. Pennelly, R. Steinfeldt, and I. Stendardo (2019). ‘Heat and Freshwater Transport by Mesoscale Eddies in the Southern Subpolar North Atlantic’. In: *Journal of Geophysical Research: Oceans* 124.8, pp. 5565–5585. DOI: 10.1029/2018JC014697.
- Murray, R. J. (1996). ‘Explicit generation of orthogonal grids for ocean models’. In: *Journal of Computational Physics* 126.2, pp. 251–273. DOI: 10.1006/jcph.1996.0136.
- Myers, P. G. (2005). ‘Impact of freshwater from the Canadian Arctic Archipelago on Labrador Sea water formation’. In: *Geophysical Research Letters* 32.6. DOI: 10.1029/2004GL022082.
- Myers, P. G. and C. Donnelly (2008). ‘Water mass transformation and formation in the Labrador Sea’. In: *Journal of Climate* 21.7, pp. 1622–1638. DOI: 10.1175/2007JCLI1722.1.
- Myers, P. G. and C. Pennelly (pers. comm.).
- Nowitzki, H., M. Rhein, A. Roessler, D. Kieke, and C. Mertens (2021). ‘Trends and transport variability of the circulation in the subpolar eastern North Atlantic’. In: *Journal of Geophysical Research: Oceans* 126.2. DOI: 10.1029/2020JC016693.
- Østerhus, S., R. Woodgate, H. Valdimarsson, B. Turrell, L. De Steur, D. Quadfasel, S. M. Olsen, M. Moritz, C. M. Lee, K. M. H. Larsen, S. Jónsson, C. Johnson, K. Jochumsen, B. Hansen, B. Curry, S. Cunningham, and B. Berx (2019). ‘Arctic Mediterranean exchanges: A consistent volume budget and trends in transports from two decades of observations’. In: *Ocean Science* 15.2, pp. 379–399. DOI: 10.5194/os-15-379-2019.
- Palter, J. B. (2015). ‘The role of the Gulf Stream in European climate’. In: *Annual review of marine science* 7, pp. 113–137. DOI: 10.1146/annurev-marine-010814-015656.
- Perez, F. F., M. Fontela, M. I. García-Ibáñez, H. Mercier, A. Velo, P. Lherminier, P. Zunino, M. de la Paz, F. Alonso-Pérez, E. F. Guallart, and X. A. Padin (2018). ‘Meridional overturning circulation conveys fast acidification to the deep Atlantic Ocean’. In: *Nature* 554, pp. 515–518. DOI: 10.1038/nature25493.
- Petit, T., M. S. Lozier, S. A. Josey, and S. A. Cunningham (2020). ‘Atlantic deep water formation occurs primarily in the Iceland Basin and Irminger Sea by local buoyancy forcing’. In: *Geophysical Research Letters* 47.22. DOI: 10.1029/2020GL091028.

- Pickart, R. S., M. A. Spall, M. H. Ribergaard, G. W. K. Moore, and R. F. Milliff (2003). 'Deep convection in the Irminger Sea forced by the Greenland tip jet'. In: *Nature* 424.6945, pp. 152–156. DOI: 10.1038/nature01729.
- Reid, J. L. (1979). 'On the contribution of the Mediterranean Sea outflow to the Norwegian-Greenland Sea'. In: *Deep Sea Research Part A. Oceanographic Research Papers* 26.11, pp. 1199–1223. DOI: 10.1016/0198-0149(79)90064-5.
- Rhein, M., J. Fischer, W. M. Smethie, D. Smythe-Wright, R. F. Weiss, C. Mertens, D.-H. Min, U. Fleischmann, and A. Putzka (2002). 'Labrador Sea Water: Pathways, CFC inventory, and formation rates'. In: *Journal of Physical Oceanography* 32.2, pp. 648–665. DOI: 10.1175/1520-0485(2002)032<0648:LSWPCI>2.0.CO;2.
- Rhein, M., . Kieke, and R. Steinfeldt (2015). 'Advection of North Atlantic Deep Water from the Labrador Sea to the southern hemisphere'. In: *Journal of Geophysical Research: Oceans* 120.4, pp. 2471–2487. DOI: 10.1002/2014JC010605.
- Rhein, M., D. Kieke, S. Hüttl-Kabus, A. Roessler, C. Mertens, R. Meissner, B. Klein, C. W. Böning, and I. Yashayaev (2011). 'Deep water formation, the subpolar gyre, and the meridional overturning circulation in the subpolar North Atlantic'. In: *Deep-Sea Research II* 58, pp. 1819–1832. DOI: 10.1016/j.dsr2.2010.10.061.
- Rhein, M., C. Mertens, and A. Roessler (2019). 'Observed Transport Decline at 47°N, Western Atlantic'. In: *Journal of Geophysical Research: Oceans* 124.7, pp. 4875–4890. DOI: 10.1029/2019JC014993.
- Rhines, P., S. Häkkinen, and S. A. Josey (2008). 'Is oceanic heat transport significant in the climate system?' In: *Arctic-subarctic ocean fluxes*. Springer, pp. 87–109.
- Robert, A. J. (1966). 'The integration of a low order spectral form of the primitive meteorological equations'. In: *Journal of the Meteorological Society of Japan. Ser. II* 44.5, pp. 237–245. DOI: 10.2151/jmsj1965.44.5\_237.
- Roessler, A., M. Rhein, D. Kieke, and C. Mertens (2015). 'Long-term observations of North Atlantic Current transport at the gateway between western and eastern Atlantic'. In: *Journal of Geophysical Research: Oceans* 120, pp. 4003–4027. DOI: 10.1002/2014JC010662.
- Rosby, T. (1996). 'The North Atlantic Current and Surrounding Waters: At the Crossroads'. In: *Reviews of Geophysics* 34.4, pp. 463–481. DOI: 10.1029/96RG02214.
- Schmitz, W. J. and M. S. McCartney (1993). 'On the North Atlantic Circulation'. In: *Reviews of Geophysics* 31.1, pp. 29–49. DOI: 10.1029/92RG02583.
- Schneider, L., D. Kieke, K. Jochumsen, E. Colbourne, I. Yashayaev, R. Steinfeldt, E. Varotsou, N. Serra, and M. Rhein (2015). 'Variability of Labrador Sea Water transported through Flemish Pass during 1993-2013'. In: *Journal of Geophysical Research C: Oceans* 120.8, pp. 5514–5533. DOI: 10.1002/2015JC010939.

- Schott, F., L. Stramma, and J. Fischer (1999). ‘Interaction of the North Atlantic Current with the deep Charlie Gibbs Fracture Zone throughflow’. In: *Geophysical Research Letters* 26.3, pp. 369–372. DOI: 10.1029/1998GL900223.
- Schott, F., R. Zantopp, L. Stramma, M. Dengler, J. Fischer, and M. Wibaux (2004). ‘Circulation and Deep-Water Export at the Western Exit of the Subpolar North Atlantic’. In: *Journal of Physical Oceanography* 34.4, pp. 817–843. DOI: 10.1175/1520-0485(2004)034<0817:CADEAT>2.0.CO;2.
- Smith, G. C., F. Roy, P. Mann, F. Dupont, B. Brasnett, J. Lemieux, S. Laroche, and S. Bélair (2014). ‘A new atmospheric dataset for forcing ice–ocean models: Evaluation of reforecasts using the Canadian global deterministic prediction system’. In: *Quarterly Journal of the Royal Meteorological Society* 140.680, pp. 881–894. DOI: 10.1002/qj.2194.
- SROCC (2019). *IPCC Special Report on the Ocean and Cryosphere in a Changing Climate* [H.-O. Pörtner, D.C. Roberts, V. Masson-Delmotte, P. Zhai, M. Tignor, E. Poloczanska, K. Mintenbeck, A. Alegría, M. Nicolai, A. Okem, J. Petzold, B. Rama, N. M. Weyer (eds.)]
- Stendardo, I., B. Buongiorno Nardelli, S. Durante, D. Iudicone, and Kieke D. (pers. comm.).
- Stendardo, I. and N. Gruber (2012). ‘Oxygen trends over five decades in the North Atlantic’. In: *Journal of Geophysical Research: Oceans* 117.C11. DOI: 10.1029/2012JC007909.
- Stendardo, I., D. Kieke, M. Rhein, N. Gruber, and R. Steinfeldt (2015). ‘Interannual to decadal oxygen variability in the mid-depth water masses of the eastern North Atlantic’. In: *Deep-Sea Research Part I: Oceanographic Research Papers* 95, pp. 85–98. DOI: 10.1016/j.dsr.2014.10.009.
- Stendardo, I., M. Rhein, and R. Steinfeldt (2020). ‘The North Atlantic Current and its Volume and Freshwater Transports in the Subpolar North Atlantic, Time Period 1993 – 2016’. In: *Journal of Geophysical Research: Oceans* 125. DOI: 10.1029/2020JC016065.
- Stommel, H. (1961). ‘Thermohaline convection with two stable regimes of flow’. In: *Tellus* 13.2, pp. 224–230. DOI: 10.1111/j.2153-3490.1961.tb00079.x.
- Sy, A., M. Rhein, J. R. N. Lazier, K. P. Koltermann, J. Meincke, A. Putzka, and M. Bersch (1997). ‘Surprisingly rapid spreading of newly formed intermediate waters across the North Atlantic Ocean’. In: *Nature* 386.6626, pp. 675–679. DOI: 10.1038/386675a0.
- Talley, L. D. and M. S. McCartney (1982). ‘Distribution and circulation of Labrador Sea water’. In: *Journal of Physical Oceanography* 12.11, pp. 1189–1205. DOI: 10.1175/1520-0485(1982)012<1189:DACOLS>2.0.CO;2.
- University of Rhode Island (2015). *Inverted Echo Sounder User’s Manual IES Model 6.2C*.
- van Aken, H. M. and G. Becker (1996). ‘Hydrography and through-flow in the north-eastern North Atlantic Ocean: the NANSEN project’. In: *Progress in Oceanography* 38, pp. 297–346. DOI: 10.1016/S0079-6611(97)00005-0.

- Warren, B. A. (1983). ‘Why is no deep water formed in the North Pacific?’ In: *Journal of Marine Research* 41.2, pp. 327–347. DOI: 10.1357/002224083788520207.
- Watts, D. R. and H. Kontoyiannis (1990). ‘Deep-Ocean Bottom Pressure Measurement: Drift Removal and Performance’. In: *Journal of Atmospheric and Oceanic Technology* 7, pp. 296–306. DOI: 10.1175/1520-0426(1990)007<0296:DOBPM>2.0.CO;2.
- Watts, D. R. and T. Rossby (1977). ‘Measuring Dynamic Heights with Inverted Echo Sounders: Results from MODE’. In: *Journal of Physical Oceanography* 7, pp. 345–358. DOI: 10.1175/1520-0485(1977)007<0345:MDHWIE>2.0.CO;2.
- Watts, D. R., C. Sun, and S. Rintoul (2001). ‘A Two-Dimensional Gravest Empirical Mode Determined from Hydrographic Observations in the Subantarctic Front’. In: *Journal of Physical Oceanography* 31, pp. 2186–2209. DOI: 10.1175/1520-0485(2001)031<2186:ATDGEM>2.0.CO;2.
- Wett, S. (pers. comm.).
- Wunsch, C. (2002). ‘What is the thermohaline circulation?’ In: *Science* 298.5596, pp. 1179–1181. DOI: 10.1126/science.1079329.
- Xu, X., A. Bower, H. Furey, and E. P. Chassignet (2018). ‘Variability of the Iceland-Scotland overflow water transport through the Charlie-Gibbs Fracture Zone: Results from an eddy simulation and observations’. In: *Journal of Geophysical Research: Oceans* 123.8, pp. 5808–5823. DOI: 10.1029/2018JC013895.
- Zantopp, R., J. Fischer, M. Visbeck, and J. Karstensen (2017). ‘From interannual to decadal: 17 years of boundary current transports at the exit of the Labrador Sea’. In: *Journal of Geophysical Research: Oceans* 122.3, pp. 1724–1748. DOI: 10.1002/2016JC012271.



# Listings

## List of Figures

1.1	Map of the subpolar North Atlantic including the bathymetry and important names of basins and regional features. . . . .	2
1.2	Simplified circulation scheme of the North Atlantic including the Subpolar and Subtropical Gyre. . . . .	4
1.3	Simplified circulation scheme for the subpolar North Atlantic, mean satellite derived geostrophic surface velocity, mean satellite sea surface height and location of the NOAC array. . . . .	5
1.4	Meridional velocity from LADCP measurements in 2003 to 2017 at 47°N. . . . .	7
2.1	Locations of Argo float and shipboard CTD profiles used to calculate the transfer functions. . . . .	16
2.2	Boundary surfaces of the ocean in the NEMO model. . . . .	21
2.3	ANHA12 horizontal mesh. . . . .	21
2.4	Curvilinear coordinate system and arrangement of variables within the Arakawa C grid used in the NEMO model. . . . .	22
2.5	Lagrangian and Eulerian perspectives depicted by a control element in a flow field. . . . .	25
2.6	Initial positions and depths of particles tracked with the Lagrangian trajectory tool ARIANE along the 47°/48° and MAR PIES transects. . . . .	26
3.1	Transfer function between the SVA and the acoustic travel time. . . . .	30
3.2	Seasonal model for SVA for the reconstructed data from the eastern basin PIES and from BP12. . . . .	32
3.3	Correlation between acoustic travel time and GPA integrated between 250 dbar and 1900 dbar for the transfer function for PIES BP12 and the three eastern PIES. . . . .	33
3.4	SVA profiles for different acoustic travel times. . . . .	34

3.5	SVA from (a) CTD measurements from cruise MSM53 in 2016, (b) SVA based on the GEM reconstructed CTD profiles of this cruise, and (c) the difference between the CTD and GEM reconstructed section. . . . .	35
3.6	Transition area between the region of the GEM transfer function for BP12 and for the eastern PIES. (a) SVA from CTD measurements, (b) SVA reconstructed from GEM for eastern PIES BP32 – BP34, (c) SVA reconstructed from GEM for BP12. . . . .	36
3.7	Fofonoff potential for CTD profiles used to create the transfer function for eastern basin PIES and BP12. . . . .	41
3.8	Sketch explaining the calculation of volume transport across a defined section in the model. . . . .	45
4.1	Comparison of time series of barotropic, baroclinic and barotropic + baroclinic SSH fluctuations to satellite SSH fluctuations for PIES BP31, BP15, BP12, and BP32. . . . .	48
4.2	Correlation between the PIES-derived barotropic (bt), baroclinic (bc) and baroclinic + barotropic (bc+bt) contribution to SSH variability and satellite altimetry at the PIES positions. . . . .	49
4.3	Total (absolute baroclinic + barotropic) PIES derived transport as daily values and 10-day low pass filtered in the period April 2016 to June 2017. . . . .	51
4.4	Total top-to-bottom transport and transport below and above the 27.68 kg/m <sup>3</sup> potential density isoline for the segments <i>NAC Central</i> , <i>NAC East 1</i> and <i>NAC East 2</i> . . . . .	53
4.5	Absolute baroclinic PIES transport expanded with satellite altimetry (1993 - 2017). . . . .	54
4.6	Mean geostrophic velocities in 2016/2017 averaged over time periods with a larger northward and smaller transport across the <i>NAC Central</i> segment. . . . .	56
4.7	Bi-monthly and annual mean altimeter-derived surface velocities (absolute geostrophic velocities) perpendicular to the <i>NAC Central</i> segment for the period 1993 to 2017 east and west of the MAR crest. . . . .	57
4.8	Bi-monthly and annual mean transport time series at the NOAC site between 1993 and 2017, for the <i>NAC Central</i> segment, the sum of the eastern segments ( <i>NAC East 1</i> and <i>NAC East 2</i> ), the <i>NAC MAR</i> segment, and the <i>NAC West</i> segment. . . . .	59
4.9	Interior circulation scheme (boundary currents are excluded) at the NOAC array. . . . .	63

5.1	Mean surface velocity from model data, mean satellite-derived geostrophic surface velocity, location of the PIES and transport sections. . . . .	66
5.2	Mean cross-section velocity and standard deviation from model data and locations of the PIES for the 47°/48°N transect. . . . .	68
5.3	Mean cross-section velocity and standard deviation from model data and location of the PIES for the PIES MAR transect. . . . .	69
5.4	Comparison of PIES and model obtained transport. . . . .	71
5.5	Circulation scheme at the NOAC array from model and observations. . . . .	72
5.6	Trajectories of particles through the fracture zones. . . . .	77
5.7	Trajectories of particles seeded in box 1. . . . .	78
5.8	Probabilities of particles to cross grid cells of a horizontal mesh after having been seeded in box 1. . . . .	79
5.9	Trajectories of particles seeded in box 2. . . . .	80
5.10	Probabilities of particles to cross grid cells of a horizontal mesh after having been seeded in box 2. . . . .	81
5.11	Trajectories of particles seeded in box 3. . . . .	83
5.12	Probabilities of particles to cross grid cells of a horizontal mesh after having been seeded in box 3. . . . .	84
5.13	Trajectories of particles seeded in box 4. . . . .	85
5.14	Probabilities of particles to cross grid cells of a horizontal mesh after having been seeded in box 4. . . . .	86
5.15	Trajectories of particles seeded in box 5. . . . .	88
5.16	Probabilities of particles to cross grid cells of a horizontal mesh after having been seeded in box 5. . . . .	89
5.17	Bar plots showing the percentages of particles exchanged in forward mode between the five boxes. . . . .	91
5.18	Bar plots showing the percentages of particles exchanged in backward mode between the five boxes. . . . .	92
5.19	Trajectories for boxes 1 to 5 of particles having their origin on the subtropics. . . . .	94
5.20	Trajectories for boxes 1 to 5 of particles flowing into the Nordic Seas. . . . .	95
5.21	Trajectories of particles for boxes 1 to 5 which were transformed from lighter into denser water. . . . .	98
A.1	Comparison of PIES and model obtained transport. . . . .	110
A.2	Trajectories of particles starting in box 1 which flow through the CGFZ and FFZ compared to trajectories of particles that did not cross the fracture zones. . . . .	111

A.3	Trajectories of particles starting in box 1 which flow through the MFZ. . . . .	111
A.4	Probabilities of particles seeded in box 3 and 4 (tracked for ten years in backward mode) to cross grid cells of a horizontal mesh. . . . .	112
A.5	Bar plots illustrating the exchange of particles between two boxes. . . . .	113
A.6	Trajectories of particles following the routes 1-2, 1-3, and 1-5. . . . .	114
A.7	Trajectories of particles following the routes 2-1, 2-3, and 2-5. . . . .	115
A.8	Trajectories of particles following the routes 3-2, 3-4, and 3-5. . . . .	116
A.9	Trajectories of particles following the routes 4-3 and 4-5. . . . .	117
A.10	Trajectories of particles following the routes 5-1, 5-2, 5-3, and 5-4. . . . .	118
A.11	Bar plots illustrating the major routes of particles. . . . .	119
A.12	Major routes of particles ending in box 3. . . . .	120
A.13	Major routes of particles ending in box 4. . . . .	121

## List of Tables

2.1	Deployment positions, depths and deployment periods for the PIES. . . . .	14
2.2	Research cruises from which CTD data are used to create the transfer function for PIES BP12. . . . .	15
2.3	Research cruises from which CTD data are used to create the transfer function for PIES BP32, BP33, and BP34. . . . .	15
2.4	Number of particles seeded for ARIANE trajectory analysis in the different boxes four times per year in each year from 2006 to 2017 and the total number of seeded particles. . . . .	27
2.5	Horizontal extent of boxes used in the ARIANE analysis. . . . .	27
3.1	Effective degrees of freedom for the individual time series. . . . .	39
3.2	Summary of the estimated daily (1st value) and yearly (2nd value) uncertainties. . . . .	39
3.3	Mean Ekman transport and corresponding standard deviation in 2016/2017 and 1993 - 2017 across the different PIES transect. . . . .	45
4.1	Mean values, standard error of the mean, standard deviation, effective degrees of freedom, and decorrelation time scale for the PIES transport time series, April 2016 - June 2017. . . . .	50
4.2	Mean values, standard error of the mean, standard deviation, degrees of freedom, and decorrelation time scale for the PIES- and altimeter-based transport time series 1993 - 2017. . . . .	55

4.3	Long-term trends and mean transports in 1993 to 2017. . . . .	57
4.4	Correlation coefficients between annual mean flow components at 47°/48°N and across the MAR. . . . .	58
5.1	Correlation coefficients between annual mean flow components at 47°/48°N and across the MAR from model data. . . . .	74
5.2	Amount of particles seeded in boxes 1 to 5 which originate in the subtropics or flow into the Nordic Seas. . . . .	96



## Abbreviations

<b>ADCP</b>	Acoustic Doppler Current Profiler
<b>ADT</b>	Absolute Dynamic Topography
<b>AMOC</b>	Atlantic Meridional Overturning Circulation
<b>ANHA12</b>	Arctic and Northern Hemisphere Atlantic configuration of the NEMO model with 1/12° horizontal resolution
<b>bc</b>	baroclinic
<b>BSH</b>	Federal Maritime and Hydrographic Agency (Bundesamt für Seeschifffahrt und Hydrographie)
<b>bt</b>	barotropic
<b>CDPS</b>	Canadian Meteorological Center Global Deterministic Prediction System
<b>CGFZ</b>	Charlie-Gibbs-Fracture-Zone
<b>CGRF</b>	Canadian Meteorological Center Global Deterministic Prediction System reforecasts dataset
<b>CMC</b>	Canadian Meteorological Center
<b>CMEMS</b>	Copernicus Marine Environment Monitoring Service
<b>CTD</b>	Conductivity, Temperature, Depth
<b>DSOW</b>	Denmark Strait Overflow Water
<b>DWBC</b>	Deep Western Boundary Current
<b>EBC</b>	Eastern Boundary Current
<b>ESRL</b>	Earth System Research Laboratory
<b>FC</b>	Flemish Cap
<b>FFZ</b>	Faraday-Fracture-Zone

<b>GEM</b>	Gravest Empirical Mode
<b>GLORYS2v3</b>	Global Ocean Reanalysis and Simulations product by Mercator Ocean
<b>GPA</b>	Geopotential Anomaly
<b>GS</b>	Goban Spur
<b>IPCC</b>	Intergovernmental Panel on Climate Change
<b>ISOW</b>	Iceland-Scotland Overflow Water
<b>LADCP</b>	Lowered Acoustic Doppler Current Profiler
<b>LIM2</b>	Louvain-la-Neuve Sea-Ice Model
<b>LSW</b>	Labrador Sea Water
<b>MADT</b>	Mapped Absolute Dynamic Topography
<b>MAR</b>	Mid-Atlantic Ridge
<b>MDT</b>	Mean Dynamic Topography
<b>MFZ</b>	Maxwell-Fracture-Zone
<b>MOC</b>	Meridional Overturning Circulation
<b>MOW</b>	Mediterranean Outflow Water
<b>MSS</b>	Mean Sea Surface
<b>NAC</b>	North Atlantic Current
<b>NADW</b>	North Atlantic Deep Water
<b>NAO</b>	North Atlantic Oscillation
<b>NBR</b>	Newfoundland Basin Recirculation
<b>NCAR</b>	National Center for Atmospheric Research
<b>NCEP</b>	National Centers for Environmental Prediction
<b>NEMO</b>	Nucleus for European Modeling of the Ocean
<b>NOAA</b>	National Oceanic and Atmospheric Administration
<b>NOAC</b>	North Atlantic Changes
<b>OAR</b>	Office of Oceanic and Atmospheric Research
<b>OVIDE</b>	Observatoire de la Variabilité Interannuelle à Décennale
<b>OPA</b>	Océan PARallélisé
<b>PIES</b>	Pressure sensor equipped Inverted Echo Sounder

<b>PSL</b>	Physical Sciences Laboratory
<b>RV</b>	Research Vessel
<b>S</b>	Salinity
<b>SLA</b>	Sea Level Anomaly
<b>SPMW</b>	Subpolar Mode Waters
<b>SROCC</b>	IPCC Special Report on the Ocean and Cryosphere in a Changing Climate
<b>SSH</b>	Sea Surface Height
<b>Sv</b>	Sverdrup ( $1 \text{ Sv} = 10 \times 10^6 \text{ m}^3\text{s}^{-1}$ )
<b>SVA</b>	Specific Volume Anomaly
<b>SWF</b>	Southward Flow west of $41^\circ\text{W}$
<b>T</b>	Temperature
<b>WBC</b>	Western Boundary Current



## Publications

Parts of the results of this work are published in:

Nowitzki, H., Rhein, M., Roessler, A., Kieke, D., and Mertens, C. (2021). Trends and transport variability of the circulation in the subpolar eastern North Atlantic. *Journal of Geophysical Research: Oceans*, 126. DOI: 10.1029/2020JC016693

Preliminary results of this work were presented at the following international conferences, workshops, and seminars as first author:

Nowitzki, H., Rhein, M., Kieke, D., and Roessler, A. (2019). Transport and sea surface height variability of the North Atlantic Current studied with observational data from pressure sensor equipped inverted echo sounders. EGU General Assembly 2019, Vienna, Austria, poster.

Nowitzki, H., Rhein, M., Myers, P., Roessler, A., Kieke, D. (2018). Variability of the North Atlantic Current studied with PIES data and NEMO model output. ArcTrain Annual Meeting 2018, Jouvence, Canada, poster.

Nowitzki, H., Rhein, M., Roessler, A., and Kieke, D. (2018). Using Argo data for PIES data analysis. Argo User Meeting, Hamburg, Germany, talk.

Nowitzki, H., Rhein, M., Roessler, A., and Kieke, D. (2018). An estimate of AMOC related transports at 47°N in the eastern North Atlantic inferred from PIES data. Ocean Sciences Meeting 2018, Portland, U.S., talk.

Nowitzki, H., Rhein, M., Roessler, A., and Kieke, D. (2017). Variability of the circulation in the North Atlantic observed with pressure sensor equipped inverted echo sounders. ArcTrain Annual Meeting 2017, Bremen, Germany, talk.

Nowitzki, H., Rhein, M., Roessler, A., Kieke, D (2017). Exchange of heat, freshwater, and water masses between the western boundary, the North Atlantic Current, and between the western and eastern subpolar North Atlantic. ArcTrain Annual Meeting 2017, Bremen, Germany, poster.

Nowitzki, H., Rhein, M., Roessler, A., Kieke, D (2017). Variability of the North Atlantic Current: A comparison of satellite altimetry and observational data from PIES. EGU General Assembly 2017, Vienna, Austria, poster.

Nowitzki, H., Rhein, M., Roessler, A., Kieke, D (2017). Variability of transport and pathways of the North Atlantic Current: A comparison of satellite altimetry and observational data from pressure inverted echo sounders. DPG Spring Meeting 2017, Bremen, Germany, poster.

## Funding and Data Acknowledgment

This study was funded by the German Science Foundation (DFG) through the International Research Training Group ArcTrain ‘Processes and impacts of climate change in the North Atlantic Ocean and the Canadian Arctic’ (IRTG 1904 ArcTrain to M. Rhein). The shipboard and moored data at 47°/48°N – the NOAC array – are part of the North Atlantic / RACE programs funded by the German Ministry of Education and Research (Grants 03F0443C, 03F0605C, 03F0561C, and 03F0792A to M. Rhein). The Senate Commission of Oceanography of the DFG granted ship time and funds for logistics and consumables (to M. Rhein and D. Kieke). The assistance and technical support from the ship crew of RV Maria S. Merian are gratefully acknowledged. R. Steinfeldt (IUP-MARUM, University Bremen, Germany) was responsible for the calibration of all NOAC CTD data used to calculate the GEMs. The study has been conducted using E.U. Copernicus Marine Service Information (product identifier: SEALEVEL\_GLO\_PHY\_L4\_REP\_OBSERVATIONS\_008\_047). The NCEP/NCAR reanalysis data were provided by the NOAA/OAR/ESRL PSL, Boulder, Colorado, USA, and were downloaded from their web site at <https://www.psl.noaa.gov/data/gridded/data.ncep.reanalysis.surfaceflux.html> on 11 June 2020. The Argo float data (Argo, 2002) were collected and made freely available by the International Argo Program and the national programs that contribute to it (<https://www.argo.ucsd.edu>, <https://argo.jcommops.org>). The Argo program is part of the Global Ocean Observing System. Birgit Klein, Federal Maritime and Hydrographic Agency (BSH), Hamburg, Germany, kindly provided quality-controlled Argo data from the North Atlantic, which were downloaded 17 July 2018 (<https://www.doi.org/10.17882/42182#58010>). The research cruise CE17007 (2017) was carried out with the support of the Marine Institute (Ireland) and funded under the Marine Research Program 2014-2020 by the Irish Government. We thank Pascale Lherminier (Ifremer, France) for providing the CTD data of the cruises BOCATS (2016) and OVIDE (2018). Detailed information on the PIES, CTD and LADCP data for the MAR region can be found in Roessler et al. (2015) and for the western basin in Rhein et al. (2019). The CTD data from the RV Maria S. Merian research cruises are available from PANGAEA (MSM43: [www.doi.org/10.1594/PANGAEA.897988](http://www.doi.org/10.1594/PANGAEA.897988), MSM53: [www.doi.org/10.1594/PANGAEA.910842](http://www.doi.org/10.1594/PANGAEA.910842), MSM64: [www.doi.org/](http://www.doi.org/)

10.1594/PANGAEA.923550, MSM73: [www.doi.org/10.1594/PANGAEA.923565](http://www.doi.org/10.1594/PANGAEA.923565)). The PIES travel time and pressure fluctuation data for the eastern basin and additional data from the MAR region ([www.doi.org/10.1594/PANGAEA.925118](http://www.doi.org/10.1594/PANGAEA.925118)) as well as additional LADCP data for the eastern basin ([www.doi.org/10.1594/PANGAEA.922859](http://www.doi.org/10.1594/PANGAEA.922859)) are also available from PANGAEA. The model output was provided by X. Hu and the ocean modeling group of the University of Alberta and model data related research was supported by Westgrid and Compute Canada (<https://www.computecanada.ca>). For data analysis, the Matlab software, version R2014a, was used including the `m_map` (version 1.4, R. Pawlowicz, <https://www.eoas.ubc.ca/~rich/map.html>) and `seawater` (version 2.0.1, P. Morgan) toolboxes. Furthermore, the Matlab routines used for the data analysis in this study partly are based on Matlab routines written by members of the Oceanography Group of the University of Bremen and the Ocean Modeling Group of the University of Alberta.

# Acknowledgment

During the last years I learned that it does not only take a village to raise a child but also to work on and to submit a doctoral thesis. This thesis would not have been possible without the continuous support of many people to whom I want to express my gratitude.

First of all, I want to sincerely thank my supervisor Monika Rhein for her constant guidance and encouragement throughout all the stages of my PhD. I am grateful for all the possibilities I had thanks to her support - be it to experience my study region through research cruises or be it the participation in scientific conferences which provided valuable input for my own work. All this cannot be taken for granted and I value these experiences even more under today's home office circumstances.

I also want to thank Paul Myers for his warm welcome during my research stay in his working group at the University of Alberta and for his permanent interest in my work.

I further thank Gunnar Spreen for his interest in my work and for being the second reviewer for this thesis.

A special thanks to the whole Oceanography group in Bremen for always providing a friendly environment and all the open doors for scientific and non-scientific discussions. Achim, thank you for all your support and for answering to my endless questions from the very beginning of my PhD until even today. Dagmar and Ilaria, thank you for all the discussions we had, for all the input you provided, for encouraging me throughout the past years, and especially also for bringing our *North Atlantic Meeting* into life. Thank you Christian, for your valuable input and for the support with my manuscript. Many thanks also to my long-term once-upon-a-time-in-a-life-with-real-personal-contacts office mates Tilia, Linn, and Ilaria and to all members of the *North Atlantic Meeting* for all your support and the great working atmosphere.

Thanks to the whole ArcTrain community for always offering a very welcoming environment in whatever circumstances one meets, for the retreats, the annual meetings, the workshops, the scientific discussions, and for supporting my research stay in Canada.

I would further like to thank all crew members of the RV Maria S. Merian and cruise participants of the MSM64 and MSM73 cruises without whom the observation part of this thesis would not have been possible as well as all members of the Ocean Modeling group in Edmonton

without whom the model part of this work would not exist.

Finally, I wish to thank my parents and my brother for supporting me from the very beginning of my studies until today, for always having an eager interest in what I am doing, for the mental support as well as for accommodating me in the critical writing phase of this thesis when needed. A special thanks also to Kathrin, a true friend without whom I would not be where I am today and without whom I probably would neither have started nor finished this thesis. And last but not least: Thank you Moritz, for the strength you gave me during the last years, for moving with me to the north, for your understanding of what this PhD position meant to me and of my long phases of absence during the cruises and my research stay, for the IT support, and especially for being the great father you are for our daughter. Thank you Svea, for grounding me and showing me what really matters, for endlessly knocking on my door reminding me that there is a life outside of this thesis, and for teaching me to work most efficiently during night shifts when the one thing I desperately need is sleep.

# Declaration of Originality

I, Hannah Nowitzki, certify that the work presented here is, to the best of my knowledge and belief, original and the result of my own investigations, except as acknowledged, and has not been submitted, either in part or whole, for a degree at this or any other University. Large parts of Chapter 1, 2, 3, and 4, have been published in the peer-reviewed Journal of Geophysical Research, (Nowitzki et al., 2021). The text of the previously published chapters has been partially adapted in order to fit the context of a thesis.

Bremen, ..... ..